University of Southampton

Faculty of Engineering and Physical Sciences

School of Engineering

Functional Polymer Materials for Use in the Prevention of Thermal Runaway in Lithium-ion Batteries

by

Jonathan Peter Charles Allen

MEng

Thesis for the degree of Doctor of Philosophy

September 2022

University of Southampton

Abstract

Faculty of Engineering and Physical Sciences

School of Engineering

Thesis for the degree of Doctor of Philosophy

Functional Polymer Materials for Use in the Prevention of Thermal Runaway in Lithium-ion Batteries

by

Jonathan Peter Charles Allen

Functional polymers integrated with battery materials have been investigated as a potential safety measure in the prevention of thermal runaway within lithium-ion batteries. To this end a positive temperature coefficient of resistivity (PTCR) was explored to increase resistance of charge carriers at elevated temperatures prior to a thermal runaway event. Studies into the effectiveness of these PTCR responses and the impact of integrating the polymers on key cell performance metrics were performed. PTCR was identified for two different polymer systems.

Electrodeposited polyacrylonitrile (PAN) on graphite-composite anodes was one explored system. This system was intended to prevent thermal runaway via a shutdown effect at elevated temperatures that stopped the flow of ions and the resulting electrochemistry of the two electrodes. Chronoamperometry and cyclic voltammetry techniques were used to deposit a thin polymer layer. The techniques were performed with acrylonitrile monomers saturated with oxygen, the polymerisation was initiated via a reactive intermediate of superoxide anions produced from oxygen reduction at the cathode. The choice of electrode surface and exposure to air was found to be of critical importance to the microstructure of the films affecting the continuity of the polymer. Cracks within the polymer films were dependent upon film thickness with precise control of thickness possible by varying deposition times. Post-treatment annealing at 120 ^{o}C was also found to remove cracks but caused large changes to the microstructure.

Extensive lithium-ion cell testing was performed for electrodeposited PAN films. This was performed within a Swagelok cell using a standard lithium-ion half-cell assembly. Graphite-composites with PAN films formed the working electrode against a lithium metal counter-reference electrode. The electrolyte used was LP57; 1 M $LiPF_6$ in an ethylene carbonate (EC) and ethyl methyl carbonate (EMC) solvent, weight ratio of EC:EMC was 3:7. This was sandwiched between two copper current collectors with glass fibre separators between the electrodes. A trade-off between charge capacity and the effectiveness of the PTCR response was found. Thinner films provided better charge capacity whilst thicker films provided a greater shutdown between

80 °C and 100 °C resulting in reduced charge capacity at elevated temperatures. This temperature is competitive with other commercial alternative solutions to thermal runaway. For example Celgard separators that experience a shutdown around 130 °C and similarly to the PAN films also create a shutdown effect by stopping the flow of ions between electrodes. Both the PAN film response and Celgard response are irreversible leading to the observed shutdown of the cell being permanent.

Percolating composites were the second explored system, these were formed from a polymer matrix (polyacrylonitrile (PAN), polyvinylidene fluoride (PVDF), high-density polyethylene (HDPE), or low-density polyethylene (LDPE)) and a conductive filler (carbon or TiC). This material system was designed to stop thermal runway by restricting electron flow via a large PTCR response. A solvent cast method was used to form PAN and PVDF based composites, this was where the polymer and filler were dissolved and mixed within 1-methyl-2-pyrrolidinone (NMP). This mixture was subsequently spread onto copper foil and punched out after drying to form 11 mm diameter electrodes. HDPE and LDPE based composites were not easily soluble and so were formed via molten casting, the polymer and filler were mixed and melted at 130 °C onto copper foil on top of a hot plate. The melt was compressed using a glass rolling pin to reduce thickness and punched out after cooling to form 11 mm diameter electrodes. A percolation transition from insulating to conducting was identified at specific filler contents. TiC was found to require 60 % to 70 % content by mass, whilst carbon only needed 15 % to 25 %. The TiC composites formed a more brittle material as a result of the lower polymer content. Transition temperatures of each composite were identified using differential scanning calorimetry (DSC) along with the magnitude of the PTCR responses around these temperatures calculated using impedance measurements. Melting-transitions were found to be far more effective at producing a PTCR than glass transition due to far greater thermal expansion. LDPE-TiC composites were found to produce the greatest PTCR response while maintaining a low room temperature resistivity. The temperature of this response was also at a suitable temperature to prevent thermal runaway, 120 °C. Unlike the PAN films and commercial Celgard, the response of this system was found to be reversible upon return to ambient conditions allowing recovery and re-use of the battery system to be possible.

Percolating LDPE-carbon composites were briefly tested in a lithium-ion cell. The electrochemistry was largely unaffected with the exception of the first charge cycle where far greater capacities than typical were drawn. This was a result of the large amount of carbon introduced to the working electrode due to the LDPE-carbon composite resulting in far greater amounts of solid-electrolyte interface (SEI) formation.

Table of Contents

Table of Tables

Table of Figures

Research Thesis: Declaration of Authorship

Print name: JONATHAN PETER CHARLES ALLEN

Title of thesis: Functional Polymer Materials for Use in the Prevention of Thermal Runaway in Lithium-ion Batteries

I declare that this thesis and the work presented in it are my own and has been generated by me as the result of my own original research.

I confirm that:

1. This work was done wholly or mainly while in candidature for a research degree at this University;
2. Where any part of this thesis has previously been submitted for a degree or any other qualification at this University or any other institution, this has been clearly stated;
3. Where I have consulted the published work of others, this is always clearly attributed;
4. Where I have quoted from the work of others, the source is always given. With the exception of such quotations, this thesis is entirely my own work;
5. I have acknowledged all main sources of help;
6. Where the thesis is based on work done by myself jointly with others, I have made clear exactly what was done by others and what I have contributed myself;
7. Parts of this work have been published as:-
    - J. Allen, A. Hector, N. Garcia-Araez, “Cell design for the electrodeposition of polyacrylonitrile onto graphite composite electrodes for use in lithium-ion cells”, *Energy Reports*, vol. 7, pp. 15-19, 2021.

Signature: Jonathan Allen ..... Date: 15 February 2023.....

Acknowledgements

Firstly, I would like to thank my supervisor, Professor Andrew Hector, for the help, ideas, and enthusiasm with which he has guided me over the last few years. I would also like to thank my secondary supervisor Doctor Nuria Garcia-Araez for her incredibly helpful and insightful comments and assistance that have aided me in my research.

I owe a debt of gratitude to several people who provided their help and expertise with running experiments: in particular Dr Josh Whittam for all of his help and advice during electrodeposition studies and cell design; Nikolay Zhelev for his help in training myself to use several experimental techniques including SEM, Raman, and optical microscopy; Dr Niamh Ryall for her help with setting up lithium-ion Swagelok cells for electrochemical of electrode materials in a half-cell arrangement; Dr Tauqir Nasir for his help running SEM imaging during the Covid-19 pandemic as access to the equipment was limited to a few users; Wilma Anyfanti for her help running DSC measurements during the Covid-19 pandemic as access to the equipment was limited to a few users.

I would also like to gratefully acknowledge the CDT ESA and the UKCRIC for their financial support, which made this thesis possible.

Finally, special thanks go to: Dr Sherry Li Shao and Dr Gilles Moehl for helping me experience a social life outside of work; Dr Sam Fitch, Dr Niamh Ryall and Nicholas Hillier for much needed guidance and emotional support at several times over the course of my work; and my parents whose support over the course of my thesis helped me to see it through.

Definitions and abbreviations

AN	Acrylonitrile
ATRP	Atom-transfer radical polymerisation
C	Carbon
CA	Chronoamperometry
CV	Cyclic voltammetry
DMC	Dimethyl carbonate
DSC	Differential scanning calorimetry
e^-	An electron
EBA	Ethylene butylacrylate
EC	Ethylene carbonate
EDS	Energy dispersive X-ray spectroscopy
EDX	Energy dispersive X-ray spectroscopy (alternative abbreviation)
EMC	Ethyl methyl carbonate
EV	Electric vehicle
EVA	Ethylene vinyl acetate
HDPE	High-density polyethylene
HFP	Hexafluoropropene
LCO	Lithium cobalt oxide
LDPE	Low-density polyethylene
LFP	Lithium iron phosphate
LiBOB	Lithium bis(oxalate)borate
LMO	Lithium manganese oxide
LP57	1 M $LiPF_6$ in an ethylene carbonate (EC) and ethyl methyl carbonate (EMC) solvent, weight ratio of EC:EMC is 3:7

NMC	Nickel manganese cobalt oxide
NMP	1-methyl-2-pyrrolidinone
NTCR	Negative temperature coefficient of resistivity
P3OT	Poly(3-octylthiophene-2,5-diyl)
PAN	Polyacrylonitrile
PC	Propylene carbonate
PE	Polyethylene
PEIS	Potentio electrochemical impedance spectroscopy
PEO	Polyethylene oxide
PI	Polyimide
PLTB	Polymeric lithium tartaric acid borate
PMMA	Polymethyl methacrylate
PP	Polypropylene
PTCR	Positive temperature coefficient of resistivity
PVDF	Polyvinylidene fluoride
SEI	Solid-electrolyte interface
SEM	Scanning electron microscopy
SN	Succinonitrile
TBAP	Tetra butyl ammonium perchlorate
TGA	Thermogravimetric analysis
TiC	Titanium carbide

Chapter 1 Introduction

1.1 Battery polymers and the impact of thermal runaway

Polymers are among the key materials used within a battery. They have found use in several areas within such systems, aside from packaging and seals of cells. Traditional forms include separators to prevent internal short-circuiting [1] [2] and binders to hold electrode materials together [3]. Polymer electrolytes have also drawn interest, not just for use in lithium-ion batteries, but also other technologies such as supercapacitors [4] [5] [6]. As such, polymers have become essential to battery performance and modification.

The requirements for those polymers used within lithium-ion cells usually include the following: electrochemical and thermal stability, low ionic resistivity at ambient temperature, and good mechanical strength [1]. The low ionic resistivity is essential to allow the transport of ions through a separator or the electrode surface (see Figure 1). This is often achieved by infiltrating an electrolyte into the polymer rather than a fundamental property of the polymer itself. Depending on the location in which the polymer is being applied, other requirements become essential. Binders must be compatible with electrode materials at their operating potentials [7], whilst electrolytes need to be compatible with electrodes and provide good cyclability [5].

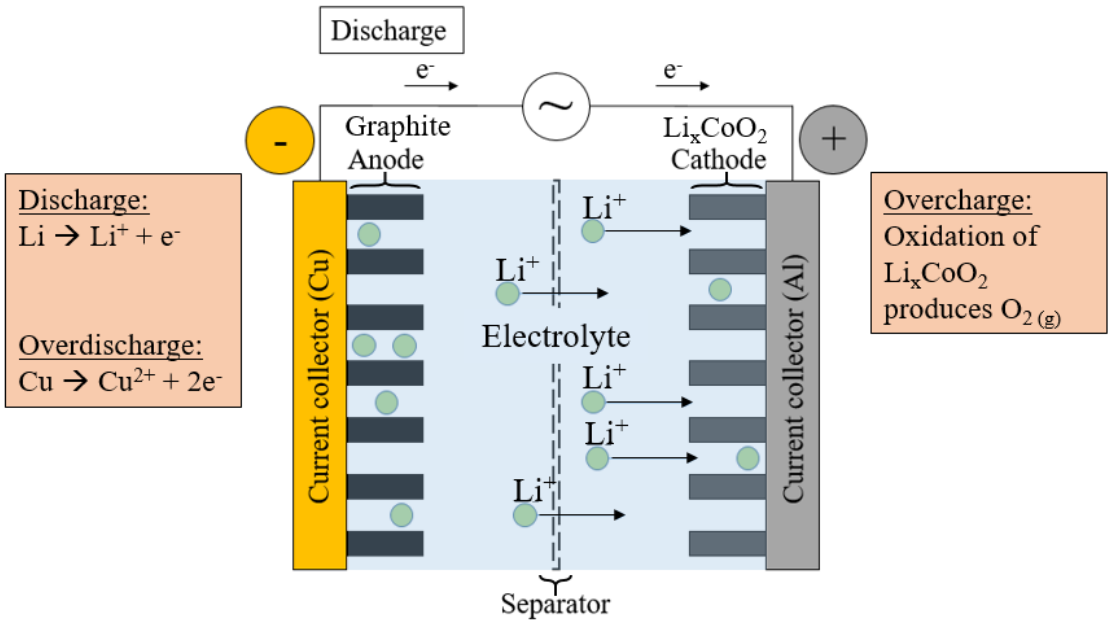

Figure 1: Transport of lithium ions for a typical battery discharge operation. Example effects of overdischarge on the anode and overcharge on the cathode are given.

One ongoing area of research is the use of polymers in the prevention of thermal runaway. Thermal runaway is one of the primary safety concerns for lithium-ion batteries and its prevention is a key area of research among industrial and scientific communities [8] [9] [10] [11]. It involves the build-up of heat due to electrochemical reactions within the cell, leading to faster reaction rates, higher temperatures, and more exothermic reactions (see Figure 2a). This positive feedback loop causes a propagating chain of decomposition reactions of the cell materials [2] [12]. Initiation can be caused by several abuse scenarios [2] [13]: mechanical abuse (punctures, excessive pressures), thermal abuse (operating the battery outside the safe temperature range), and electrical abuse (overcharging, excessive currents, operating the battery outside the safe potential range). Ultimately, the loop ends with an internal short circuit if the rate of heat generation out paces the rate of heat loss (see Figure 2b). At this point, thermal runaway begins and excessive temperatures are observed. Depending on materials, thermal runaway can reach a critical point at temperatures as low as 160 °C [12].

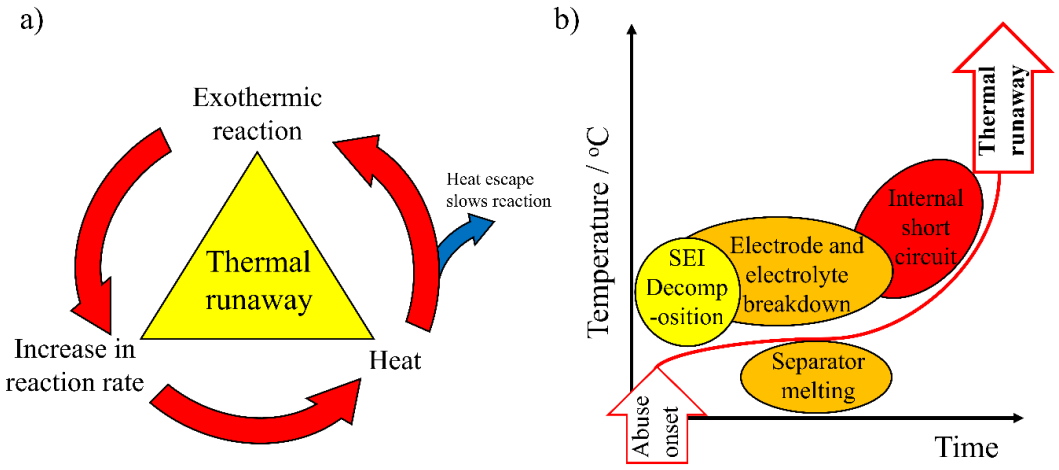

Figure 2: (a) Thermal runaway positive feedback loop; (b) Qualitative interpretation of the chain reactions during thermal runaway.

Abuse conditions reduce potential operating ranges for batteries limiting possible applications, such as fast charging in EVs. Because lithium-ion cells have become the battery of choice in most portable gadgets, finding reliable and cheap methods to improve their safety is of economic importance. The thermal runaway phenomenon has resulted in several news worthy events; for example: in 2016 Samsung Galaxy Note 7 smartphones caught fire prompting the withdrawal of thousands of electronic devices and severe economic losses [14], and in 2013 a Tesla Model S electric car caught fire after being damaged by road debris [15]. More recently, a fire at a home in Staffordshire caused by a lithium-ion battery in a hoverboard left a woman hospitalised in November 2021 [16]. This was caused by the hoverboard having been left charging without supervision. Tragically, thermal runaway has also led to the deaths of two firefighters in Beijing in April 2021 [17]. The fire started at a lithium-ion storage system connected to a rooftop solar panel

installation. This was likely due to variable quality of the cells used in the battery storage leading to excessive strains on the system. All these thermal runaway incidents highlight the ongoing risk to peoples well-being posed by these thermal runaway events and the need to prevent them from occurring. As such, there is significant industrial interest in preventing thermal runaway to expand potential markets alongside the obvious safety benefits.

Currently, several methods exist to respond to thermal runaway, which can be preventatives or fail-safes [18]. Preventatives include adding retardants to battery electrodes, electrolyte, or separators to reduce heat generation. These improve thermal stability reducing the likelihood of thermal runaway. Fail-safes stop or decrease damage caused by thermal runaway, and include shutdown separators and cell venting. Unfortunately, fail-safe measures tend to activate in such a way to render a cell inoperable, such as the melting of a shutdown separator or activating a thermal fuse [8]. Some thermal runaway safety measures involve building large or expensive external systems to the battery. Ancillary sensors for temperature or potential monitoring within a battery management system can also be used, but these responses may be delayed until after the cells behaves abnormally and damage has occurred. Varying materials within a battery can provide a smaller, more-refined, and immediate response [2]. There are several cases of polymers being used as both preventatives and fail-safes [2] [8].

Polymers used to prevent thermal runaway often rely on a positive temperature coefficient of resistivity (PTCR), which results in increases in material resistance at elevated temperatures [19]. Depending on the material and its application this PTCR can be either irreversible, leaving the cell inoperable, or reversible, allowing cell recovery after temperatures are normalised [19]. The effectiveness of such materials depends upon their PTCR intensity; in other words, the ratio of the resistivity from room temperature to elevated temperatures [20]. A larger PTCR intensity means a lower room temperature resistivity to a higher elevated temperature resistivity leading to a restriction in the flow of charged particles (electrons or ions) as temperature increases. This fundamentally results in a reduction in the flow of charges within a cell to prevent further electrochemical reactions and temperature increases. Polymers are highly tuneable, allowing reliable employment of a PTCR tailored to suit the required application. Polymer properties can be varied through several means such as: co-polymerisation, forming composites, and by varying chain length or structure. The PTCR results in automatic battery shutdown when temperature increases beyond a certain threshold. However, even relatively small increases up to 70 ^{o}C can result in irreversible structural damage to the electrodes that make up the cell [21]. Cell performance can then degrade or shutdown permanently. These cells would then naturally need replacing, leading to economic cost.

1.2 Thermal runaway effects on battery materials

Temperatures at which decomposition reactions occur are highly dependent on the materials used. Lithium-ion batteries themselves can use many different materials as anodes and cathodes, electrolytes, separators, and other components. As such, cell materials can be tailored to delay and aid in the prevention of thermal runaway [2].

The most common material for lithium-ion anodes is graphite, which develops a protective solid-electrolyte interface (SEI) layer during cycling [22]. However, this protective layer is also susceptible to breakdown as temperature increases. SEI decomposition occurs at lower temperatures than the breakdown of other cell materials. This tends to happen near to 69 °C [21], with some reports at temperatures as low as 57 °C [23]. SEI formation inherently produces gas; as the SEI is broken down it is also regenerated by reacting with lithium ions in the electrolyte releasing gases such as flammable hydrocarbons [24] [25]. Gassing increases internal pressures and can exacerbate abuse conditions. Cathode materials have a great variety in their thermal runaway onset temperatures and several studies have been performed on identifying the onset of self-heating for various cathodes in practical settings, such as use in an 18650 cell [26]. Excessive gassing in thermal runaway tests with lithium iron phosphate (LFP) was found by Golubkov *et al.* [27] at 195 °C, which is widely regarded among the safer cathode materials. Most other cathodes experience thermal runaway onset at temperatures far lower than this. Golubkov *et al.* [27] identified that nickel manganese cobalt oxide (NMC) experienced thermal runaway near 170 °C. Boxia *et al.* [26] found lithium manganese oxide (LMO) cathodes to have an onset around 110 °C, whilst Jhu *et al.* [28] found onset with lithium cobalt oxide (LCO) at temperatures as low as 116 °C.

Around 130 °C to 150 °C, the electrolyte and separator within the cell are no longer stable and decompose to generate more heat [12] [18]. One common lithium electrolyte is $LiPF_6$ in ethylene carbonate/dimethyl carbonate (EC/DMC) solvent [2]. As temperature increases, the anode and cathode react with electrolyte producing further heat and several by-products; hydrofluoric acid as well as several gases that increase pressure within the cell and are highly flammable. These include oxygen, carbon dioxide, carbon monoxide, and flammable hydrocarbons. Pressure build-up can lead to venting of the gases that can be ignited. Polyethylene (PE) is a commonly used polymer separator that melts around 85 to 140 °C [29] [30]. At this point, pores within the separator close making ion transfer difficult. This stops abuse conditions resulting from high current flow but is not useful against thermal abuse. Should the temperature further increase, the separator shrinks and collapses allowing the two electrodes to contact leading to an internal short circuit. This short circuit releases the greatest amount of heat during thermal runaway.

1.3 Polymer battery materials in the prevention of thermal runaway

Within the cell, there are four main polymer uses to stop thermal runaway or reduce the damage caused by it (see Figure 3) [2]. Separators are the most commonly used. As temperatures increase some are designed with a shutdown effect to stop ion flow between the electrodes [2] [13]. This occurs via a loss in porosity that typically coincides with a transition temperature, such as a melting point. The intention is to prevent further chemical reactions and stop or reduce heat generation; natural heat dissipation of the cell must then reduce the temperature to safe operating limits. Coatings or films [31] [32] are like shutdown separators in operation but the polymer is applied as a thin layer directly onto the electrode surface. Solid electrolytes [4] or gel-polymer electrolytes [5] [6] are another form that remove the need for liquid electrolyte systems and separators. Typically, they are made up of a non-conductive polymer host that is then infiltrated by conductive lithium salts into their pores. Solids have the dry lithium salts infiltrated into their polymer matrix, whilst gels are wetted by a liquid electrolyte. The thermal decomposition of liquid systems releases many flammable gases that increase internal pressures, worsening the situation. With the reduced usage of liquids comes the reduced release of such gases. Lastly are binders [19] [33]; these hold the conductive additives and sometimes active materials of the electrodes. If the binder polymer matrix has a large enough thermal expansion, temperature increases cause the binder to expand to the point that electronic pathways are broken preventing electrons from travelling to and from the reaction sites and hence preventing further chemical reactions.

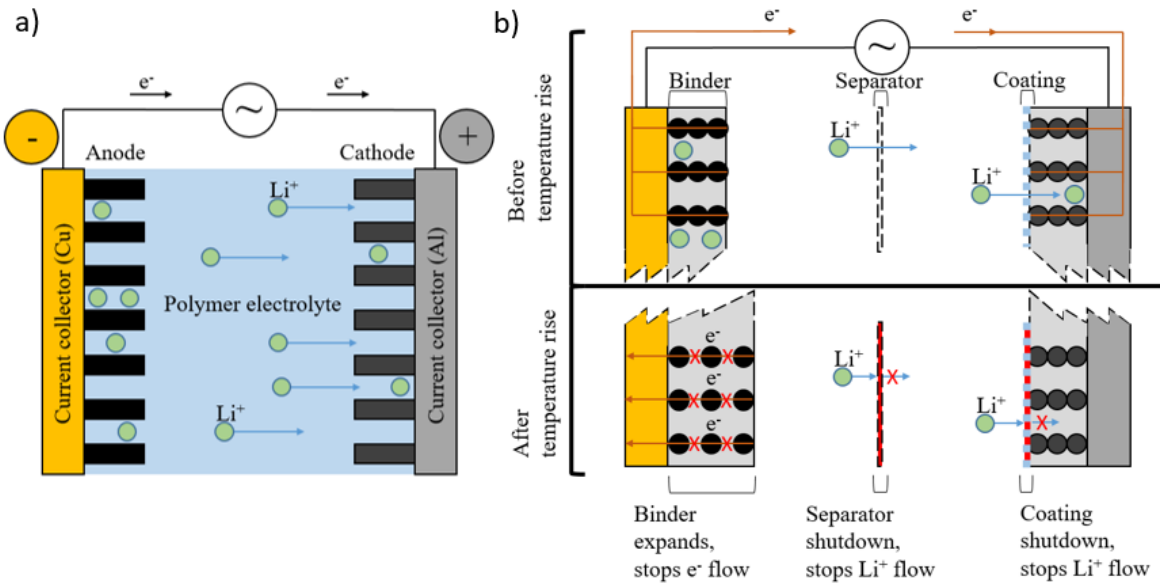

Figure 3: (a) Battery discharge operation with polymer electrolytes; (b) actions of preventative polymer components to the onset of thermal runaway.

Ideally, materials must be ionically conductive (or electronically for binder composites), have a PTCR, have a large PTCR intensity (the ratio of room temperature to elevated temperature resistivities), and not suffer degradation on recovery when returning to room temperature [19] [20]. The larger the PTCR intensity is the greater the shutdown effect. For several of the before mentioned applications, a suitable transition temperature is also important as this determines the point at which PTCR occurs. Both glass transition and melting are of interest as these are accompanied by increases in thermal expansion coefficients (see Table 1). It is worth noting that an increase in temperature often comes with a decrease in ionic resistivity in polymers, as the structure becomes more amorphous allowing for easier charge transport. However, for non-conductive polymer hosts an expansion in the polymer may result in an increase in resistivity if the pores through which liquid electrolyte infiltrates are closed off [34]. For the PTCR effect to be reversible, it is ideal to avoid a melting point in the material as this will come with unavoidable structural changes. Glass transition temperature and crystallinity of the materials can be altered via mixing or creating composite polymers.

Table 1: Common polymer materials that have been used in batteries as separators and binders with their respective glass transition and melting temperatures.

Polymer materials	**Glass transition temperature (°C)**	**Melting temperature (°C)**	**Common use within lithium-ion cells**
PVDF [30]	-30 to -20	155 to 185	Binder and separator
HDPE [30]	-125	130 to 140	Binder and Separator
LDPE [30]	-130	85 to 125	Binder and Separator
PAN [35]	95	325 to 350	Binder and Separator
Polypropylene [30]	-20 to -5	165 to 175	Separator
Polytetrafluoroethylene [30]	120 to 130	320 to 330	Binder and Separator
Polyvinyl chloride [30]	65 to 85	N/A	Separator
Polyamide [30]	40 to 60	210 to 220	Binder and Separator

1.3.1 Shutdown separators

Separator materials are typically made from a polymer that forms a gel electrolyte on wetting with a liquid electrolyte, allowing them to become ionically conductive. This allows the transport of lithium ions through the separator so the battery electrochemistry can occur. For shutdown responses this ionic transport is reduced or stopped by sealing pores though which ions can flow within the separator via a melt or some other transition [2].

Ideally, separators require a suitable melt temperature to allow shutdown of ion transport and a suitable collapse temperature to avoid an internal short-circuit [2]. By carefully selecting the polymer used or using combinations of polymers, melting and collapse temperatures can be tailored. Celgard have developed a polypropylene/polyethylene/polypropylene (PP/PE/PP) trilayer material; the PE has a melt temperature around 130 ^{o}C in Celgard [30], allowing a shutdown effect, whilst the PP provides mechanical strength on either side. There is little sign of shrinkage or collapse until the melt temperature of PP around 165 to 175 ^{o}C [36]. This allows thermal runaway to be slowed once temperatures above the PE melt temperature are reached. Unfortunately, once the shutdown effect has occurred the melt is irreversible and the cell becomes inoperable. The collapse temperature can also be an issue if heat generation is excessively high; temperatures may exceed the 175 ^{o}C before the shutdown response becomes effective. The collapse temperature of PP may be enhanced using ceramic coatings of Al_2O_3 and SiO_2 [37], giving reported temperatures between 200-260 ^{o}C [13] [38]. Other promising alternatives have been investigated, such as the polyimide/polyvinylidene fluoride/polyimide (PI/PVDF/PI) tri-layer [39]. Bi-layers can also be used, such as PP/PE or PVDF/PE [40].

Whilst PE is one of the most extensively researched shutdown separator materials, progress has also been made on polyacrylonitrile (PAN) shutdown separators [34] [41] [42]. Huai *et al.* [34] has reported for PAN-ethylene vinyl acetate (PAN-EVA) membranes a rapid increase in resistivity above 80 ^{o}C due to the swelling of the PAN polymer within the liquid electrolyte. This swelling cuts the ionic pathways resulting in a PTCR of several orders of magnitude. Melting temperatures for PAN are reported as low as 325 ^{o}C [31], meaning it maintains its mechanical strength until this point. The result is a shutdown effect that is also reversible. This material has greatly improved miscibility, avoiding reported leaking issues of PE and PP. PVDF shares these advantages but is more expensive [34].

1.3.2 Polymer electrolytes

Liquid electrolytes produce flammable gases upon decomposition [2], which can be significantly reduced by using polymer electrolytes. These come in two forms: solid-polymer electrolytes, and gel-polymer electrolytes [43]. Gel-polymers are formed from a solid that has been wetted with a standard liquid electrolyte, whilst the solid-polymer has no liquid at all. They have improved thermal stability and reduce the amount of liquid used (or remove it entirely in the case of the all-solid electrolyte), reducing potential sources of flammable gas. The main drawback is inferior power density due to high ionic resistivities, forming the greatest barrier to large-scale adoption [44] [45]. Gel polymer hosts require a substantial mechanical strength, as much is lost when they are wetted by electrolyte [4] [5] [6]. This loss of mechanical strength leads to poor practical application. Gel polymers tend to have limited operating temperatures up to 90 ^{o}C but improved room temperature resistivity [46].

An example solid polymer electrolyte is polyethylene oxide (PEO) mixed with $LiClO_4$ lithium salt, which is stable up to 120 ^{o}C. However, it has a high resistivity at room temperature and low voltage operation [47]. Composite polymer electrolytes can be formed, which may have varying resistivities between values of 4 x 10^5 Ω m for PEO_8-[$LiClO_4$] with α-Al_2O_3 filler to over 50 Ω m for $PEO_3PMMA_{0.3}$-[$LiClO_4$], a copolymer of PEO and polymethyl methacrylate (PMMA), with MgO 6 % by weight filler [48]. Resistivities in the magnitude of 10^4 Ω m for PEO_8-[$LiClO_4$] without any additional filler materials have also been reported. A different composite system is formed by casting lithium bis(oxalate)borate-succinonitrile-polyethylene oxide (LiBOB-SN-PEO) polymer electrolyte solution into porous polyimide nanofibrous films, which has been shown to operate at temperatures as high as 170 ^{o}C [49]. This has an ionic resistivity around 7 Ω m at 170 ^{o}C. For an example gel electrolyte, polymeric lithium tartaric acid borate @ PVDF-co-hexafluoropropene (PLTB@PVDF-HFP) is stable up to 80 ^{o}C, with ionic resistivities of 71 Ω m at 20 ^{o}C and 13 Ω m at 80 ^{o}C [50].

Promising polymer materials for use as solid [4] or gel electrolytes [5] would be those already in use within lithium-ion cells but in other forms. Such materials are known to satisfy basic requirements of an electrochemical system such as stability. A selection of these polymers is shown in Table 2. From a practical point of view, the polymers must satisfy several requirements [6]: low ionic resistivity (in the magnitude of 10 to 1 Ω m), high power density, thermal and electrochemical stability, and high mechanical strength.

Table 2: Polymers known to form both solid and gel electrolytes [4] [5] [6].

Polymer materials	**Ionic resistivity at ambient (Ω m)**	**Other information**
Poly (ethylene oxide) (PEO)	~10^6 to ~10^2 (depending on composite)	Extensively studied with many composite alternatives, wide stability window (<4.8 V).
Poly (acrylonitrile) (PAN)	~10^1	Appreciable transference number of 0.6 (the ratio of electric current contributed by Li^+ to the total electric current), wide stability window (<4.5 V). Undergo severe passivation upon contact with lithium metal anodes.
Poly (methyl methacrylate) (PMMA)	~10^1	Poor mechanical strength of plasticised PMMA. Wide stability window (<4.8 V). Variable transference number (0.4 to 0.7) depending on lithium salt used.
Poly (vinylidene fluoride) (PVDF)	~10^3 (reportedly 10^1 obtained [6])	Dielectric constant (8.4) assists in ionisation of salts. Reaction of Li and F forms LiF (poor safety)
Poly (vinylidene fluoride-hexafluoro propylene) (PVDF-HFP)	~10^2	PVDF crystalline phase acts as mechanical support, HFP amorphous phase helps trap liquid electrolyte.

1.3.3 Shutdown coatings

Thermo-responsive coatings are yet another application of polymers to prevent thermal runaway. Previous research by Ji *et al.* [31] investigated the use of a poly(3-octylthiophene-2,5-diyl) (P3OT) layer between a LCO cathode and the aluminium current collector. A strong PTCR effect is observed between 90-100 ^{o}C, which reduced cell capacity to 4 % of the theoretical. This effectively shuts down the cell before thermal runaway occurs. However, despite only being 1 µm in thickness a severe drop in capacity was experienced at ambient. Around 150 mA h g^{-1} was achieved under normal operating conditions. Theoretical capacity of LCO is 274 mA h g^{-1}, substantially higher than the polymer coated samples.

An alternative form of coating in the form of dispersed microspheres has also been investigated by Baginska *et al.* [32]. Three different approaches were made: 1) PE microspheres on the anode surface, 2) paraffin wax microspheres on the anode surface, and 3) PE microspheres on the separator surface. All three showed a shutdown effect as the temperature increased and the polymers softened then melted, cutting the ionic conduction pathways. Baginska *et al.* [32] specifically studied 4 µm thick layers of PE microspheres coated onto a graphite surface. Once again, a severe drop is experienced despite only applying a thin layer with reported capacities around 310 mA h g^{-1} or around 83 % of the theoretical capacity of graphite. Such capacity drops are common among studied coating materials and must be considered when performing any investigations into alternatives. The shutdown for this graphite coated with PE microspheres occurred at 110 ^{o}C and was incredibly effective reporting a remaining 7 % theoretical capacity.

1.3.4 Percolating binder composites

Polymers may also be used as electronically conductive composites, with conductive properties tailored using certain additives. The composites formed involve a non-conductive polymer matrix and a conductive filler that forms conduction pathways for electrons [19] [33]. For the purposes of mitigating thermal runaway, the matrix should have a high thermal expansion. As the temperature rises, the polymer expands resulting in the movement of the conductive particles. When expansion of the matrix is great enough, the conductive pathways separate and break preventing electronic conduction. This is the commonly accepted mechanism behind PTCR effects reported with such materials [33] [51]. These percolating composites may be mixed with the electrode active materials, as in Figure 3b, or applied as a coating on the electron pathway towards the electrodes.

Simple polymers involve the widely studied PE with conductive carbon black additive, showing a large resistivity increase around 130 °C [52]. The effect is also highly tailorable depending on not only the materials but also the proportions used. More complex carbon black particles in ethylene butylacrylate (EBA) copolymer matrix have been studied, showing a large increase in resistivity at around 60 °C [53]. Many PE composites, whether HDPE or LDPE, typically have a PTCR response around the melting point around 130 °C [52] to 145 °C [54]. Studies by Kono *et al*. [55] using PVDF-nickel composites found a PTCR increasing from 50 °C with 20 % nickel volume up to near the melting point of the polymer at 150 °C for 50 % nickel. This highlights a dependence on the proportions of filler materials used.

1.4 Polyacrylonitrile

PAN is a semi crystalline organic polymer with the formula $(C_3H_3N)_n$. Notable features of its unit structure include a cyano (CN) functional group attached on a polyethylene backbone [56], as shown in Figure 4. The polyethylene backbone has a large dipole between the electron-deficient carbon atoms and the electron-rich cyano group. This lends itself to relatively strong interactions between polymer chains, providing both mechanical strength and stability in various organic solvents. The unit structure also allows certain synthesis methods from the acrylonitrile (AN) monomers to be pursued, as explained later within this section.

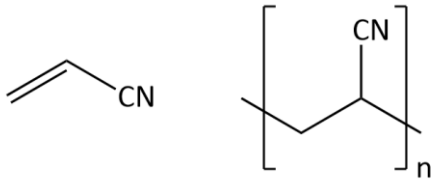

Figure 4: Molecular structure of AN monomers (left) and PAN polymers (right).

PAN is predominantly a white powder and displays thermoplastic properties. However, under atmospheric conditions it will undergo thermal degradation to carbon fibres becoming darker. As a result, PAN needs to be melted in the absence of oxygen or other oxidising mediums otherwise it will undergo oxidative stabilisation in the region of 180-300 °C [57], as shown in Figure 5. If oxygen is present, the thermal oxidation induces the degradation of PAN to carbon fibres. Due to PAN possessing a relatively high glass transition temperature, around 95 °C [35] [58] [59], polymer chains exhibit a low thermoplasticity below this temperature and are difficult to mould and shape when compared to other commercial plastics. The temperature of the glass transition can be

modified through copolymerisation or the addition of plasticisers in order to make the polymer less brittle and easier to shape. Crystallised PAN has a high melting temperature around 325 °C [35] [58] making it a useful choice for high temperature applications. Its limited solubility in common organic solvents coupled with superior mechanical properties of its fibres is due to intermolecular forces between polymer chains [56]. For chemical stability against chemical reagents, the nitrile group has relatively low reactivity against most chemical materials.

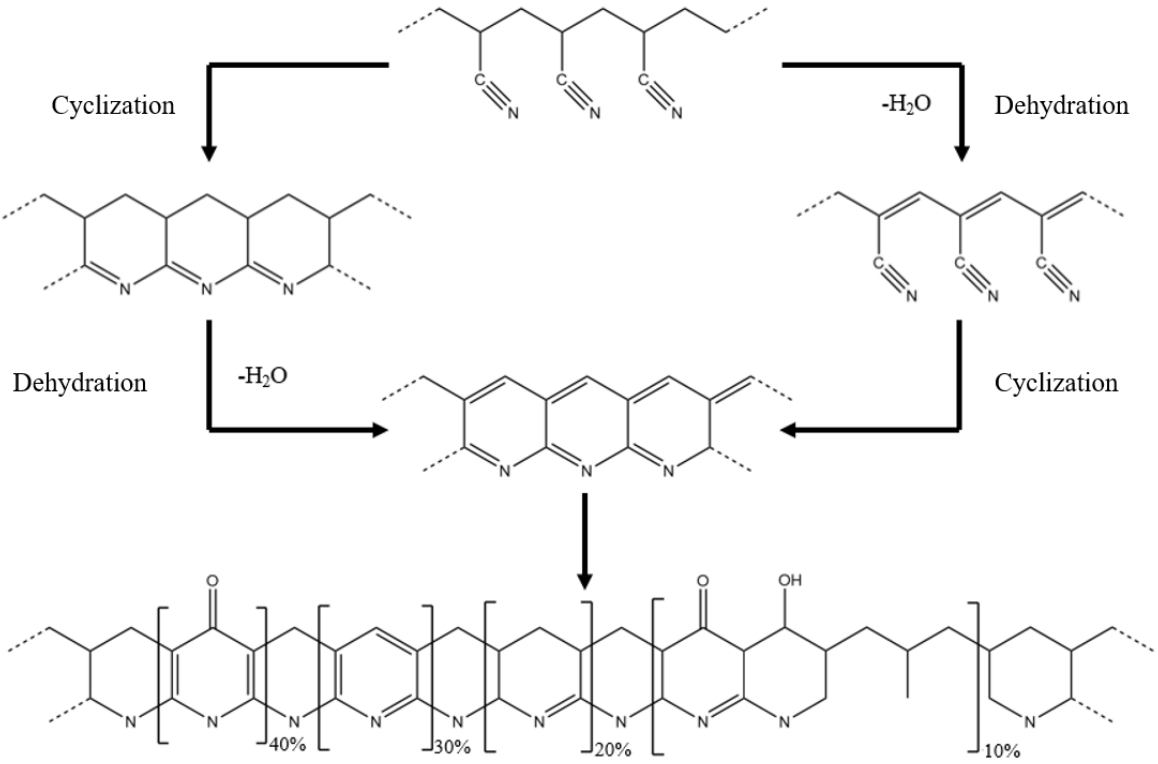

Figure 5: Proposed chemistry of PAN oxidative stabilisation. Figure adapted from [57].

With respect to utilisation of PAN as a material, PAN has the following well-known characteristics [56]: low density, thermal stability, high strength, high modulus of elasticity, and good chemical stability against most chemical solvents. These properties have established PAN as an essential polymer material in the chemical industry and a key role in high-tech industry. For an example, because of its transparency, higher barrier ability for gas and low swellability in chemicals, PAN is used as wrapping materials for foods, chemicals, drugs, electronics and cosmetics. Due to the chemical stability and hydrophilicity of PAN, PAN is used as nonwoven meshes for ultrafiltration, inner support of hollow fibres for reverse osmosis membranes, and membrane support, especially in biotechnology and environmental engineering applications. Other applications of PAN are found due to the high-strength fibres yielding a good material for outdoor awnings like tents, sails for yachts, knitted clothing like socks and sweaters, and fillers for high-strength materials for military and commercial aircrafts.

The vinyl group of the AN unit monomer is stabilised by bonding with the cyano group. This provides the carbon backbone of the monomer with electron-deficient behaviours due to the strong electron-withdrawing ability of the cyano group. Several synthesis routes for PAN can be used taking advantage of the monomer properties [58].

Commercially, PAN is synthesised via free radical polymerisation without control over molecular structure. Simple co-polymerisations with various vinyl compounds and covalently linked composite materials with other polymers and nanomaterials have been prepared in similar radical polymerisation. For example, the mixture of starch and Ce^{4+} ion (redox initiator) can initiate polymerisation of AN, known as starch grafting [56], and the following hydrolysis of the cyano group produces superabsorbent hydrogel with water absorption larger than 400 times its weight [60]. Controlled radical polymerisation of AN with narrow distribution can be accomplished by using atom-transfer radical polymerisation (ATRP) catalysed by a copper complex [61]. Dithioesters [62], alkoxyamines [63], and nitroxides [64] are also usable for controlled radical polymerisation of AN.

PAN can also be prepared by anionic polymerisation, which shows better control than free radical polymerisation. This is initiated by reducing AN monomers to form a radical monomer unit that then propagates the addition of further AN monomers [56]. The monomer unit AN is determined as a C group monomer in Tsuruta's classification, indicating sodium alkoxide, alkyl zinc, and alkyl aluminium can initiate its polymerisation [56]. However, the living character of anionic polymerisation is lost because of side reactions such as attack on α-protons activated by the cyano groups or direct attack of the propagating anion on the cyano groups. This causes lower molecular weight, non-uniform chain lengths, and an uneven polymer chain growth rate compared to radical polymerisation [65]. The side reactions cause branched structures or deactivation of active sites.

Coordination polymerisation is also applicable to the synthesis of PAN by employing alkyl iron, alkyl copper, or rare earth complexes. Current researchers have discovered that, in some coordination polymerisations systems of AN, the polymerisation proceeds according to anionic polymerisation mechanism [66].

1.4.1 Polyacrylonitrile as an electrografted coating

In 1982, Lécayon *et al.* [67] published a pioneering report demonstrating the effective electrografting of PAN onto metal surfaces via an anionic polymerisation mechanism. The report

showed that metal surfaces can be coated with PAN films by using an electropolymerisation approach induced by the reduction of the monomer unit. It was proposed that the polymerisation initiated with the reductive adsorption of one monolayer of the monomer on the metal surface, which was assumed to involve one electron per adsorbed molecule. It was found that the PAN film coatings had very good adhesion to the metal electrode, which was ascribed to the formation of a chemical bond between the polymer and the metal surface, shown in Figure 6 [68] [69]. A strongly adhering, thin, insulating polymer layer deposits on the electrode surface. Further research showed that covalently attached polymer thin films are stable in both aqueous and non-aqueous chemical environments, elevated temperatures, and moderate potential windows [70]. According to electrochemical impedance measurements, metal surfaces with an electrodeposited PAN coating are more effective at blocking ion transport than a solvent cast PAN film. On carbon, the polymer layer yields a more robust electrode coating that is capable of a self-assembly morphology.

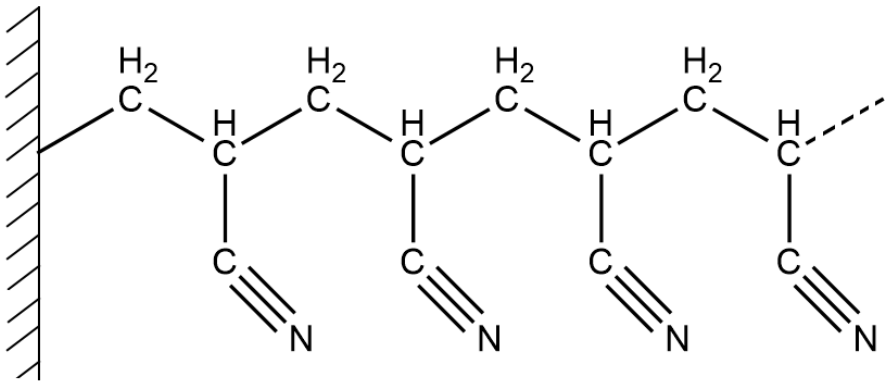

Figure 6: Structure of the electrografted PAN on metal electrodes, formed via cathodically induced anionic polymerisation [68] [69].

More recently, Lacey *et al.* [41] and El-Enany *et al.* [42] studied the electrodeposition of PAN onto glassy carbon and found that in the presence of molecular oxygen the polymerisation started at less cathodic potentials. This was ascribed to the involvement of a superoxide species in the polymerisation process, formed as the product of the one electron reduction of oxygen. Using electrochemical quartz crystal micro balance experiments, combined with cyclic voltammetry measurements, they demonstrated the successful deposition of the polymer on the glassy carbon electrode. However, the mechanism of electropolymerisation in the presence of oxygen is not fully understood and it is not clear if the involvement of superoxide affects the final structure of the polymer coating.

Earlier work by Baute *et al.* [71] and Mertens *et al.* [72] demonstrated the potential employed for the cathodic polymerisation critically affects the final structure of the polymer coating. By performing electrochemical quartz crystal micro balance experiments coupled with cyclic

voltammetry measurements they could identify that when electrodeposition was conducted at mildly cathodic potentials, close to the onset of the electroreduction of the monomer, then a polymer coating fixed to the electrode was obtained. However, when electrodeposition was performed at more cathodic potentials, then the attachment of the polymer coating to the electrode was weak.

Lacey *et al.* [41] and El-Enany *et al.* [42] went into detail on the initiation of their polyacrylonitrile films. The monomer should be used in a non-aqueous organic solvent under a dry atmosphere. The conducting surface of the working electrode will develop a uniform layer of the intended polymer within a few seconds of reaching the appropriate working potential, which will result in the passivation of the electrode surface. The polymerisation itself, in this case, is initiated by superoxide anion radicals that react with the vinyl group of AN monomers [41]. Propagation of the polymer chain should then follow an anionic polymerisation mechanism. It is generally recognised that the O_2/O_2^- redox couple is quasi-reversible in aprotic solvents such as acetonitrile, where the superoxide radical anion has a half-life of approximately 40 minutes at room temperature in the presence of tetraalkylammonium cations [73] [74] [75]. Therefore, there is ample time for the polymerisation to occur after the formation of superoxide. O_2/O_2^- is a moderately strong nucleophile, which reacts with sufficiently active Michael acceptors (e.g. vinyl groups with an electron-withdrawing substituent, such as acrylonitrile). Indeed, the use of electrogenerated superoxide as a nucleophile in organic synthesis is reported in the literature [76], as is the use of potassium superoxide as an initiator for the polymerisation of a range of vinyl monomers [77].

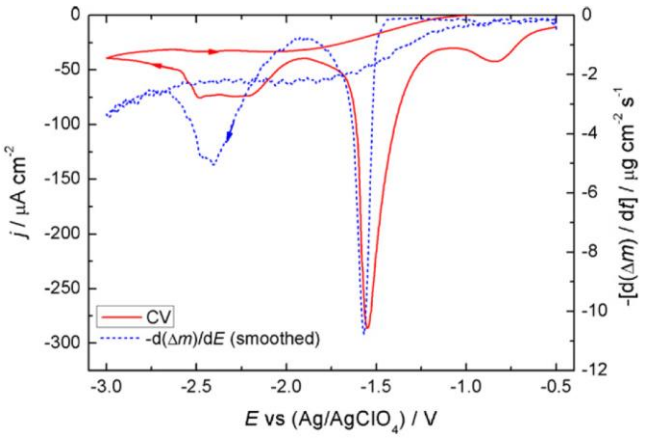

Figure 7: Cyclic voltammogram and mass change from electrochemical quartz microbalance study for the first cycle of air-saturated acrylonitrile electrografting containing 50 mmol dm^{-3} TBAP on a 1.37 cm^2 gold disc electrode against $Ag/AgClO_4$ at a scan rate of 50 mV s^{-1}. Figure from: [41].

Cyclic voltammograms for the electrografting of acrylonitrile solvent with 0.05 mol dm^{-3} tetra butyl ammonium perchlorate (TBAP) supporting electrolyte onto a gold disc electrode can be seen in Figure 7 [41]. The first notable feature to observe on a CV, according to Lacey *et al.* [41], will be a peak for oxygen reduction to superoxide anions at -1.6 V *vs.* $Ag/AgClO_4$, termed the superoxide trigger. These superoxide anions initiate polymerisation with AN monomers, reducing the monomer unit to form a radical anion. The superoxide anion reaction with the electron deficient vinyl group of AN is shown in Figure 8. As anions are involved the process can be treated as an anionic polymerisation. The superoxide chemical bond with the growing polymer chain is later substituted for a chemical bond to the electrode surface, grafting the polymer to the electrode [41]. Superoxide then decays back to an oxygen molecule within the electrolyte over time.

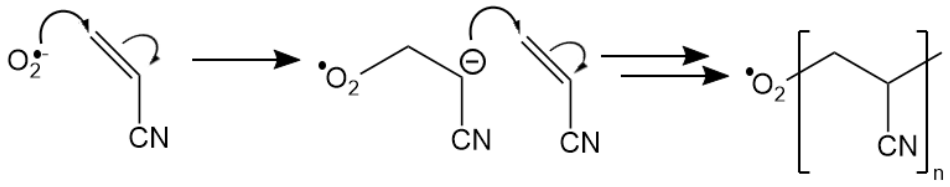

Figure 8: Suggested reaction mechanism for the polymerisation of acrylonitrile by electrogenerated superoxide anions [41].

A second broad peak corresponding to the reduction of AN monomers can also be observed around -2.5 V *vs.* $Ag/AgClO_4$ [41]. Literature suggests that the reduction of a vinyl group to form a radical anion in reductive electrografting takes place between -2.0 V to -2.5 V *vs.* $Ag/AgClO_4$ [78]. It is this reduction of the vinyl group to form the radical anion that is the accepted mechanism for the electropolymerisation of vinyl monomers in aprotic solvents [70].

It is at the two CV features around -1.6 V and -2.5 V *vs.* $Ag/AgClO_4$ that the largest change in mass is detected using an electrochemical quartz microbalance study [41]. Before the superoxide anions form, no mass change is observed. Figure 9 shows the mass change over three cycles [41]. Most deposition occurs in the first cycle, with reducing amounts in successive cycles. This indicates a self-limiting growth behaviour.

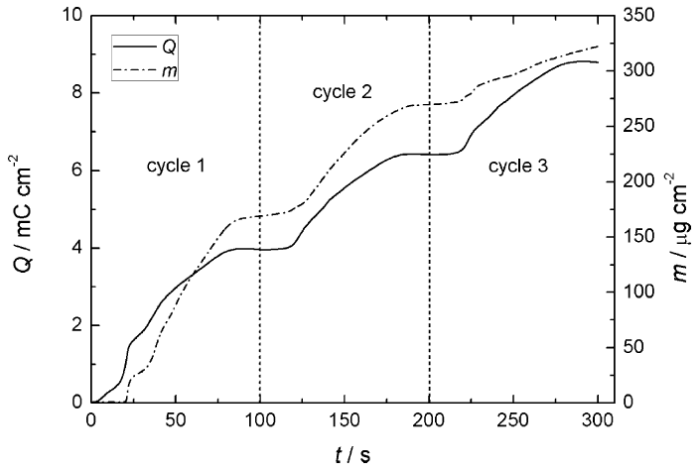

Figure 9: Charge and film mass change over time for the first three cycles of the electrodeposition of PAN from air saturated AN containing 50 mmol dm^{-3} TBAP on a 1.37 cm^2 gold disc at a scan rate of 50 mV s^{-1}. Figure from: [41].

Chain propagation in the electrografting process of methacrylonitrile can be seen in Figure 10 [78]. A chemical bond is formed between a conductive surface (normally metal or carbon) and the polymer to form a thin film. As the electrografting reaction is a reduction it takes place at the cathode and the species responsible for the growth of the layer is an anion; the process is therefore an anionic polymerisation. The steps are as follows:

1. Monomer adsorption. Electron transfer creates a radical anion that covalently binds to the conductor. The anion is achieved via superoxide initiation in the proposed Figure 8.
2. The bonded anion is not stable because of the negative charge being repelled by the negative electrode and is subsequently stabilised by the attack of a new monomer.
3. A bonded dimer anion is created.
4. Anionic polymerisation continues moving the charge further from the electrode.
5. Chain termination via the addition of a proton. No proton providing species are present during the acrylonitrile studies of Lacey *et al.* [41], so termination may occur through typical radical terminating methods, due to recombination or disproportionation [79].
    a. Recombination, two radical polymers meet and form one terminated chain.
    b. Disproportionation, two radical polymers meet and terminate via proton exchange, one forms a saturated polymer and the other has a single unsaturated C=C bond.

A second proposed route for polymerisation in solution branches off from step **2**, represented by step **6**. The radical monomer may desorb from the surface and become the origin for polymers in the solution. These need to be washed away after grafting as these polymers are not bonded to the conductive surface but are still present. It should be noted that in this proposed mechanism, only the initiation step is electrochemical whilst chain growth and propagation is purely chemical.

Despite the studies on electrodepositing PAN onto metal surfaces by Lécayon *et al.* [67] and glassy carbon by Lacey *et al.* [41] and El-Enany *et al.* [42] discussed, no attempts have been made onto practical lithium battery electrodes. Lacey *et al.* [41] and El-Enany *et al.* [42] went as far as to

suggest that the electrodeposition of PAN could be used to facilitate gel-electrolytes within a lithium system but did not pursue this in the literature. As such, these studies can be used as a basis to explore the novelty of electrodeposition of PAN onto standard lithium electrodes, such as graphite-composite anodes or lithium metal oxide cathodes. PAN has been reported in gel-electrolyte systems, such as lithium-ion batteries and supercapacitors, formed via blending and mixing rather than electrodeposition [5] [6]. However, the electrodeposition techniques control of deposit mass is potentially crucial in controlling thickness of the deposit and potential resistivities imposed onto the battery system as a consequence. Forming a polymer coating at the electrode surface can also provide several advantages to simplify the schematic of a typical lithium-cell. These include [43] [44] [45]: no internal shorting removing the need for separator materials, and a decrease in the amount of liquid electrolyte reducing a source of gas production that can combust and exacerbate thermal runaway conditions. However, standard electrodes are not typical planar surfaces as often studied for electrodeposition, but are a composite of powders. The materials that form an electrode are typically: active materials, conductive additives, and binders. Therefore, electrodeposition may differ from that in literature and would require further study.

The chemistry and structure of electrodeposited PAN films is far simpler compared to other competitive polymers used to prevent thermal runaway. For instance, commonly used Celgard separators make use of a trilayer of PP/PE/PP that are formed through several manufacturing stages such as coating and calendaring laminated layers [36] as opposed to a single-step electrodeposited PAN layer. Celgard also has a poor miscibility with polar electrolyte solvents, a disadvantage that PAN does not share [34]. For electrodeposited PAN, no cross-linking or co-polymerisation is required unlike PAN separator materials for thermal runaway prevention reported on by Huai *et al.* [34]. Therefore, there are several advantages to pursing PAN electrodeposited coatings as an area of research in the prevention of thermal runaway in lithium-ion batteries.

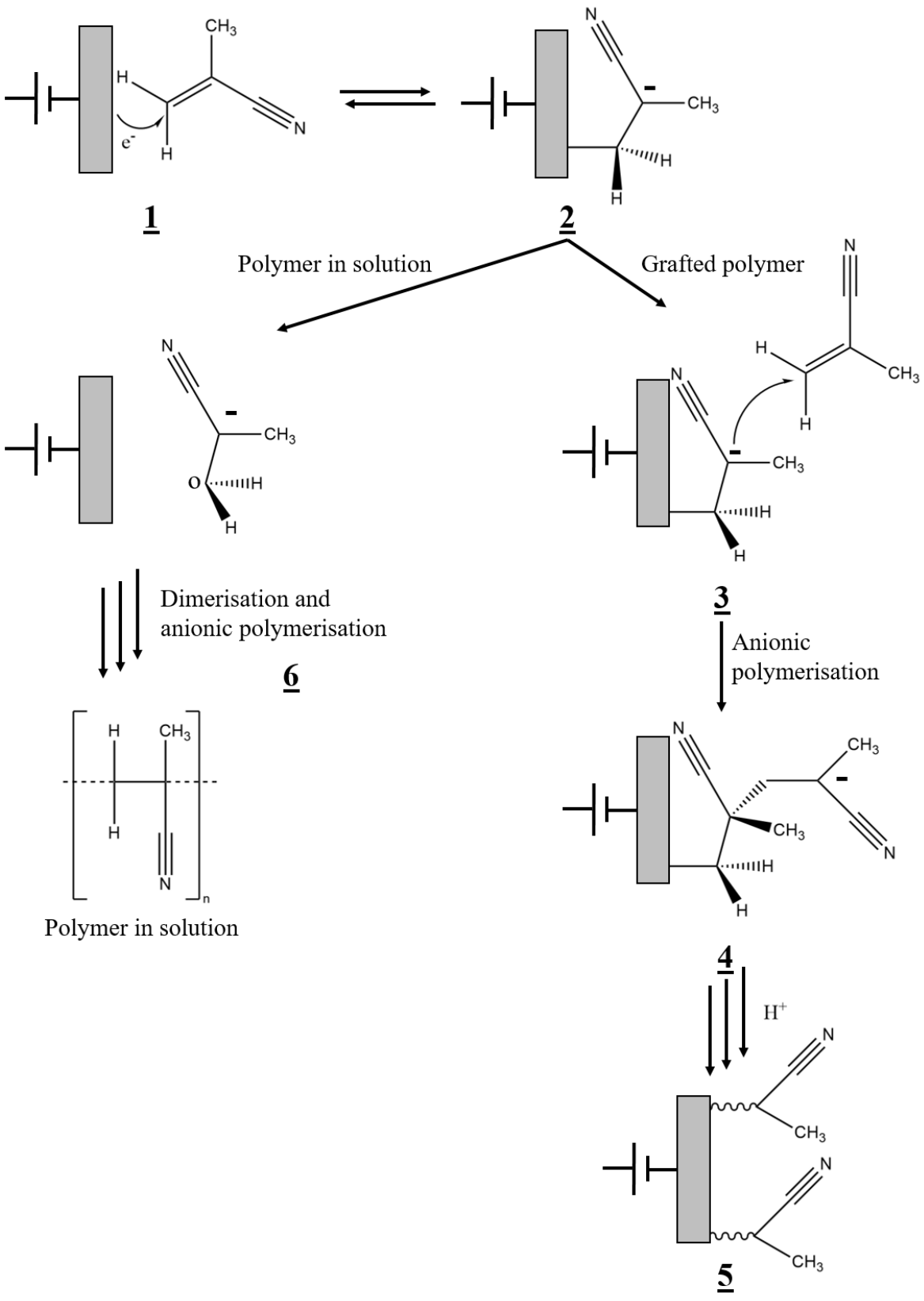

Figure 10: Mechanism of the electroreductive grafting of vinyl monomers. Methacrylonitrile is used as an example. Figure adapted from: [78].

1.4.2 Polyacrylonitrile as a polymer host for gel-electrolyte

PAN is used as a polymer host for electrolytes defined as a membrane that possesses the ability to transport ions for electrochemical systems such as fuel cell, lithium batteries, supercapacitors, and electrochromic devices [5] [6]. The advantages of the gel-electrolytes include no internal shorting, no leaking of electrolytes, and non-combustible reaction products at the electrode surface existing in the electrolyte solution. Among polymer hosts, PAN can provide homogeneous and hybrid electrolyte membranes consisting of electrolyte salts (such as $LiClO_4$ or $LiN(CF_3SO_2)_2$) and a plasticiser (such as ethylene carbonate (EC) or propylene carbonate (PC)) [80]. The resistivity of PAN-based gel-electrolytes reaches the order of 10 Ω m at ambient temperature [81]. Other lithium salts can be encapsulated providing a similar ionic resistivity, such as solutions of $LiN(CF_3SO_2)_2$, $LiAsF_6$, $LiCF_3SO_3$, and $LiPF_6$ in a plasticiser mixture of EC and PC. Cyclic voltammetry studies revealed that the electrolytes have an inherent oxidation stability window exceeding 5 V *vs.* Li/Li^+ [82]. The relatively low resistivity is a favourable characteristic of PAN-based gel-electrolytes, although PAN is inactive in the ionic transport mechanism. PAN also has good structural stability due to its compatibility to both plasticisers and Li salts.

1.4.3 Polyacrylonitrile as a separator membrane

PAN has been previously reported in the formation of separator membranes. One of these methods forms the membranes in two steps, synthesis of PAN emulsion and formation of the microporous membrane [34]. The result was PAN-based microporous membranes of about 40 µm in thickness coated with ethylene-vinyl acetate copolymer (EVA). A microporous gel electrolyte is formed on wetting with a standard liquid electrolyte, 1 mol dm^{-3} $LiPF_6$ in the mixture of ethylene carbonate, dimethyl carbonate, and ethylene methyl carbonate (1:1:1 by weight). The polymer has excellent miscibility with commonly used liquid electrolytes and swells on addition. The wetting of the polymer creates several interfaces between the liquid electrolyte, gel electrolyte, and polymer matrix. The electrolytes provide low ionic resistivity and good interfacial compatibility, whilst the polymer matrix enhances dimensional stability and mechanical properties. PVDF also shares these advantages, however research shows PVDF is unstable under some conditions with the negative electrode of lithium-ion systems, potentially causing exothermic reactions presenting a further thermal runaway risk [83] [84]. PAN is shown to be stable with both cathode and anode, making it promising for use within lithium-ion systems [85].

Huai *et al.* [34] showed that ionic resistivity of PAN-based microporous membranes decreased with decreasing distance of ion transport, enhancing ion transport through the membrane. The

thicker the membranes produced the greater the resistivity. Ionic resitivity values are quoted between 14 Ω m to 100 Ω m. The thermal stability and performance of PAN is of key interest. Huai *et al.* [34] performed a TGA study of their PAN membranes, finding an onset temperature of weight loss around 227 °C. Other research has shown the thermal degradation of PAN starts at around 230 °C, giving off HCN and NH_3 [86]. This is, therefore, the operating limit of the membrane. Fortunately, this is high enough for lithium-ion battery uses. Figure 11 shows the relationship between resistivity of the PAN-based microporous membranes and temperature [34]. Resistivity decreases with temperature from around 15 Ω m to 9 Ω m at 20 °C to 80 °C, respectively. After 80 °C, resistance increases rapidly reaching two orders of magnitude higher by 150 °C. The phenomenon is attributed to the softening point upon heating of the EVA protective layer that restrains the penetration of liquid electrolyte into the PAN particles. The PAN particles can then meet the liquid electrolyte directly and are quickly swollen and incorporated with each other by the help of the solvent of the electrolyte. This results in the complete blockage of the membrane pores used for ion transport. This is a typical shutdown operation and may be useful in the application of lithium-ion battery safety.

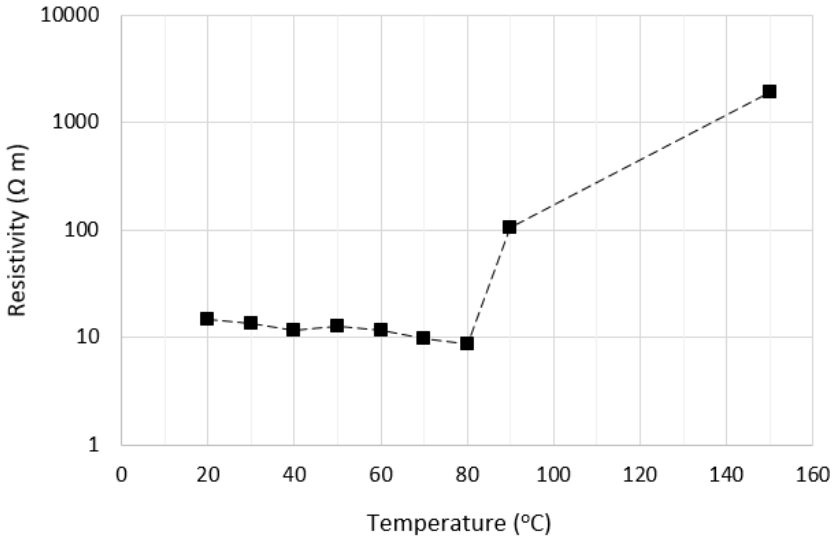

Figure 11: Temperature dependence of resistivity of PAN-based microporous membranes (area = 0.79 cm^2, thickness = 40.3 µm). Figure adapted from: [34].

1.5 Percolating materials

A key area of interest is that of percolating polymer-composites [51]. The simplest overview of these materials is that of a blend of an insulating polymer matrix with a conductive additive filler. The matrix binds the filler together and the filler builds a conductive framework through which electrons may flow. However, there is a critical volume fraction of filler, known as the percolation threshold, at which a PTCR effect can be observed [33] [51] [52]. Thanks to this effect, these materials are useful in current-limiting device and self-regulating devices against over-temperature and over-current [51] [54].

The conductive behaviour of a conductive polymer-composite has been reported to have two transition points related to the fraction of filler particles [55]. The initial stage is dominated largely by the resistivity of the insulating polymer and occurs at low volume fraction of conductive additive. The gap between conductive particles is too large and the resistivity of the matrix takes precedence [51]. These resistivities can be of the order of 10^{13} Ω m. After the first transition conduction via quantum tunnelling between conductive particles occurs when the conductive filler reaches a certain threshold [19] [55] [87]. Resistivity of the composite decreases rapidly until the second transition where percolation occurs at high volume fractions. An extensive conductive framework is formed and the resistivity of the fillers takes precedence. Resistivities can vary from 10^{-7} Ω m for conductors such as metals or around 10^{-1} Ω m to 10^{-3} Ω m for intermediate conductors such as carbon black. As such, the choice of filler is critical to the resistivity performance of the composite. Unique properties are observed at the percolating point where filler content is such that only a single conductive pathway can be formed. Any small variations in filler content leads to drastic changes in resistance, as well as any changes to the geometry of the matrix. As such, the key property of the polymer matrix is thermal expansion and plays the most significant role in establishing a PTCR effect. If the composite materials are designed such that the matrix has a higher coefficient of thermal expansion than the filler, then the thermal expansion of the materials can lead to a breakdown of these conductive pathways [33].

Ordinarily, the PTCR effect is only observed near to a threshold temperature of the polymer matrices, such as glass transition or melting temperatures [33]. At these points the coefficient of thermal expansion of materials increases substantially [88]. Figure 12 shows simulation data for the thermal expansion of pristine PE and PE-carbon nano-tube composites by Wei *et al*. [88]. Melting temperature is self-explanatory in that it is the point at which the material transitions from solid to liquid, whist glass transition is not so obviously named. Glass transition is the point at which a material goes from brittle at low temperatures to ductile at higher temperatures, or

from a glassy state to an elastic-rubbery one. This is understood to be due to higher temperatures overcoming weaker intermolecular interactions within the material and allowing movement of planes or chains within the material to slide over each other. The result of most interest is the increase in the thermal expansion although other elastic behaviours would be strengthened over the transition point. Simulations by Wei *et al*. have shown an increase in volume expansion in the presence of carbon nano-tube filler materials from 18 % greater below T_g and 40 % greater above T_g [88]. Importantly T_g has been shown to increase from -93 °C to -23 °C depending on polymer chain length indicating a heavy dependence on molecular weight and degrees of cross-linking [89] [90] [91]. There is also a dependence upon filler materials. Wei *et al*. found an increase from -123 °C to -103 °C from pristine polymer to composite polymer in glass transition temperatures [88]. This was linked to the presence of carbon nano-tubes restricting polymer chain movement, thus higher temperatures were required to overcome interactions between chains. This effect has been shown experimentally [33] by Kar *et al*. by comparing differential scanning calorimetry (DSC) data between poly(styrene-co-acrylonitrile) copolymer-stainless steel and copolymer-carbon black composites. The glass transition of the pristine copolymer was found to be around 107 °C and remained unaffected at 80 % and 85 % weight stainless steel. A slight increase was observed in the presence of 10 % carbon black up to 109 °C, which further increased again in the presence of a nano-clay blend up to 112 °C. This study highlights that certain additives can have an effect on the T_g of composites whilst others might have negligible effects.

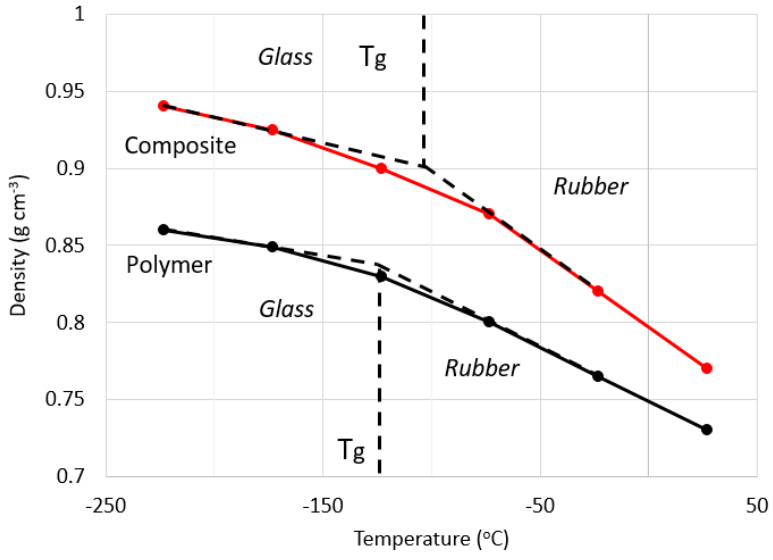

Figure 12: Simulation data of density as a function of temperature for short-chained PE (N_p = 10) and its composite with 20 Å long carbon nano-tubes embedded (averaged from 6 sample sets). Below glass transition, T_g, the systems are in glassy state and above T_g the systems are in a rubber-like state. Figure adapted from: [88].

The resistivity of a material decreases with increasing degrees of crystallinity of the conductive polymer-composites [55]. The proposed model is that the polymer crystallises and excludes the conductive filler materials. This leads to fillers becoming concentrated spatially within the crystallisation of the polymer matrix. These spatial concentrations allow for easier conductive pathways to form, forming a minor phase within the composite [87]. With a transition temperature, the polymers become more amorphous and fillers diffuse more easily within the melt breaking routes of conduction and increasing resistivity. As such, it is generally accepted that percolation is a result of a geometric transition like the volume expansion experienced at transition temperatures and not some other property of the materials [87]. This places a critical importance on the role of the microstructure on the effects of percolation.

Many percolating composite materials have been investigated, each giving unique responses depending upon selection of polymer matrix and conductive filler. Polyethylene materials are among the more studied. Studies on the PTCR effect of HDPE with several different carbon black additives shows a large resistivity increase around 130 ^{o}C, regardless of the carbon black additive chosen or volume fraction of the filler [52]. Smaller surface areas and small amounts of aggregate structure lead to greater PTCR intensity. This was reportedly because of a microscopic mechanism occurring under this macroscopic thermal expansion, but no direct cause was given. Lower proportions of additive also gave a greater PTCR intensity. More complex carbon black particles in ethylene butylacrylate copolymer matrix have been studied, showing a large increase in resistance at around 60 ^{o}C [53]. Studies on ultra-high molecular weight polyethylene found a PTCR closer to 145 ^{o}C and also showed the potential for heat treatment to tailor the PTCR response, with graphene nano-sheets increasing in PTCR intensity with longer heat treatments whereas standard carbon black materials would decrease in intensity [54]. Meanwhile, other studies by Zheng *et al.* [19] have managed to introduce PTCR far below melting temperatures with specific additives. LDPE could be found to have a PTCR as low as 50 ^{o}C with the introduction of 10 % volume of graphene coated spiky nickel particles. However, this effect appears to occur because of the nano-spikes on the nickel surface and not the choice of material itself allowing for much lower resistivities and sensitivity to temperature by the additives and not the matrix. Of note, transition temperatures of polymers appear to increase with increasing molecular weight. This can be observed in certain studies such as the HDPE-carbon black study with a PTCR around 130 ^{o}C [52] and the ultra-high molecular weight-graphene study with a PTCR around 145 ^{o}C [54]. Simulations have also managed to produce this effect, with glass transition at -123 ^{o}C for polyethylene chain lengths of 10 and at 27 ^{o}C for chain lengths of 100 [88]. Indeed, the studies by Zheng Chen *et al*. [19] specifically chose LDPE over HDPE because it would have a lower melting point. This is likely because of a higher degree of crosslinking allowing for denser packing of

molecules, higher molecular weights, and stronger bonds between molecules to resist the onset of transition temperatures and structural changes.

Many other polymers have been studied for percolation, including PVDF [55] and polystyrene [33]. Studies by Kono *et al*. [55] using PVDF-nickel composites found a PTCR increasing from 50 ^{o}C with 20 % nickel volume up to near the melting point of the polymer at 150 ^{o}C for 50 % nickel. Prativa Kar *et al*. [33] investigated the PTCR response of poly(styrene-co-acrylonitrile) with stainless steel and carbon black additives. This study is of note as the PTCR transition coincided with a glass transition rather than a melting point. The copolymer has a glass transition around 107 ^{o}C. However, PTCR was observed at a temperature distant from the glass transition with carbon black around 125 ^{o}C and with stainless steel around 94 ^{o}C, highlighting the importance on chosen additive material on transition points.

Percolating additives when investigating electrical shutdown in cells can take many forms, provided the material is inherently conductive. These additives can be: carbon black, carbon fibres, graphite, metallic particles, intrinsically conductive polymers, and carbon nanotubes [33]. TiB_2 in HDPE has also been reportedly used [51]. Silver particles are commonly used as conductive filler in ceramic composites [87], but have also been used as filler in silicon rubber [51]. For use within a lithium-ion cell, electrochemical stability is also key. As such, metallic particles like nickel are normally avoided in cell applications as they require extra processing to avoid activity with electrolyte and electrodes within a cell [19]. Carbon black materials are also widely studied in percolation systems [33] [92] [52]. Titanium carbide (TiC) is a conductive ceramic material that is known for its mechanical, thermal, and chemical stability and is even used as a heat-shield for atmospheric re-entry on space craft [93]. Studies by Lozano *et al*. [93] investigated the electrical properties of polymer-TiC composites for the purpose of electromagnetic interference shielding. Further studies of percolation with TiC composites include a niobium-TiC material [94] looking at electrical properties at elevated temperatures and poly(3-hexylthiophen)-TiC [95] looking at DSC, percolation threshold and high temperature responses.

1.6 Aims and objectives

The overall aim of this research was to: *improve lifetime performance and safety of lithium-ion batteries through the application of functional polymer materials to prevent thermal runaway.* Researching all polymers was too broad; a narrow selection was required for a manageable workload over the course of a few years. As such, selection was initially limited to those polymers with known stability and testing within lithium-ion cells. After a careful review of literature surrounding thermal runaway, further weight was given to those polymers that experience a transition temperature within a suitable range; either a glass transition or a melting point near to 160 ^{o}C was ideal. Thermal runaway has been cited as reaching a critical point at temperatures as low as 160 ^{o}C, so temperatures exceeding this should avoided [12]. Competitive temperatures to other commercial alternatives that are commonly used in shutdown applications of lithium-ion cells, such as Celgard at 130 ^{o}C [30], was also important for the potential impact of the research. This naturally led to the selection of PAN [3] [96], PVDF [3] [96], and PE [19].

A final decision was made on how to apply the polymers within a cell for studying. Electrodeposited film coatings were selected to study effects of restricting ion transport. With careful control of deposition parameters, such as current duration or voltage, film properties can be simply controlled and tailored [41]. Electrodeposited gel electrolytes within 3D micro-batteries was the suggested application for the electrografting of PAN performed by Lacey *et al.* [41] and Roberts *et al.* [97] confirming the ionic conductive properties of PAN. Functionally, a PTCR effect of a coating should be experienced by closing pores for ionic transport between the two electrodes that would lead to a cell shutdown. As studies were readily available for PAN deposited onto glassy carbon electrodes [41] [42] but none for applications with lithium-ion battery anodes this was chosen as a novel point of research. PAN was deposited onto graphite anodes with extensive data gathered on the effects of different conditions on the deposition. Subsequently, this was then tested within a lithium-ion half-cell at varying temperatures to identify the potential as a PTCR application.

A separate study was then planned to pursue the percolating material route. These materials work differently to film coatings in that they stop electron transport rather than ion transport. Both polymer matrix materials and conductive additives had to be carefully selected. Selection of polymers came down to two criteria: electrochemically stable in lithium-ion systems, and suitable transition temperatures. PAN [3] [96], PVDF [3] [96], and PE [19] are all commonly used within lithium-ion systems and so made for obvious choices. In terms of transition temperatures, there needed to be either a glass transition or a melting point sufficiently above room temperature such

that small temperature fluctuations at ambient do not trigger a PTCR response. PVDF [30] was at the extreme high end with a melting temperature at 155 to 185 ^{o}C and a glass transition far too low around -30 to -20 ^{o}C. PE [30] tends to have a range of different melting point temperatures dependent upon polymer density, HDPE is commonly noted as having a melting point between 130 to 140 ^{o}C and a glass transition at -125 ^{o}C. The most appropriate transition temperature possibly comes from PAN [35]. Although melting was too high at 325 ^{o}C, the glass transition occurs at a comfortable 95 ^{o}C. PAN was also selected to compare effectiveness with the electrodeposited film application studies. PAN materials were also rarely cited in literature for percolation studies and should prove a more novel area of research than the more common HDPE and LDPE materials that can instead be used as comparison with more standard materials. PAN, PVDF, LDPE and HDPE were all therefore selected for these studies. In terms of additives, carbon black materials are often used in percolating composites and have known stability within electrochemical systems. For this reason, carbon black materials were selected to allow for easy comparison of percolation properties between several different polymer materials. As a point of comparison with carbon additives, a second material was selected to see if this would affect the transition temperatures and PTCR. This was chosen to be TiC. Many studies have looked at the performance of TiC in percolating systems, but none have looked at TiC within electrochemical systems such as lithium-ion cells. A careful look at the effects on glass transition temperature changes as well as system resistivities was performed on these polymer-additive systems. This was followed by a study of the best identified percolating-composite within a lithium-ion half-cell at various temperatures.

Chapter 2 Experimental

In this chapter, the general experimental approaches used across several results chapters are detailed. Firstly, the apparatus and methods used to test materials electrochemically are detailed. This includes the method to manufacture graphite-composite ink electrodes for use in PAN film electrodepositions and lithium half-cell cycling as well as the equipment used for accurate temperature control for PTCR studies at room and elevated temperatures. Lastly, physical characterisation techniques employed across all results chapters are detailed. More specific experimental details are given within dedicated section of their respective results chapters.

2.1 Materials

Table 3: List of materials used within studies as well as the respective supplier names. Listed in alphabetical order according to material.

Material	Component	Supplier
Acetonitrile (99.8 %)	Solvent	Sigma-Aldrich
Acrylonitrile, AN (≥99 % with 35-45 ppm monomethyl ether hydroquinone inhibitor)	Solvent, monomer for electrodeposition of PAN	Sigma-Aldrich
Alumina powder (1 µm, 0.3 µm, and 0.05 µm)	Polishing powder for glassy carbon electrodes	Buehler
Calcium hydride, CaH_2 (95 %)	Drying agent	Sigma-Aldrich
Carbon, (Super C65 carbon black powder, 99 %)	Conductive additive	Timcal
Copper foil (0.05 mm thickness, 99.9 % purity)	Current collector	Advent
Glass fibre (GF/F, Whatman™)	Separator (50 µm thickness)	GE Healthcare Life Sciences

Graphite powder (99 %)	Active material	Hitachi Chemical
High-density polyethylene, HDPE (HMPE95A fine polyethylene powder)	Percolating polymer matrix	Goonvean Fibres
Lithium metal foil, Li (0.12 mm thickness, 99.9 % purity)	Counter-reference electrode	Goodfellow
Low-density polyethylene, LDPE (HMPE35A fine polyethylene powder)	Percolating polymer matrix	Goonvean Fibres
LP57 (1 M $LiPF_6$ in EC:EMC 3:7)	Lithium-ion electrolyte	Soulbrain MI
N-methyl-2-pyrrolidone, NMP (99.5 %)	Solvent	Sigma-Aldrich
Polyacrylonitrile, PAN (M_w 150,000)	Percolating polymer matrix	Sigma-Aldrich
Polyvinylidene difluoride, PVDF (Solef® 5130)	Electrode binder and percolating polymer matrix	Solef
Tetrabutylammonium perchlorate, TBAP (≥99 %)	Supporting electrolyte	Sigma-Aldrich
Titanium carbide nanopowder, TiC (<200 nm particle size)	Percolating conductive filler	Sigma-Aldrich

2.2 Electrochemical characterisation techniques

2.2.1 Lithium-ion half-cell

A lithium-ion half-cell is a standard arrangement of either a cathode or anode material against lithium metal. These electrodes are separated by an ionically conductive separator material and are wetted by an appropriate electrolyte, see Figure 13. Focus was given primarily to graphite anodes against a lithium metal cathode. LP57 was used as electrolyte with two glass fibre separators separating the two electrodes. Two separators were used to increase distance between the electrodes to ensure short circuiting did not occur if the electrodes were misaligned within the half-cell arrangement.

Half-cell arrangements are used to allow a focused study of the electrochemistry of the working electrode in isolation of the features of standard cathode or anode counter electrodes in a full-cell. Lithium metal acts as a counter-reference in this setup. These half-cells were used to quantify and compare the performance of pristine graphite-composite electrodes and electrodes with functional polymer films (either electrodeposited PAN films or percolating-composite films).

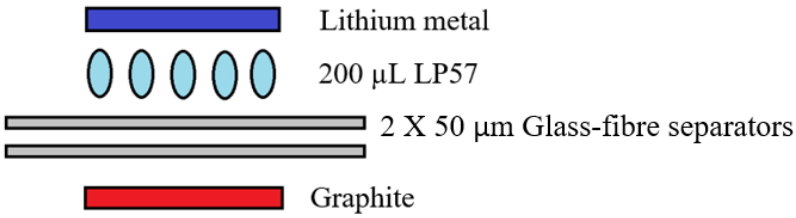

Figure 13: Material arrangement in Swagelok half-cell electrochemical studies. Graphite is the working electrode, lithium metal is the counter-reference electrode, GF/F is used as the separators, and 200 µL LP57 was used as the electrolyte.

2.2.2 Graphite-composite ink electrode preparation

Graphite is the anode material of choice in many lithium-ion systems due to its low cost, relative abundance, high power and energy densities, and very long cycle life [98]. Graphite is also a well-known conductive material, a property that is essential for electrografting of materials such as polymers. As such, graphite was chosen for electrochemical studies within this paper.

Preparation of the graphite-composite electrodes used a typical solvent cast approach [3] [19] [96], which was as follows:

1. PVDF was dissolved in NMP such that the solution was 10 % by weight PVDF.
2. A mixture of graphite active material (the material to be studied), super C65 carbon black conductive additive (to ensure electrical contact between active material particles), and PVDF binder (to hold the graphite and carbon powders together) was weighed; the ratio used was 94:3:3 by weight, masses used were 3.7 g : 0.12 g : 0.12 g. PVDF mass was measured without NMP solvent.
3. 6.7 mL NMP was added to the mixture; NMP is a solvent in which PVDF is soluble and allows homogeneous binding.
4. The mixture vial was then placed in a Thinky Planetary Mixer and mixed for a total of 15 minutes at 2000 rpm. This produced a composite electrode ink.
5. The ink was spread onto a polished copper foil surface (0.05 mm thickness, 99.9 % purity). Spreading was performed with a TQC Sheen Dr blade set to an ink thickness of 0.25 mm, 200 mm s^{-1}. An ink area around 250x150 mm was obtained.
6. The ink was left to dry in a vacuum oven at 80 ^{o}C for 2-3 hours.
7. Electrodes were cut to 11 mm diameter with a precision punch (EL-CELL, EL-Cut) and pressed at 10 tonnes with a manual hydraulic press (Specac FTIR + XRF pellet press) for 1 minute to improve packing density.

2.2.3 Swagelok cell assembly

Electrochemical studies were performed within a Swagelok cell. An exploded view of a Swagelok cell design can be seen in Figure 14. The cells used had a half-inch diameter hole bored through the middle of polymer tube fittings. These fittings were used to house: the current collectors for electron transport, the ferrules to hold the current collectors in place and seal the system, and the electrodes, electrolyte, and separators that make up the electrochemical system. Current collectors were made from copper as the surface is easily polished and smoothed preventing discrepancies in resistivity measurements due to surface roughness. One of the current collectors contained a spring to apply pressure to the electrodes to ensure a good contact area is maintained. Electrochemistry used an 11 mm diameter graphite-composite anode working electrode against an 11 mm diameter lithium metal counter-reference electrode. Between the two electrodes were two 12 mm diameter GF/F glass fibre separators wetted with 200 µL LP57 electrolyte, as seen in the half-cell arrangement in Figure 13. Half-cells were assembled in a Belle Technology Ltd argon environment glovebox. Pristine graphite-composite electrodes and separators were dried in a BUCHI Glass Oven B-585 under vacuum at 120 ^{o}C for 24 hours before

being moved to the glovebox. Lithium metal and electrolyte came pre-made from suppliers and were stored under an argon environment and so were transferred directly to the glovebox.

Chapter 4 made use of graphite-composite electrodes with electrodeposited PAN films on the upper surface within Swagelok cells. Meanwhile Chapter 5 used several percolating-composite mixtures of several different polymer materials within Swagelok cells. These materials were dried under vacuum for 72 hours at room temperature to prevent any deformation or annealing of the polymer film due to high temperatures.

Plastic Swagelok cells made from PTFE were used for room temperature measurements with copper current collectors to avoid activity with the electrochemistry. For measurements at elevated temperatures, increases in temperature can lead to expansion of plastic Swageloks potentially affecting the seal of the ferrules and exposing the chemistry to air. Aluminium-cased Swageloks cells were therefore used having the end nuts and cell body made from aluminium, see Figure 14. Teflon FEP film of 125 µm thickness was cut to size to cover the entire area of the inner cell body during cell assembly. This was done to prevent short-circuiting between the current collectors.

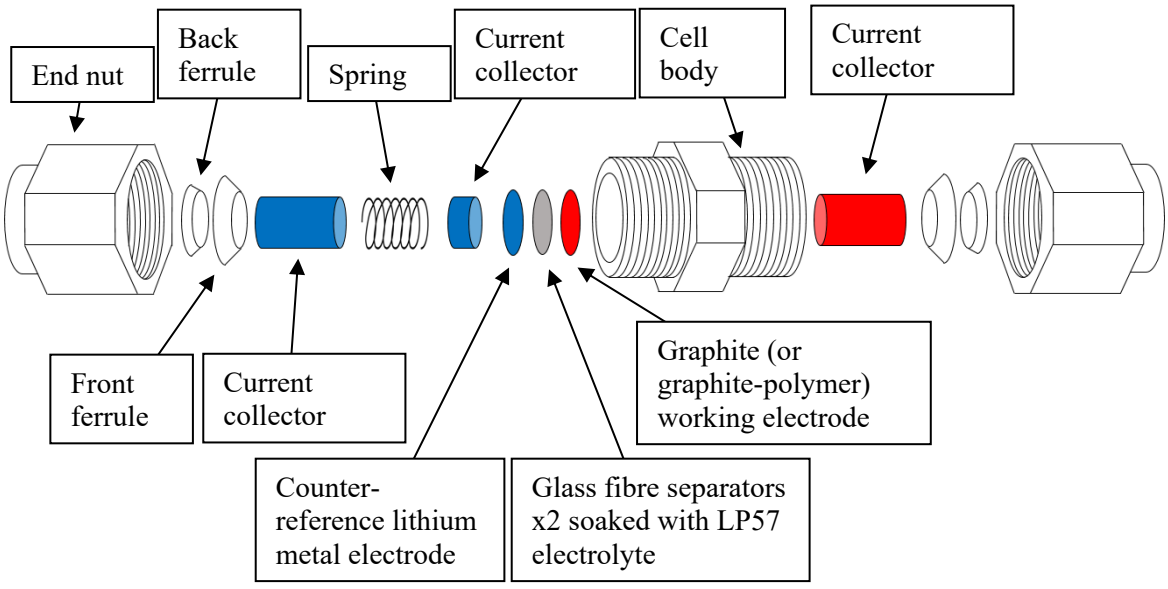

Figure 14: Exploded view of a Swagelok cell. Figure not to scale.

For resistivity studies of percolating composites in Chapter 5 the electrochemical half-cell, that is to say the lithium metal counter electrode and graphite-composite working electrode along with the two glass fibre separators wetted with LP57 electrolyte, were replaced. Instead an 11 mm diameter film of the polymer-composite being studied was placed alone between the current collectors to measure the electrical properties of the material. The materials were once again

prepared within an argon environment glovebox and sealed within the Swagelok cell arrangement.

Further studies in Chapter 5 looked at electrochemical performance of the half-cell with a backing of the polymer-composite materials to observe practical performance of the samples. Polymer-composite films were layered behind the graphite-composite anode working electrode, both 11 mm in diameter. The polymer-composite acted as the current collector, transporting electrons to the graphite-composite layer. The remainder of the half-cell was unaltered with two 12 mm diameter GF/F glass fibre separators wetted with 200 µL LP57 electrolyte and an 11 mm diameter lithium metal counter-reference electrode.

2.2.4 Galvanostatic cycling at room temperature

The primary electrochemical characterisation technique used on half-cell materials was galvanostatic cycling. Galvanostatic cycling was performed on the electrode materials within the Swagelok cells. This involves oxidising and reducing an electrode material at constant current whilst measuring potential [99]. Potential will change as the current is applied, a lower and upper potential limit is set during the technique. Potential is then often plotted against time or capacity. This is done to determine the viability of materials when in use through comparing capacities and efficiencies on charge-discharge with theoretical values of the active material as well as reversible/irreversible capacity. The shape of charge-discharge curves can also be crucial, plateaus or notable changes can identify phases and redox reactions occurring within the electrochemistry. From a practical view, curves with a flat charge-discharge can be desirable as it reduces the need for complex electronic management systems to maintain constant power.

The current used during cycling is governed by the intended C-rate [100]. A C-rate of 1 means that a fully charged 1 A h battery should provide a current of 1 A for 1 hour. The same battery discharging at 0.5 C should provide 0.5 A for 2 hours, 2 C delivers 2 A and ½ hours, and so on; however, these times are only true for an ideal system. At higher C-rates the battery degradation is accelerated leading to greater capacity fade [101]. There are also greater internal losses due to the relatively slow diffusion of lithium-ions into solid state materials resulting in lower capacities [102], see Figure 15. High C-rates can also pose problems of dendrite formation, which can short-circuit a cell and cause thermal runaway. Unfortunately, lower C-rates result in lower power outputs that can limit potential applications of a cell. To calculate required current for the system, the following equation is used:

$$Current(mA) = Active\ material\ mass(g) \times Theoretical\ specific\ capacity(mA\ h\ g^{-1}) \times C_{rate}\ (h^{-1})$$

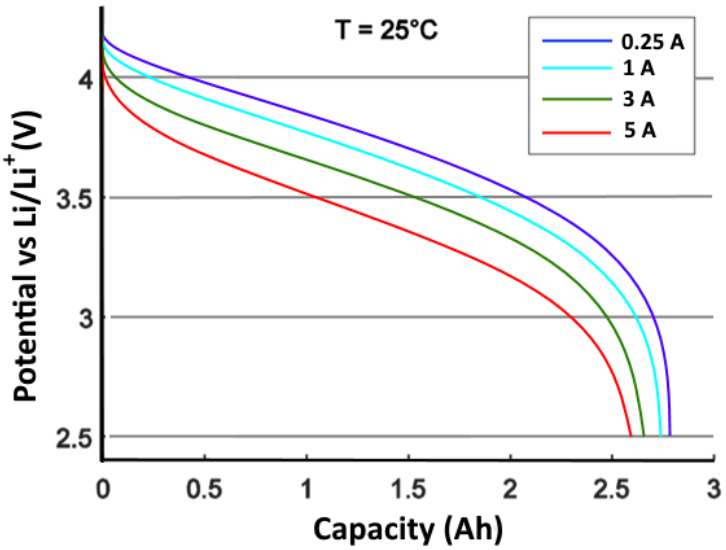

Figure 15: Representation of a typical discharge curve for a $LiNiCoAlO_2$ cathode lithium-ion cell at 25 °C for various currents shown in the legend in units of amperes. Data expressed as potential against capacity. This graph is an illustration of $LiNiCoAlO_2$ cathode data and not an actual cycled $LiNiCoAlO_2$ cathode. Figure adapted from: [102].

For room temperature studies cycling measurements were performed at a C-rate of 0.1 C for at least 10 cycles with potential limits at voltages of 0.005 V to 1.5 V, a standard potential window for graphite *vs.* Li/Li^+ half-cells. Ideally, capacity should be near to the theoretical value of 372 mA h g^{-1} with little to no reduction upon adding a polymer film. Both pristine graphite-composites and graphite-composites with functional polymers to facilitate a PTCR were studied.

Room temperatures were maintained by an environmental chamber (Memmert, IPP 55 Plus) held at a temperature of 25 °C. Active mass was calculated by weighing an average copper control mass, subtracting that value from the full electrode ink on copper foil, and then multiplying by the ratio of active graphite mass within the ink. The ratios and ink manufacture were discussed in Section 2.2.2.

In order to apply the appropriate cycling regime a potentiostat was used. BCS-805 battery cycler or SP-150 potentiostats were used with BT-Lab or EC-Lab software, respectively. Currents were maintained at the same magnitude but switched between positive and negative to charge and discharge the cells. Figure 16 shows a representation of the current during galvanostatic cycling.

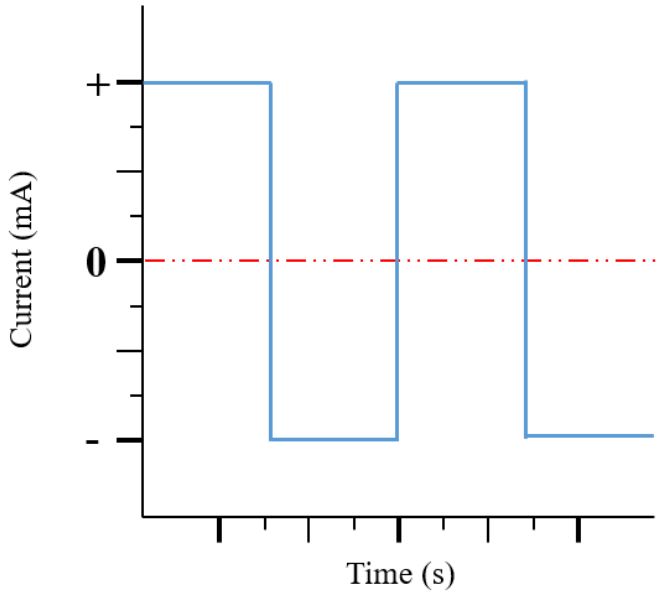

Figure 16: Representation of current during galvanostatic cycling.

2.2.5 Elevated temperature measurements

Reliable and accurate temperature control was an important consideration in this work. Two methods were available for temperature control that were adopted to test the effects of temperature on cell performance: constant temperature cycling in an environmental chamber, and elevated temperature cycling in a laboratory oven. The first was used in room temperature cell cycling measurements. The second method was used to give information on cell performance over a range of temperatures and identify promising PTCR responses. Both methods used a potentiostat to control cycling; however, the environmental chamber used to maintain temperature at ambient could not be reliably used to ramp temperatures for elevated temperature studies. As such, a Genlab classic oven from the laboratory range (Agar Scientific, MINO/6) was used, see Figure 17. In Chapter 4 this equipment was used to test the galvanostatic cycling of materials within a Swagelok cell. Chapter 5 also made use of this equipment to study the resistivity of polymer-composites without any electrochemistry.

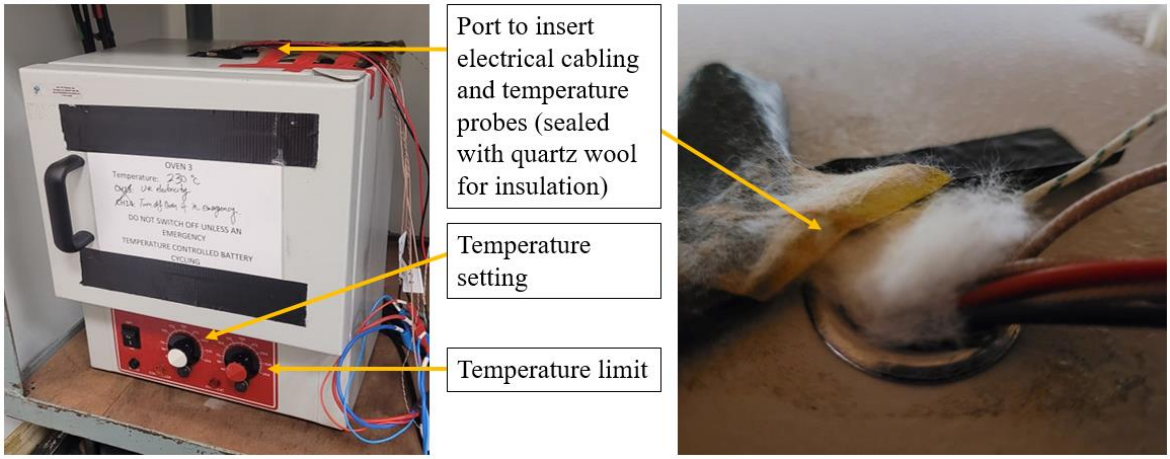

Figure 17: (Left) Genlab classic oven from the laboratory range. Cells were placed inside with cables fed through the top port to connect to temperature probes and potentiostats. (Right) Close-up image of the top port, quartz wool was used to insulate and prevent heat leakage which was held in place by electrical tape.

Most electrical measurement cabling was designed to work at room temperature. As such, specially designed cables were created to work at higher than room temperatures. Coaxial cable with an insulating outer-lining of FEP polymer was used to make cables that could be operated up to 200 °C. Banana plugs of 2 mm diameter were soldered to the ends and then secured with heat shrink to cover and protect the connection. The highest temperature required was PVDF's melting temperature of 155 to 185 °C [30], so temperatures were not planned to exceed 200 °C.

Temperature monitoring within the oven was performed with a k-type thermocouple probe. The cables and thermocouple were fed through the top port of the oven and insulated with quartz fibre to maintain temperature inside. Upon reaching the required temperature, cell cycling would be started and after completing the cycling regime temperatures would then be increased again to the next set point.

2.3 Physical characterisation techniques

The structure of materials was characterised and compared using several different techniques. Optical microscopy and scanning electron microscopy (SEM) were used for both films and percolation composites to provide insight into the morphology of the materials. The thermal properties were also explored. Thermogravimetric analysis (TGA) was used on a number of the materials that would be placed within a cell at elevated temperature to assess any thermal degradation that might take place.

2.3.1 Optical microscopy

Optical microscopy is one of the simplest and easiest ways to view magnified images of a sample [103]. Optical microscopy uses visible light and usually requires little sample preparation before use. This technique was used to view surface features, mainly the cracks on PAN film surfaces, and give a preliminary understanding of the surface morphology of the materials. Crack sizes or size of any deformities were also recorded. This was mainly used to assess the quality of techniques used to deposit PAN films and cast films in percolation studies. Samples were simply placed on a glass slide and placed under a Nikon Eclipse LV100ND microscope system. Images were captured between 10 X to 100 X magnification.

2.3.2 Scanning electron microscopy

Optical microscopy is limited in how far it can magnify an image. To see greater magnifications and smaller structures with clarity, other techniques such as SEM can be used [104] [105] [106] [107]. Magnifications can range from 10 X to 3,000,000 X in SEM. SEM uses a focused beam of high-energy electrons to generate signals at the surface of solid specimens. The electron-sample interactions reveal information about the external morphology, chemical composition (a technique known as energy dispersive X-ray spectroscopy (EDS or EDX)), crystalline structure and crystallographic orientation of materials (a technique known as electron backscatter diffraction). It is important to note the interactions are non-destructive and do not lead to any volume loss within samples, so samples can be analysed repeatedly.

The accelerated electrons carry kinetic energy, which is dissipated as a variety of signals when they are decelerated in the solid sample [104] [105] [106]. Secondary electrons are produced by elastic collisions of electrons and are used to produce SEM images to view morphology and topography of samples. Backscattered electrons are produced by elastic reflections and are useful for producing images to illustrate contrasts in composition of multiphase samples and study their crystallography. Conversely, X-ray generation is produced by inelastic collisions of incident electrons with electrons in the orbitals of atoms in the sample. These X-rays are utilised in EDS in chemical composition studies. The number and energy of the X-rays emitted can be measured by an energy-dispersive spectrometer. This also allows the proportion of each element in the sample to be determined. These interactions are shown in Figure 18.

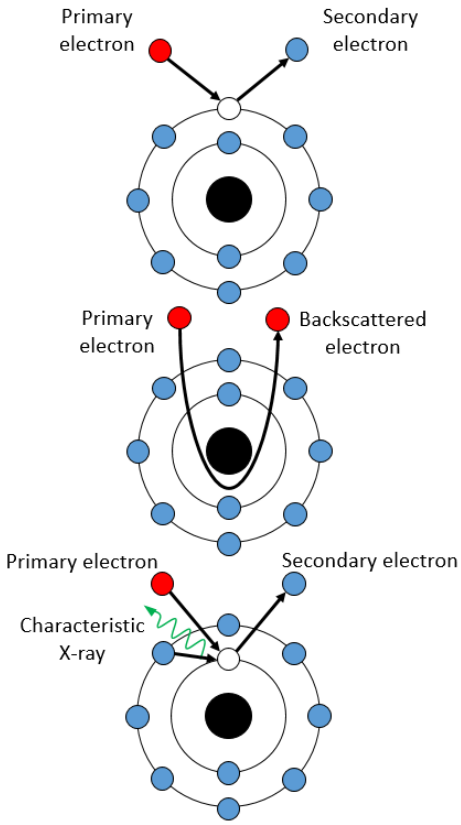

Figure 18: Mechanisms of emission of secondary electrons, backscattered electrons, and characteristic X-rays from incident primary electrons.

SEM images were captured using a FEI/Philips XL30 FEG ESEM with Thermo Fisher Scientific Ultra Dry 10 mm^2 EDX. Samples were stuck to stubs with double-backed sticky conductive carbon tape before being mounted onto the SEM sample holder within the microscope chamber. Images of the sample topography were captured using secondary electrons with subsequent EDS measurements taken to help verify that the films were chemically the desired polymer.

2.3.3 Thermogravimetric analysis

Thermogravimetric analysis (TGA) is a method of thermal analysis in which the mass of a sample is measured over time as the temperature changes. This is done to provide information about physical phenomena, such as phase transition, absorption, adsorption, and desorption; as well as chemical phenomena including chemisorption, thermal decomposition, and solid-gas reactions such as oxidation or reduction.

TGA measurements were recorded using a TG 209 F1 Libra. Alumina crucibles were used to house samples within the TGA. The TGA chamber was purged with argon gas, and an argon gas flow of 20 mL/minute was maintained during TGA measurements. The temperature was ramped at 2 ^{o}C/minute from room temperature to 250 ^{o}C. Mass was recorded against time and subsequently plotted. This was performed for the common electrode materials: Super C65 carbon black, and graphite; as well as the polymer materials to be used as binders in electrodes and for percolation: PAN, PVDF, HDPE, and LDPE. TGA was performed with a supplier provided PAN powder to be used in percolation composites and also with PAN electrodeposited on graphite electrodes. Electrodeposited PAN was scraped off the graphite electrode surfaces before being transferred to the alumina crucibles used for TGA analysis. TGA was also performed on TiC as this was used in elevated temperature studies of percolation composite materials.

Chapter 3 Electrodeposited polyacrylonitrile films

Research into functional polymer materials that are integrated with lithium half-cell electrodes was one of the key objectives of this thesis. The aim of these polymer materials was to introduce a PTCR effect to prevent the potentially catastrophic failure introduced by thermal runaway within a lithium-ion cell. This chapter investigates the production of one said polymer, PAN film coatings that are electrodeposited onto an electrode surface. These electrodes should then be ready for use and testing within a practical lithium cell arrangement. Graphite-composite electrodes were chosen to be coated with PAN due to their widespread usage within lithium-cells as an anode material [2] [12] [18].

PAN was successfully electrodeposited onto glassy carbon in previous studies performed by Lacey *et al.* [41] and El-Enany *et al.* [42]. Indeed several electrodeposition studies have been performed on smooth planar surfaces such as the glassy carbon and metallic surfaces [68] [69], but few studies on rough practical electrode surfaces have been done. As such, initial feasibility studies were performed onto graphite-composite materials to assess the stability of the electrode ink in depositing solvents AN and acetonitrile. This was subsequently followed by attempts to replicate the depositions onto glassy carbon. The intent was to assess if experimental procedures for depositing PAN onto glassy carbon were viable for the practical graphite-composite electrodes employed in lithium-ion cells. These initial tests were performed in a sealed glass cell arrangement with a controlled nitrogen environment to best determine any electrochemical features without introducing possible contaminants.

Cyclic voltammetry tests were performed on graphite electrodes in a Teflon cell to produce electrodes ready for use in a lithium half-cell. Comparisons were made with results in a glass cell to highlight changes due to the new arrangement, the Teflon cell had a greater distance between electrodes and was open to air instead of a sealed nitrogen environment like in the glass cell. After validation of the depositing procedure, chronoamperometry studies were performed to control the thickness and morphology of the polymer film. Inconsistencies that arose during the deposition and between depositions were explored in detail before moving onto lithium half-cell electrode production.

3.1 Experimental

PAN electrodeposition techniques are widely known, but limited application has been used for battery electrode materials. To examine the practicality of such techniques on electrodes several experimental studies are detailed within this section. Prepartion of the deposition electrolyte and the electrochemical cells used are explained. The electrochemical techniques used to deposit PAN (cyclic voltammetry and chronoamperometry) are also detailed. Several physical characterisation techniques used in this chapter were explained in Chapter 2 and are used in the other results chapters: optical microscopy, TGA, SEM and EDS. Similarly, preparation of the graphite-composite ink electrodes were detailed in Chapter 2 and are used in other chapters. The only additional physical characterisation technique used and detailed in this chapter is Raman spectroscopy.

3.1.1 Polyacrylonitrile electrodeposition electrolyte preparation

Materials used to prepare PAN depositing electrolyte were: acetonitrile solvent, AN solvent, and TBAP supporting electrolyte. These materials were formed into a depositing solution of either AN(0.05 mol dm^{-3} TBAP) or acetonitrile(2 mol dm^{-3} AN, 0.05 mol dm^{-3} TBAP). An additional solution of acetonitrile(0.05 mol dm^{-3} TBAP) was also used without AN monomers to characterise O_2 saturation and water contamination in certain studies. Solvents were distilled at 90-100 ^oC using CaH_2 as a drying agent under a N_2 environment, refluxing for 8 hours to remove water. TBAP was dried beforehand under vacuum for 24 hours. TBAP was added to an ampule in an N_2 glovebox, before being sealed and added to a Schlenk line for the addition of solvents. The Schlenk line was set up to flush the ampule and connecting line with N_2 to maintain the N_2 environment of the mixture. A rubber stopper was used to seal the ampule and allow the required amounts of solvents to be syringed in. This was subsequently stirred at 500 rpm for 2 hours using an IKA™ Digital Color Squid Magnetic Stirrer with Fisherbrand™ Magnetic Stirring Bars (PTFE, 12x4, 5mm cylindrical, small pivot ring). After each deposition attempt, electrodes were left to dry in air for 24 hours to allow evaporation of most of the remaining monomer. Electrodes were then washed in ethanol for 10 minutes and left to dry for a further 24 hours to remove any remaining TBAP, monomers and non-attached polymer chains. Mass of electrodes was recorded using a scientific balance after washing and drying; this was compared to the mass before electrodeposition to determine the mass of PAN deposited. The balance had an absolute uncertainty of ± 0.1 mg.

Acetonitrile(2 mol dm^{-3} AN, 0.05 mol dm^{-3} TBAP) was used to test depositions with a different concentration of monomer. This was also the same concentrations used in studies by Lacey *et al.* [41] and El-Enany *et al.* [42] and would therefore be a useful point of comparison with previous literature. Previous research has shown that the monomer concentration is an important factor in controlling the amount deposited during vinyl monomer electrografting [70].

3.1.2 Electrodeposition electrode preparation

Depositions were performed on one of three surfaces; initially 3 mm diameter glassy carbon electrodes were used to characterise electrochemical behaviour on as smooth and controlled an electrode surface as possible. Glassy carbon rods were prepared by polishing with increasingly fine alumina powders in an ethanol slurry, from 1 µm to 0.3 µm to 0.05 µm.

Further depositions onto practical graphite-composite electrodes were performed. These deposits were 14 mm diameter to allow 11 mm diameter anodes to be cut. Anodes would be later used in Chapter 4 in Swagelok half-cell arrangements for reliable measurements of practical performance. 11 mm diameter electrode discs were punched out of the deposition area using a precision punch (EL-CELL, EL-Cut), the required size for use in the Swagelok half-cell arrangements available.

Pristine copper foil surfaces (0.05 mm thickness, 99.9 % purity) were also used. Graphite-composites were formed as an ink and spread onto a copper foil surface, explained in Chapter 2. Hence, tests were performed to assess the effect of the presence of this copper foil without the graphite layer. Copper foil was polished using fine 400 grit size silicon carbide abrasive paper, then washed and dried with ethanol prior to use within a deposition.

Synthesised polymer material was deposited onto the surface of the working electrodes in the cell arrangements explained in the following sections. For the purposes of deposition the glassy carbon, graphite, or copper surfaces formed the working electrode in a three-electrode setup. Platinum gauze counter with silver wire pseudo reference or a $Ag/AgNO_3$ reference were used as the other two electrodes, as used within other electrodeposition studies [78]. The $Ag/AgNO_3$ was prepared from a silver wire in acetonitrile with 10 mmol dm^{-3} $AgNO_3$ and 50 mmol dm^{-3} TBAP. Initial tests used a $Ag/AgNO_3$ reference electrode, later tests switched to a silver wire pseudo reference due to Ag^+ leakage from the $Ag/AgNO_3$ reference frit. Silver wire pseudo reference has the notation Ag/Ag^+ and has potential +0.799 V *vs.* NHE, whilst $Ag/AgNO_3$ has +0.541 V *vs.* NHE [108] [109]. Therefore, potentials should be shifted by +0.258 V between the two. Ag/Ag^+ references suffer from a drifting potential, which should be kept in consideration [109].

3.1.3 Electrodepositing cell studies – glass cell

The glass cell design was made to allow the testing of oxygen and water sensitive electrochemistry, see Figure 19. This contained the working and counter electrode surfaces running parallel to each other entering the cell from two ports in the ceiling of the cell. A port near to the base was present to allow entry of the reference electrode into a pool of the electrolyte. During deposition, the glass cell was sealed to air and flushed with N_2 through a second port near the base that also contained a gas outlet. 10 mL electrolyte was then added through the rubber stopper of the reference electrode, syringed from a N_2 ampule to prevent any moisture or oxygen entering the system. Oxygen was bubbled into the solution for 15 minutes prior to the deposition cycles through the sparger, which entered through a third port in the ceiling. This was done to reintroduce oxygen to the distilled solvents and ensure saturation; the electrochemical mechanism investigated uses superoxide anions to initiate polymerisation, which are formed via oxygen reduction [41]. Depositions were then performed using cycling regimes with a SP-150 potentiostat and EC-Lab software.

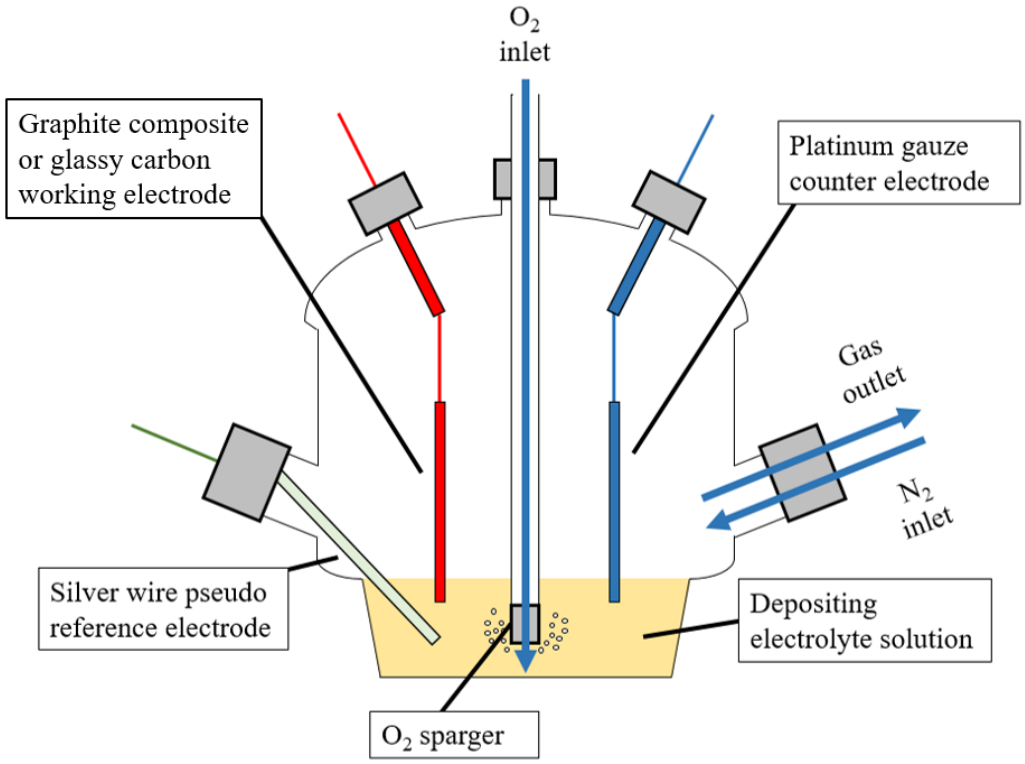

Figure 19: Schematic of the glass cell used in PAN electrodeposition studies. Figure not to scale.

The glass cell, whilst useful for confirming the properties and mechanics of the PAN deposition, was not suitable for depositing onto graphite-composite working electrodes. This was because both the graphite and copper surfaces are exposed in the solvent and it was difficult to insulate the copper side reliably without damaging the electrode or disturbing the deposition. The result

was a PAN deposit on the front and back, electrically insulating the electrode on both surfaces, with a thicker and more strongly adhered polymer to the copper surface due to greater conductive properties [67]. Properties for each are copper = 1.7 x 10^{-8} Ω m and graphite = 5 x 10^{-6} to 3 x 10^{-6} Ω m parallel to the basal plane or 3 x 10^{-3} Ω m perpendicular to the basal plane [110]. Graphite resistivity will be even higher within the graphite-composite electrodes as conduction will have to occur between particle-particle interfaces and not through a pure sheet of material. Graphite-composite working electrodes were essential for later use in a practical Swagelok lithium half-cell, so a Teflon cell arrangement was devised to allow easy deposition onto these surfaces.

3.1.4 Electrodepositing cell studies – Teflon cell

Figure 20 shows a schematic of the Teflon cell design. The Teflon cell came in two pieces that were used to house the electrochemical materials. There were three major changes when compared to the glass cell. The first and most crucial of these was that the arrangement was no longer sealed from the air. In part, this was to allow easier assembly but also because exposure to the environment was found to have little to no impact on the deposition during the glass cell experiments. This was likely due to the slow diffusion rate of gases. The diffusion coefficient for a molecule in a gas is around 10^{-6} to 10^{-5} m^2 s^{-1} [111]. In contrast, diffusion of molecules dissolved in liquid is far slower. In an aqueous solution, coefficients between 10^{-10} to 10^{-9} m^2 s^{-1} are commonly observed [111]. The result of this is that diffusion of gases into liquids is very slow over realistic length scales and is almost always dominated by convection. For oxygen diffusion in 20 °C water the typical diffusion coefficient is around 1.97 x 10^{-9} m^2 s^{-1} [112]. Oxygen was therefore introduced to the electrolyte in the Teflon cell via a sparger for 15 minutes, similar to how it was done in the glass cell, despite being open to air. The sparger was then removed to allow placement of the counter and reference electrodes. The low amounts of water vapour present in the environment were also not found to significantly impact Teflon cell electrodepositions. Around 10 mL of electrolyte was used for each of these studies.

The second change for the Teflon cell was that the reference electrode now sits behind the counter electrode and was unable to rest near the working electrode surface. Ideally, a reference electrode would be as close to the working as possible to allow as accurate a reading of the potentials between the two. This was unfortunately not possible due to practical difficulties present when assembling the cell.

The third change for the Teflon cell was a 14 mm diameter hole through the top segment which separated the counter and working electrodes that ended with a Teflon O-ring to provide a good

seal around the graphite surface. Teflon is stable in AN and acetonitrile solvents and so was a good practical choice. The O-ring was crucial to prevent the electrolyte from contacting the copper backing of the working electrode; PAN electrodeposits onto metal surfaces like copper, which would be avoided if no electrolyte contact is made [67]. This 14 mm diameter hole allows a consistent equally sized deposition area for the studies.

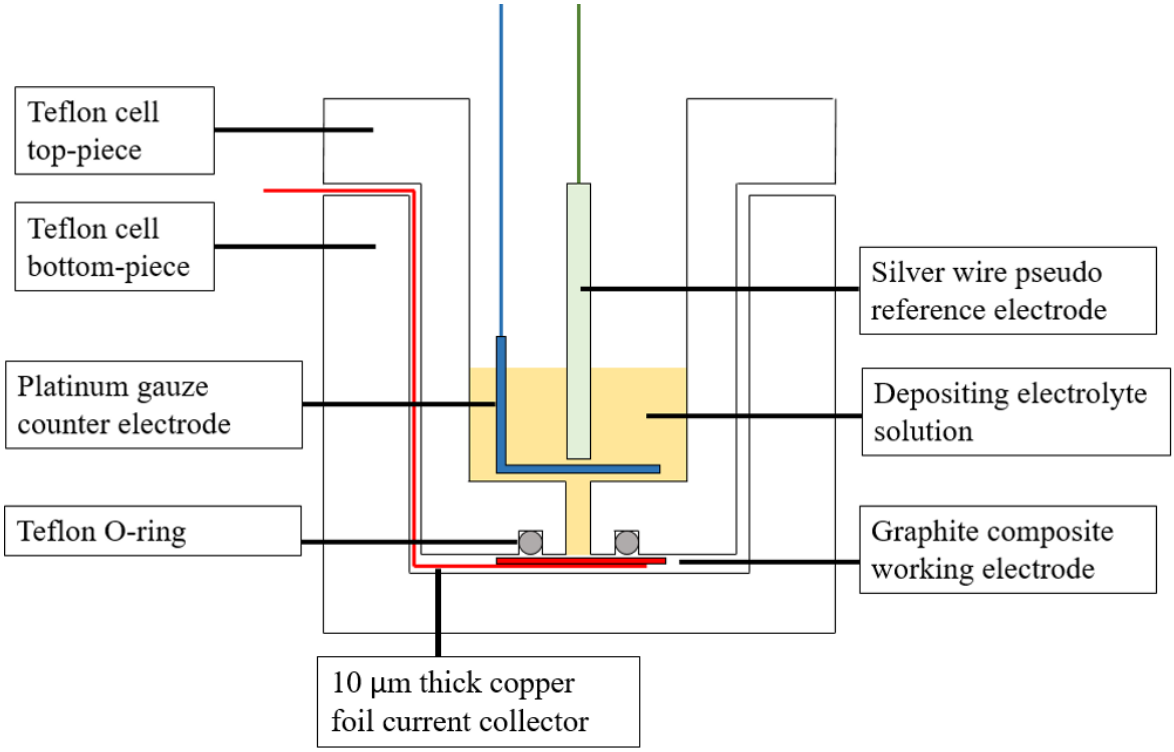

Figure 20: Schematic of the Teflon cell used in PAN electrodeposition studies. Figure not to scale.

3.1.5 Electrodeposition techniques – cyclic voltammetry

Cyclic voltammetry (CV) scans were performed in the glass and Teflon cells to induce electrodeposition of PAN onto electrode surfaces. CV involves a sweep of potential between two values at a fixed scan rate [99] [113], see Figure 21. Potential is swept in two directions, once in a forward scan and then back in a reverse scan. This technique is useful for identifying redox peaks relating to the reactions occurring, the reversibility of said reactions, and for finding the rate constants of the reactions. Each peak corresponds to a different reduction or oxidation.

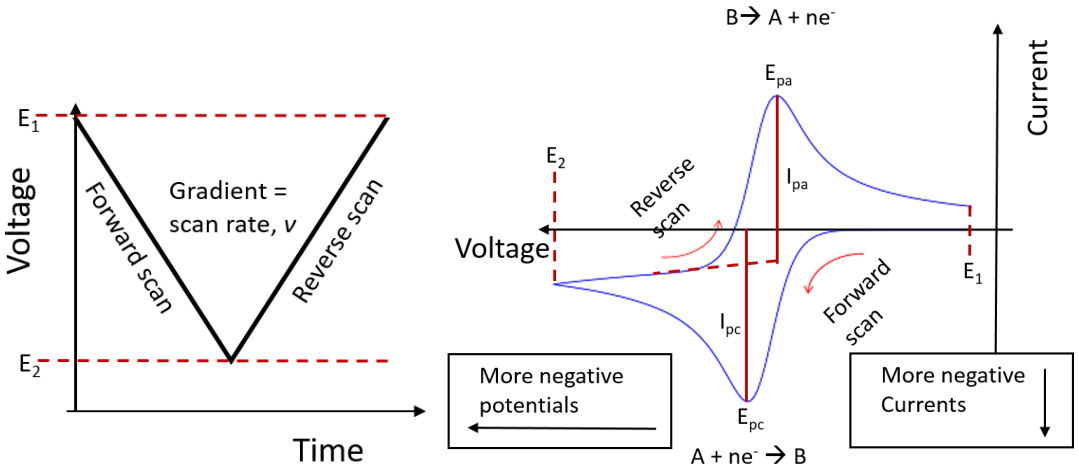

Figure 21: (Left) Linear sweep of potential during a CV, (Right) a typical reversible CV with potential and current positions of the oxidation and reduction peaks annotated, *A* is the bulk reactant and *B* is the resulting product with *n* number of electrons.

Figure 21 shows a typical reversible CV scan [113]. Potential is swept from E_1 to E_2 at a constant scan rate. Reduction occurs on the forward scan around the cathodic peak E_{pc}, oxidation occurs on the reverse scan around the anodic peak E_{pa}. In a reversible CV, the Randles-Sevcik equation can be used to determine the diffusion coefficient of the system [114]. At 298 K, the equation is:

$$i_p = (2.69 \times 10^5) n^{3/2} A C D^{1/2} \upsilon^{1/2}$$

Where i_p is the peak current (A), *n* is the number of electrons, *A* the electrode area (cm^2), *C* the concentration (mol cm^{-3}), *D* the diffusion coefficient (cm^2 s^{-1}), and υ the potential scan rate (V s^{-1}). 2.69 x 10^5 is a constant (with the units C mol^{-1} $V^{-1/2}$).

These studies were performed using the SP-150 potentiostat with EC-lab software. Analysis of oxidation and reduction features was subsequently performed. Electrodeposition potential windows were normally 0.0 V to -3.0 V against $Ag/AgNO_3$ or Ag/Ag^+ as this covered all major features expected from PAN electrodeposition [41] [42], with occasional adjustments made to highlight potential features extending outside this range or focus on a specific feature within the range. Scan rates of 50 mV s^{-1} were used for 5 or more cycles. Tests were performed using both the acetonitrile(2 mol dm^{-3} AN, 0.05 mol dm^{-3} TBAP) electrolyte [42] and AN(0.05 mol dm^{-3} TBAP) electrolyte [41]. Film thicknesses were measured using an 'External Digital Micrometer, 0-25 mm/0-1 inches' from RS Components with an absolute uncertainty of ± 1 µm.

3.1.6 Electrodeposition techniques – chronoamperometry

Chronoamperometry (CA) is an electrochemical technique often used to study the kinetics of chemical reactions, diffusion processes and adsorption [99] [113]. CA involves holding the potential of the system at a specific value and recording the current against time. A double-potential step CA study is also sometimes used to determine reversibility of a reaction by comparing the results of the two steps, see Figure 22. However, CA is also useful for the purposes of electrografting and electrodeposition for controlling film thicknesses.

CA studies were performed in the Teflon cell to induce electrodeposition of PAN onto graphite-composite electrode surfaces. These studies were performed over a range of voltages for a variable amount of time to tailor the qualities of the polymer deposit more accurately than possible with the CV scans. Properties such as the level of impurities and the thickness of the film deposit were explored. Potential difference was varied from -0.7 V to -3.0 V to cover the full range of features found in the CVs. Initially tests were performed for 100 seconds; this was because initial deposition CVs on graphite were performed at 50 mV s^{-1} from 0.0 V to -2.5 V and then reversed from -2.5 V to 0.0 V. This was a total sweep of 5 V over 100 seconds. Different time values were subsequently studied following this.

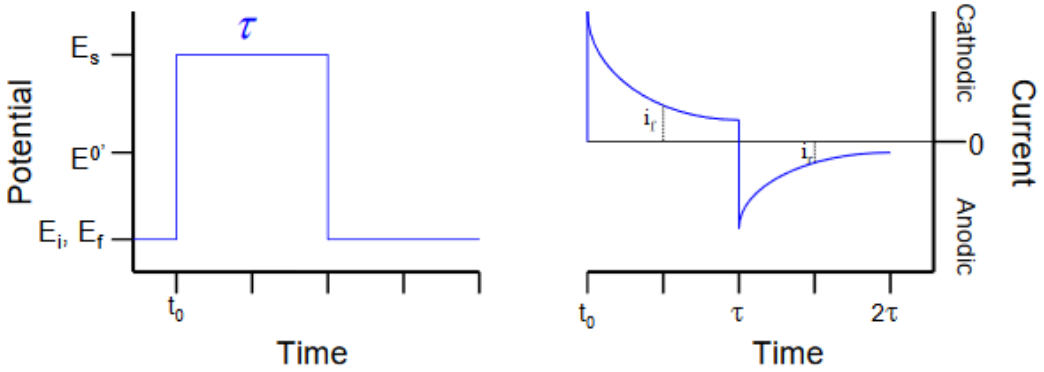

Figure 22: (Left) A typical double potential step for a reversible system applied during a chronoamperometry study, (Right) the corresponding current versus time graph from a double potential step chronoamperometry study.

These studies were performed using the SP-150 potentiostat with EC-lab software. Analysis of CA features was performed and comparisons between the masses and impurities of resulting deposits were made. Tests were performed using AN(0.05 mol dm^{-3} TBAP) electrolyte [41]. An 'External Digital Micrometer, 0-25 mm/0-1 inches' from RS Components was used to measure film thicknesses with an absolute uncertainty of ± 1 µm.

3.1.7 Physical characterisation – Raman spectroscopy

Raman spectroscopy was used to determine the chemical composition of PAN films electrodeposited onto electrode surfaces. Raman produces characteristic signals depending on the bonds present within molecules allowing the compounds and molecules present to be determined [115] [116] [117].

When light is incident upon a molecule it can be absorbed. Some light is transmitted through the sample from source to detector, which is used during infrared spectroscopy. During Raman, however, the detector is used to record light that is scattered instead of transmitted. Transmitted light leaves the sample in only one direction whilst scattered light is emitted in every direction. Typically, a monochromatic laser would be used during a Raman study that will ramp through various wavelengths. When the laser photons interact with the bonds in a molecule, the molecule is moved to a higher virtual energy state. The molecule will then fall back to a final energy state and emit a photon. If this final state is equal in energy to the initial state Rayleigh scattering will occur, but if there is a change in energy between the two states Raman scattering occurs, see Figure 23. As such, Rayleigh scattering is often referred to as elastic scattering whilst Raman scattering is inelastic. If the scattered photon is of greater energy than the incident photon, the molecule has lost energy and anti-Stokes scattering has occurred. However, if the scattered photon is of less energy than the incident photon, the molecule has gained energy and Stokes scattering has occurred. Stokes scattering is most often recorded in a Raman study as it is typically of a greater intensity and hence easier to analyse. Because frequency modulation of the emitted photons is specific to molecular vibrations within the analysed structure, it is possible to analyse the bond composition of the molecules present and crystal lattice information.

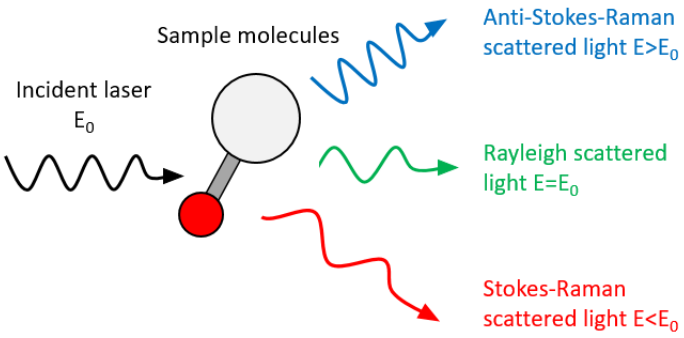

Figure 23: Illustration of the scattering of light by molecules during Raman spectroscopy.

Raman spectra were taken on a 785 nm Renishaw inVia Confocal Raman Microscope between 3500 cm^{-1} and 150 cm^{-1} to capture the full range of features of interest in PAN [41] [42]. This was performed for three accumulations at 1 % laser power. Samples were simply prepared by placing

onto a glass slide and positioning under a microscope that also acted as the Raman laser source. The incident laser can be destructive for samples due to the high power of lasers so care must be taken to manage the power of the laser whilst performing the technique. A Raman spectrum plots the wavenumber along the x-axis against the intensity in the y-axis. The position of peaks along the x-axis will determine the chemical bonds present as this relates to the wavelength of emitted photons and hence the frequency of the emitted photons. Moreover, if it is a crystalline substance the degree of crystallisation and distortion of the crystal lattice can be identified. These variations are annotated on Figure 24.

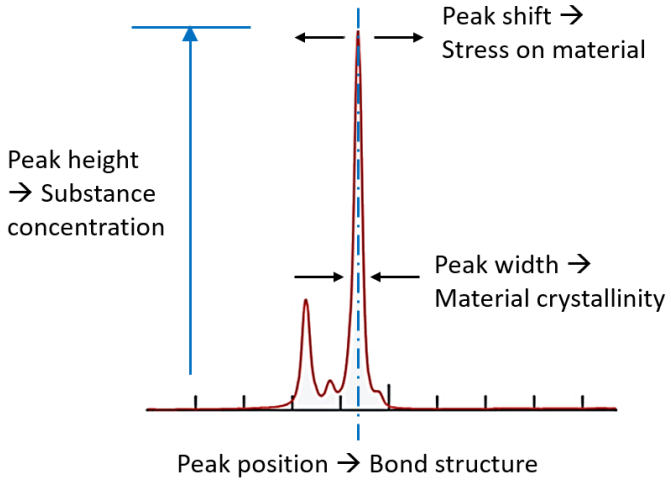

Figure 24: Illustration of the peaks of a typical Stokes-Raman spectrum. Annotations of additional information that can be read from the graph is provided.

3.2 PAN electrodeposition redox studies

Cyclic voltammetry (CV) was initially explored as an electrodeposition route. This was in part to replicate the studies of Lacey *et al.* [41] and El-Enany *et al.* [42] but also to highlight any redox peaks that occurred during depositions. Features of CVs were used to provide clear evidence of any electrochemical processes, allowing the modelling and execution of more tailorable deposition techniques to be applied later such as chronoamperometry.

3.2.1 Initial feasibility study

An initial experiment was performed using the glass cell setup with a graphite-composite ink electrode, replicating the studies of El-Enany *et al.* [42] only replacing the glassy carbon electrode by a graphite-composite. Depositing solvent was acetonitrile(2 mol dm^{-3} AN, 0.05 mol dm^{-3} TBAP) with depositions performed for 30 CV cycles between -0.5 V and -3.0 V. Observations of the feasibility of using the graphite surface for PAN electrodepositions were made. Figure 25a shows the resulting CV; the shape appears to match that reported by El-Enany *et al.* [42] on a glassy carbon electrode in Figure 25b. A slight peak was observed near -1.0 V, seen in El-Enany's studies at -1.3 V, followed by a plateau until -2.1 V where a steep cathodic slope appears. This slope was not seen in literature reporting on pure AN deposition by Lacey *et al.* [41] and so appears to be a characteristic of acetonitrile decomposition at much more negative voltages. Potential of this acetonitrile decomposition appears to start around -2.1 V in Figure 25a but at -2.7 V in Figure 25b. The likely cause was the rough non-planar surface of the graphite-composite working electrode in the former whereas the latter uses a planar glassy carbon working electrode resulting in a range of overpotentials. This leads to the expression of CV features at less negative potentials for the graphite.

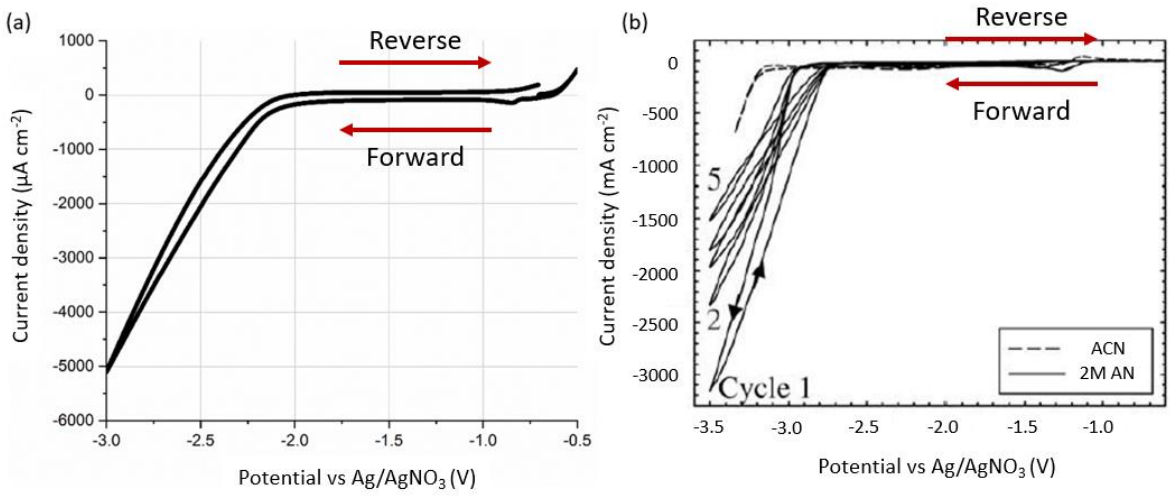

Figure 25: (a) First cycle voltammogram for the deposition of PAN onto a 400 mm^2 graphite electrode in a glass cell using acetonitrile(2 mol dm^{-3} AN, 0.05 mol dm^{-3} TBAP) electrolyte. Deposition performed at 50 mV s^{-1} from -0.5 V to -3.0 V for 30 cycles, only the first cycle is shown. Forward and reverse scan directions are annotated. (b) Cyclic voltammograms from literature [42] of acetonitrile(0.05 mol dm^{-3} TBAP) (ACN) at 50 mV s^{-1} and acetonitrile(2 mol dm^{-3} AN, 0.05 mol dm^{-3} TBAP) (2M AN) at 100 mV s^{-1} on a 3 mm diameter vitreous carbon disc electrode. The passivation of AN traces over consecutive cycles indicate the occurrence of deposition. Forward and reverse scan directions are annotated.

Upon visual inspection of the electrode a preferential deposit was observed on the copper side with little on the graphite side, see Figure 26. This was possible as both sides of the electrode are exposed to the depositing solvent within the glass cell design, see Figure 19. Deposit on the copper side was more prevalent due to a lesser resistivity; the properties for each are copper = 1.7 x 10^{-8} Ω m and graphite = 5 x 10^{-6} to 3 x 10^{-6} Ω m parallel to the basal plane or 3 x 10^{-3} Ω m perpendicular to the basal plane [110]. Deposit on the copper side also flaked and fell from the surface, a problem that occurs during drying processes when deposits become too thick. Care must therefore be taken to insulate the copper from deposition. An additional concern was that the graphite ink had delaminated from the copper surface, possibly due to swelling or dissolving of the polymeric PVDF binder in the solvent. Submersion of other graphite inks into pure acetonitrile and pure AN indicated delamination in the acetonitrile but not the AN. Therefore, acetonitrile studies were not further investigated for production of practical electrodes.

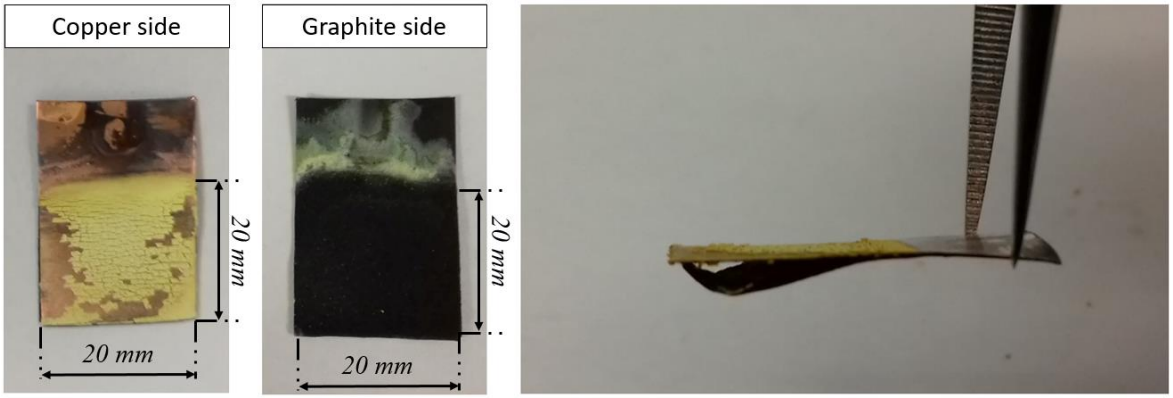

Figure 26: Images for the deposition of PAN onto a 400 mm^2 graphite electrode in a glass cell using acetonitrile(2 mol dm^{-3} AN, 0.05 mol dm^{-3} TBAP) electrolyte. From left to right, copper side with flaked deposit, discoloured graphite side, side view showing delamination of graphite ink from copper foil. Deposition performed using cyclic voltammetry at 50 mV s^{-1} from -0.5 V to -3.0 V for 30 cycles.

Raman results of the deposit on the copper side are shown in Figure 27, as well as a comparison with PAN and copper standards. The copper(PAN) deposit was similar to the clean copper foil as light from the Raman laser can penetrate through the PAN film; the large slope from the copper background signal was clearly present. However, several notable PAN features are observed. Most obviously are the peaks at 2250 cm^{-1} and 3000 cm^{-1}, corresponding to the C≡N cyano group and the C-H alkyl group respectively. Several smaller PAN peaks are observed between 1000 cm^{-1} and 1500 cm^{-1}. It can therefore be stated that a material with similar bond structure to PAN was deposited.

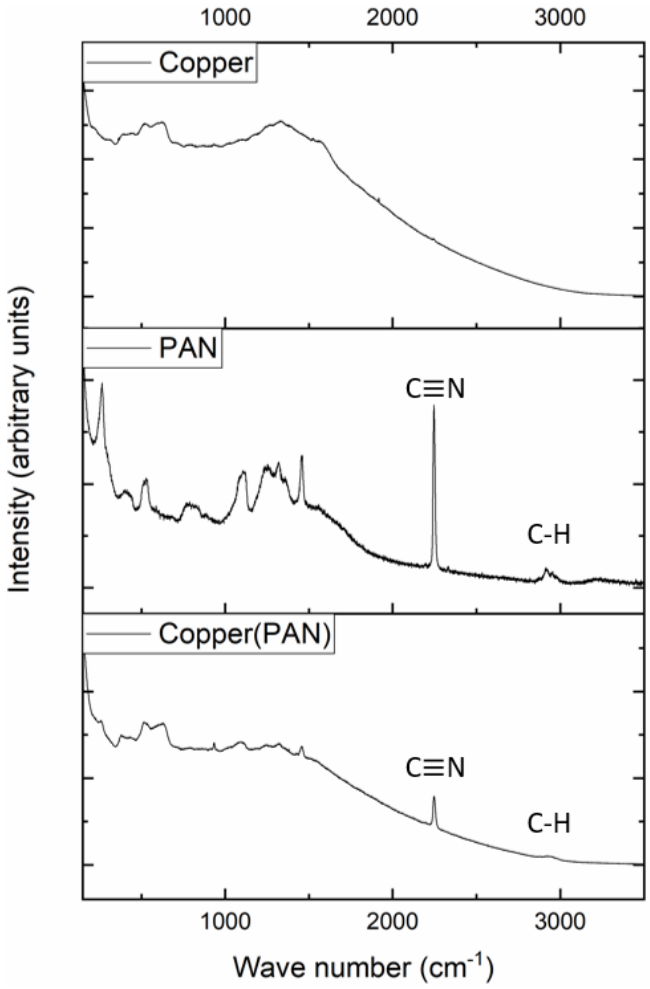

Figure 27: Raman data for the deposition of PAN onto a 400 mm^2 graphite electrode in a glass cell using acetonitrile(2 mol dm^{-3} AN, 0.05 mol dm^{-3} TBAP) electrolyte. Data for the copper side of the graphite electrode. From top to bottom: copper standard, PAN standard (Sigma-Aldrich), deposition area on the copper side of the graphite electrode used. Key bonds are annotated. Raman data taken at 1 % laser power on a 785 nm Raman laser for 3 accumulations.

Additional characterisation experiments were performed using SEM and EDS, see Figure 28. This was performed on the discoloured graphite-composite side from Figure 26. From the SEM image, a clear transition from clean graphite on the right to a deposited area on the left can be seen. An EDS length scale was then used to determine the elemental proportions of the deposit. The chemical formula for a PAN monomer unit is $(C_3H_3N)_n$. The calculated ratios between the carbon and nitrogen of the EDS are compared to the ideal PAN chain resulting in values of:

- C_{EDS} = 70 %, C_{ideal} = 72 %
- N_{EDS} = 30 %, N_{ideal} = 28 %

Only carbon and nitrogen proportions were considered for the above percentages. The similarity in ratios was reassuring for the deposition method. It was therefore concluded with support from the Raman data in Figure 27 that the deposited polymer was PAN.

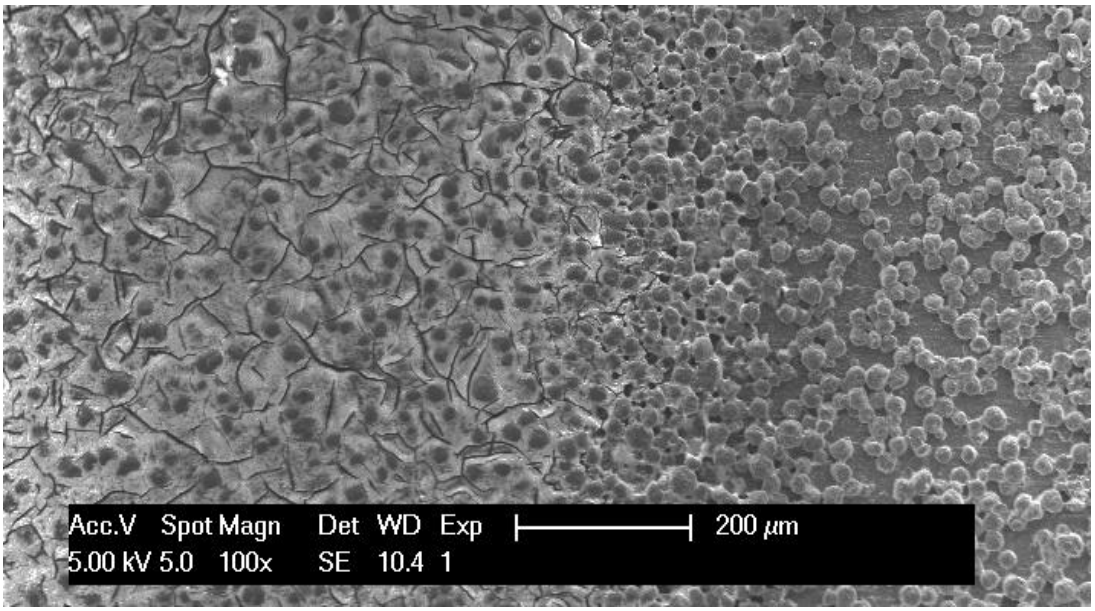

Figure 28: SEM image for the deposition of PAN onto a 400 mm^2 graphite electrode in a glass cell using acetonitrile(2 mol dm^{-3} AN, 0.05 mol dm^{-3} TBAP) electrolyte. A deposit is seen on the left that transitions to clean graphite on the right. Image taken at 100X magnification.

Closer magnifications revealed brighter areas on the exposed graphite particles in the deposition region, see Figure 29a. EDS revealed this to be silver impurities with greater quantities on the brighter regions, see Figure 29b. The only presence of silver in the system was from the $Ag/AgNO_3$ reference electrode. Ag^+ leakage from $Ag/AgNO_3$ is a known issue and has been reported elsewhere [118]. Therefore, the reference electrode was changed for a Ag/Ag^+ silver wire pseudo reference. Fluoride was found in both regions, likely present in the PVDF binder of the composite.

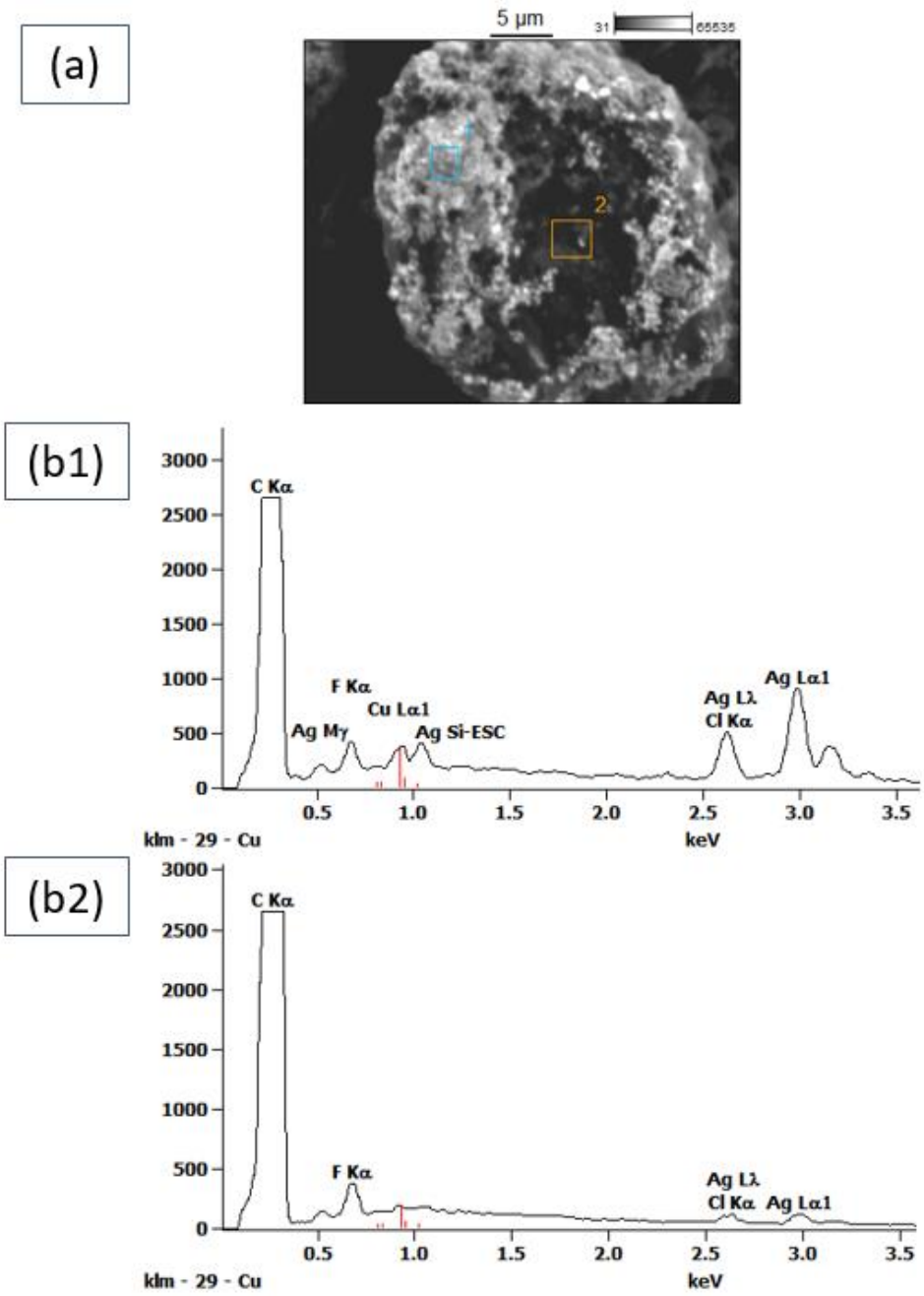

Figure 29: SEM and EDS of exposed graphite particles between deposited PAN. Depositions were performed onto a 400 mm^2 graphite electrode in a glass cell using acetonitrile(2 mol dm^{-3} AN, 0.05 mol dm^{-3} TBAP) electrolyte. (a) SEM image of an exposed graphite particle, noticeable brighter and darker areas are observed on the graphite surface. Image taken at 2000X magnification. (b1) EDS of a brighter area on the exposed graphite surface. (b2) EDS of a darker area on the exposed graphite surface.

3.2.2 Oxygen as a polymerisation initiator and water contamination studies

Several studies were performed in the glass cell using glassy carbon working electrodes to assess effects of oxygen saturation and water contamination on PAN depositions. 10 mL of electrolyte was prepared and used as is or saturated with O_2 for 15 minutes using a sparger through the top port of the glass cell. O_2 free and O_2 saturated samples were tested with and without 0.5 mol dm^{-3} H_2O. As stated in Section 3.1.1, deposition solvents were prepared by adding TBAP to an ampule in an N_2 glovebox that was sealed and added to a Schlenk line where required solvents were then syringed into the mixture. These mixtures were stirred at 500 rpm using a stir bar with stir plate for 2 hours. For the water contamination studies, the measured water was also syringed in and stirred. In total four conditions were investigated, the relevant details are displayed in Table 4 along with the designated sample names.

Table 4: Square diagram for the presence or lack thereof of oxygen or water within oxygen saturation and water contamination studies. The diagram gives the designated names of these samples at each intersection of the columns and rows.

Water? / Oxygen?	**H_2O free**	**H_2O contaminated**
O_2 free	O_2 free	O_2 free with 0.5 mol dm^{-3} H_2O
O_2 saturated	O_2 saturated	O_2 saturated with 0.5 mol dm^{-3} H_2O

Initially, the effects of conditions were studied on acetonitrile(0.05 mol dm^{-3} TBAP) to determine the behaviour of water and oxygen at the applied voltages in the absence of the monomer. This was done from 0.0 V to -3.0 V, the region where AN monomer reduction is reported but little acetonitrile activity [41] [42]. Later experiments investigated AN(0.05 mol dm^{-3} TBAP) to study the effects of the conditions on the polymerisation itself.

Figure 30 shows first and fifth cycles of cyclic voltammograms using acetonitrile(0.05 mol dm^{-3} TBAP) for the oxygen saturation and water contamination studies. Of note was the lack of activity in the absence of oxygen until around -2.5 V where the acetonitrile solvent appears to be reduced. The most important features, however, corresponded to the reduction of oxygen to

superoxide at -1.25 V followed by a further reduction of superoxide to peroxide at -2.25 V [41] [74] for O_2 saturated without water. The reactions for these steps are as follows:

$$O_2 + e^- \rightleftharpoons O_2^{\bullet -}$$

$$O_2^{\bullet -} + e^- \rightarrow O_2^{2-}$$

Reduction of oxygen to superoxide appears to be quasi-reversible, evidenced by the pair of anodic and cathodic peaks, whilst the superoxide to peroxide appears to be irreversible. Peak intensity also reduces on successive cycles, a result of decreasing oxygen concentrations as irreversible peroxide formation progresses. The presence of water on the system appears to have shifted these oxygen and superoxide reduction peaks to less negative potentials. However, the peak for irreversible superoxide to peroxide reduction appears shifted much greater and may correlate to the electroreduction of hydrogen peroxide via the following mechanism [119] [120] [121] [122]:

$$O_2 + e^- + H^+ + * \rightarrow HOO*$$

$$HOO* + e^- + H^+ \rightarrow H_2O_2 + *$$

$$H_2O_2 + 2H^+ + 2e^- \rightarrow 2H_2O$$

* is the conductive surface chemical materials adsorb onto. The origin of the hydrogen peroxide would be explained by one of two paths. The reaction of superoxide with water, as superoxide was rapidly decomposed in aqueous solutions to produce O_2 and H_2O_2 [123]. This would explain the lack of the superoxide to peroxide reduction peak. Alternatively, hydrogen peroxide can be formed via the reduction of oxygen with two protons [124].

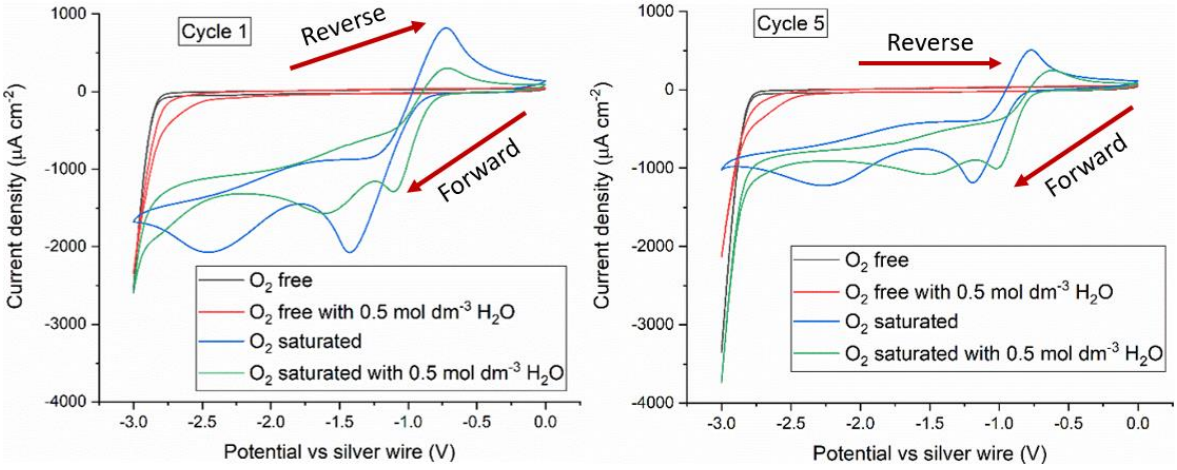

Figure 30: (Left) First cycle and (right) fifth cycle voltammograms for 3 mm diameter glassy carbon electrodes in a glass cell using acetonitrile(0.05 mol dm^{-3} TBAP) electrolyte; studies performed to investigate oxygen saturation and water contamination. No AN monomer was present. The studies performed were an O_2 free study, O_2 saturated study, O_2 free with 0.5 mol dm^{-3} H_2O study, and O_2 saturated with 0.5 mol dm^{-3} H_2O study. Studies performed using cycling voltammetry from 0.0 V to -3.0 V at 50 mV s^{-1}. Forward and reverse scan directions are annotated.

An additional study was performed to determine the reversibility of the O_2 reduction to superoxide. This is essential for understanding the behaviour of the superoxide anion as an electrogenerated initiator. CVs were performed with varying scan rates from 5 to 200 mV s^{-1} between 0.0 V and -2.0 V. For a reversible CV, the peak current of these scans is proportional to the square root of the scan rate ($i \propto v^{\frac{1}{2}}$) and the separation of the two peaks ($|E_{pa} - E_{pc}|$) is equal to 57/n mV, where n is the number of electrons (n = 1 for the reduction of O_2 to superoxide). Deviations from this behaviour will tend from reversible to quasi-reversible where the kinetics of the reactions are slower. Slow reaction kinetics can be caused by both resistance to charge transfer or diffusion limited mass transport. This leads to increased peak separation from higher overpotentials as equilibrium at the electrode surface is established less rapidly. Peak current is also no longer proportional to the scan rate.

It is recognised that the $O_2/O_2^{\bullet-}$ redox couple is quasi-reversible in aprotic solvents, such as acetonitrile or AN. The superoxide radical anion will typically have a half-life around 40 minutes at room temperature [74]. $O_2^{\bullet-}$ is a moderately strong nucleophile and as such will react with sufficiently active Michael acceptors (i.e. vinyl groups with an electron-withdrawing substituent, such as that found in AN). The use of electrogenerated superoxide as a nucleophile in organic synthesis is reported in the literature as an initiator for a range of vinyl monomers [70].

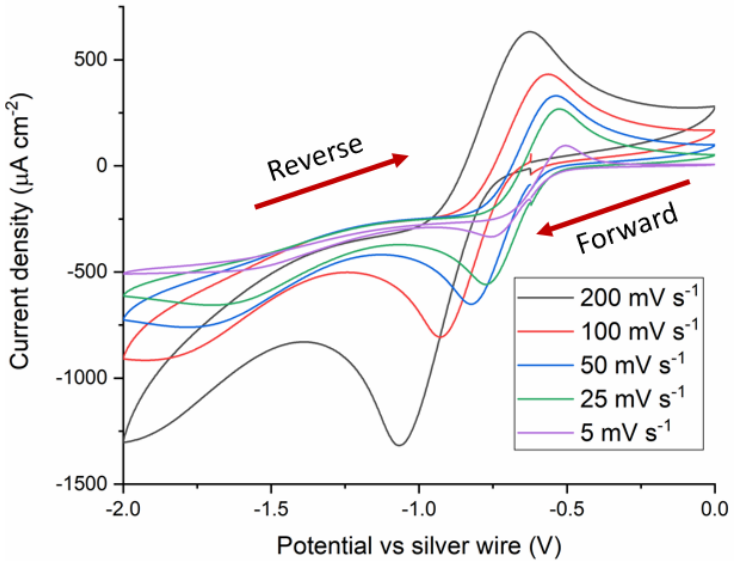

Figure 31: Cyclic voltammograms for oxygen on 3 mm diameter glassy carbon in O_2 saturated acetonitrile(0.05 mol dm^{-3} TBAP) without water contamination. Voltammetry performed at a range of scan rates between 0.0 V and -2.0 V. Platinum gauze counter electrode and silver wire reference were used. Forward and reverse scan directions are annotated.

Figure 31 shows the cyclic voltammograms for O_2 saturated acetonitrile without water contamination, performed on a glassy carbon working electrode. No AN monomers were present for this study. The quasi-reversibility of the $O_2/O_2^{\bullet-}$ redox couple is indicated by the increasing peak separation and far greater values than 57 mV shown in Table 5. Peak currents are also shown to not be proportional with the square root of the scan rate.

Table 5: Key values from cyclic voltammograms in $O_2/O_2^{\bullet-}$ reversibility studies from Figure 31. 3 mm diameter glassy carbon in O_2 saturated acetonitrile(0.05 mol dm^{-3} TBAP) without water contamination was used. Voltammetry performed at a range of scan rates between 0.0 V and -2.0 V, with a Platinum gauze counter electrode and silver wire reference. pc = cathode peak values, pa = anode peak values.

Scan rate, v (mV s^{-1})	I_{pc} (µA cm^{-2})	E_{pc} (V)	E_{pa} (V)	$I_{pc}/v^{\frac{1}{2}}$ (mA $V^{-1/2}$ $s^{-1/2}$)	$\lvert E_{pa} - E_{pc} \rvert$ (mV)
200	-1318	-1.065	-0.626	-0.21	439
100	-807	-0.926	-0.562	-0.18	364
50	-652	-0.823	-0.538	-0.21	285
25	-558	-0.774	-0.525	-0.25	249
5	-334	-0.759	-0.504	-0.33	255

These oxygen saturation and water contamination studies were also run using AN(0.05 mol dm^{-3} TBAP) to investigate the effects of these conditions on the polymerisation itself. Voltammograms for the first and fifth CV cycles are shown in Figure 32. Table 6 shows the key potentials identified for the reactions during the electropolymerisation of PAN onto glassy carbon during these studies. Similar to the acetonitrile studies in Figure 30, O_2 free has no features corresponding to oxygen. Unlike the acetonitrile study, there was no large reduction below -2.5 V indicating that this feature was due to the bulk reduction of acetonitrile and not any other electrochemistry. For O_2 free with water, a large peak was observed around -2.2 V with a large reduction at -2.5 V and above during the first cycle. On the fifth cycle, only the feature above -2.5 V remains although at much lower current densities, having fallen from -12000 µA cm^{-2} down to -4000 µA cm^{-2}. This feature was observed in the O_2 saturated with water, and was therefore likely due to an interaction with the water molecules. This feature at -2.5 V appears to correspond with the acetonitrile reduction in the previous studies; however unlike the acetonitrile reduction the peak current in these cases was initially four times greater but was reduced substantially by the fifth cycle indicating interaction with the AN monomers that was not present in the acetonitrile

studies. The peak at -2.2 V was also no longer present after the first cycle, also seeming to indicate an interaction with the monomer units. Indeed, this feature at -2.2 V corresponds to a feature highlighted by Lacey *et al*. [41] as the monolayer reduction of the vinyl group to form a radical anion, which is the accepted mechanism for electropolymerisation of vinyl monomers in aprotic solvents [70] [125].

Table 6: Key potentials and the corresponding reactions identified during the electropolymerisation of PAN onto glassy carbon electrodes.

Reduction potential *vs.* silver wire pseudo reference (V)	**Reaction**
-1.25 V	$O_2 + e^- \rightleftharpoons O_2^{\bullet -}$
-2.25 V	$O_2^{\bullet -} + e^- \rightarrow O_2^{2-}$
-1.4 V	Electropolymerisation of PAN to electrode
-2.2 V	Electropolymerisation of PAN in solution

No PAN deposit was recorded for either of the O_2 free studies, however a yellow discolouration was observed with the O_2 free study with water indicating polymerisation in solution providing further evidence to an interaction with AN occurring. A yellow discolouration of the solution has been reported in two previous studies by Mertens *et al*. [72] [126] and has been linked to the effects of polymerisation in solution. Two noticeable PAN polymerisation peaks might be observed, one at a less negative potential that was followed by an immediate passivation and a reduction in current density after the peak. This passivation links this first feature to the electrografting on PAN onto an electrode surface and is observed in the works of Mertens *et al*. [72] [126] near to -2.3 V *vs.* a platinum pseudo reference and is seen in Figure 32 at around -1.4 V in the O_2 saturated and water free study. This potential shift was expected as a silver wire pseudo reference has an electrode potential of +0.799 V *vs.* NHE [108]. The second peak occurring around -2.2 V in the presence of water was the one identified as polymerisation in solution by Mertens, where no passivation occurs and was followed by a large reduction. This peak has a much greater current density than the electrografting feature and was more noticeable in studies performed with water in both O_2 free and O_2 saturated studies. It was therefore assumed that the presence of water promotes vinyl monomer reduction. Indeed, Gabriel *et al*. [70] reports that the presence of water are a source of problems for vinyl monomer electrografting because of an earlier electroreduction than the monomer that prevents the polymer from being chemisorbed to the electrode and causing polymerisation in solution.

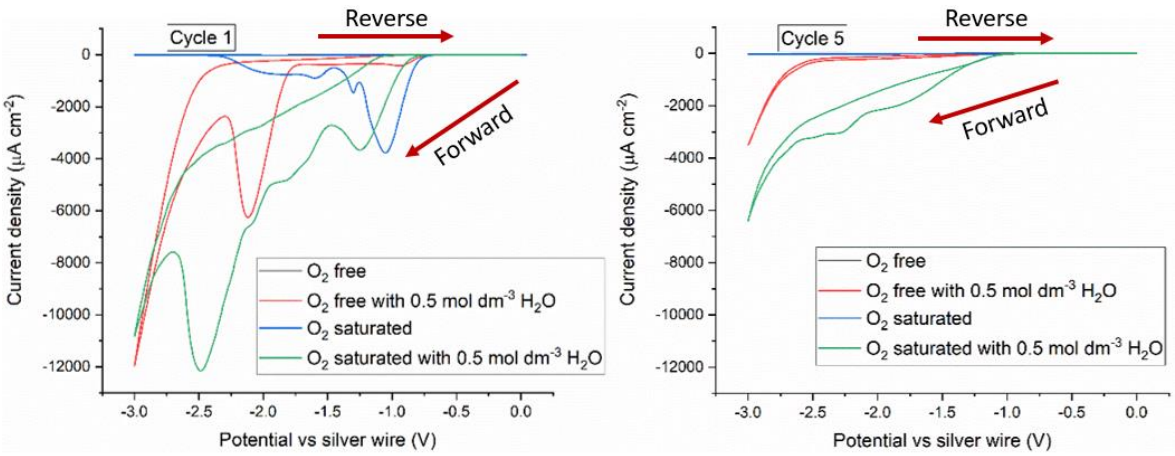

Figure 32: (Left) First cycle and (right) fifth cycle voltammograms for 3 mm diameter glassy carbon electrodes in a glass cell using AN(0.05 mol dm^{-3} TBAP) electrolyte; studies performed to investigate oxygen saturation and water contamination. The studies performed were an O_2 free study, O_2 saturated study, O_2 free with 0.5 mol dm^{-3} H_2O study, and O_2 saturated with 0.5 mol dm^{-3} H_2O study. Studies performed from 0.0 V to -3.0 V at 50 mV s^{-1}. Forward and reverse scan directions are annotated.

The final two conditions, O_2 saturated and O_2 saturated with water both show an oxygen reduction peak at around -1.25 V during the first cycle and have a resulting PAN deposit. This feature was not present in successive cycles and does not share the quasi-reversible behaviour shown in Figure 31, indicating an immediate passivation of the electrode surface by polymerisation or the usage of the superoxide anions in the polymerisation electrochemistry. O_2 saturation without water shows a second peak around -1.4 V followed by a passivation, indicating polymerisation of AN and electrografting onto the electrode surface. The O_2 reduction peak was much broader in the presence of water and this AN polymerisation peak was likely obscured by the O_2 reduction. Both show a feature from -1.5 V to -2.5 V, this was likely the peak linked to the polymerisation of AN in solution and can be seen in both conditions during the first cycle. During the fifth cycle, the second broader feature was still observed in the study with water indicating either a failure to fully passivate the surface or further electrochemistry occurring. Indeed, if water prevents chemisorption to the electrode surface as suggested by Gabriel *et al*. [70] then it was likely that the surface is not fully passivated in the presence of water. Despite this clear activity due to the water contamination, PAN deposit mass doubled from 1.0 mg (14.1 mg cm^{-2}) without H_2O to 2.0 mg (28.2 mg cm^{-2}) with 0.5 mol dm^{-3} H_2O indicating that water might promote growth of polymer chains electrografted to the electrode as well as growth of polymer chains in solution. Further studies with H_2O introduced to depositing solutions of graphite-composite electrodes were therefore carried out in Section 3.3.4 to see if the introduction of water was of benefit to the PAN deposition onto other surfaces.

The glassy carbon electrode before and after electrodeposition of PAN in the O_2 saturated study without water is shown in Figure 33. The deposit of PAN appears as a thin white film over the glassy carbon electrode surface. Raman data for the O_2 saturated without water study is shown in Figure 34. The characteristic PAN peaks of C≡N cyano group at 2250 cm^{-1} and C-H alkyl group at 3000 cm^{-1} are observed. Additionally, peaks of carbon corresponding to the glassy carbon are seen at 1350 cm^{-1}, 1600 cm^{-1}, and 2700 cm^{-1}.

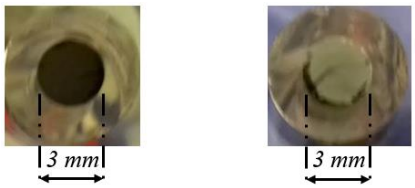

Figure 33: Images for the deposition of PAN onto a 3 mm diameter glassy carbon electrode in a glass cell using AN(0.05 mol dm^{-3} TBAP) electrolyte with O_2 saturation and without water, (left) before and (right) after. Deposition performed using cyclic voltammetry from 0.0 V to -3.0 V at 50 mV s^{-1} for 5 cycles.

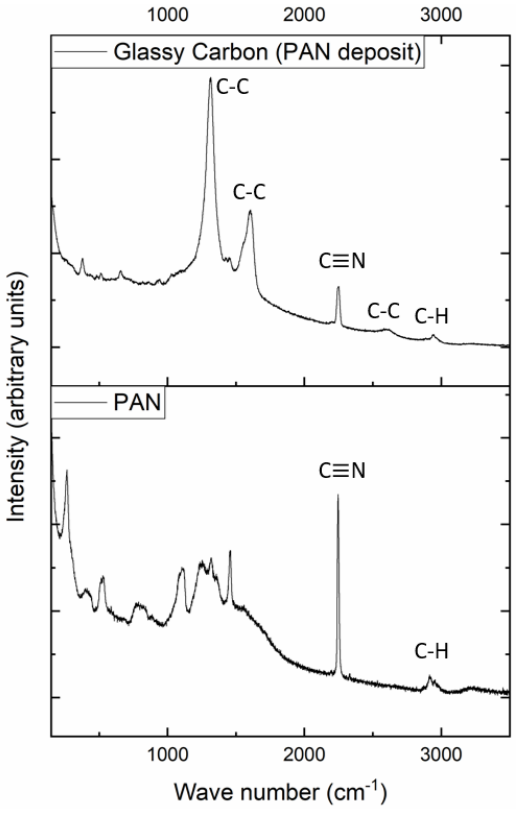

Figure 34: Raman data for the deposition of PAN onto a 3 mm diameter glassy carbon electrode in a glass cell using O_2 saturated AN(0.05 mol dm^{-3} TBAP) without water. Deposition performed using cyclic voltammetry from 0.0 V to -3.0 V at 50 mV s^{-1} for 5 cycles. (Top) PAN deposit onto a glassy carbon surface and (Bottom) PAN standard (Sigma-Aldrich). Key bonds are annotated. Raman data taken at 1 % laser power on a 785 nm Raman laser for 3 accumulations.

There are several key conclusions to be drawn from these oxygen saturation and water contamination studies. Firstly, was that the reduction of oxygen to superoxide anions was a quasi-reversible process occurring around -1.25 V *vs.* Ag/Ag^+. Secondly, was that the presence of oxygen was necessary for the electrografting of PAN onto the electrode surface with recorded masses only occurring during oxygen saturation studies. This electrografting onto the electrode surface provides a polymerisation peak around -1.4 V *vs.* Ag/Ag^+ that immediately passivates the electrode. An additional polymerisation peak was observed around -1.5 V to -2.5 V *vs.* Ag/Ag^+ that does not passivate the surface and was linked to polymerisation in solution, evidenced by a yellow discolouration of the solution. Finally, additional water contamination studies onto graphite-composite electrode surfaces are required (performed in Section 3.3.4) to validate if the benefits of increasing mass were still applicable onto other surfaces.

3.3 Graphite-PAN electrodeposition practicality

Following studies performed in Section 3.2, providing an in depth understanding of the electrochemistry involved in PAN electrodeposition, work was performed on electrodepositing consistent films onto graphite-composite electrodes. Studies expanding upon the CVs used previously were explored on graphite-composite electrodes as well as clean copper foil surfaces onto which graphite-composites were cast. These studies used O_2 saturation without water unless stated otherwise. The potential effects of water contaminants on the system were briefly revisited with the new graphite surface. The intention was to investigate the potential discrepancies by depositing onto differing surfaces than the planar glassy carbon surfaces. As demonstrated by Mertens *et al*. [72], when depositing PAN onto nickel and zinc surfaces, the expression of polymerisation peaks is highly dependent upon the surface deposited onto. This may also yield promising information for further studies onto any other electrode surfaces other than graphite. A transition was also made from the controlled and sealed glass cells to a non-sealed but more practical Teflon cell to facilitate easier production of graphite-PAN electrodes (graphite-composite electrodes coated with PAN films).

3.3.1 Copper surface electrodepositions

Graphite-composite electrodes were prepared by mixing graphite, carbon, and PVDF with NMP solvent before casting onto a copper surface. Because of the nature of electrografting forming strongly adhering films onto conductive surfaces, the deposition of PAN onto copper surfaces was investigated as the material would unavoidably be present during the depositions even if covered by an electrode ink. It is possible that PAN films may nucleate and grow between graphite particles from the copper itself. Therefore, it was prudent to understand any differences in morphology and electrochemistry that might arise due to this differing deposition surface.

PAN electrodepositions were performed in a glass cell using AN(0.05 mol dm^{-3} TBAP). Depositions were performed onto a 20 mm X 8 mm (160 mm^2) area of copper foil submerged into the electrolyte with 15 minute O_2 saturation and no water presence. To avoid depositing onto both sides of the electrodes, the side furthest from the counter and reference was coated with a silicone grease. Potential was cycled at 50 mV s^{-1} from 0.0 V to -3.0 V for 5 cycles.

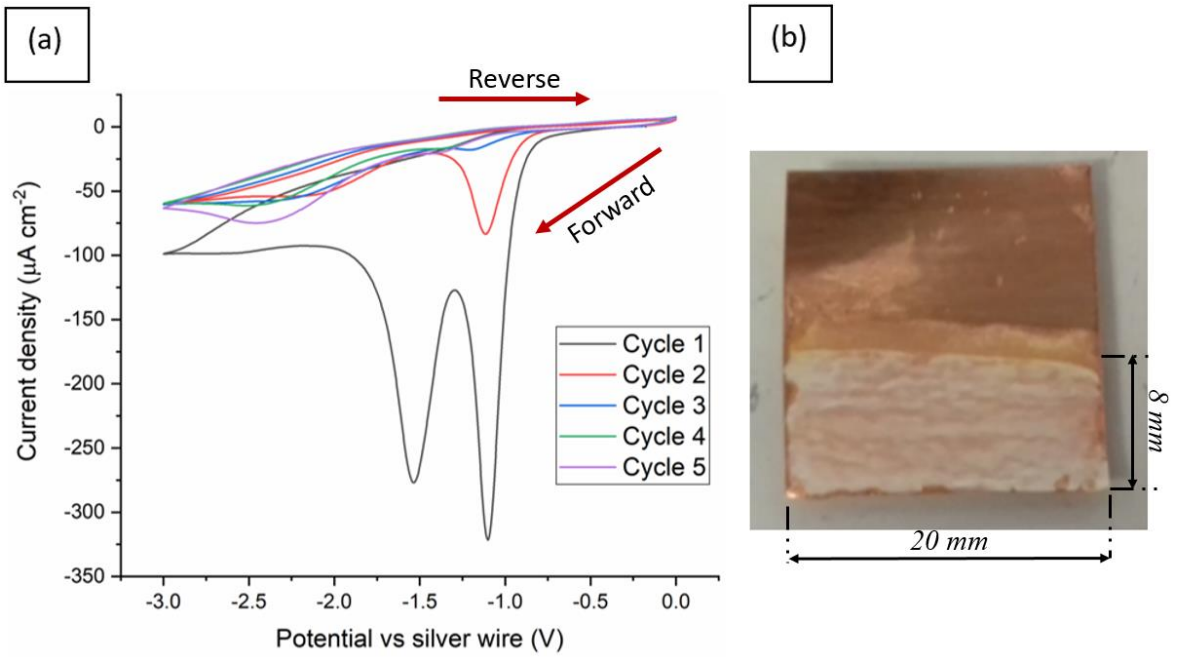

Figure 35: (a) Cyclic voltammogram data for PAN deposition onto a 20 mm X 8 mm (160 mm^2) copper foil electrode in a glass cell using AN(0.05 mol dm^{-3} TBAP) electrolyte with O_2 saturation and without water. Deposition performed at 50 mV s^{-1} from 0.0 V to -3.0 V for 5 cycles. Forward and reverse scan directions are annotated. (b) Image of the PAN deposit onto a 20 mm X 8 mm copper foil electrode. One side of the foil was exposed to electrolyte whilst the reverse side was insulated with a silicone grease.

As is immediately obvious in Figure 35b, a successful deposit of a white-yellow coating was achieved onto the area in the electrolyte. Total mass of 3.0 mg was deposited, giving 1.9 mg cm^{-2}. The deposit did not appear wholly uniform, however, appearing thicker and thinner in certain locations. This was a potential concern for lithium-ion electrodes where a homogeneous surface is ideal, something to consider when depositing onto graphite-composite or other electrode materials. The cyclic voltammogram data in Figure 35a can provide key insight as to how the growth of the polymer film led to the variation in film thickness. A strong oxygen reduction peak was seen in the first cycle at -1.1 V, with reducing intensities in the second and then third cycles. This behaviour was not seen in the glassy carbon electrode studies in Section 3.2.2 where immediate passivation was observed after the first cycle in O_2 studies without water. This would imply that immediate passivation did not occur for the copper surface suggesting either areas were still exposed and did not nucleate polymer growth, or that cracks were readily available in the resulting deposit surface due to excessive stresses introduced during polymer growth. Interestingly, a strong polymerisation passivation peak was seen at -1.5 V during the first cycle, suggesting that the majority of the electrode surface was coated after this first cycle. In successive cycles, polymerisation in solution appears to occur much more strongly around -2.25 V when compared to the passivation peak in the first cycle. The height of this polymerisation in solution peak also seems to increase during later cycles. This did not occur with the glassy carbon electrode where complete passivation was observed after the first cycle, implying the increased presence of cracks during successive cycles.

A comparison was made with PAN deposition onto a copper surface in the Teflon cell. O_2 saturated AN(0.05 mol dm^{-3} TBAP) electrolyte without water was again used, however there was no need to insulate the reverse side of the copper due to the seal provided by a Teflon O-ring over the deposition area. The deposition area was within a 14 mm diameter bore, giving 154 mm^2. The potential was cycled at 50 mV s^{-1} from 0.0 V to -3.0 V for 5 cycles. The Teflon cell, unlike the glass cell, was open to air so the affects of moisture on the system were of interest.

Figure 36b shows a white-yellow PAN deposit was obtained over the deposition area. Once again, there was questionable uniformity due to some areas of seemingly varying thickness. However, passivation was more apparent from the CV data in Figure 36a. Oxygen reduction occurs at just around -1.4 V *vs.* Ag/Ag^+ in the first cycle. At -1.75 V, the passivation peak was observed. There was a shift between the oxygen reduction and polymerisation peaks from glass cell to Teflon cell, around 0.25 V to 0.3 V. This may be due to better oxygen saturation within the Teflon cell evidenced by the greater peak current of -800 µA cm^{-2} compared to -300 µA cm^{-2} in the glass cell. This can cause a peak shift to greater potentials as more reactant is present within the bulk solution allowing greater currents to be reached as the diffusion to the surface is less limited. The

peak extends further and greater potentials are observed. There was a small oxygen reduction peak in the second cycle, as well as a polymerisation in solution feature in successive cycles. However, these features are smaller than the initial passivation peak implying good coverage of the polymer film when deposited using the controlled Teflon cell area. Total PAN deposit recorded was 2.8 mg, giving 1.8 mg cm^{-2}. This mass per area was comparable to the glass cell study.

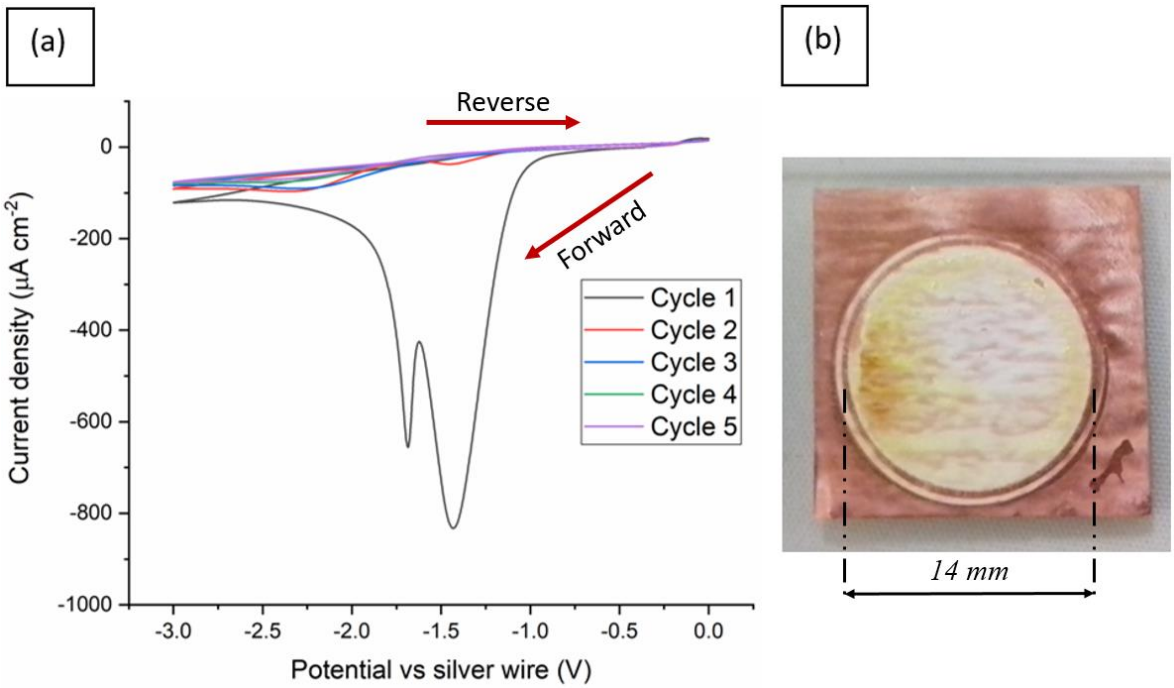

Figure 36: (a) Cyclic voltammogram data for PAN deposition onto a 14mm diameter (154 mm^2) copper foil electrode in a Teflon cell using AN(0.05 mol dm^{-3} TBAP) electrolyte with O_2 saturation and without water. Deposition performed at 50 mV s^{-1} from 0.0 V to -3.0 V for 5 cycles. Forward and reverse scan directions are annotated. (b) Image of the PAN deposit onto a 14mm diameter copper foil electrode.

3.3.2 Graphite-composite surface electrodepositions

Similar to PAN electrodeposition performed on copper in Section 3.3.1, PAN was deposited onto graphite-composite electrodes in both a glass cell and Teflon cell for comparison of practicality. O_2 saturated AN(0.05 mol dm^{-3} TBAP) was used once more, leading to PAN electrodeposits in both arrangements. The potential was cycled at 50 mV s^{-1} from 0.0 V to -3.0 V in the glass cell for 5 cycles. An extended range from 0.0 V to -3.5 V at a 50 mV s^{-1} scan rate was used in the Teflon cell for 5 cycles to fully cover observed features.

Similar to other studies performed in a glass cell on copper and glassy carbon surfaces, a white deposit was obtained on the graphite-composite surface, see Figure 37b. The reverse side of the copper was insulated with silicone grease to ensure activity only occurred on the graphite side of the electrode. A total mass of 15.2 mg was recorded, giving 7.6 mg cm^{-2}. This was over 4 times the amount recorded for the copper surface studies in the previous section. This is potentially due to a higher surface roughness of the graphite powder compared to the flat copper foil surface providing more deposition sites. However, masses of 15.1 mg cm^{-2} were recorded for the polished glassy carbon surface. This would imply a much greater surface adhesion to carbon surfaces compared to the metal copper. The polished glassy carbon mass was also greater than the graphite, suggesting the change was not due to increased surface area. The cyclic voltammogram in Figure 37a shows a very broad reduction peak around -1.3 V that overlaps with the later polymerisation peaks. This was a result of the surface roughness of the graphite-composite electrodes leading to non-planar behaviour. This causes many overlapping overpotentials that result in a large singular peak. This was immediately followed by a passivation. On successive cycles, a growing polymerisation peak can be seen around -1.3 V to -2.0 V. Similar to studies performed on copper, this growing peak would suggest an increase in polymerisation growth either in solution or attaching to the electrode surface. This was likely caused by a growing polymer film that has cracked due to becoming too thick [127]. Excess thickness introduces stresses into the system that can degrade film integrity.

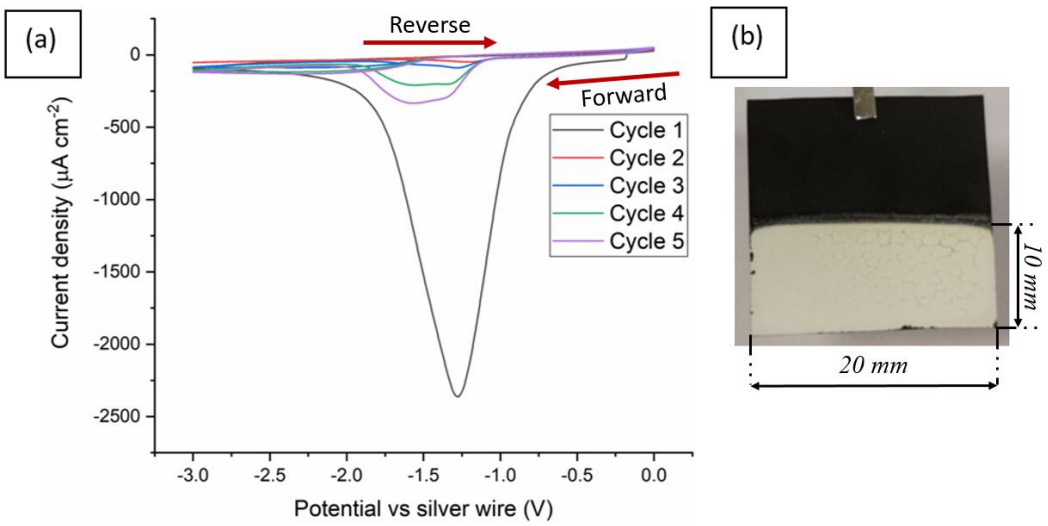

Figure 37: (a) Cyclic voltammogram data for PAN deposition onto a 20 mm X 10 mm (200 mm^2) graphite-composite electrode in a glass cell using AN(0.05 mol dm^{-3} TBAP) electrolyte with O_2 saturation and without water. Deposition performed at 50 mV s^{-1} from 0.0 V to -3.0 V for 5 cycles. Forward and reverse scan directions are annotated. (b) Image of the PAN deposit onto a 20 mm X 10 mm graphite-composite electrode. One side of the foil was exposed to electrolyte whilst the reverse side was insulated with a silicone grease.

Figure 38 shows the optical microscopy images of the graphite-PAN surface after electrodeposition in the glass cell. A clear difference can be seen between the graphite and polymer surfaces, with a cracked white film covering the graphite particles after polymer deposition. Cracks up to 10 µm thickness could be found. This could have a detrimental impact on potential shutdown operations if the cracks are not sealed at higher temperatures allowing Li^+ ions to infiltrate the graphite surface allowing electrochemistry to occur. Crack sizes were measured using MIPAR Image Analysis software defect analysis.

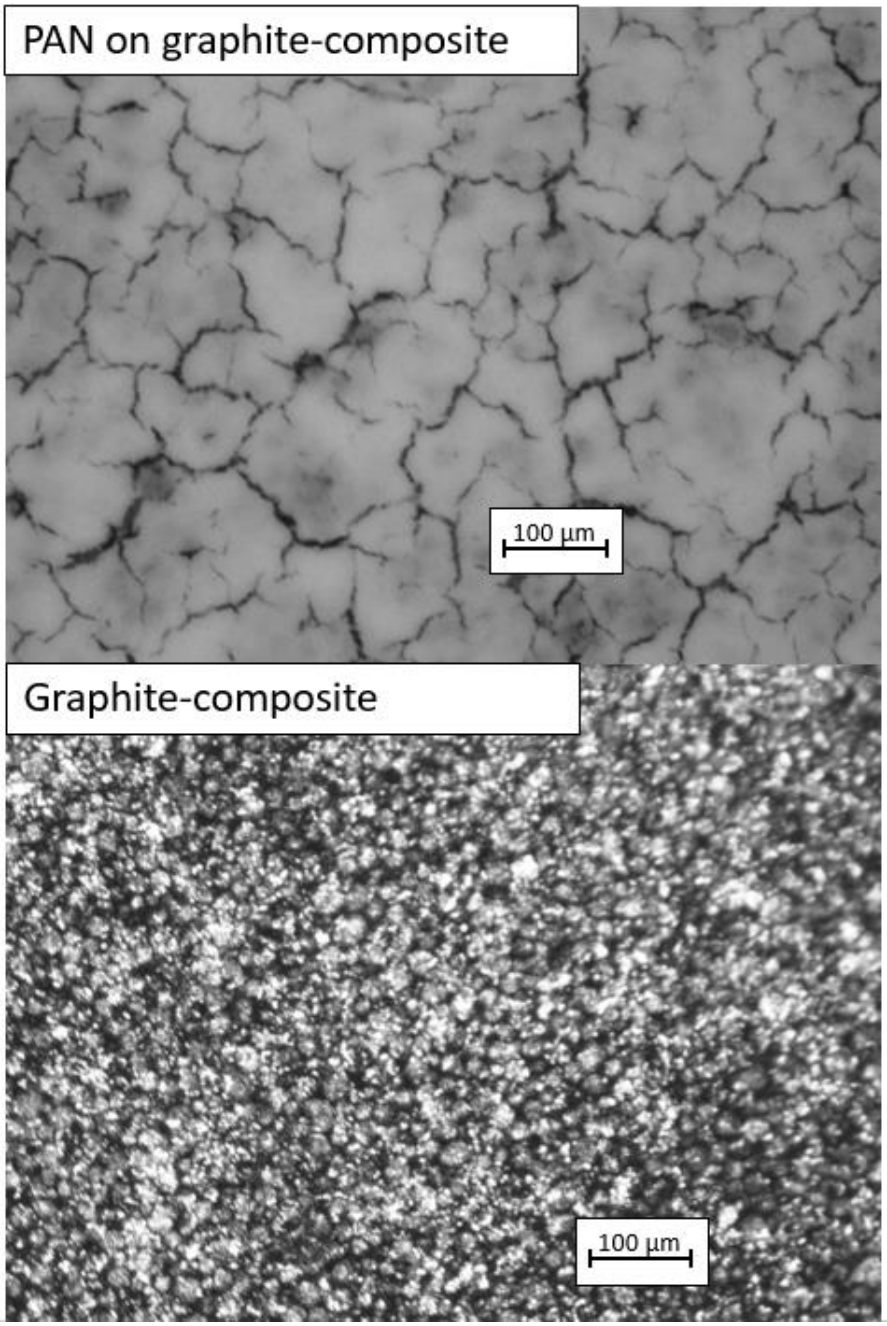

Figure 38: Optical microscopy images of a PAN deposit onto a 20 mm X 10 mm (200 mm^2) graphite-composite electrode. Deposition performed in a glass cell using AN(0.05 mol dm^{-3} TBAP) electrolyte. (Top) The deposit on the graphite-composite surface and (Bottom) the clean graphite surface. Images taken at 10X magnification.

Uniquely, studies with graphite-composite in the Teflon cell produced a clear PAN deposit, see Figure 39. Ordinarily PAN casting is recorded as developing a white-powdery film, however a few studies have been performed investigating the phenomena of clear PAN deposits. According to Lacey *et al*. [41], a white polymer was obtained on glassy carbon in glass cell studies that softened to a clear state upon annealing at 150 ^{o}C (PAN glass transition, T_g = 95 ^{o}C [35] [128]). However, the clear polymers in the Teflon cell were obtained without any post-treatment after the deposition procedure.

Pellon *et al*. [129] investigated a similar phenomena where typical procedures that produced a white cast PAN polymer managed to produce a clear one, similar to other cast polymers such as poly(methyl methacrylate). The mechanism identified for producing a clear polymer was to ensure monomer was readily available and could freely flow to all parts of the growing polymer film even at high conversion rates. The clear cast film was continuous and remaining monomer was either distributed molecularly or in very minute droplets; opaque PAN was heterogeneous and was composed of a compressed powder containing either air or remaining monomer in inter-particle spaces. Oplatka *et al*. [130] went further and managed to post-process white PAN films into clear films using a mercury nitrate initiator. Introduction of this new material led to investigations into any chemical changes. Oplatka *et al*. [130] found no chemical difference between the white and clear films and that the change is a purely physical change in state. Shavit *et al*. [131] further linked the dependence on producing a clear film to several factors that need to fall within an optimal range: catalyst type, catalyst concentration, temperature, volume of electrolyte, shape of the system, presence and supply of oxygen above the reaction mixture. The presence of oxygen above the electrolyte was found to act as a retarder to the polymerisation on the upper layers of the system, maintaining a concentration gradient of monomers to polymers toward the electrode surface at the bottom. This was necessary as it facilitates the through flow of the reaction mixture, preventing the formation of voids in the inter-particle space of the polymer, preventing an opaque film from forming.

In the glass cell, a nitrogen environment was maintained so there was no oxygen present above the mixture hence why graphite-composites deposited in the glass cell were white. Graphite-composites deposited in the Teflon cell were open to air and therefore produced clear films. Oxygen in the air acted as a retarder to polymerisation at the electrolyte surface allowing a supply of monomers whilst oxygen within the electrolyte was reduced to superoxide anion initiator for polymerisation to occur. The careful balance of the many conditions was also likely why the copper Teflon cell depositions maintained a white deposit despite being open to air; however, it was difficult to know which condition specifically due to the many potential options [131].

Oxygen reduction was observed at -1.45 V *vs.* Ag/Ag^+, likely due to better oxygen saturation within the Teflon cell. A slight shoulder can be seen around -1.7 V, indicating polymer growth on the electrode, followed by a wider feature from -1.8 V to -2.5 V for polymerisation in solution. On successive cycles all features can be observed indicating incomplete passivation, similar to the glass cell. The deposit obtained was 14.3 mg, or 9.286 mg/cm^2. The deposition area has clearly formed a clear layer on top of the graphite-composite.

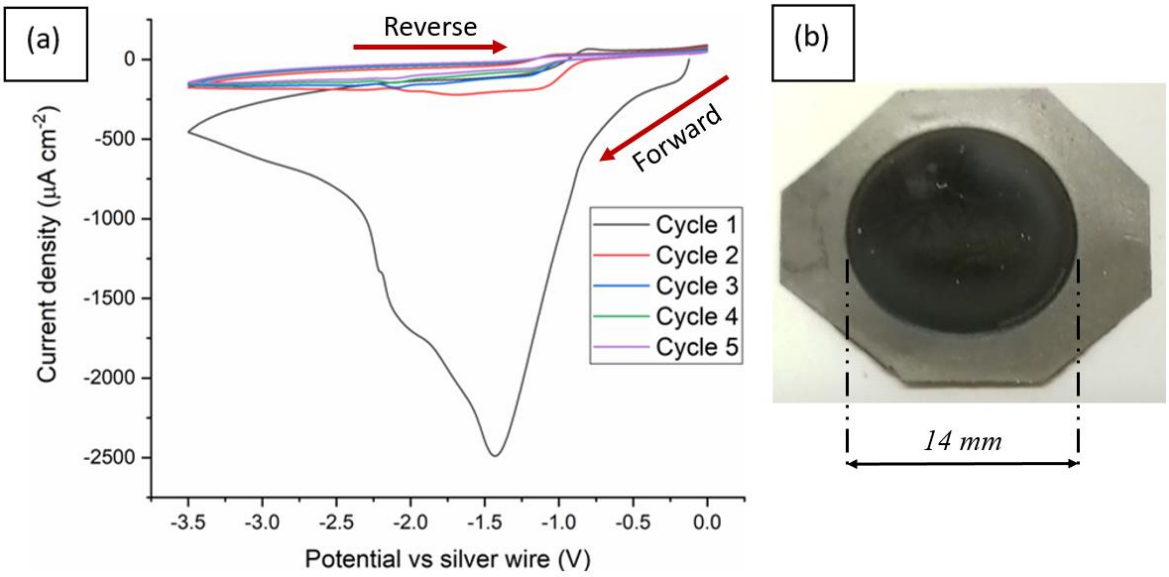

Figure 39: (a) Cyclic voltammogram data for PAN deposition onto a 14 mm diameter (154 mm^2) graphite-composite electrode in a Teflon cell using AN(0.05 mol dm^{-3} TBAP) electrolyte with O_2 saturation and without water. Deposition was performed at 50 mV s^{-1} from 0.0 V to -3.5 V for 5 cycles. (b) Image of the PAN deposit on a 14 mm diameter graphite-composite electrode. Forward and reverse scan directions are annotated.

Figure 40 shows SEM images of the PAN deposit in Figure 39b. The film forms clear distinct grains on top of the composite surface. Cracks separate each grain of around 3 to 5 µm thickness, nearly half the size of cracks in the glass cell. These crack sizes were measured using MIPAR Image Analysis software defect analysis. This was likely due to the more homogeneous, ordered structure of clear films. Once again, this was still more than sufficient for Li^+ ions to infiltrate should the cracks remain after any potential shutdown effect but it was a significant improvement over the white film crack sizes of 10 µm. The carbon and nitrogen composition calculated from EDS length scale was compared to the composition of an ideal PAN monomer unit and were similar enough to allow further studies of PAN deposition onto graphite surfaces to continue with confidence. The calculated values considering carbon and nitrogen were:

- C_{EDS} = 70 %, C_{ideal} = 72 %
- N_{EDS} = 30 %, N_{ideal} = 28 %

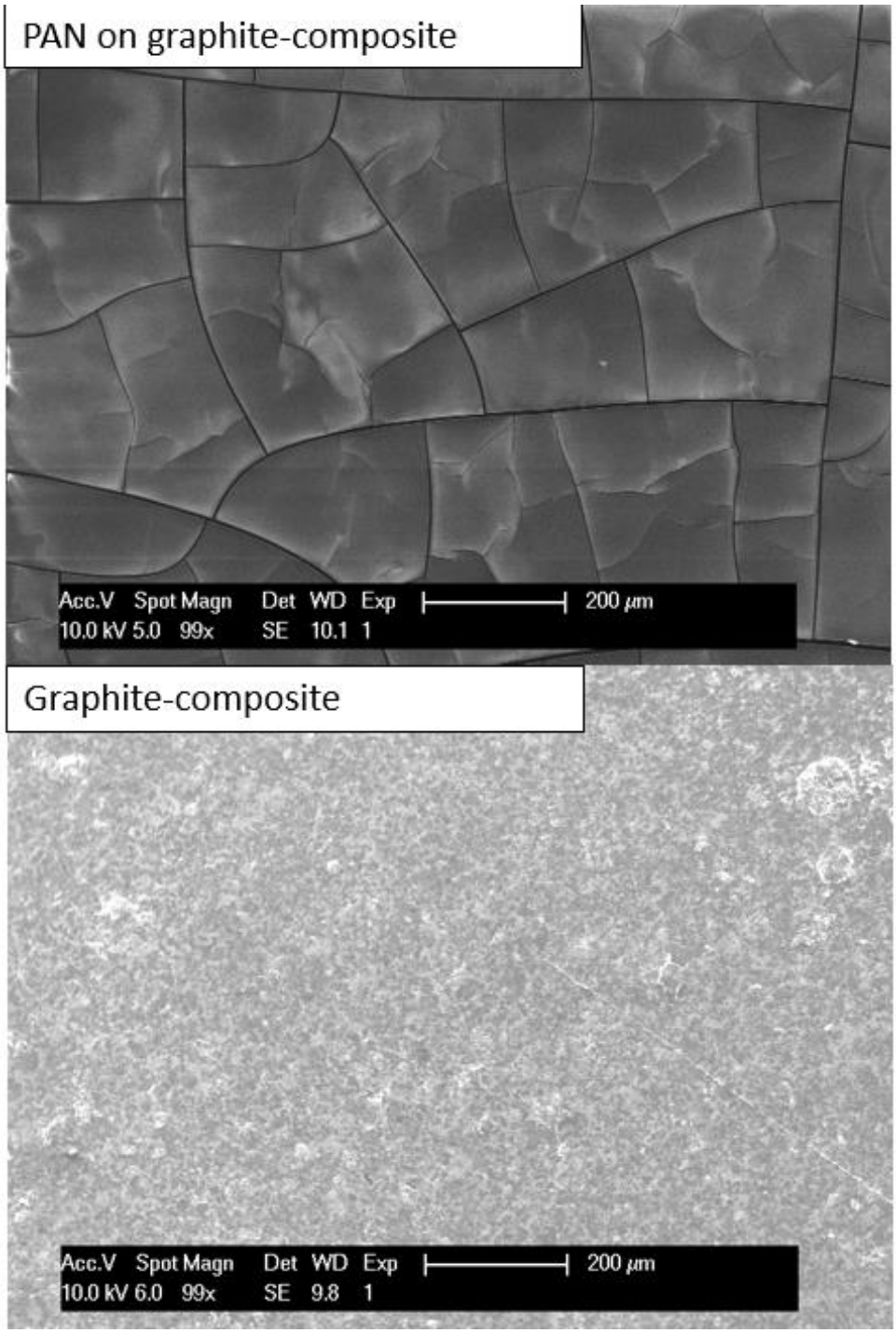

Figure 40: SEM images of a PAN deposit onto a 14mm diameter (154 mm^2) graphite-composite electrode. Deposition performed in a Teflon cell using AN(0.05 mol dm^{-3} TBAP) electrolyte. (Top) The deposit on the graphite surface and (Bottom) the clean graphite surface. Images taken at 100X magnification.

Comparison of Raman data of the graphite-composite and glassy carbon PAN deposits using AN(0.05 mol dm^{-3} TBAP) electrolyte is shown in Figure 41. The characteristic PAN peaks of C≡N cyano group at 2250 cm^{-1} and C-H alkyl group at 3000 cm^{-1} are observed in all samples. However, the peaks are more intense in the graphite Teflon cell sample. Conversely, C-C bonds at 1600 cm^{-1} and 1350 cm^{-1} are weaker in the graphite Teflon cell sample. This would suggest the Raman laser

was less able to penetrate the PAN film in the Teflon cell case to receive a signal from the graphite underneath, resulting in a reduced carbon signal relative to the PAN. The Teflon cell deposit may be better at preventing beam penetration due to the continuous structure of clear PAN observed under SEM. A greater mass per unit area of PAN was also deposited onto the Teflon cell sample than the glass cell (9.3 mg cm^{-2} to 7.6 mg cm^{-2}) implying a thicker film that was likely able to hinder beam penetration. No other significant differences were observed between the clear and white PAN deposits.

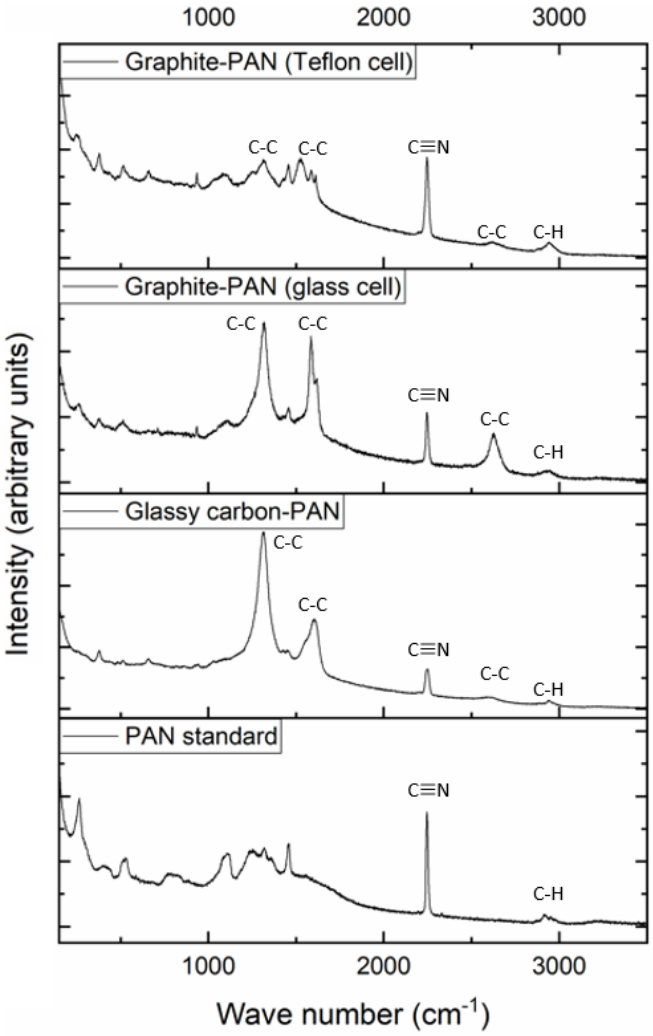

Figure 41: Raman data for the deposition of PAN onto graphite-composite surfaces in glass and Teflon cells and glassy carbon in a glass cell. From top to bottom: graphite-PAN deposited in a Teflon cell, graphite-PAN deposited in a glass cell, glassy carbon-PAN deposited in a glass cell, PAN powder standard. All depositions performed between 0.0 V to -3.0 V at 50 mV s^{-1} for 5 cycles using AN(0.05 mol dm^{-3} TBAP). Key bonds are annotated. Raman data taken at 1 % laser power on a 785 nm Raman laser for 3 accumulations.

3.3.3 Surface deposit mass comparison

A tentative link may be drawn between the masses deposited onto the various surfaces investigated and the peak current of oxygen reduction, see Table 7. The geometric area was used to normalise and compare the data of the dissimilar surfaces. Comparing the peak currents alone against the mass per unit area deposited onto glassy carbon, copper, and graphite-composite surfaces it can be seen that the mass per area increases as the peak current increases. However, when looking at the mass per current, the relationship was clearly not entirely linear with large discrepancies occurring. For example, copper-PAN deposited in a glass cell recorded 5.8 mg mA^{-1} whilst copper-PAN in a Teflon cell recorded 2.2 mg mA^{-1}. Unfortunately, from the cyclic voltammograms on graphite-composite in Figure 37 and Figure 39 it was difficult to interpret the polymerisation passivation peaks due to the broadness of the oxygen reduction peaks. As a result, oxygen reduction is used here as a point of comparison. The issue with this observation is that oxygen reduction does not necessarily mean polymerisation has occurred. That being said whilst oxygen reduction does not precisely give polymerisation current, it is still an indicator of the amount of superoxide annion intiators produced. Increased oxygen reduction would lead to a greater concentrataion of superoxide anions, potentially creating more opportunities for polymerisation to occur. Greater amounts of oxygen reduction may also result from more polymer binding to the electrode surface causing the oxygen bond with the polymer to break. This would replenish the oxygen molecule in the electrolyte that may then be reduced once more to superoxide. Greater deposit masses would then naturally lead to greater oxygen reduction peaks.

Table 7: Comparison of mass deposited and oxygen reduction currents for cyclic voltammograms of PAN deposition onto glassy carbon, copper and graphite-composite surfaces. PAN depositions were performed in both glass cell and Teflon cell arrangements.

Surface material	Cell type used	Mass per area (mg cm^{-2})	Peak oxygen reduction current (mA cm^{-2})	Mass per absolute peak current (mg mA^{-1})
Glassy carbon	Glass	15.1	-3.8	4.0
Copper	Glass	1.9	-0.3	5.8
Copper	Teflon	1.8	-0.8	2.2
Graphite-composite	Glass	7.6	-2.4	3.2
Graphite-composite	Teflon	9.3	-2.5	3.7

From looking at Figure 42, the overall trend was linear between mass deposited per area and peak oxygen reduction currents per area with an R^2 value of 97 % indicating a strong relationship. No large discrepancy was seen between the clear and white deposits. Since oxygen reduction must occur before any polymerisation and change in mass can occur, this would indicate a dependence on a Faradaic process linked to the amount of mass that would be deposited, at least initially. Microbalance studies by Lacey *et al*. [41] found no dependence on the overall mass deposited and the amount of chrarge passed during successive cycles, concluding that PAN polymerisation was non-Faradaic. Considering this, it would seem reasonable to conclude that the amount of PAN deposited would instead be dependent upon the superoxide initiator concentration. The initial Faradaic reduction of oxygen primarily occurs in the first cycle before any passivation. As such, little oxygen reduction occurs after, highlighting a Faradaic relationship for only this initial reduction. As for why different surfaces could show such varying behaviour, Zhang *et al*. [132] reported on how the oxygen reduction rate constants could vary substantially depending upon differently treated platinum surfaces. Easter *et al.* [133] has also reported how noble metal surfaces such as platinum, produce a thicker deposit than oxidisable metals, such as copper. This was linked to an oxidised surface passivating the copper preventing PAN electrodeposition. Because of the presence of superoxide anions within these studies, it is likely that a degree of copper oxidation has occurred. Carbonaceous surfaces, such as graphite and glassy carbon, has also been found to act as a catalyst for oxygen reduction to superoxide [134]. This would increase the concentrator of initiator present and further increase the mass of deposit, hence why the copper surface may have a lower mass than the other surfaces. Therefore, when depositing PAN onto other electrode surfaces, care should be taken to note any change in deposit mass when compared to a standard surface such as glassy carbon.

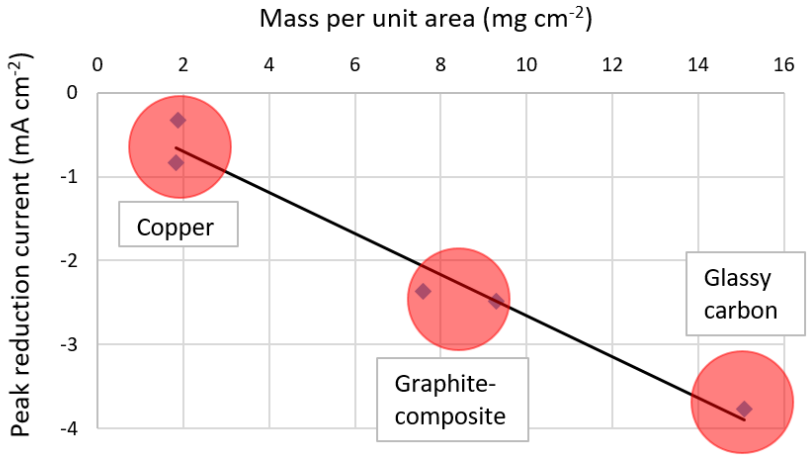

Figure 42: PAN deposit mass per unit area against peak oxygen reduction current per unit area from cyclic voltammograms of PAN depositions onto various surfaces. A trendline is superimposed to highlight a possible trend between the sets of data. Annotations show which data points relate to which deposition surfaces.

3.3.4 Water contamination studies

Effects of water contamination and oxygen saturation on the deposition of PAN in the Teflon cells was further studied. This was done to highlight any potential interactions between graphite-composites and the reactions that may not have been present with glassy carbon surface studies, see Section 3.2.2. Studies were performed using 10 mL of AN(0.05 mol dm^{-3} TBAP) electrolyte. This was either saturated with O_2 for 15 minutes using a sparger or left O_2 unsaturated. Further variations were made via the addition of 0.5 mol dm^{-3} H_2O to some studies. Unlike glass cell studies, the Teflon cell was left open to air, so O_2 and H_2O was able to infiltrate the electrolyte from the atmosphere. As such, some response was expected even when neither molecule was added to the electrolyte. In total four conditions were investigated: O_2 free, O_2 saturated, O_2 free with 0.5 mol dm^{-3} H_2O, and O_2 saturated with 0.5 mol dm^{-3} H_2O. CVs were performed on these samples for 5 cycles from 0.0 V to -3.5 V at 50 mV s^{-1}.

Mass of the electrodes was recorded before and after to quantify the amount of PAN deposited, see Table 8. The first observation was that no deposition occurred in O_2 free studies, indicating a necessity for the O_2 reduction to superoxide anions for initiation. Obvious clear depositions were recorded from the electrolyte saturated with O_2. Of note in the O_2 saturated studies, however, was that the mass of deposit in the water-contaminated study was greater than without showing 34.2 mg as opposed to 14.3 mg of PAN. Whilst this was an interesting effect and may be of use in another project to promote the amount of PAN deposited, damage to the ink structure was discovered that would be detrimental for lithium half-cell electrodes obtained from the ink, see Figure 43. Rather than a delamination, the ink appeared to have blistered indicating potential gas formation beneath the ink surface during cycling. The water-contaminated electrolyte also stained the graphite-composite yellow, which could not be removed with an ethanol wash. A further problem introduced by water was the potential for polymer swelling. PAN is a semi-crystalline polymer, with the more amorphous phases introducing greater degrees of hydrophilic behaviour. This behaviour allows PAN to be easily swollen by water as if it were a plasticiser. Unfortunately, when PAN is subsequently dried this volume was removed from the internal structure making PAN brittle [135]. Ultimately this would lead to increased cracking. Because of the apparent blistering and the potential for increased cracking due to swelling, the removal of water was deemed a necessity to provide as uniform an electrode surface as possible for good lithium-ion half-cell performance.

Table 8: Mass measurements of PAN deposits on 14 mm diameter graphite-composite electrodes in a Teflon cell using AN(0.05 mol dm^{-3} TBAP) electrolyte. Studies performed varied the presence of H_2O contaminant in the system and whether the electrolyte was saturated or not with O_2 before depositing.

Study parameters	PAN deposit mass (mg)
O_2 free	N/A
O_2 free with 0.5 mol dm^{-3} H_2O	N/A
O_2 saturated	14.3
O_2 saturated with 0.5 mol dm^{-3} H_2O	34.2

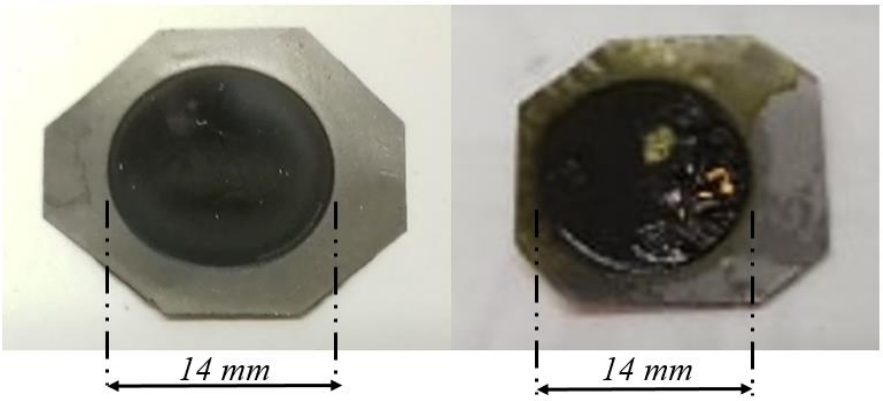

Figure 43: Images of PAN deposits on 14 mm diameter graphite electrodes in a Teflon cell using AN(0.05 mol dm^{-3} TBAP) electrolyte. (Left) O_2 saturated study without H_2O and (Right) O_2 saturated study with 0.5 mol dm^{-3} H_2O contaminant.

Figure 44 show the first and fifth cycles of the cyclic voltammograms obtained from these four studies. During the first cycle, current recorded for the O_2 free studies was lower than the O_2 saturated. There was also a notable peak around -1.5 V for the O_2 saturated studies that was not present in the O_2 free studies, and was linked to oxygen reduction. The presence of water appears to cause a long tail downwards from about -2.25 V in both O_2 saturated and O_2 free cases. During the fifth cycle, studies without H_2O reduce in current density significantly. This would normally be linked to a passivation of the electrode surface, however no PAN mass was recorded for the O_2 free studies. A yellow discolouration was observed in the O_2 free case so polymerisation in solution is likely to have occurred. The O_2 free 0.5 mol dm^{-3} H_2O appears largely unchanged from first to fifth cycles. On the other hand, the O_2 saturated 0.5 mol dm^{-3} H_2O current density has reduced greatly and the tail feature has become much wider by the fifth cycle. This may be an interaction with an exposed copper surface, as the ink layer has become damaged and blistered as shown in Figure 43.

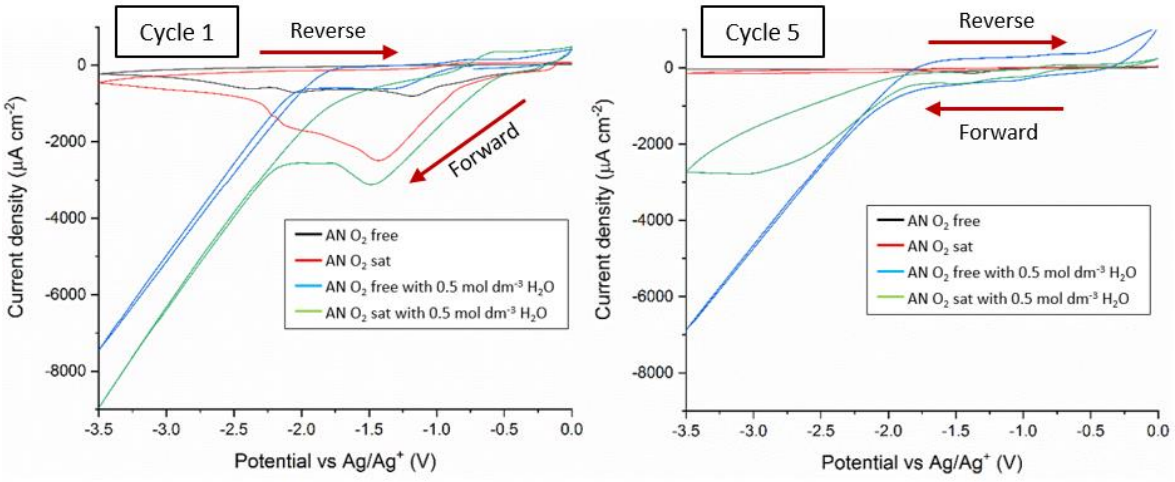

Figure 44: Cyclic voltammograms for PAN deposition onto 14 mm diameter graphite-composite electrodes in a Teflon cell using AN(0.05 mol dm^{-3} TBAP) electrolyte; studies performed with or without oxygen saturation and water contamination. The studies performed were: O_2 free study, O_2 saturated study, O_2 free with 0.5 mol dm^{-3} H_2O study, and O_2 saturated with 0.5 mol dm^{-3} H_2O study. Depositions performed at 50 mV s^{-1} from 0.0 V to -3.5 V for 5 cycles. (Left) First cycle CV data and (Right) fifth cycle CV data. Forward and reverse scan directions are annotated.

3.4 Controlled graphite-PAN film surface morphology

Chronoamperometry (CA) was investigated as an alternative deposition procedure to allow more controlled and thinner PAN deposits to reduce cracking observed in previous studies, see Section 3.3.2. The parameters for CA depositions were decided based upon the previously performed CV studies, see Figure 45. Oxygen reduction peaks clearly shift from -1.05 V to -1.45 V from glass cell glassy carbon to Teflon cell graphite-composite PAN deposition. This was repeatable across several tests. All voltage values, therefore, should shift by -0.4 V when using the Teflon cell. The polymerisation in solution region, appearing -1.5 V to -2.3 V in the glass cell, should be present from -1.9 V to -2.7 V. This range was the most negative potential of any feature observed in glass cell studies and all CA studies were consequently based around this. Subsequent studies made several further variations to reduce previously observed cracking. The variations made and the intended effects were:

- More-negative CA potentials to encourage polymer deposition and further cross-linking.
- Shorter CA deposition times to reduce amount of PAN and produce thinner films.
- Redepositing over previous PAN deposits in an attempt to fill cracks with new deposit.

- Annealing the deposit after CA to encourage polymer chain movement to close cracks.

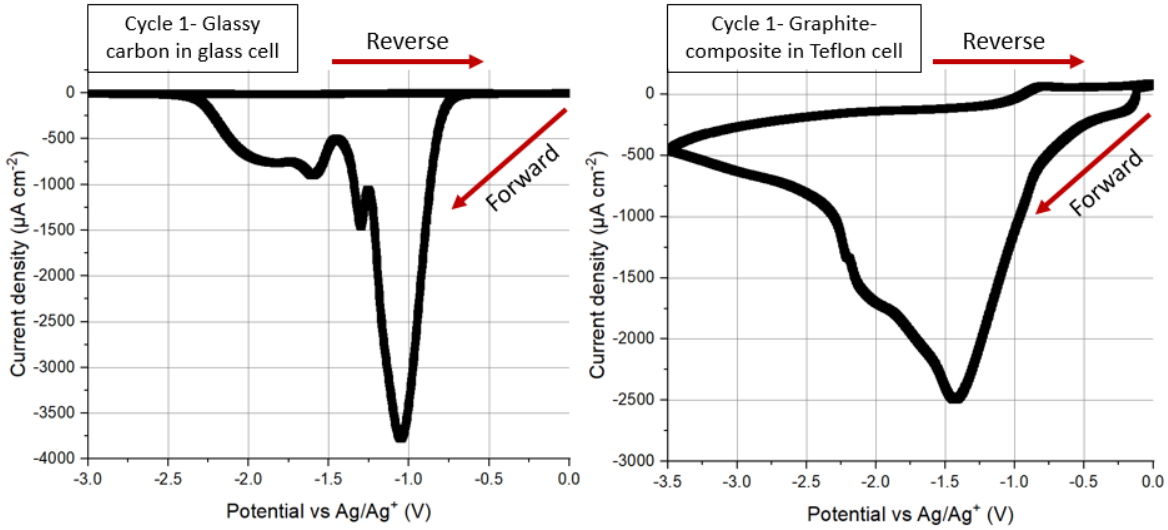

Figure 45: Side-by-side comparison of the first cycle PAN electrodeposition cyclic voltammograms onto (Left) 3 mm diameter glassy carbon electrode in a glass cell and (Right) 14 mm graphite-composite electrode in a Teflon cell. Both used AN(0.05 mol dm^{-3} TBAP) electrolyte with O_2 saturation and without water. CVs performed at 50 mV s^{-1}. Forward and reverse scan directions are annotated.

3.4.1 Chronoamperometry studies – varying voltage

CA studies were varied in voltage from -0.7 V (below the oxygen reduction peak) to -3.0 V to provide information on the full range of activity observed in the electrodeposition of PAN on graphite-composite electrodes. These were all performed for 100 seconds using AN(0.5 mol dm^{-3} TBAP) in a Teflon cell arrangement. All electrolytes were 10 mL in volume and were O_2 saturated for 15 minutes before applying a potential.

Figure 46 shows the current against time of varying potentials from -0.7 V to -3.0 V for several CA studies. An obvious inflection can be seen within the first few seconds at -1.3 V and above. The peak currents of this area of activity increase as potentials become more negative. This was because the greater overpotentials cause a more rapid reduction of oxygen to superoxide anions, leading to higher peak currents. Current then steeply decreases before plateauing at near-zero current as AN forms PAN deposits on the electrode surface, passivating it and preventing further flow of current. At -1.1 V there was a slight plateau, likely as potential was at the onset for oxygen reduction. Below -1.1 V no inflections or plateaus can be seen. This was because the potentials were below that required for oxygen reduction seen in the cyclic voltammograms in Figure 45. Therefore, no oxygen reduction can occur and so no electrochemical activity is observed.

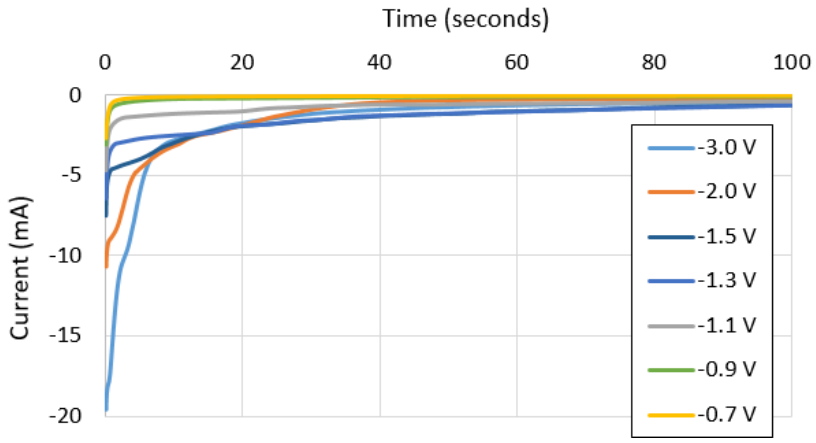

Figure 46: Chronoamperometry for the deposition of PAN onto 14 mm diameter graphite-composite electrodes in a Teflon cell using AN(0.05 mol dm^{-3} TBAP) electrolyte. Chronoamperometry was performed for 100 seconds whilst being held at a constant potential *vs.* Ag/Ag^{+}. Results for several potentials are superimposed.

The resulting PAN masses deposited onto graphite-composite electrodes at varying voltages is shown in Figure 47. At -0.7 V no mass was recorded; this is reflected in the CA data in Figure 46. This was below the potential for oxygen reduction, highlighting the importance of superoxide as an initiator in the depositions. Mass rapidly increases from -1.1 V to -1.3 V, from oxygen reduction onset up to the peak of oxygen reduction. Above -1.3 V a steady decrease in mass was observed followed by a larger fall above -2.3 V. This coincides with the reduction of superoxide to peroxide, seen around -2.25 V in Section 3.2.2 studies. The reductions of oxygen to superoxide and superoxide to peroxide along with the potentials observed in Section 3.2.2 were as follows:

$$O_2 + e^- \rightleftharpoons O_2^{\bullet -} \qquad \text{-1.25 V } \textit{vs.}\ Ag/Ag^{+}$$

$$O_2^{\bullet -} + e^- \rightarrow O_2^{2-} \qquad \text{-2.25 V } \textit{vs.}\ Ag/Ag^{+}$$

The loss of superoxide initiator concentration results in less polymerisations of AN to PAN, leading to lower deposit masses. Mass increases above -2.6 V. According to Lacey *et al.* [41], there are two potentials of significant mass increase for PAN electrodeposition, above the peak of oxygen reduction at -1.3 V *vs.* Ag/Ag^{+} and above the reduction of AN at -2.5 V *vs.* Ag/Ag^{+}. Reduction of AN occurs at far more negative potentials in the absence of oxygen and results in lower masses of PAN deposits than superoxide initiated polymerisation [41]. It was likely this reduction, which does not require superoxide anions, leading to the smaller mass increase above -2.6 V.

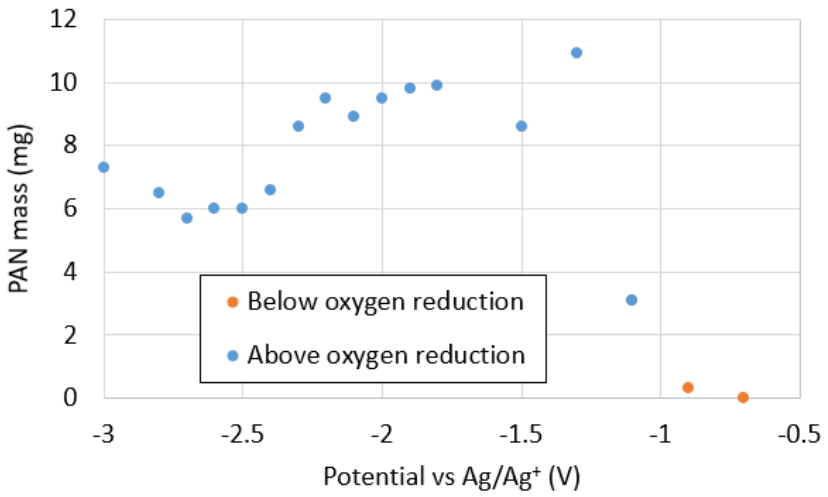

Figure 47: Mass of PAN deposits produced by chronoamperometry for 100 seconds over a range of potentials *vs.* Ag/Ag^{+}. Deposition performed on graphite-composite electrodes of 14 mm diameter in a Teflon cell using AN(0.05 mol dm^{-3} TBAP) electrolyte. Data above and below oxygen reduction are shown in different colours.

Figure 48 presents images of the PAN deposit at 10X magnification under optical microscopy at different potentials of deposition. The cracked morphology was present throughout, however there were notable differences in the surface features of the morphology at different potentials. In samples with thinner masses, most notably at -2.4 V and -2.6 V, the graphite particle shapes can be seen beneath the PAN film creating an uneven surface. Also of significant interest was a reduction in the size of the cracks. At -2.4 V the cracks were barely visible and were of 4 µm maximum. This is compared to -2.0 V and -3.0 V where cracks of 7 µm and 8 µm were recorded respectively. At these higher and lower potentials a thicker mass was recorded; therefore, this effect on crack size seems closely linked to the thickness of the PAN films rather than the potential applied. Film thickness may be tailored through varying the length of time of depositions rather than potential. Crack sizes were measured using MIPAR Image Analysis software defect analysis.

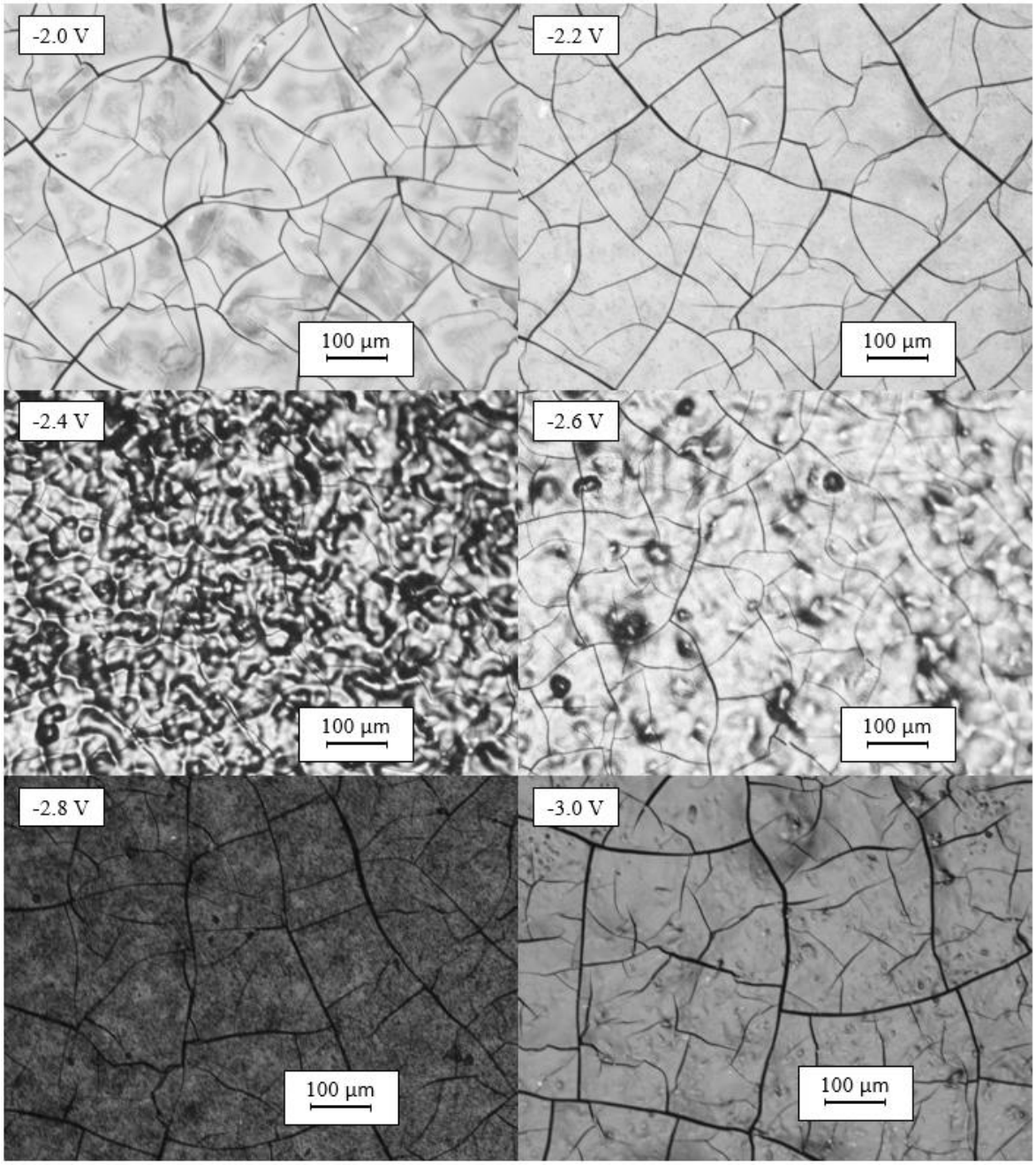

Figure 48: Optical microscopy images of PAN deposits at 10X magnification. Deposition performed using chronoamperometry for 100 seconds over a range of voltages *vs.* Ag/Ag^{+} on 14 mm diameter graphite-composite electrodes in a Teflon cell using AN(0.05 mol dm^{-3} TBAP) electrolyte.

3.4.2 Chronoamperometry impurity studies – Raman and thermogravimetric analysis

Figure 49 shows the images of the deposit produced at four different potentials using CA deposition techniques. These images are superimposed on the forward scan direction of the depositing CV voltammogram in Figure 45 at their corresponding potentials. This CV was performed on a 14 mm graphite-composite electrode in a Teflon cell using AN(0.05 mol dm^{-3} TBAP) electrolyte with O_2 saturation and without water. The CV was performed at 50 mV s^{-1}. As CA was performed at more negative potentials deposits lost a dis-uniform yellow discolouration, becoming clearer. Deposits also lost a reflective quality, which was most apparent around -2.1 V, instead becoming much duller. Yellow discolouration is often linked to cyclization and dehydrogenation in PAN [136] [137], which will turn white PAN to yellow as the level of impurities increase. Cyclization can occur due to temperature [137] or attack by a nucleophile [136] such as superoxide. As superoxide was present within the depositing mixture during electropolymerisation, cyclization becomes more likely. Hence, further investigation into the presence of impurities was required over the voltage range.

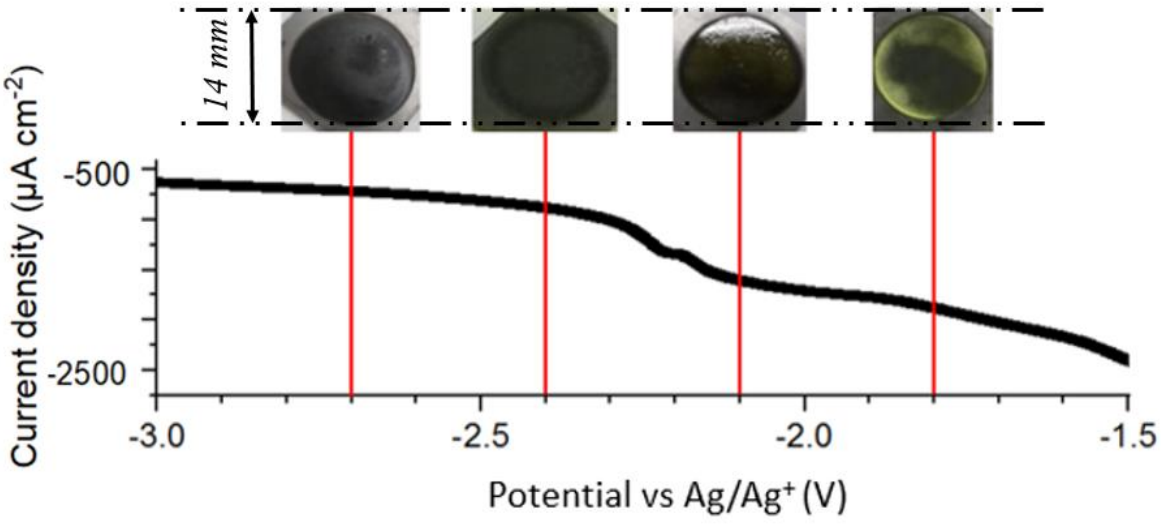

Figure 49: Images for the deposition of PAN using chronoamperometry superimposed onto the forward scan direction of the CV voltammogram in Figure 45 on a 14 mm diameter graphite-composite. The CV was performed in a Teflon cell using AN(0.05 mol dm^{-3} TBAP) electrolyte with O_2 saturation and without water. The CV was performed at 50 mV s^{-1}. Chronoamperometry depositions were also performed on 14 mm diameter graphite-composite electrodes in a Teflon cell using AN(0.05 mol dm^{-3} TBAP) electrolyte with O_2 saturation and without water. Images for PAN deposits at -1.8 V, -2.1 V, -2.4 V, and -2.7 V *vs.* Ag/Ag^+ are shown. Images are superimposed at their corresponding potentials.

Commonly cited impurities for PAN polymerisations largely involve cyclization [136] [137], with the proposed mechanism shown in Figure 50 for the cyclization of PAN via nucleophile attack of a superoxide anion. Raman was initially employed to identify any common peaks associated with PAN cyclization, see Figure 51. Typical wave numbers for PAN features include 2250 cm^{-1} C≡N bonds and 3000 cm^{-1} alkyl C-H bonds [41] and for graphitic features at 2600 cm^{-1}, 1600 cm^{-1} and 1350 cm^{-1} [138]. A few additional features were present in the PAN standard that were mirrored in the CA deposited PAN studies across the whole voltage range. However, additional peaks can be observed in the deposited samples that were not in the standard, notably at 660 cm^{-1} and at 930 cm^{-1} relating to a CNC ring structure [139]. An additional peak was seen around 1425 cm^{-1} that was consistent with a fused ring structure formed from a polymerisation of the nitrile groups as a consequence of the anionic polymerisation mechanism [140].

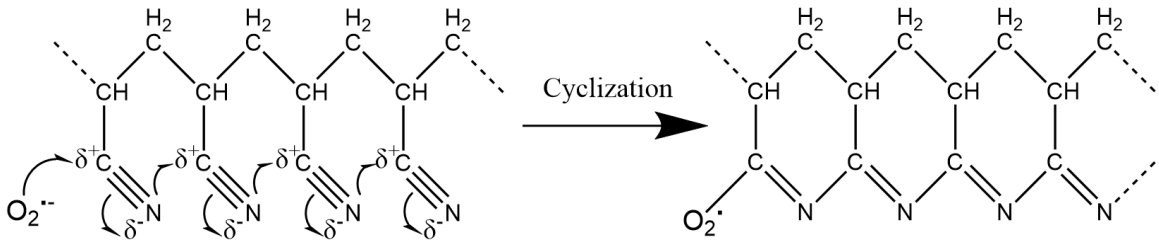

Figure 50: Partial mechanism for the cyclization of PAN involving attack by a superoxide nucleophile.

Yellow discolouration in PAN structures has also been attributed to the formation of conjugated C=C double bonds on the polymer backbone or colour centres associated with radical species trapped within glassy polymer matrices [141] [142]. Possible impurities of C=C bonds would require carbon atoms on the polymer backbone as the C≡N group cannot provide the required carbon. Unfortunately, C=C bonds would be difficult to identify by Raman as the peaks line up with graphitic features at 1600 cm^{-1} [143]. However, the relative intensities of cyclic feature impurities can give insight into the presence of dehydrogenated carbon impurities.

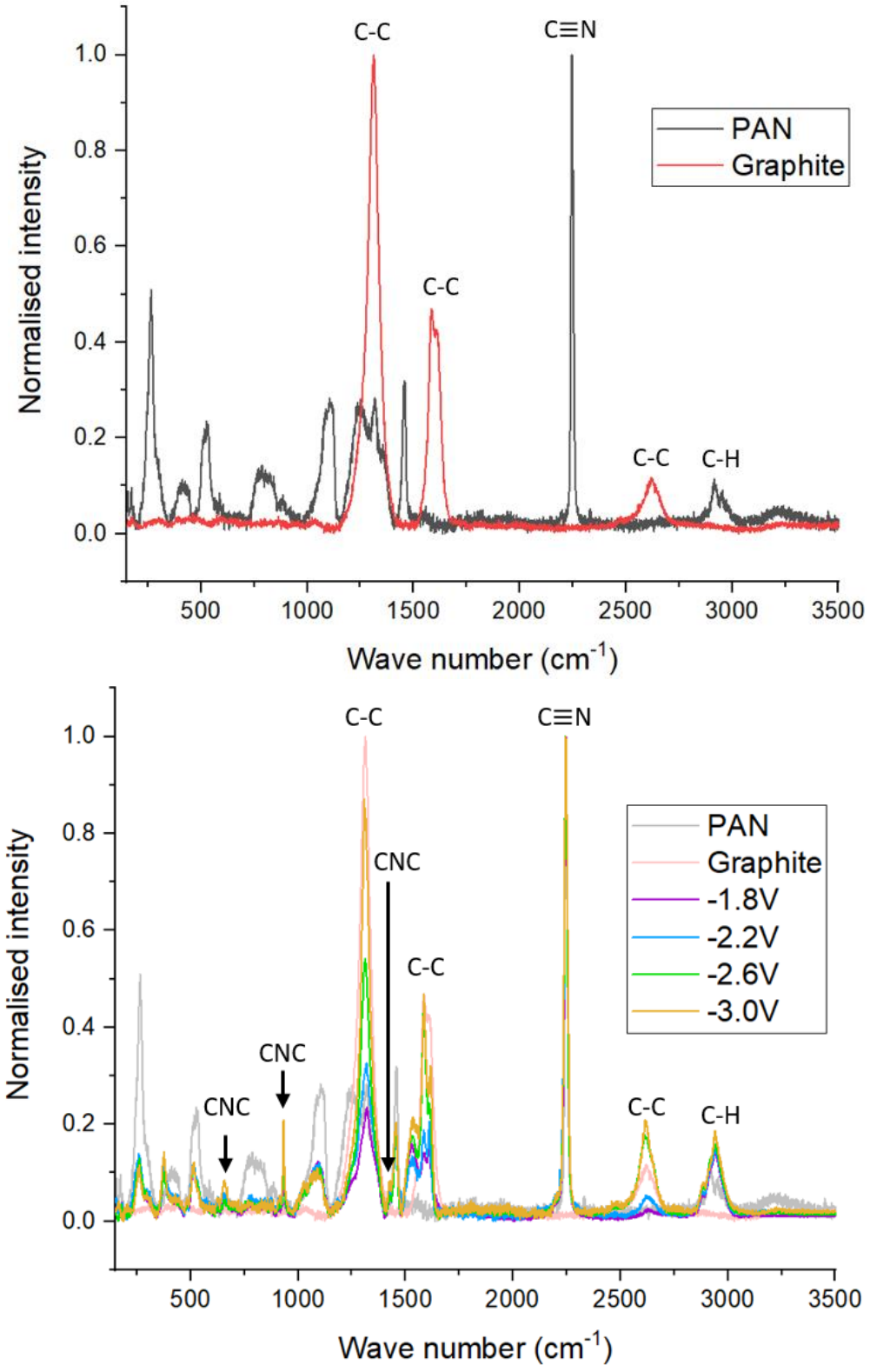

Figure 51: Normalised Raman data for the deposition of PAN using chronoamperometry onto a 14 mm diameter graphite-composite electrode in a Teflon cell. (Top) PAN and graphite standards superimposed and (Bottom) standards as well as depositions performed at -1.8 V, -2.2 V, -2.6 V, and -3.0 V *vs.* Ag/Ag^{+} superimposed. Key bonds are annotated on both. Raman data taken at 1 % laser power on a 785 nm Raman laser for 3 accumulations.

Table 9 shows the normalised intensities for ring structure impurities for the Raman data shown in Figure 51. All Raman data showed 2250 cm^{-1} C≡N bonds to be the strongest, giving maximum intensity and hence the value of 1.00 when normalised. However, during cyclization the cyano group is substituted for a CNC ring structure, see Figure 50, which would cause a lower intensity at 2250 cm^{-1} and higher intensity at the ring impurities at 660 cm^{-1}, 930 cm^{-1}, and 1425 cm^{-1}. It can be seen from the table that the PAN standard consistently showed a low intensity of 0.03 for all the ring features. All CA deposited samples across the voltage range showed a greater intensity for ring feature CNC bonds, with more negative potentials leading to greater intensities of these cyclic features. These more negative potentials provide greater energy to allow less thermodynamically favourable ring structures to form during the polymerisation [140]. What can be concluded from this information is that more negative CA potentials lead to higher degrees of cyclization within the deposited polymer samples.

Samples deposited at lower potentials had a yellow discolouration, see Figure 49, despite having a lower degree of cyclic impurities. Therefore, there must be a higher degree of other impurities that give a yellow discolouration such as conjugated C=C bonds on the polymer backbone. It was inferred that the lower potentials encourage the formation of C=C bonds. Unsaturated carbon bonds are expected to form during radical polymerisation due to termination by disproportionation. This occurs when two growing radical polymer chains interact and terminate their growth via the exchange of a hydrogen atom, leading to one chain with a conjugated C=C bond and the other without. As deposits at higher potentials had less yellow discolouration this would also suggest higher potentials discourage disproportionation or encourage termination by recombination.

Table 9: Normalised intensities of Raman data corresponding to PAN ring structure feature wavenumbers.

PAN CNC ring feature wavenumbers (cm^{-1})	**Normalised intensities**				
	Standard	**-1.8 V**	**-2.2 V**	**-2.6 V**	**-3.0 V**
660	0.03	0.04	0.05	0.04	0.08
930	0.03	0.12	0.13	0.13	0.21
1425	0.03	0.06	0.06	0.05	0.08

TGA data was taken to supplement the Raman study of impurities in Figure 51. The intention of these studies was to identify any effect from the different impurities (cyclization or dehydrogenation) at elevated temperatures that might be experienced during thermal runaway. During PTCR studies in later chapters the highest temperature required would be PVDF's melting temperature around 155 to 185 °C [30] with temperatures not planned to exceed 200 °C. Therefore TGA was studied beyond this point up to 250 °C to highlight any key mass changes that could be expected should PTCR fail to shutdown the cell and temperatures continue to rise beyond the melting point of PVDF. TGA studies were performed on a CV deposited sample and a CA deposited sample onto graphite-composite electrodes with an additional study for a CA deposited sample onto a copper electrode, see Figure 52. The PAN deposit was scraped from the samples and collected for TGA. The copper study was performed to highlight the presence of impurities when electrodeposition was performed onto other surfaces than the graphite-composite. A CV sample from 0.0 V to -3.0 V at 50 mV s^{-1} was used as the full range of electrodeposition potentials would be covered, allowing all impurities to be expressed. CA electrodeposited samples used -3.0 V for 100 seconds as these should result in a higher proportion of cyclic impurities according to Raman data in Table 9.

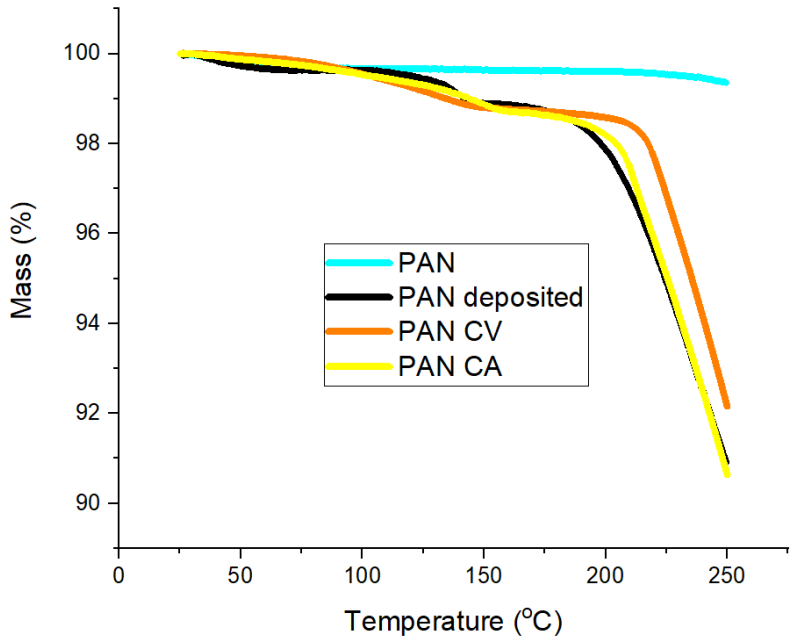

Figure 52: TGA performed on various PAN samples under an argon environment, percentage remaining mass plotted against temperature. In cyan, PAN industrial standard from Sigma-Aldrich. In orange and yellow, PAN deposited onto graphite-composites using CV (0.0 V to -3.0 V at 50 mV s^{-1}) and CA (-3.0 V, 100 seconds) respectively. In black, PAN electrodeposited onto a copper surface using CA (-3.0 V, 100 seconds). Studies ramped at 2 °C/minute from 25 °C to 250 °C.

Mass changes at key temperatures during TGA studies are detailed in Table 10. PAN T_g is around 95 °C, at which point all samples remained stable. A slight drop in mass was seen in electrodeposited samples at 100 °C and then further at 120 °C. However, for the electrodeposited samples there were two areas of significant mass decrease at just below 150 °C and again at just above 200 °C. George Konstantopoulos *et al*. [137] identified that the thermal stabilisation of PAN takes place in two separate steps that can be performed in either order, cyclization or dehydrogenation. At 150 °C thermal degradation is dominated by cyclization. Above 200 °C degradation by dehydrogenation dominates leading to mass loss via the loss of hydrogen atoms leading to of C=C bonds forming. At 250 °C, the PAN standard had not dropped below 99 % whilst the CV deposited sample dropped to 92.15 %. On the other hand, both CA deposited samples fell by nearly 10 % at 90.63 % and 90.83 % for graphite-composite and copper respectively. Greater mass loss above 200 °C for the CA samples suggests more mass loss via dehydrogenation meaning an initial lower composition of C=C bonds for more negative CA electrodepositions. Therefore, lower potentials have a greater degree of impurities due to unsaturated bonds leading to a more distinct yellow shade of the deposited films and to lower mass loss by 250 °C. The TGA response for the PAN industrial standard remains fairly constant up to 250 °C, never dropping below 99 % of its original mass, suggesting little to no impurities within the powder from Sigma-Aldrich.

CA samples are more stable at 95 °C to 150 °C, the areas of interest for any PTCR response due to the PAN T_g at 95 °C. Hence, these more negative potentials were of more interest to the thermal runaway studies due to greater stability within the required temperature window. Depositions at -3.0 V were therefore continued in the CA studies of the following sections.

Table 10: Percentage remaining mass for TGA samples at key temperatures. Techniques used to create electrodeposited samples were CV = cyclic voltammetry, and CA = chronoamperometry. Surfaces electrodeposited onto were Gr = graphite-composite, and Cu = copper.

Key temperatures (°C)	**Percentage mass remaining (%)**			
	Standard	**CV Gr**	**CA Gr**	**CA Cu**
95	99.68	99.74	99.67	99.64
100	99.68	99.55	99.53	99.63
120	99.68	99.25	99.35	99.51
150	99.64	98.80	98.88	98.89
200	99.61	98.58	98.19	97.87
250	99.35	92.15	90.63	90.83

3.4.3 Chronoamperometry studies – varying time

Varying thickness of PAN deposits was explored to reduce cracking of polymer films. To this end, CA deposition studies were performed at various time scales. These were performed at -3.0 V *vs.* Ag/Ag^+, in line with conclusions of varying voltage studies from Section 3.4.1 and Section 3.4.2. At this voltage, clear consistent films were attained that were more stable below 150 °C. These were all done using AN(0.5 mol dm^{-3} TBAP) electrolyte in a Teflon cell arrangement. All electrolytes were 10 mL in volume and were O_2 saturated for 15 minutes before applying a potential.

The mass of the PAN deposits against deposition time for many of the CA studies is shown in Figure 53. Deposit mass increased as greater amounts of time were allowed for deposition. However, the trend was only linear for depositions performed for longer than 1 second, with depositions performed for less than 1 second not following the same trend. This was reflected in a y-intercept value of 2.7 mg for a trendline based on depositions run for 1 second or longer. This was likely in part due to the wide variation in deposited mass for the same conditions. For instance, mass values deposited for 100 seconds varied between 7.3 mg and 8.8 mg. However, a strong linear relationship is observed for the trendline for values above 1 second with an R^2 value of 95 %. Below 1 second, mass increased much more rapidly. Only 0.5 seconds of deposition time gave a mass of 0.4 mg, which would suggest an increase of 0.8 mg s^{-1}. However, the gradient recorded from the linear trendline is significantly lower than this giving 0.0547 ± 0.0013 mg s^{-1}.

No mass was recorded when leaving the electrodes in the electrolyte for 1 hour with no applied potential and left at open circuit potential. Nor was mass recorded when leaving the electrodes in the electrolyte that had undergone oxygen reduction prior to the addition of the electrode; the presence of superoxide initiator without a potential did not encourage any PAN deposition. A potential must be applied to the electrode under investigation for a mass change to be observed.

The trend of increasing PAN mass with deposition time was likely a result of greater amounts of time available for mass transport to occur under the driving potential. Literature mentions the electrodeposition of PAN is driven by the applied voltage and not convection making it a diffusion limited process [144]. Indeed, the deposition does not appear to continue to a significant degree without the applied potential; the amount deposited in a 20 second study left to sit in the electrolyte over a 24 hour period after removing the -3.0 V potential was 4.0 mg. This was similar to the 3.4 mg during the 20 second study in Figure 53.

Diffusion limited growth has been reported in several literature [41] [42] and does appear to follow similar trends for polymer chains [145], nanocrystals [146], and even in clathrate hydrates in outer space [147], to name a few. It appears to be common that an initial rapid growth period

is observed followed by a slow decline in growth rate that tends towards a plateau at greater time scales. At small deposition times (less than 1 second in this case) there is little to no diffusion layer over the working electrode and so the effect of concentration of the bulk solution has little effect on the deposition rate near the graphite-composite surface. It is only at greater deposition times that the diffusion layer grows due to a drop in concentration of reactants at the electrode surface. Hence, diffusion becomes a limiting factor and growth rate rapidly decreases. As such, diffusion-limited growth tends to follow a non-linear trend. It can therefore be assumed that either the growth of the polymer film tends towards this linear model after 1 second, or the growth follows a non-linear trend beyond 100 seconds as the diffusion layer continues to grow. The non-linear idea can be explored by investigating depositions times longer than 100 seconds to identify clear changes in gradient. Either way, the linear trendline was a reasonable approximation for the data it represents between 1 second and 100 seconds, allowing predictions of how much mass would be deposited for depositions within this time window.

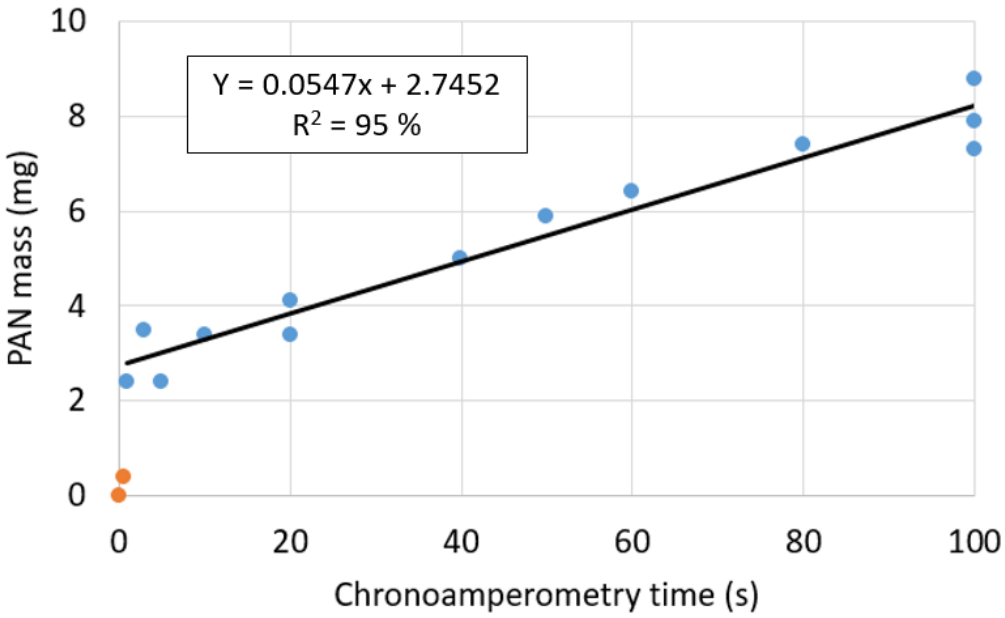

Figure 53: Mass of PAN produced by chronoamperometry studies at -3.0 V *vs.* Ag/Ag^{+} at varying times for applied potential. Deposition performed on 14 mm diameter graphite-composite electrodes in a Teflon cell using AN(0.05 mol dm^{-3} TBAP) electrolyte. A linear trendline is superimposed for deposition studies performed for longer than 1 second with the line equation and R^2 values shown. Depositions below 1 second were not included in the trendline and are shown in orange.

The other potential source of growth for the polymer film would be Faradaic growth, or the polymerisation of PAN via the direct transfer of an electron from the electrode to a monomer or growing chain [78], shown in Figure 54. Direct electron transfer can result in polymer growth in the absence of oxygen but requires much more negative potentials, -2.5 V *vs.* Ag/Ag^{+} according to

Lacey *et al.* [41]. Deposit mass tends to be much lower under such a mechanism and polymer growth typically occurs in the solution without grafting to the electrode surface [2]. This is distinct from the predicted radical anion polymerisation model where the Faradaic process reduces the oxygen to form superoxide anions, which go on to initiate polymerisation. Should Faradaic growth of the polymer be present and significant it might be possible to predict an amount of growth by the amount of charge passed by the electrons.

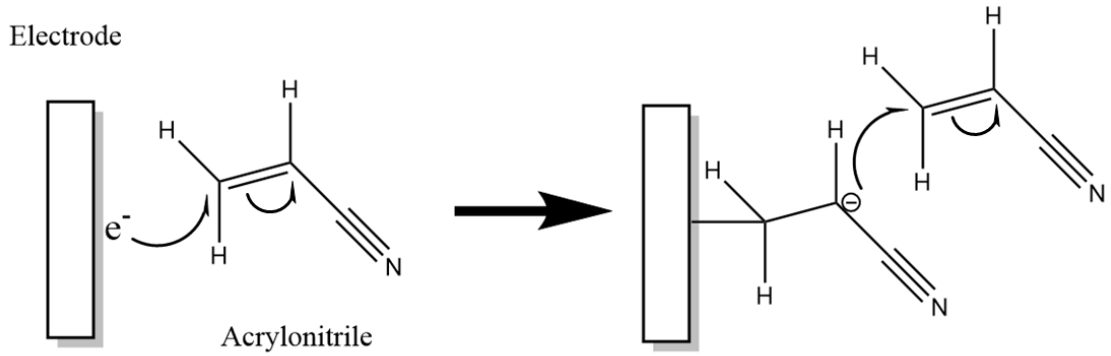

Figure 54: Proposed mechanism for Faradaic chain growth of PAN.

A Faradaic process would have a corresponding Faradaic efficiency calculated by the following:

$$n = \frac{mzF}{M_r Q}$$

Where *n* is the Faradaic efficiency, *m* is the mass of the product (or the mass of deposit in this case), *z* is the number of electrons involved (1 electron to monomer), *F* is the Faraday's constant (96485 C mol^{-1}), M_r is the molar mass of the AN monomer (53.031 g mol^{-1}), and *Q* is the charge passed. PAN mass was simply found by weighing the graphite-composites. The charge passed was found by integrating current and time for the CA data; the area under the curve provides the total charge passed by the CA study. A Faradaic efficiency of 1 is ideal for a Faradaic process and indicates all charge consumed produced the desired products. Less than 1 indicates inefficiencies and side reactions. However, greater than 1 indicates more mass is being produced than the amount of passed charge allows implying non-Faradaic processes. This would mean polymer chain growth without electrochemical input, such as a chemically driven process.

Figure 55 shows the Faradaic efficiency for PAN deposits obtained at varying deposition times. It can be seen from the superimposed CA graph that the current passed for the various times remains consistent for all time scales until the time limit was reached. Hence, charge passed remained consistent within the time limits of the studies. Firstly, Faradaic efficiencies were magnitudes greater than 1. Therefore, growth of the PAN polymer chain was primarily chemically driven by a diffusion-limited process rather than an electrochemical process. Oxygen reduction to

a superoxide anion is a Faradaic process but was only responsible for the initiation of the polymerisation and so only accounts for one monomer unit in the several unit long polymer chain. Indeed, this was to be expected with radical anionic polymerisation as the superoxide initiator acts as a catalyst that drives the polymerisation [41]. Secondly, an initial rapid increase in efficiency was observed from 0 to 1 seconds; this was consistent with observations in Figure 53 where an initial steeper gradient was observed at this smaller time scale. This was a result of the kinetics of superoxide formation. The superoxide was not initially present and hence an initial lower period of deposition was to be expected. A peak was seen at 1 second followed by a steep decline that tends towards a plateau. From looking at the CA data, the electrode was passivated during the process resulting in reduced currents being passed. As PAN mass increase appeared linear with time above 1 second and continues this trend despite the rapid decrease in Faradaic efficiency, the growth pattern was clearly independent of the charge passed. Hence, the limiting factor would be the movement of monomers to the reaction sites via diffusion.

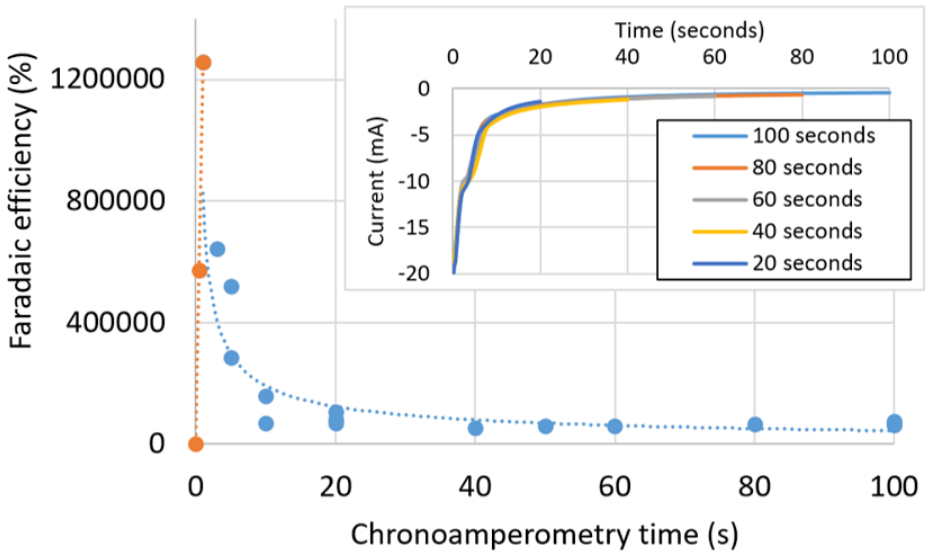

Figure 55: Faradaic efficiency against chronoamperometry time for PAN deposits produced at -3.0 V *vs.* Ag/Ag^{+}. Depositions performed on 14 mm diameter graphite-composite electrodes in a Teflon cell using AN(0.05 mol dm^{-3} TBAP) electrolyte. Orange and blue data points and trendlines represent identified regions of differing activity. Superimposed is a graph of chronoamperometry current against time for several different studies with varying time limits at -3.0 V *vs.* Ag/Ag^{+}.

Figure 56 presents several PAN deposits at 10X magnification under optical microscopy for varying times of deposition. A cracked film was present throughout, with width becoming noticeably lessened as deposition time and subsequently deposit mass was reduced. At 10 seconds, the film became too thin and the graphite was exposed in places. This was apparent at 50X magnification, shown in Figure 57. A stark contrast was observed between the rougher exposed graphite areas

and the areas with a thin glossy layer of polymer. This lack of uniformity would negatively impact any thermal runaway prevention as the graphite surface would not be blocked by the PAN film. This was also likely to impact the electrochemical performance of lithium-ion half-cells even at room temperature as certain regions would have a greater ionic resistance due to the disparity of polymer present. As such, lower deposition times than 20 seconds were considered unreliable for future study with the 20 second deposits having the best morphology by appearance.

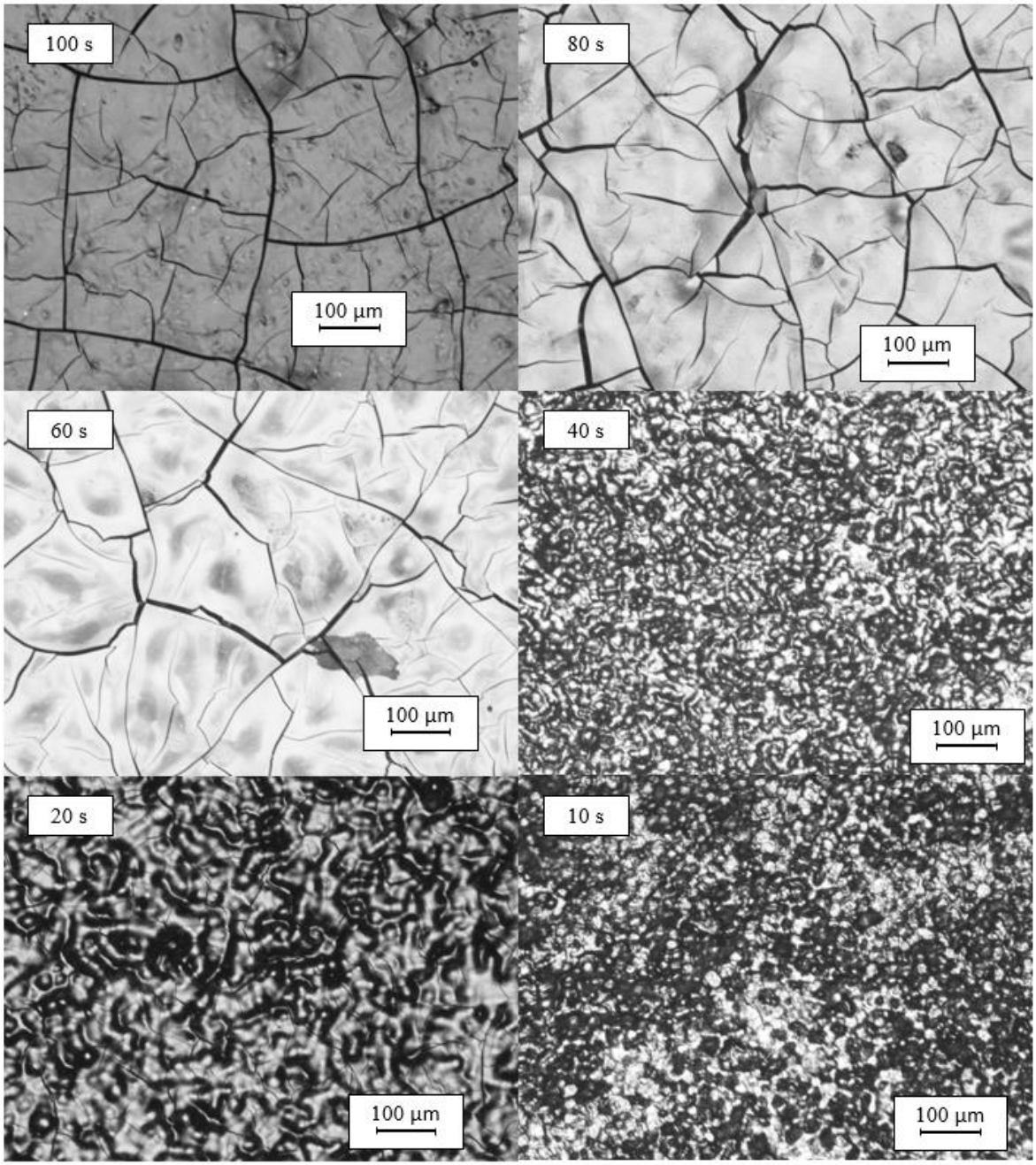

Figure 56: Optical microscopy images of PAN deposits at 10X magnification. Deposition performed using chronoamperometry at -3.0 V *vs.* Ag/Ag^{+} over a range of times on 14 mm diameter graphite-composite electrodes in a Teflon cell using AN(0.05 mol dm^{-3} TBAP) electrolyte.

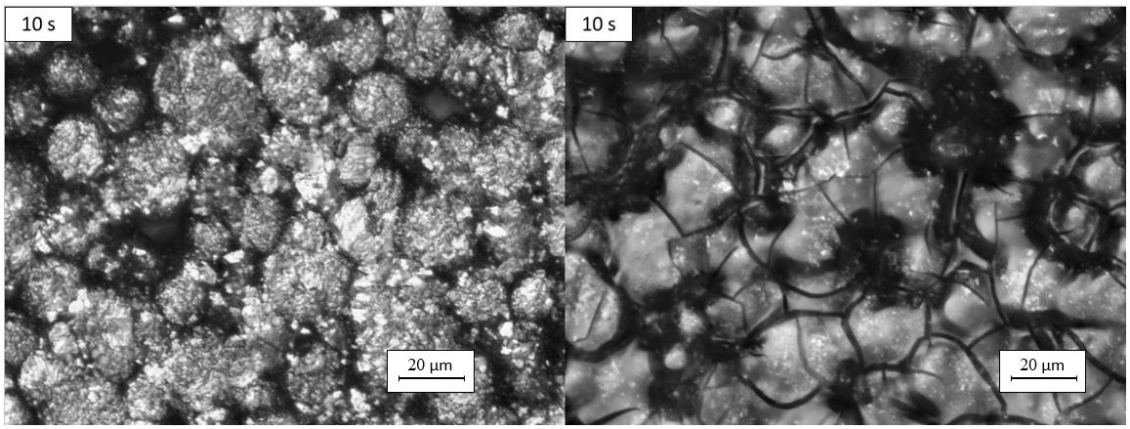

Figure 57: Optical microscopy images of PAN deposits at 50X magnification. Deposition performed using chronoamperometry at -3.0 V *vs.* Ag/Ag^+ for 10 seconds on 14 mm diameter graphite-composite electrodes in a Teflon cell using AN(0.05 mol dm^{-3} TBAP) electrolyte. (Left) Image of exposed graphite within the deposition area and (Right) Image of graphite with PAN deposited on top.

Table 11 quantifies the reduced crack sizes with decreasing deposition times and hence decreasing film thikcnesses. For the deposits at 60 to 100 seconds, a wide range of cracks sizes were observed with cracks as wide as 8 µm commonly observed. This was due to the greater thickness introducing greater levels of stress within the film surface ultimately leading to worse cracking. However, cracks from 10 to 40 seconds were more consistent. Cracks were almost non-existent with only a few areas showing cracks. There was also far less variation in crack sizes of less than 1 µm to a maximum of 2 µm. This was compared to the 3 to 9 µm observed for thicker deposits. As such, there was a far greater degree of uniformity observed at lower deposition times, and hence a more uniform ionic resistance across the surface. These thinner films would more likely produce repeatable data during electrochemical lithium-ion studies.

Table 11: Size of cracks identified for PAN deposits shown in Figure 56. Measurements performed using MIPAR Image Analysis software defect analysis. Depositions performed using chronoamperometry at -3.0 V *vs.* Ag/Ag^+. Time scales varied from 10 seconds until 100 seconds. Crack size shown in a range to reflect the variation observed at longer deposition times compared to lower deposition times.

Deposition time (s)	10	20	40	60	80	100
Crack sizes (µm)	1-2	1-2	1-2	3-8	3-9	4-8

3.4.4 Chronoamperometry studies – predicting film thickness

The idea of predicting PAN mass at deposition times was extended to predicting film thickness. This was done by plotting the thickness of PAN deposits against their mass, see Figure 58. Thickness was measured using an 'External Digital Micrometer, 0-25 mm/0-1 inches' from RS Components with an absolute uncertainty of ± 1 µm.

A linear trend was observed, with a 91 % R^2 value on the experimental trendline indicating a strong statistical relation with the data. The gradient of the trend shows 5.98 ± 0.13 µm mg^{-1}. Using the electrode area of 1.54 cm^2, average PAN density was found to be 1.09 g cm^{-3}. PAN density at 25 °C for PAN with an average molecular weight of 150,000 from Sigma Aldrich was 1.18 g cm^{-3} [148]. This gave an experimental PAN density 92.4 % that of the commercial product. Calculating theoretical film thicknesses for a PAN film of the commercial product density gives thicknesses lower than the experimental trendline. The commercial product would increase in film thickness by 5.49 µm mg^{-1}. Therefore, the film thicknesses of the experimental values are 8.9 % above theoretical films formed from the commercial product, shown by the experimental trendline in Figure 58 resting above the theoretical trendline by 8.9 %.

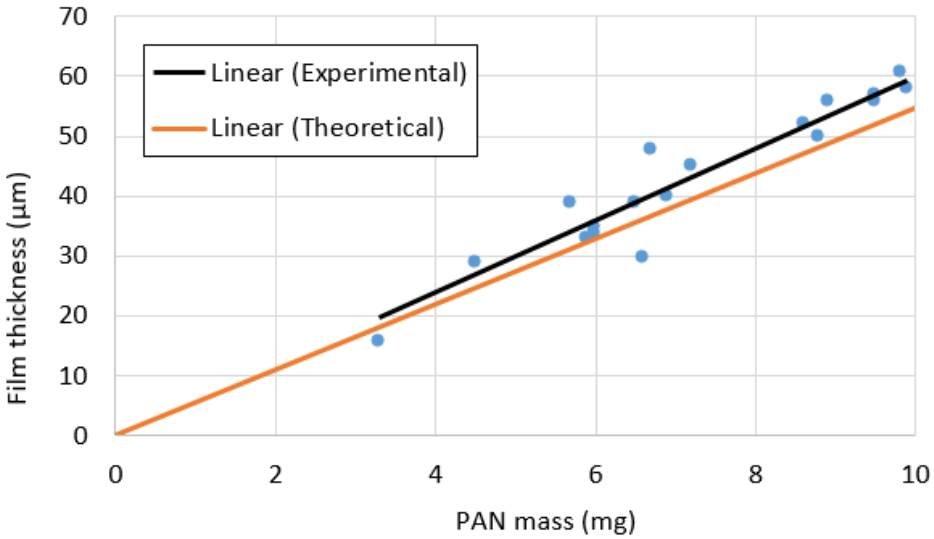

Figure 58: Mass of PAN deposits against film thickness produced by chronoamperometry at -3.0 V *vs.* Ag/Ag^+ over a range of different times. Deposition performed on 14 mm diameter graphite-composite electrodes in a Teflon cell using AN(0.05 mol dm^{-3} TBAP) electrolyte. A theoretical trendline of film thickness assuming a density of 1.18 g cm^{-3} [148] is superimposed.

Combined with the linear trend of PAN masses against CA deposition time in Figure 53, film thickness can be simply predicted and tailored through control of the deposition time. The gradients for mass per unit time and thickness per unit mass, along with the predicted gradient for thickness per unit time, are shown in Table 12. From this data, it was expected that 0.327 ± 0.015 µm film thickness would be gained every second of CA deposition time between 1 and 100 seconds. Figure 59 shows the PAN mass against deposition time for the data points used to calculate the linear trend only (excluding the 0 and 0.5 second data points that occurred before the 1 second linear trend). The figure also shows the measured film thicknesses for these samples against deposition time. An experimental line from measured film thicknesses with a micrometer is shown against the deposition time for those samples as well as a predicted line calculated from the relationships in Table 12.

From the initial mass against time data, a y-intercept of 2.7 mg was found. This was used to predict a y-intercept for the thickness against time relationship by using the thickness per mass value of 5.98 ± 0.13 µm mg^{-1}. A value of 16.4 µm was found for the intercept and was added to the values for the predicted line between 1 and 100 seconds using the calculated gradient of 0.327 ± 0.015 µm s^{-1}. Although the thickness per time line was not a trendline, the data fitted relatively well with the measured thickness values with an R^2 value of 88 %. Comparatively, the trendline lined up almost identically with the predicted line with an R^2 value of 88 %. It was therefore concluded that 0.3 µm s^{-1} was a good estimate for film growth.

Table 12: The gradients of mass gained per unit time for PAN films and thickness per unit mass are shown. These measured values were used to calculate the possible gradient for film thickness per unit time.

$\frac{\boldsymbol{Property\ 1}}{\boldsymbol{Property\ 2}}$	$\frac{\boldsymbol{Mass\ (mg)}}{\boldsymbol{Time\ (s)}}$	$\frac{\boldsymbol{Thickness\ (\mu m)}}{\boldsymbol{Mass\ (mg)}}$	$\frac{\boldsymbol{Thickness\ (\mu m)}}{\boldsymbol{Time\ (s)}}$
Gradient	0.0547 ± 0.0013	5.98 ± 0.13	0.327 ± 0.015

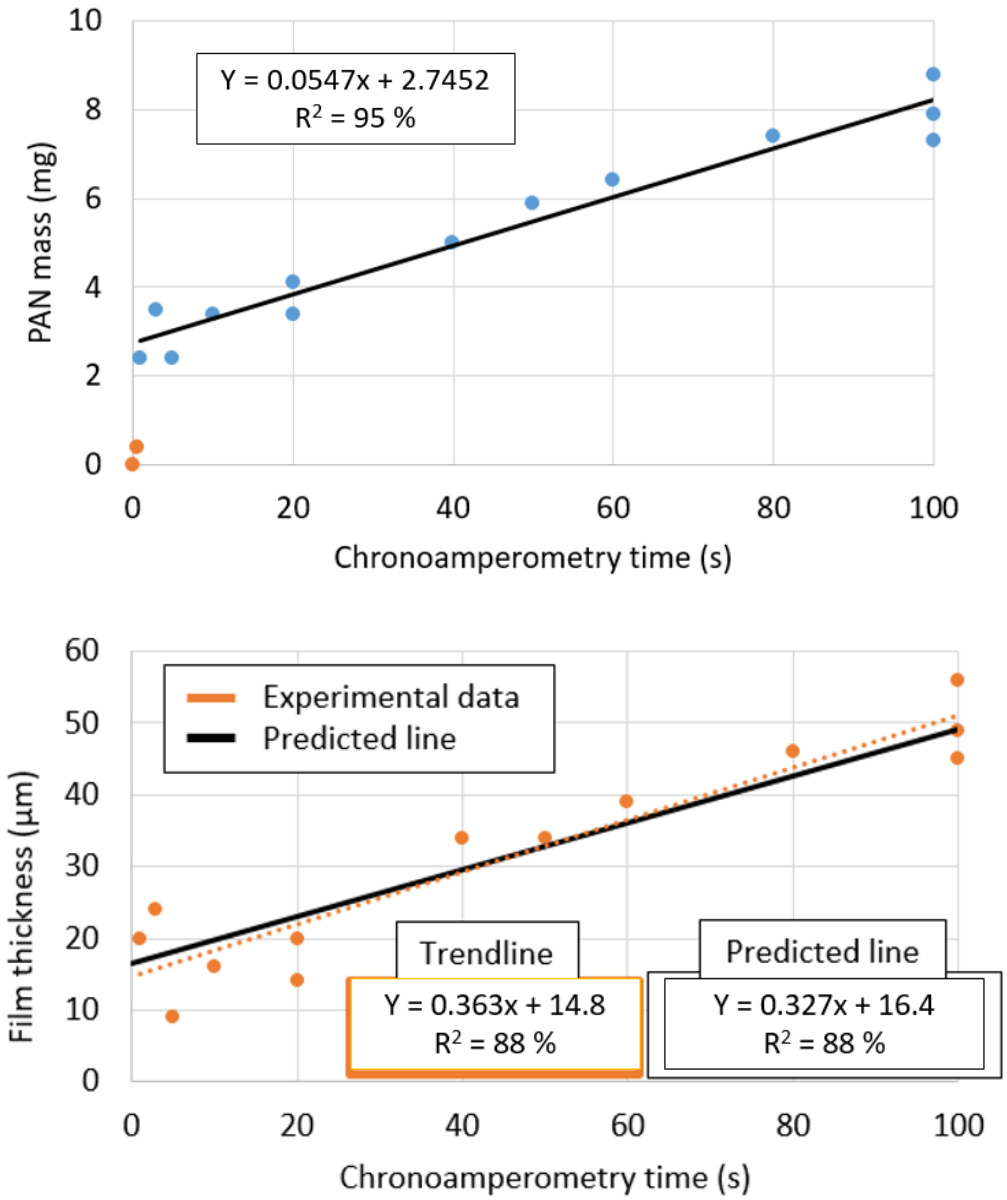

Figure 59: (Top) PAN mass against chronoamperometry time for data used to calculate the linear trend between 1 and 100 seconds; trendline equation and R^2 values are superimposed. Chronoamperometry studies performed at -3.0 V *vs.* Ag/Ag^+. (Bottom) PAN film thickness against chronoamperometry time. Data points measured from the samples in the top graph. A trendline for experimental data is superimposed and is compared with a predicted line calculated from gradients in Table 12.

3.4.5 Chronoamperometry studies – post-treatment redepositions

Post-treatment procedures were explored to improve PAN films further, specfically to remove any cracks present. One of these post-treatments was redepositions. Redeposition was performed in two cycles using a standard CA electrodeposition of PAN each time onto a graphite-composite electrode. The first cycle was performed followed by washing and drying of the electrode and performing a second standard CA onto the same deposition area. Fresh AN(0.05 mol dm^{-3} TBAP) electrolyte was used for each cycle in a Teflon cell with 15 minutes of O_2 saturation without water each time. Redeposition should preferentially deposit more polymer onto exposed conductive surfaces between the cracks in the films. Redepositions were performed using CA at -3.0 V *vs.* Ag/Ag^+ during the first cycle and again at -3.0 V *vs.* Ag/Ag^+ during the second cycle. After the first CA cycle, washing and drying was performed as such: remove electrodes from the Teflon cell and dry for 24 hours, wash electrodes in ethanol for 10 minutes, dry for an additional 24 hours. The second cycle was then performed with the PAN coated graphite-composite as the working electrode. This was then followed by an additional washing and drying procedure that was the same as the first.

Figure 60 shows PAN mass against deposition time for redeposition studies superimposed onto data for one cycle depositions explored in Section 3.4.3. Running studies for 10 seconds and another 10 seconds increased mass from 3.0 mg to 3.8 mg. This increasing trend was repeated for two 20 second depositions and two 50 second depositions. Each time the increase in mass closely followed the linear trend identified for 1^{st} cycle depositions above 1 second. Polymer coatings have been shown to have near complete coverage of the film surface after the first cycle. Should growth only occur in the crack areas, growth should be minimal. The fact that increases were so large implies the polymer chain growth is reinitiated and further continues. Interestingly as similar masses for 100 seconds were obtained by running depositions for two 50 second cycles, or similar masses for 40 seconds were obtained with two 20 second cycles, PAN film masses and ticknesses can be accurately increased to greater amounts if desired.

Redepositions do not experience an initial faster growth period as seen in Section 3.4.3. This was despite fresh electrolyte being used for each redeposition cycle. This may imply the initial faster growth period below 1 second in Section 3.4.3 was experienced as the AN monomers were coated onto the graphite directly without passing a polymer layer. For redepositions there was a polymer layer present and so chain growth primarily initiates from this surface instead of the electrode.

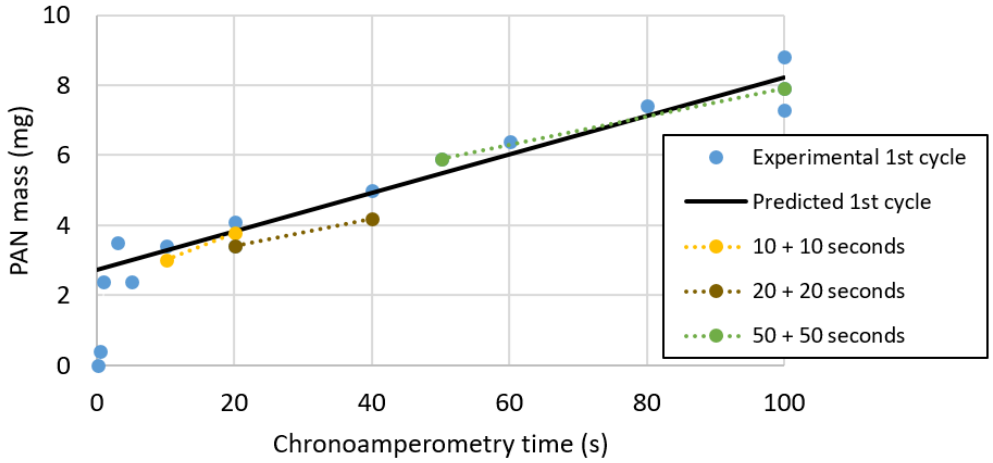

Figure 60: Mass of PAN depositions produced by chronoamperometry at -3.0 V *vs.* Ag/Ag^{+} over a range of different times. Initial one cycle experimental data is included along with a trendline to predict PAN film growth. Several redeposition studies are included. The time that first and second cycles of the redeposition studies was performed for was: 10 + 10 seconds, 20 + 20 seconds, and 50 + 50 seconds. A dotted line is superimposed between first and second redeposition cycles. Deposition performed on 14 mm diameter graphite-composite electrodes in a Teflon cell using AN(0.05 mol dm^{-3} TBAP) electrolyte with O_2 saturation and without water.

The effect of redepositions on cracks was variable depending on the times used, see Figure 61 and Table 13. For 10 + 10 seconds and 20 + 20 second studies, cracks were almost completely sealed with only slight cracks remaining visible. This was contrasted with 50 + 50 seconds where there was a negligible effect on crack size. As mass of the redepositions follows a similar trend to initial depositions over the same time scale, this was likely a result of the redeposit thickness at longer times introducing more stress. Thicker films introduce greater internal stresses leading to the original cracking issue observed. This cracking was less pronounced at 10 and 20 seconds for one cycle, and hence the redepositions for a similar time are able to aid in sealing of the cracks. However, at 10 + 10 seconds and 20 + 20 seconds a degree of surface roughness was observed. Non-uniformity in surfaces of electrodes may lead to poorer lithium-ion half-cell performance.

Table 13: Size of cracks identified for PAN redepositions shown in Figure 61, studied for: 10 seconds and 10 seconds, 20 seconds and 20 seconds, and 50 seconds and 50 seconds. Measurements performed using MIPAR Image Analysis software defect analysis. Crack size shown in a range to reflect the variation observed.

Deposition time (s)	10	20	50	10 + 10	20 + 20	50 + 50
Crack sizes (µm)	1-2	1-2	2-6	<1	<1	3-5

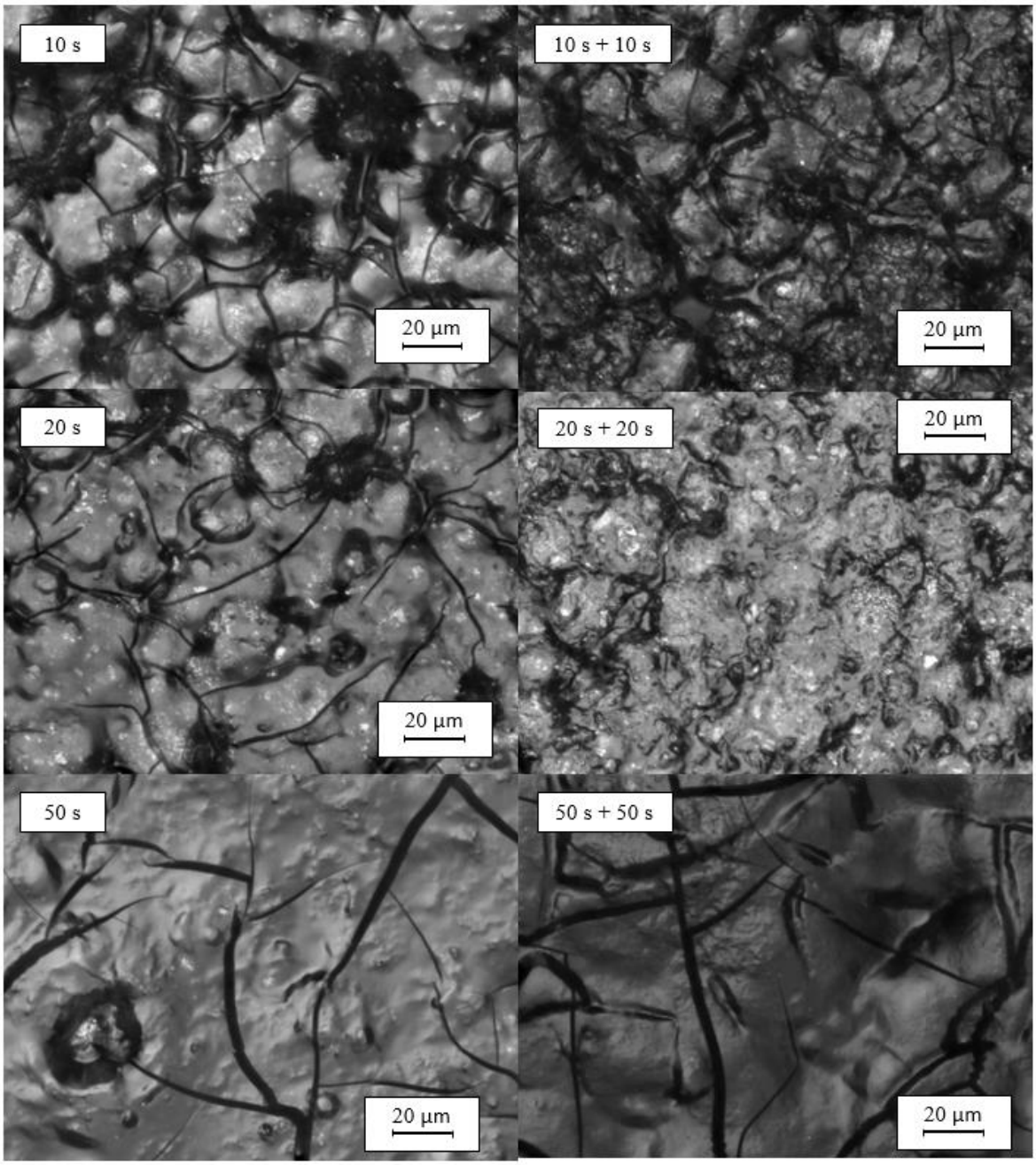

Figure 61: Optical microscopy images of PAN redepositions at 50X magnification. (Left) First cycle depositions, and (Right) second cycle depositions. Depositions performed using chronoamperometry at -3.0 V *vs.* Ag/Ag^{+} on 14 mm diameter graphite-composite electrodes in a Teflon cell using AN(0.05 mol dm^{-3} TBAP) electrolyte saturated with O_2 and without water. From top to bottom: 10 seconds and 10 seconds, 20 seconds and 20 seconds, and 50 seconds and 50 seconds.

3.4.6 Chronoamperometry studies – post-treatment annealing

Annealing polymer chains can cause them to unfold and encourage chain movement, this is commonly done to improve crystallinity and remove cracks in structures [57] [135]. According to Gupta and Chand [149], the size of PAN crystals begins to grow at and above the glass transition temperature of 95 °C [35] [128]; the annealing of PAN results in enhancement of crystallisation and the size of crystallite leading to the removal of surface defects. Temperatures used to anneal PAN vary greatly in literature. Jung *et al*. [135] reported using temperatures at 80 °C in a water bath for PAN annealing to improve crystallinity, with promising results. Lacey *et al.* [41] used temperatures of 150 °C to soften the film and improve uniformity, turning the PAN deposit from a white structure to a clear one. However, higher temperatures should be avoided to minimise risk of mass loss and thermal degradation found during TGA studies at around 150 °C (see Section 3.4.2). Subsequently, the following annealing studies used temperatures of 120 °C, above the glass transitions of 95 °C and high enough to evaporate any water within the structure. Annealing was performed under vacuum in a vacuum furnace for varying time scales to remove the presence of oxygen and reduce the risk of unwanted side-reactions.

Annealing of all polymers whether initially white, white-yellow, or clear would result in a clear film with no apparent yellow discolouration, see Figure 62 for a comparison. This would occur even when annealed at the lowest studied time of 1 hour. Pellon *et al*. [129] identified opaque white films as being heterogeneous and composed of a compressed powder containing either air or remaining monomer in inter-particle spaces. Clear films were continuous and remaining monomer was either distributed molecularly or in very minute droplets. It can therefore be concluded that annealing has encouraged chain movement and allowed the redistribution of surface defects to produce a more homogeneous surface film.

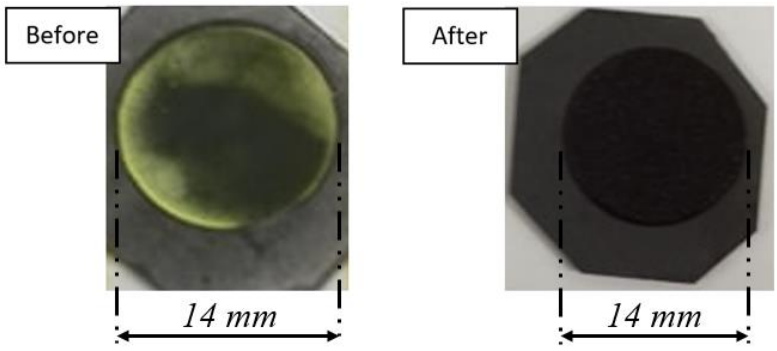

Figure 62: Image of a graphite-composite PAN electrodes deposited using chronoamperometry at -1.8 V *vs.* Ag/Ag^+ for 100 seconds. AN(0.05 mol dm^{-3} TBAP) electrolyte saturated with O_2 and without water was used in a Teflon cell. From left to right: PAN deposit before annealing, PAN deposit after 72 hours of annealing at 120 °C.

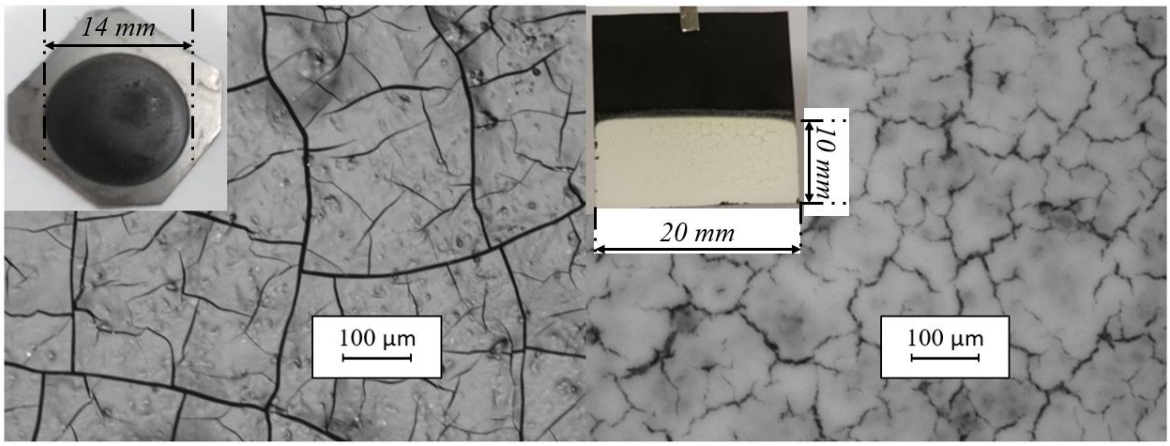

Figure 63: Optical microscopy of PAN deposited graphite-composite electrodes at 10X magnification using AN(0.05 mol dm^{-3} TBAP) electrolyte saturated with O_2 and without water. (Left) clear PAN deposit using chronoamperometry at -3.0 V *vs.* Ag/Ag^+ for 100 seconds in a Teflon cell, (Right) white PAN deposit using cyclic voltammetry at 0.0 V to -3.0 V *vs.* Ag/Ag^+ at 50 mV s^{-1} in a glass cell. Images of the full electrodes are superimposed to highlight difference in opacity between samples.

Figure 63 highlights the initial morphology difference between clear and white samples before annealing took place. Before and after annealing showed no significant mass change. Mass changes that were observed were of the order of 0.1 mg. The instrument used to measure mass of the deposits had a maximum precision of 0.1 mg and, hence, any change was attributed to instrumental error. No significant difference was recorded for varying CA voltages, and hence level of impurity does not seem to significantly affect the mass change either at 120 °C annealing, see Table 14.

Table 14: Mass of PAN deposits before and after annealing for 72 hours at 120 °C. Deposits were formed using chronoamperometry over a range of potentials for 100 seconds. Deposition performed on 14 mm diameter graphite-composite electrodes in a Teflon cell using AN(0.05 mol dm^{-3} TBAP) electrolyte saturated with O_2 and without water.

Deposition parameters	PAN mass before annealing (mg)	PAN mass after annealing (mg)
-1.8 V, 100 s	9.9 ± 0.1	9.9 ± 0.1
-2.0 V, 100 s	9.5 ± 0.1	9.3 ± 0.1
-2.2 V, 100 s	9.5 ± 0.1	9.1 ± 0.1
-2.4 V, 100 s	6.6 ± 0.1	6.2 ± 0.1
-2.6 V, 100 s	6.0 ± 0.1	5.9 ± 0.1

Optical microscopy images provided more insight into the changes of surface morphology. Figure 65 shows a range of images for annealing of clear PAN deposits from 1 hour to 144 hours. It was observed that little change occurs until 24 hours where cracks are eliminated almost entirely with only small circular surface defects seen. Beyond this, surface defects appeared to re-emerge with darker areas forming that might be interpreted as new cracks forming. However, Figure 64 observes the 72 hour image and the 144 hour image at a greater magnification showing that the cracks had not reopened. Contrarily, a thin polymer film was seen sealing the darker areas providing complete coverage of the graphite-composite surface.

Figure 66 shows the images for white polymer films over the same time scales. Changes in the surface were immediately obvious after 1 hour. At 48 hours a near homogeneous film was observed with increasing defects after longer annealing periods. However, darker areas were far more prevalent for white annealed films implying a greater degree of surface variation. Similarly to clear films, the darker areas are still covered with a thin film although these darker areas took up much more of the surface area.

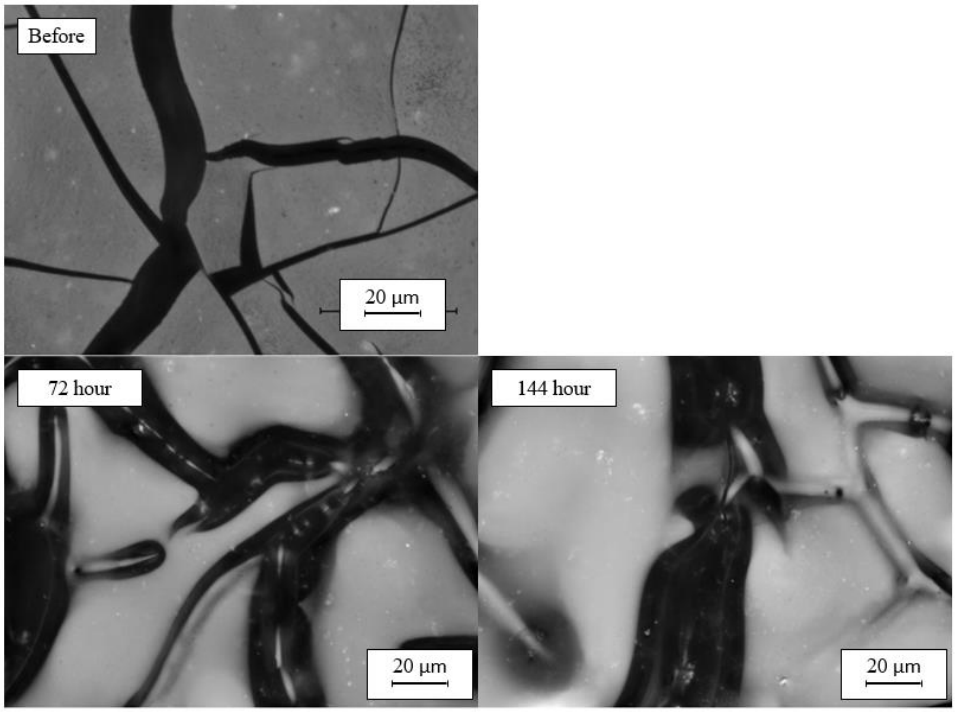

Figure 64: Optical microscopy images for clear PAN deposits at 50 X magnification. Images labelled before annealing, and after annealing of the same sample for 72 hours and later after 144 hours. Annealing performed at 120 °C. Depositions performed with chronoamperometry at -3.0 V *vs.* Ag/Ag^{+} for 20 seconds in a Teflon cell using AN(0.05 mol dm^{-3} TBAP) electrolyte saturated with O_2 and without water onto a graphite-composite electrode.

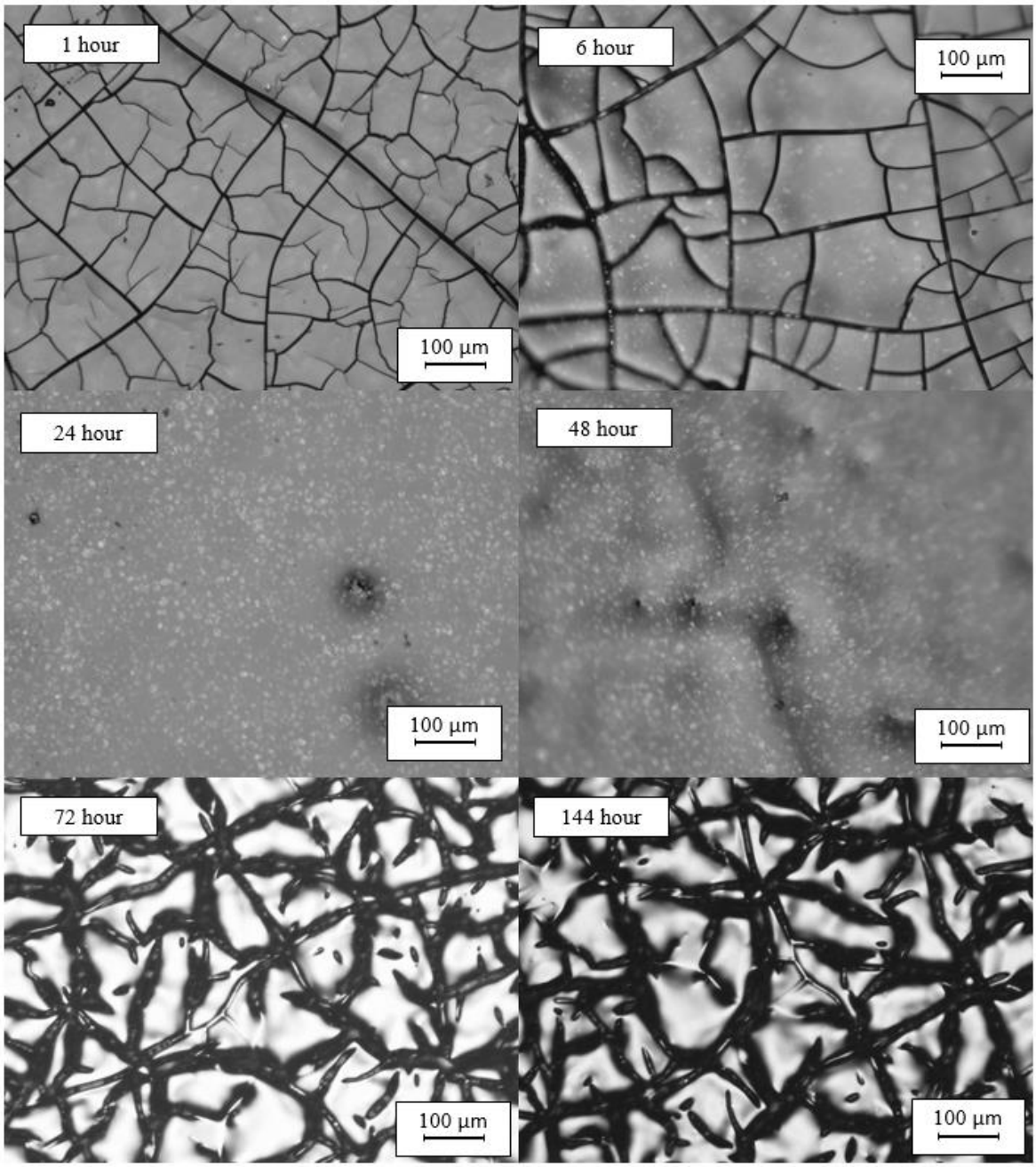

Figure 65: Optical microscopy images for clear PAN deposits at 10 X magnification over a range of time scales. Images labelled with their length of annealing time. Annealing performed at 120 ^{o}C. Depositions performed with chronoamperometry at -3.0 V *vs.* Ag/Ag^{+} for 20 seconds in a Teflon cell using AN(0.05 mol dm^{-3} TBAP) electrolyte saturated with O_2 and without water onto graphite-composite electrodes.

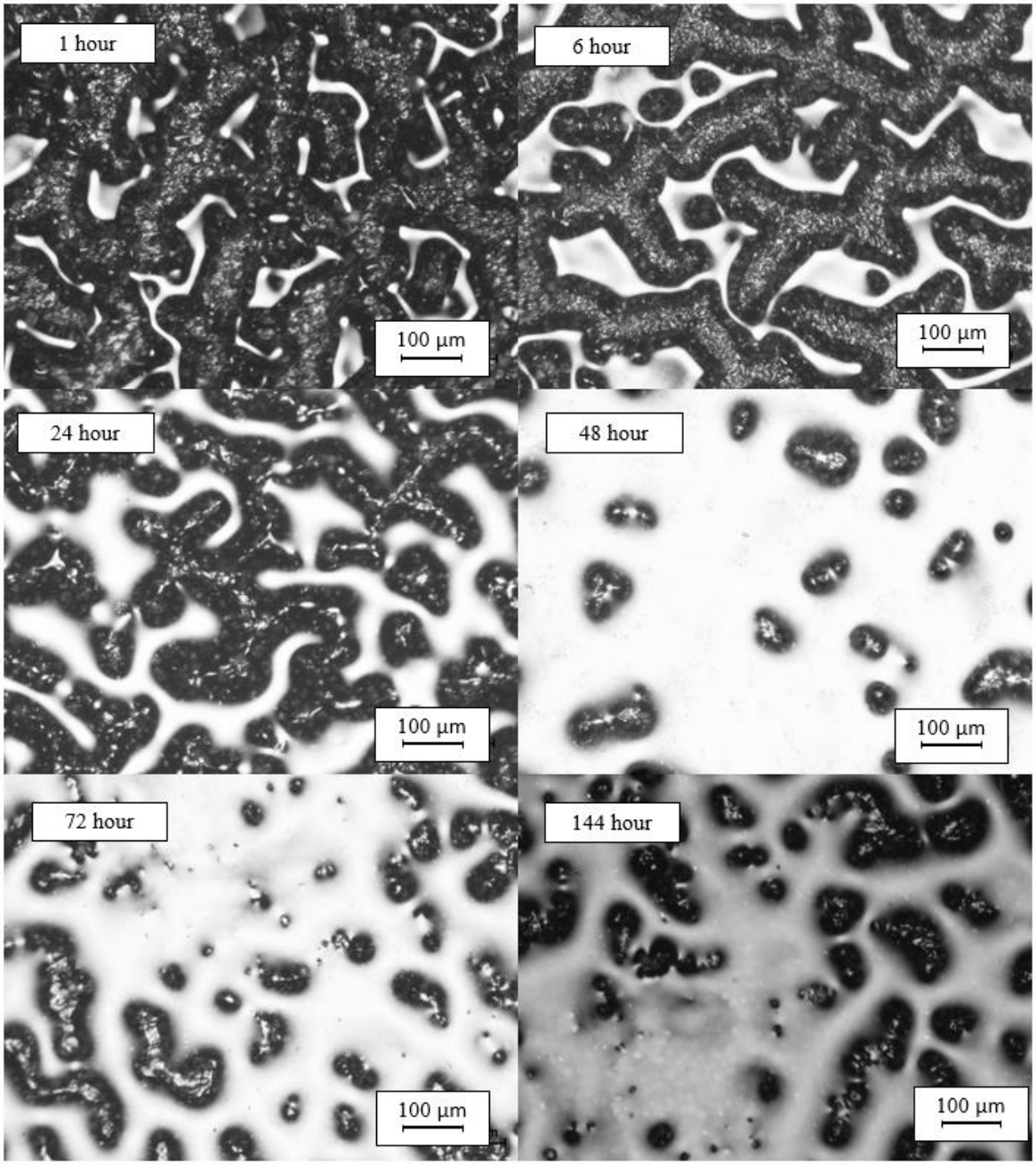

Figure 66: Optical microscopy images for white PAN deposits at 10 X magnification over a range of time scales. Images labelled with their length of annealing time. Annealing performed at 120 °C. Depositions performed with chronoamperometry at -3.0 V *vs.* Ag/Ag^{+} for 20 seconds in a Teflon cell using AN(0.05 mol dm^{-3} TBAP) electrolyte saturated with O_2 and without water onto graphite-composite electrodes.

3.5 Conclusion

PAN electrodepositions were performed with an extensive look at some conditions that were likely to effect the resulting films. The intent was to produce a polymer film coating on a commonly used lithium-ion cell electrode material, graphite is an anode material used within such systems. Electrodes produced were intended for use in later studies to identify any exhibited PTCR response at elevated temperatures. A PTCR response would provide valuable functionality in the prevention of thermal runaway in lithium-ion cells.

By performing cyclic voltammetry or chronoamperometry with AN(0.05 mol dm^{-3} TBAP) electrolyte, PAN was found to deposit onto several conductive surfaces. These surfaces were glassy carbon, metallic copper, and graphite-composites. Raman measurements performed on the glassy carbon and graphite showed chararcteristic PAN peaks at 2250 cm^{-1} C≡N cyano group and 3000 cm^{-1} C-H alkyl group. EDS measurements found a near identical composition of carbon and nitrogen to an ideal PAN monomer unit further supporting that PAN was indeed deposited.

Cyclic voltammetry studies of oxygen saturation and water contamination provided valuable information on electrochemical activity. Oxygen reduction to superoxide was found to occur in a quasi-reversible behaviour. This superoxide was a necessary initiator for PAN electrodepositions. Oxygen reduction would occur around -1.25 V *vs.* Ag/Ag^+ whilst the polymerisation and electrografting of PAN initiated around -1.4 V *vs.* Ag/Ag^+, provided superoxide was present. This electrografting would lead to the passivation of the electrode surface. An additional polymerisation was found near -2.25 V *vs.* Ag/Ag^+ relating to polymerisation in solution that does not typcially graft to the electrode surface [70], which left electrolyte with a yellow discolouration. The presence of water in the system appeared to encourage polymeristion, leading to polymerisation in solution and a yellow discolouration even with no oxygen present. When oxygen was present, the mass of PAN deposited onto the electrode surface would as much as double. However, water contamination would lead to a blistering and dicolouration of the electrode surface itself damaging the integrity of potential lithium-ion electrodes obtained via methods used.

Greater PAN deposit masses were identified onto carbon surfaces, such as glassy carbon and graphite, as opposed to metallic copper. A tentative link is made between the concentration of initiator (superoxide anions) to the amount of PAN deposited. Studies by Singh *et al*. [134] found carbonaceous surfaces, such as graphite and glassy carbon, act as a catalyst for oxygen reduction to superoxide.

Two PAN morphologies were found for electrodeposition onto graphite-composites, controlled by using different deposition cells. White non-continuous films were seen for deposition in a sealed nitrogen-enviroment glass cell, whereas clear continuos films were seen for deposition in a Teflon cell that was exposed to air. Raman and EDS studies found no chemical change from white to clear PAN, the change can therefore be concluded as a purely physical one. Studies by Shavit *et al*. [131] investigated several conditions that affected whether a white or clear PAN film was observed. They found polymerisation in solution was prevented at the air-interface of the electrolyte due to the presence of oxygen acting as a retarder. This ensured a concentration gradient and flow of monomers to the deposition surface. This constant flow of monomers to the deposition area allowed a clear film to develop. Clear films were more uniform and hence better for lithium-ion electrodes. Unfortunately, both white and clear films had micrometer width cracks large enough for lithium-ion infiltration, potentially affecting any PTCR response studied in later chapters.

Chronoamperometry studies were used to tailor properties of clear PAN films, reducing crack sizes and impurity concentrations. As potential became more negative PAN films began to deposit beyond -1.1 V *vs.* Ag/Ag^+, after oxygen reduction. Raman data found more negative potentials included more cyclization impurities and less dehydrogenation impurities. Samples with more cyclization had less mass loss during TGA studies and so negative potentials of -3.0 V *vs.* Ag/Ag^+ were chosen to avoid mass loss in PTCR studies. However, crack sizes were not found to be dependent upon applied potential.

Varying chronoamperometry time showed promise in removing film cracks, with 20 seconds appearing optimal. Above 20 seconds had greater crack sizes, likely due to dry cracking. Below 20 seconds resulted in non-uniform films that did not coat the entire graphite-composite surface.

Varying deposition times also allowed for easily tailorable film thicknesses. Between 1 and 100 seconds a linear trend was identified. Below 1 second a steeper increase was observed, although this may be due to more rapid kinetics of oxygen reduction compared to PAN polymerisation and more rapid polymer nucleation compared to growth. Superoxide anions were not initially present and so initiator concentration would greatly increase when potential was first applied leading to polymer nucleation. For the linear trend, film thickness increased by 0.327 ± 0.015 µm per second with an intercept of 16.4 µm. This was a reasonably accurate estimate for PAN film growth. No polymer growth was experienced without a driving potential being applied, however, even if superoxide was produced in the electrolyte prior to inclusion of the depositing electrode. This indicated a diffusion limited growth behaviour of monomers to the electrode surface. The process was also non-faradaic with superoxide anions acting more like a catalyst for polymerisation.

Further post-treatment methods to remove film cracks were explored. Attempts to redeposit onto polymer films showed limited success. Lower redeposition times of 20 seconds + 20 seconds allowed polymer growth to initiate on non-coated conductive surfaces sealing the cracks present. Longer redeposition times, such as 50 seconds + 50 seconds, resulted in further dry cracking. Unfortunately redeposited film surfaces were less uniform, which is undesirable for lithium-ion cell electrode performance.

Annealing post-treatment was very successful for clear polymer films. Above 24 hours of annealing at 120 ^{o}C resulted in sealed cracks. However, darker areas with thin PAN film coatings began to develop above 48 hours and so excessive annealing times should be avoided to prevent non-uniform films. White annealed films showed crack sealing above 1 hour, but there were far more thinner film areas and less uniformity than annealed clear films.

In conclusion, PAN films were successfully deposited onto graphite-composite electrodes for use in lithium-ion half cells. Studies found PAN electrodepositions were highly dependent upon the presence of an initiator to start PAN growth. Water contamination was also found to be undesirable due to damage of the graphite-composite electrode surface. Two key morphologies were identified for depositions onto graphite-composites, white (non-continuous) or clear (continuous) dependent upon the presence of air above the electrolyte surface. Through controlling chronoamperometry potential impurities can be controlled with -3.0 V *vs.* Ag/Ag^{+} providing minimal mass loss at elevated temperatures. Through controlling chronoamperometry time film thicknesses can be controlled with reasonable accuracy; 20 seconds appeared as an ideal due to minimal film cracking. Post-treatment of PAN films was possible to help remove cracks, however redepositions were non-uniform even if cracks sealed. Annealing was a potential solution but uniformity must be closely observed for longer annealing times. Following all these studies, standard electrodes of 11 mm diameter were punched out from the graphite-composite deposition areas for use in the next chapter in lithium-ion half-cell arrangements.

Chapter 4 PAN film lithium half-cell studies

In the previous chapter, PAN films were successfully deposited onto graphite-composite anodes. Not only this, but they were able to be produced to tailorable thicknesses. Several samples also underwent post-treatment conditions in order to improve surface morphology. Following on from these studies, graphite-composite electrode discs with and without polymer coatings were produced and compared. Electrodes of 11 mm diameter were punched from PAN electrodepositions. These electrodes were cycled in a half-cell arrangement against lithium metal inside Swagelok cells.

The initial scope of this thesis was to produce practical electrodes with functional polymer materials in order to prevent thermal runaway. To this end, the PAN films must provide comparable performance to pristine graphite anodes under normal operating conditions. This is in regards to not only capacity and impedance, but also maintaining a high standard of performance over several cycles. Extensive studies were performed at room temperature within Swagelok cell systems using graphite anodes with PAN film coatings. These films were of varying thicknesses and underwent different post-treatment conditions to identify the best possible performance, if any. All these studies were then compared to pristine graphite.

Charge-discharge cycling studies were then repeated at elevated temperatures, increasing temperatures in intervals to identify if a PTCR response occurs and approximately when this occurs. Studies were also performed to investigate if observed PTCR responses were reversible or irreversible. PTCR onset should be followed by increases in impedance leading to a severe reduction in cell capacity [8] [19] [20] [34]. This is most likely to occur near to transition temperatures and for PAN films this would be expected to be the glass transition temperature of 95 ^{o}C [35] [58]. Hence, elevated temperature studies were performed up to 120 ^{o}C and data on cycling capacities over this range were recorded. This was performed for a range of PAN thicknesses and compared to the response from pristine graphite-composite electrodes.

4.1 Experimental

Graphite-composite ink electrodes were used as the substrate for PAN film depositions, as investigated in Chapter 3. Following these studies several different PAN morphologies were produced, each of which were tested as electrodes within an electrochemical arrangement. These PAN morphologies were also compared with the pristine graphite-composite performance. The electrochemical arrangement and Swagelok cell schematic used are detailed in Chapter 2.

4.1.1 PAN film coating electrode preparation

The graphite-composite in this case forms the anode onto which the PAN film was electrodeposited prior to cycling within a cell. There were four different PAN film surface morphologies that were prepared: clear, white, clear annealed, and white annealed. All of the films formed in this chapter were prepared using chronoamperometry to electrodeposit onto the graphite-composite ink electrodes using O_2 saturated AN(0.05 mol dm^{-3} TBAP) without water as the deposition electrolyte. O_2 saturation of the electrolyte was performed for 15 minutes via a gas sparger. Clear films were produced via electrodeposition within a Teflon cell whilst white films were produced via electrodeposition in a glass cell. The schematics of these cells and the preparation of the electrodeposition electrolyte were discussed in Chapter 3. Annealing was performed on several of these PAN coated graphite-composites by heating to 120 ^oC under vacuum within a Buchi tube for 144 hours, as described in Chapter 3.

Most electrodepositions were performed using chronoamperometry at -3.0 V *vs.* Ag/Ag^+ for 20 seconds to produce clear films around 22 µm film thickness. This used the relationship between deposition time and film thickness calculated in Chapter 3; a value of 16.4 µm after 1 second was obtained with an additional 0.3 µm per second for film growth up to 100 seconds. Greater thicknesses were produced by increasing chronoamperometry time. Thicknesses lower than 16.4 µm were produced by using depositions times lower than 1 second, however, a clear trend was not identified for these film thicknesses and so it was difficult to produce films of these thicknesses reliably. A further complication was that for white films a trend was not seen as clearly with fluctuating thicknesses as much as 10 µm and so all electrodepositions were performed at -3.0 V *vs.* Ag/Ag^+ for 20 seconds for white films.

From these electrodeposited areas, 11 mm diameter electrode discs were punched out using a precision punch (EL-CELL, EL-Cut). 11 mm was the required size for use in the Swagelok half-cell arrangements available.

4.1.2 Elevated temperature cycling

Varying temperature can affect cycling performance [102]. Most battery systems are run at room temperature. Running at higher temperatures can improve some aspects of performance but prolonged usage shortens cycle life. Alternatively, colder temperatures increase internal resistance and lowers capacity of the battery, see Figure 67. For the studies within this chapter, lower than room temperatures were not required as these would not initiate the intended PAN shutdown effect in response to a thermal runaway event. Theoretically, PAN would undergo a shutdown around its glass transition temperature of 95 °C [35], so temperatures were not planned to exceed 120 °C.

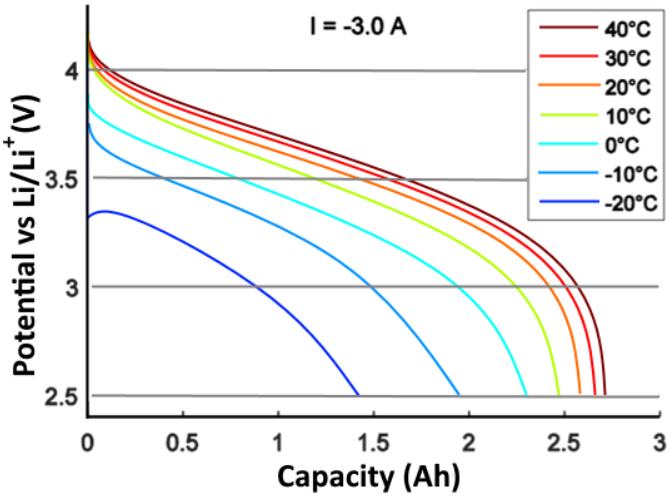

Figure 67: Representation of a typical discharge curve for a $LiNiCoAlO_2$ cathode lithium-ion cell at 3 A discharge current for various temperatures shown in the legend in units of Celsius. Data expressed as potential against capacity. This graph is an illustration of $LiNiCoAlO_2$ cathode data and not an actual cycled $LiNiCoAlO_2$ cathode. Figure adapted from: [102].

Elevated temperatures were explored in intervals for Swagelok cell cycling in this chapter. A Genlab classic oven from the laboratory range (Agar Scientific, MINO/6) was used to achieve these temperatures, the setup of which was explained in Chapter 2. These studies were performed similar to room temperature studies also explained in Chapter 2, at a C-rate of 0.1 C between voltages of 0.005 V to 1.5 V. Unlike these studies, only two cycles were performed at each temperature interval before proceeding onto the next. Temperatures were cycled from 25 °C up to 120 °C. This temperature maximum was informed by TGA measurements in this chapter as a point of low thermal degradation of the deposited PAN films but still above the 95 °C glass transition [35]. An additional interval was sometimes performed by rapidly cooling from 120 °C back to the 25 °C normal operating condition temperature in order to study the reversibility of any shutdown effect observed and the return capability of the electrodes. Cooling was achieved

with a fan and removal of the Swagelok from the oven until temperature probes showed a steady return to 25 ^{o}C. A further two cycles were then performed at this temperature.

Controlling the timing of temperature control with the number of cycles was difficult as the amount of time for each cycle changes, especially so if a PTCR effect shuts down the function of the cell completely or partially. Automation would require complex electronics to control the oven with the potentiostat to match the cycling of the cells. An added complication of cell cycling was that cells continuously age, so by the time elevated temperatures are applied the cell would have been subject to a degree of ageing. This means the length of time a cell runs for will be a function of the temperature and the number of cycles it was subjected to. The number of variables can also complicate interpretation of results. Therefore, several cell were tested at room temperature in the environmental chamber and within the oven systems to gather an understanding of the effects of ageing on the system. This allows the effects of ageing on cells at elevated and room temperatures to be removed as a variable when considering thermal degradation or PTCR responses.

4.1.3 Post-cycling optical microscopy sample preparation

Standard optical microscopy sample preparation is detailed in Chapter 2. Further to these experimental details, samples in this chapter were required to be carefully washed and dried after cycling to avoid producing hazardous materials. Primarily, the LP57 electrolyte used contains $LiPF_6$ salt that produces hydrofluoric acid when exposed to air. This also risks damaging the electrode surface before any images can be taken should this hydrofluoric acid be produced.

After cycling, electrodes were removed from their Swagelok cells inside an argon Belle Technology glove box environment to avoid contact with air. They were subsequently washed in ethyl methyl carbonate (EMC), the solvent used to form the LP57 electrolyte used in galvanostatic cycling, to remove the $LiPF_6$ salt. This was also done to remove any ethylene carbonate (EC), which forms solid crystals upon drying that may obscure any images taken.

Optical microscopy was used to view any surface features of the PAN films before and after cycling. The intent was to observe any potential damage or deformation to electrode surfaces due to the electrochemical environment. This was performed for both the PAN films and pristine graphite-composites. Possible changes due to elevated temperatures were also explored. Samples studied were placed on a glass slide and placed under a NIKON Eclipse LV100ND microscope system. Images were captured at 10X or 20X magnification.

4.2 Room temperature studies

Initial battery cycling studies were performed at room temperature to assess performance of electrode materials under normal operating conditions. This primarily consisted of galvanostatic measurements of graphite with and without PAN films. Comparisons were then made between capacities and efficiencies as well as key features observed during cycling.

4.2.1 Graphite cycling

Graphite is a commonly used anode material in industry and hence the electrochemical features during galvanostatic cycling are well understood. In a half-cell *vs.* Li/Li^+ the theoretical capacity of graphite is 372 $mAhg^{-1}$ [150]. A notable feature during the first cycle is the formation of an SEI layer, likely a result of reduction of organic solvents in the electrolyte. Formation of an SEI will normally initiate between 0.6 V and 0.8 V and result in a shoulder on a graph of potential against capacity that is not repeated in successive cycles. The formation shoulder will continue to 0.2 V [151]. Figure 68 shows the first two cycles for a graphite-composite ink electrode performed at a C-rate of 0.1 C. The SEI formation can be clearly seen in the first cycle as a shoulder on the graph around 0.7 V, which was absent during the second cycle. SEI formation was only present during the first charge cycle and does not affect the corresponding discharge cycle.

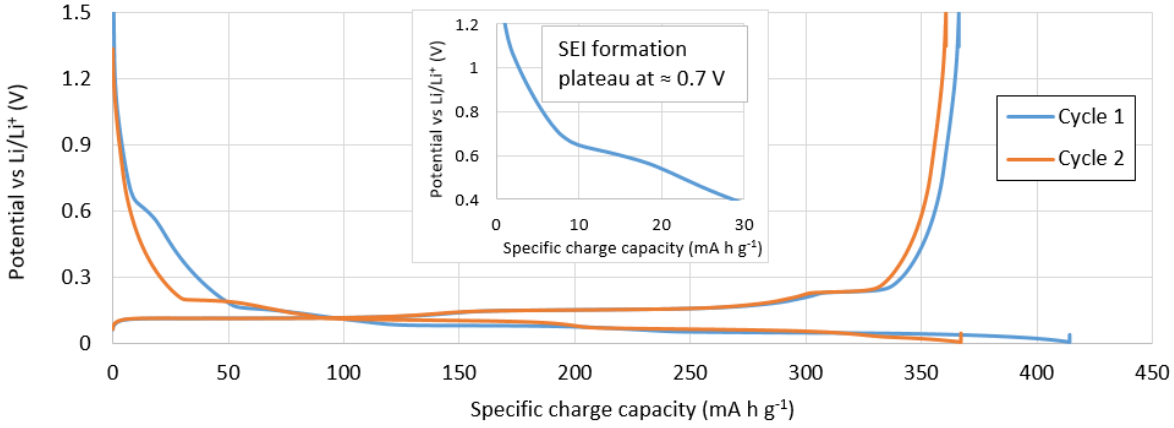

Figure 68: Galvanostatic cycling of a pristine graphite-composite ink electrode performed at a C-rate of 0.1 C at room temperature. A lithium metal counter/reference electrode was used in LP57 electrolyte (1M $LiPF_6$ in EC/EMC (vol:vol = 1:1)). The first cycle (blue) and second cycle (orange) are shown. Inset is an expanded view of the feature showing SEI formation during the first cycle charge.

Half-cells studying graphite against lithium metal or a lithium metal oxide cathode had an excess of lithium to allow graphite to limit cell capacity. Corresponding half-cell reactions are [100] [152]:

- Graphite anode: $xLi^+ + xe^- + C_6 \rightleftharpoons Li_xC_6$
- Lithium metal cathode: $Li_{x+y} \rightleftharpoons xLi^+ + xe^- + Li_y$
- Lithium metal oxide cathode: $LiMO_2 \rightleftharpoons xLi^+ + xe^- + Li_{1-x}MO_2$

The charge process is biased to the right and the discharge to the left. Intercalation of lithium into graphite occurs over several stages [153]. These stages result in several small plateaus with long flat potentials during cycling. A schematic for this staging mechanism is shown in Figure 69, taken from the second charge cycle of a studied graphite-composite ink electrode. Stage III/IV transition is often displaced by the SEI formation during the first cycle but is present in later cycles. In Stage IV, every fourth layer of the graphite structure is fully lithiated. Further lithiation leads to Stage III where every third layer is lithiated, one additional layer out of twelve is opened. Two additional layers out of twelve are opened from Stage III to Stage II and the final six are opened from Stage II to Stage I, resulting in LiC_6 in the above half-cell reactions.

Data for the first 10 cycles is shown in Table 15. Over these cycles the capacity remained stable between 369 mA h g^{-1} to 359 mA h g^{-1}, near to the theoretical capacity of 372 mA h g^{-1} [150]. This translated to a percentage utilisation of active material of 99.2 % to 96.6 %. This change was small and highlights the stability of the electrodes over these 10 cycles. Important to note was the effect of the SEI formation on the first cycle charge capacity. Charge capacity for cycles 2 to 10 fluctuated between 367 mA h g^{-1} and 362 mA h g^{-1}. However, the first cycle charge capacity was 414 mA h g^{-1} resulting in a coulombic efficiency of 88.4 %, nearly a 10 % lower efficiency than all other cycles. This was due to irreversible losses encountered during first cycle SEI formation.

Table 15: Specific capacity data for the first 10 cycles of the pristine graphite-composite ink electrode studied in Figure 68. Corresponding coulombic efficiency and active material utilisation percentages for each cycle is also given.

Cycle number	**1**	**2**	**3**	**4**	**5**	**6**	**7**	**8**	**9**	**10**
Discharge capacity (mA h g^{-1})	366	361	360	359	366	361	361	369	364	366
Charge capacity (mA h g^{-1})	414	367	364	363	362	363	362	364	366	366
Coulombic efficiency (%)	88.4	98.2	98.9	99.1	101.2	99.4	99.7	101.2	99.6	99.9
Active material utilisation (%)	98.4	96.9	96.7	96.6	98.3	97.0	97.1	99.2	97.9	98.3

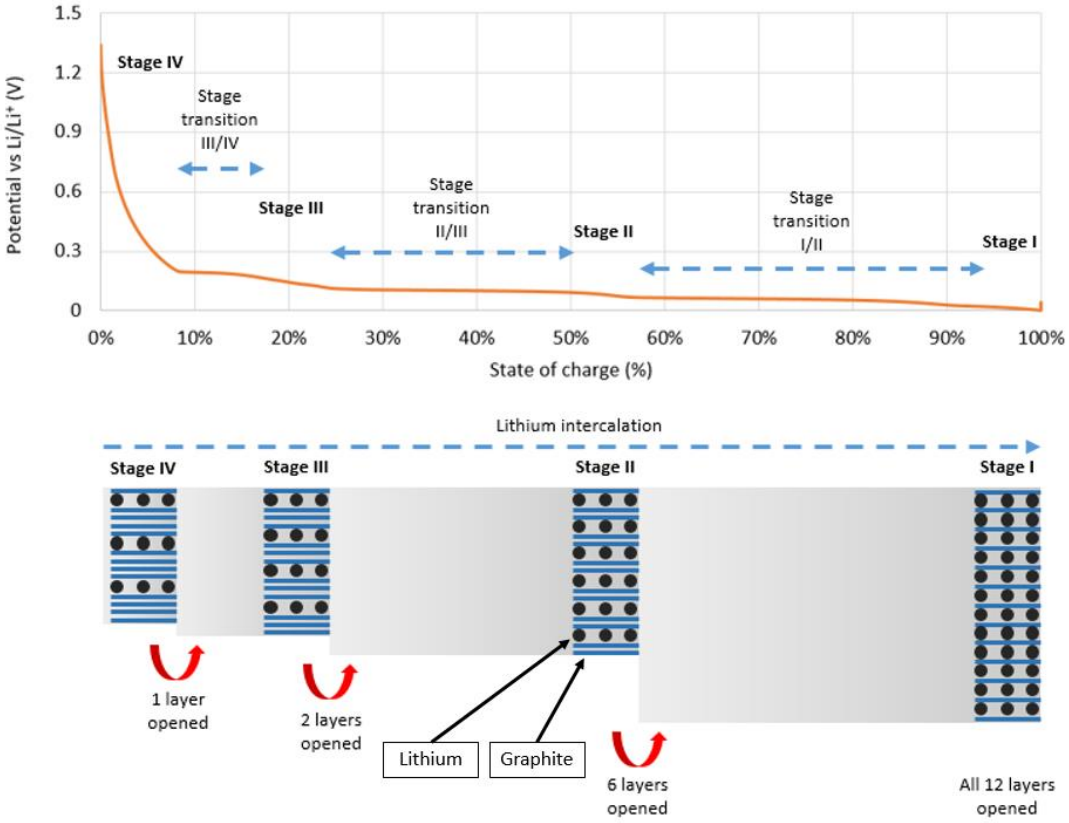

Figure 69: Schematic of lithium intercalation during a second charge cycle of a pristine graphite-composite ink electrode performed at a C-rate of 0.1 C at room temperature. A lithium metal counter/reference electrode was used in LP57 electrolyte (1M $LiPF_6$ in EC/EMC (vol:vol = 1:1)). The number of graphite layers opened at each stage is annotated. Figure adapted from: [153].

Optical microscopy images of the pristine graphite-composite electrodes before and after cycling are shown in Figure 70. There was little change to the structure morphology that can be observed for 0.1 C cycling for 10 cycles at normal room temperature operating conditions. At both periods in time the graphite structure appeared as a layer of small particles coating the electrode surface.

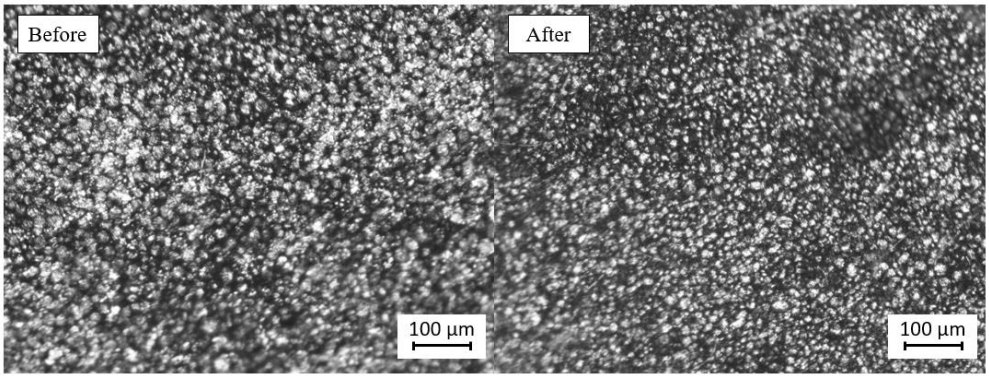

Figure 70: Optical microscopy images for a pristine graphite-composite ink electrode before (left) and after (right) cycling in a Swagelok cell at room temperature at 0.1 C for 10 cycles. Images taken at 10X magnification.

4.2.2 Annealed graphite cycling

An additional study was performed on an annealed graphite-composite electrode without a PAN film. This electrode was annealed at 120 °C for 144 hours prior to cell assembly to investigate if exposure to elevated temperatures effects performance of the graphite-composite in the absence of a polymer coating. Figure 71 shows cycling behaviour for the first two cycles of an annealed graphite-composite electrode. SEI formation was observed during the first cycle, initiating around 0.7 V and ending around 0.2 V. The several stages of intercalation were also observed in the second cycle.

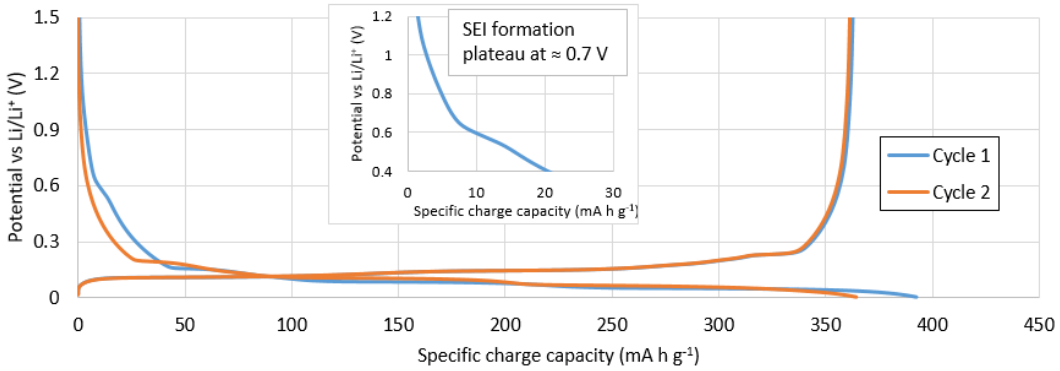

Figure 71: Galvanostatic cycling of an annealed graphite-composite ink electrode performed at a C-rate of 0.1 C at room temperature. The graphite electrode was annealed at 120 °C for 144 hours. A lithium metal counter/reference electrode was used in LP57 electrolyte (1M $LiPF_6$ in EC/EMC (vol:vol = 1:1)). The first cycle (blue) and second cycle (orange) are shown. Inset is an expanded view of the feature showing SEI formation during the first cycle charge.

Additional data for the first 10 cycles is shown in Table 16. Discharge capacity was stable between 369 mA h g^{-1} and 359 mA h g^{-1}, corresponding to an active material utilisation between 99.2 % and 96.6 %. These values were identical to the values of a pristine, non-annealed graphite-composite ink electrode shown in Section 4.2.1. Behaviour of the SEI formation and the effect on charge cycles also appeared unchanged due to annealing. Charge capacity for the subsequent cycles from 2 to 10 varied between 364 mA h g^{-1} and 359 mA h g^{-1}. Charge capacity for the first cycle was significantly higher at 393 mA h g^{-1}. The result was a coulombic efficiency of 92.4 % during the first cycle, around 7 % lower than all other cycles.

Table 16: Specific capacity data for the first 10 cycles of the annealed graphite-composite ink electrode studied in Figure 71. Corresponding coulombic efficiency and active material utilisation percentages for each cycle is also given.

Cycle number	1	2	3	4	5	6	7	8	9	10
Discharge capacity (mA h g^{-1})	363	361	359	365	360	360	369	361	360	360
Charge capacity (mA h g^{-1})	393	364	362	360	362	362	359	362	361	362
Coulombic efficiency (%)	92.4	99.2	99.4	101.3	99.6	99.5	102.8	99.7	99.5	99.5
Active material utilisation (%)	97.5	97.1	96.6	98.1	96.9	96.8	99.2	96.9	96.7	96.7

Optical microscopy images of the annealed graphite-composite electrodes before and after cycling are shown in Figure 72. Like the pristine graphite-composite electrodes, there was little apparent change to the surface morphology after cycling with the graphite structure appearing as a layer of small particles coating the electrode surface. It can therefore be concluded that heating the graphite-composite inks prior to cell assembly neither affects the cycling performance or the structural morphology of the graphite-composite in a significant way.

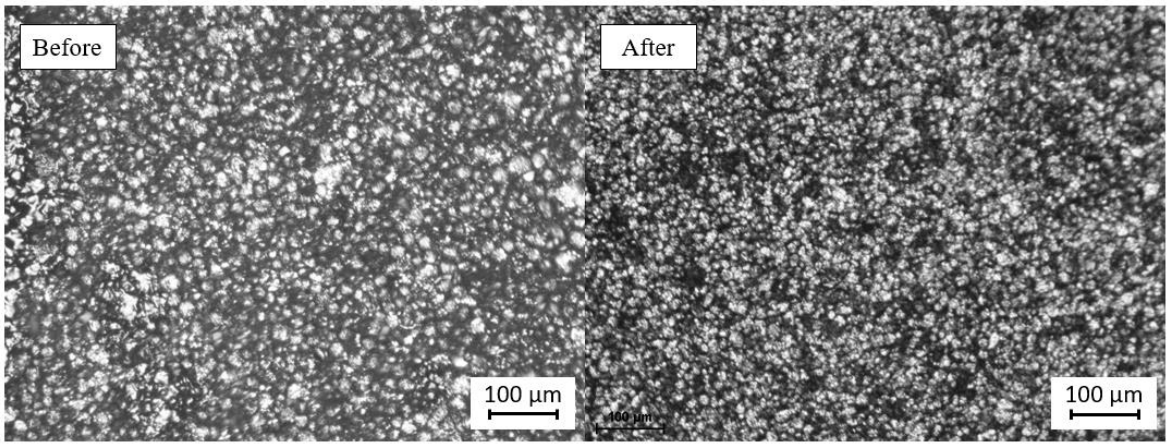

Figure 72: Optical microscopy images for an annealed graphite-composite ink electrode before (left) and after (right) cycling in a Swagelok cell at room temperature at 0.1 C for 10 cycles. Images taken at 10X magnification.

4.2.3 Graphite-polyacrylonitrile film cycling

Several different surface morphologies were obtained for PAN films developed in Chapter 3. These included clear films produced via Teflon cell electrodeposition and white films produced via glass cell electrodeposition, with the clear films appearing more ordered with less microstructure defects. Samples of both clear and white films were also annealed to remove cracks within the polymer surface, which was largely successful but led to non-uniform surfaces in many cases. As a result, several different samples required studying: clear, white, clear-annealed, and white-annealed. These annealed samples were prepared at 120 ^{o}C for 144 hours under vacuum.

Graphite-composites with clear PAN films showed promise with a specific discharge capacity at 193 mA h g^{-1} and 223 mA h g^{-1} for the first two cycles, 52 % to 60 % of the theoretical capacity. However, capacities were greatly reduced compared to the first two cycles of pristine graphite-composite where capacities of 366 mA h g^{-1} and 361 mA h g^{-1} were recorded, shown in Figure 73. This drop in capacity was due to an internal resistance introduced by the PAN films. Severe drops in capacity are reported for other coated electrode materials within lithium batteries. Ji *et al.* [31] reported capacities for lithium cobalt oxide (LCO) coated with poly(3-octylthiophene) (P3OT) less than 1 µm in thickness around 150 mA h g^{-1} at ambient. Theoretical capacity of LCO is 274 mA h g^{-1}, substantially higher than the polymer coated samples. Studies using 4 µm thick layers of PE microspheres coated onto a graphite surface reported capacities around 310 mA h g^{-1} or around 83 % of the theoretical capacity, as reported by Baginska *et al.* [32]. This drop in capacity experienced by the clear PAN films is therefore expected and additional tailoring of the polymer film properties may allow competitive capacity compared to other polymer film alternatives.

By comparing the potential of the stable plateau at 50 % state of charge from the clear PAN study and also the pristine and annealed graphite studies the potential IR drop can be estimated. For pristine graphite, potential of 0.0957 ± 10^{-6} V was recorded during first cycle charge, which was similar to the 0.0979 ± 10^{-6} V from the annealed graphite. However, for the PAN film sample in Figure 73 a potential of 0.0490 ± 10^{-6} V was found. This was a drop of 0.0467 ± 10^{-6} V from the pristine sample. This IR drop would lead to the potential limit during the galvanostatic cycling of 0.005 V being reached sooner during the cycle resulting in a lower specific capacity. If this was indeed caused by the PAN film, the effect should decrease with decreasing film thickness. Indeed, the drop of 0.0489 ± 10^{-6} V was recorded for a 32 µm sample whilst a 20 µm sample found a drop of 0.0450 ± 10^{-6} V, an 8 % change in IR drop. This thinner PAN sample was accompanied by a greater recorded discharge capacity of 247 mA h g^{-1}. Therefore, reducing PAN film thickness will increase the capacity achieved by the graphite-composite ink likely tending toward the capacity of pristine graphite.

Another concern with clear PAN samples was a large change in capacity from first to second cycles of 30 mA h g^{-1}, an 8 % jump of the total theoretical graphite capacity. Compare this to pristine graphite where a total 10 mA h g^{-1} variation was recorded over 10 cycles. This was attributed to incomplete infiltration of the electrolyte through the polymer film during the first cycle.

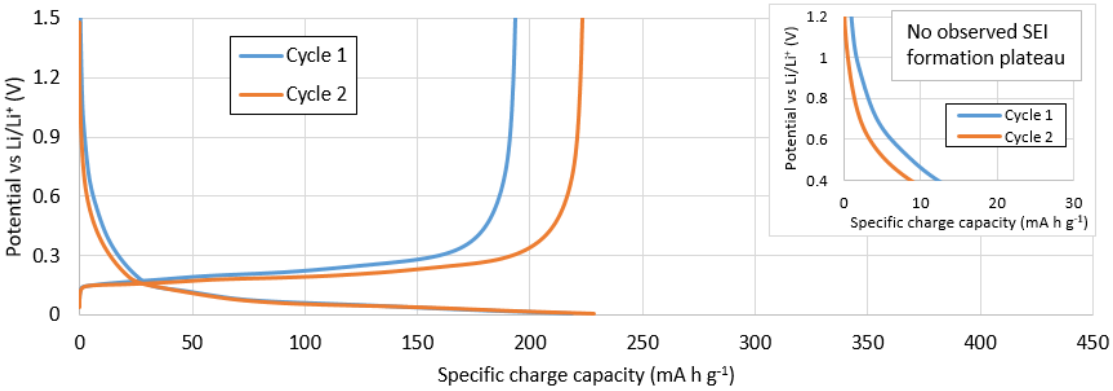

Figure 73: Galvanostatic cycling of a clear PAN graphite-composite ink electrode performed at a C-rate of 0.1 C at room temperature. A lithium metal counter/reference electrode was used in LP57 electrolyte (1M $LiPF_6$ in EC/EMC (vol:vol = 1:1)). The first cycle (blue) and second cycle (orange) are shown. Inset is an expanded view of the expected region where SEI formation would normally occur during the first cycle charge.

The features of graphite cycling are also less defined in the presence of a PAN film, see Figure 74. There was no observed SEI plateau, implying either no or reduced SEI formation suggesting the PAN film could act as a protective layer for graphite. However, the feature might be suppressed by the presence of the film. The other features of intercalation were difficult to recognise. Stage IV and Stage III were observable, but the features of Stage II and Stage I were less pronounced.

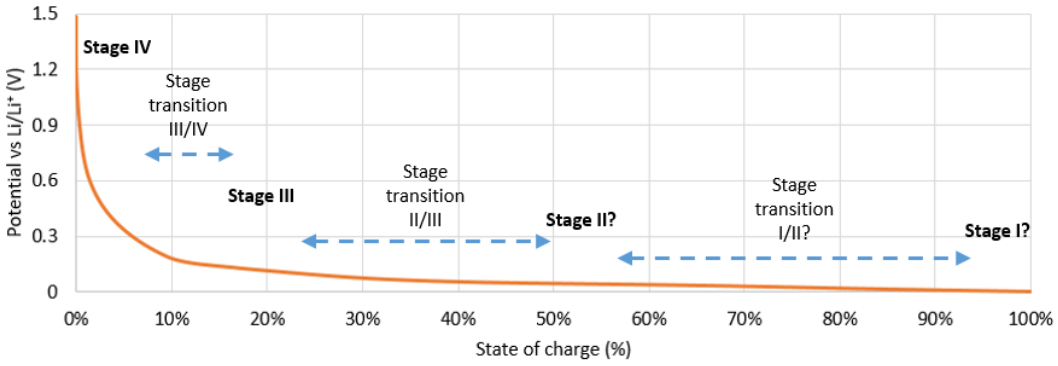

Figure 74: Schematic of lithium intercalation during a second charge cycle of a clear PAN graphite-composite ink electrode performed at a C-rate of 0.1 C at room temperature. A lithium metal counter/reference electrode was used in LP57 electrolyte (1M $LiPF_6$ in EC/EMC (vol:vol = 1:1)). The features from Stage II to Stage I are difficult to distinguish.

In films with white, white annealed, and clear annealed surfaces capacity was greatly reduced, see Figure 75. The total amount of active material utilised never exceeded 5 % of the theoretical. Capacities were so low that no graphitic features can be observed whether from SEI or from intercalation. This was true for the clear annealed polymer as well as the white and white annealed polymers. White polymers in general should be avoided whether annealed or not, the reduction in capacity was likely a result of the disordered microstructure when compared to clear polymers [129]. This disorder resulted in a more difficult ion transport of lithium to and from the graphite surfaces.

In terms of preventing thermal runaway, the greatly reduced capacity of the clear annealed samples was of interest. The reorganised structure must have closed both the cracks in the polymer surface and any pores or channels through which ionic transport can occur. If this annealing can occur within a cell whilst cycling, the capacity of the cell can effectively be shutdown to prevent cell operation and thermal runaway. However, the annealing in this case was performed before cell operation at 120 °C for 144 hours. For the shutdown to be useful, this effect must be observed quickly within a few seconds or minutes.

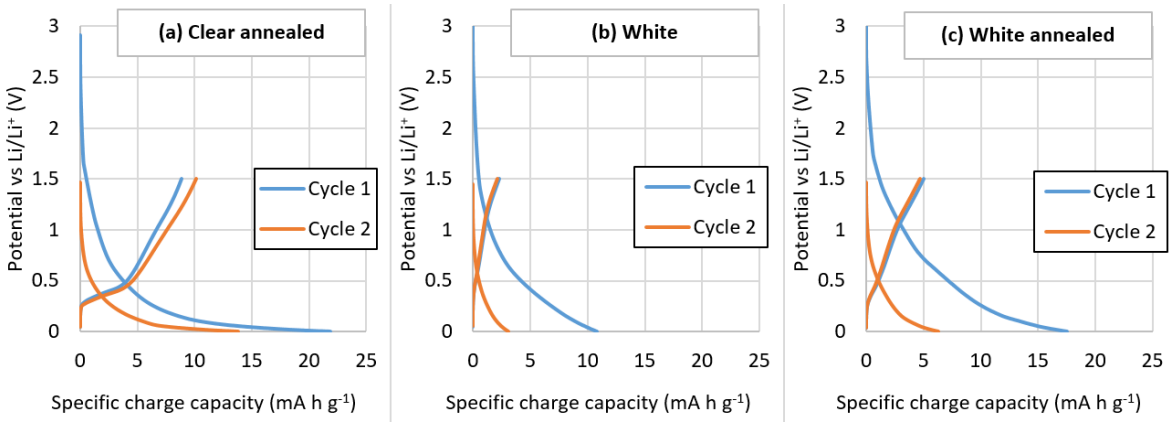

Figure 75: Galvanostatic cycling of graphite-composite ink electrodes coated with a film of (a) clear annealed PAN, (b) white PAN, and (c) white annealed PAN. Cycling was performed at a C-rate of 0.1 C at room temperature. A lithium metal counter/reference electrode was used in LP57 electrolyte (1M $LiPF_6$ in EC/EMC (vol:vol = 1:1)). The first cycle (blue) and second cycle (orange) are shown.

Table 17 shows the first 10 cycles for all the previously mentioned PAN coated graphite studies. It was obvious from looking at the data that only the clear PAN samples were suitable for cell operation. Active material utilised as a percentage of the total theoretical varied between 50 % and 60 %, compared to the other samples that never exceed 5 %. This translated to a specific discharge capacity in the order of hundreds, rather than ones or tens. Of concern for clear PAN performance was the comparatively quick decrease in discharge capacity over successive cycles.

There was a peak at 223 mA h g^{-1} during the second cycle, but this dropped 17 % to 186 mA h g^{-1} by the tenth cycle; or a total loss of theoretical capacity of 9.9 %. Battery operation would require hundreds if not thousands of cycles at stable capacity values. As a result, the clear PAN film may not be suitable for a full practical setting at this stage. On the other hand, the low annealed clear PAN capacities does show promise in the investigation of the prevention of thermal runaway.

Table 17: Specific capacity data for the first 10 cycles of the graphite-composite ink electrode studies coated with: clear PAN, white PAN, clear annealed PAN, and white annealed PAN. Corresponding coulombic efficiency and active material utilisation percentages for each cycle is also given.

	Cycle number	1	2	3	4	5	6	7	8	9	10
Clear PAN, 32 µm thickness	**Discharge capacity (mA h g^{-1})**	193	223	211	203	198	195	193	191	188	186
	Charge capacity (mA h g^{-1})	219	228	214	205	200	196	194	192	190	188
	Coulombic efficiency (%)	88.4	97.7	98.5	98.7	99.0	99.2	99.3	99.3	99.3	99.4
	Active material utilisation (%)	52.0	60.0	56.6	54.5	53.3	52.4	51.8	51.2	50.7	50.1
White PAN, 65 µm thickness	**Discharge capacity (mA h g^{-1})**	2.31	2.13	2.04	1.99	1.96	1.94	1.92	1.91	1.90	1.89
	Charge capacity (mA h g^{-1})	10.8	3.05	2.63	2.44	2.33	2.26	2.20	2.16	2.13	2.11
	Coulombic efficiency (%)	21.3	69.7	77.5	81.6	84.1	85.8	87.1	88.2	89.0	89.6
	Active material utilisation (%)	0.6	0.6	0.5	0.5	0.5	0.5	0.5	0.5	0.5	0.5
Clear annealed PAN, 25 µm thickness	**Discharge capacity (mA h g^{-1})**	8.89	10.1	11.3	11.8	12.1	12.3	12.5	12.7	12.8	13.0
	Charge capacity (mA h g^{-1})	21.9	13.8	14.2	14.2	14.1	14.0	13.9	14.0	14.0	14.1
	Coulombic efficiency (%)	40.6	73.5	79.1	83.1	85.9	88.0	89.5	90.6	91.5	92.2
	Active material utilisation (%)	2.4	2.7	3	3.2	3.3	3.3	3.4	3.4	3.5	3.5
White annealed PAN, 23 µm thickness	**Discharge capacity (mA h g^{-1})**	5.01	4.70	4.55	4.43	4.35	4.27	4.20	4.15	4.10	4.06
	Charge capacity (mA h g^{-1})	17.5	6.30	5.66	5.30	5.08	4.91	4.77	4.67	4.58	4.50
	Coulombic efficiency (%)	28.6	74.7	80.4	80.6	85.6	86.9	88.1	88.9	89.6	90.1
	Active material utilisation (%)	1.3	1.3	1.2	1.2	1.2	1.1	1.1	1.1	1.1	1.1

What was more obvious in all samples other than the clear PAN sample was a greater first cycle charge capacity than the subsequent cycles, implying a similar effect to SEI formation. This translated to a much lower coulombic efficiency in the first cycles, as demonstrated in Figure 76. For the significantly low capacity cells, coulombic efficiency slowly climbed and seemingly tended towards a plateau around 90 %. Interestingly for the clear PAN cell, when compared to Figure 73, the SEI formation was not immediately obvious from cycling graphs but the coulombic efficiency of the first cycle was near 10 % lower than all subsequent cycles. This would imply some reaction was occurring that was using some of the initial charge capacity, either an SEI formation or something introduced by the presence of the PAN polymer films.

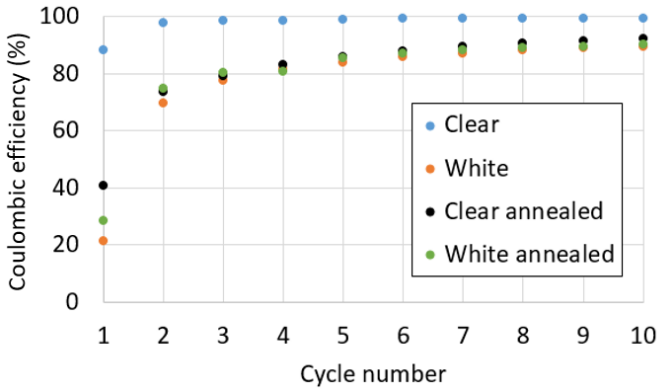

Figure 76: Coulombic efficiencies for the first 10 cycles of several graphite-composite ink electrodes. Electrodes had varying PAN films deposited: clear, white, clear annealed, and white annealed. Cycling was performed in a Swagelok cell for 10 cycles at 0.1 C at room temperature.

Because clear PAN samples were potentially useful in cell cycling operation, additional studies were performed on them including optical microscopy before and after cycling. This was done for both the annealed and non-annealed samples as the annealed samples were a potentially useful comparison for high temperature thermal runaway studies despite their low capacities.

Optical microscopy images before and after cycling for both the clear and clear annealed samples are shown in Figure 77. Cracks of the clear sample were completely sealed after cycling, with a surface that appears almost uniform with the exception of wrinkling on the polymer surface. The optical microscopy image was taken after washing and drying the electrode; it can be concluded that the polymer rearranges when wetted by electrolyte to seal the cracks and that the seal was maintained after drying. This would imply that annealing before cycling to remove the cracks may be unnecessary. On the contrary, the annealed sample remained mostly unchanged, with thicker white areas of PAN film and thinner dark areas of PAN film between. The only observable change was some line marks on the surface that were left by the glass fibre separators of the half-cell or were the glass fibres themselves that were embedded in the surface.

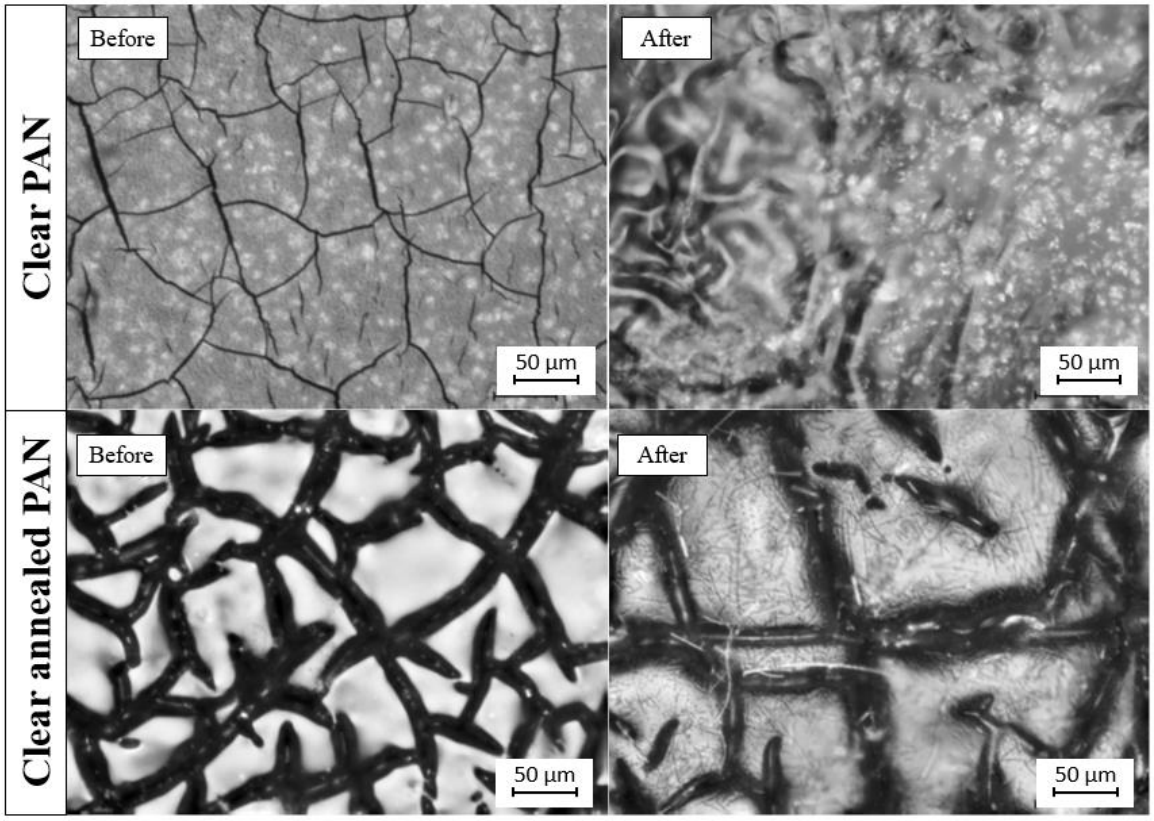

Figure 77: Optical microscopy of PAN deposits at 20X magnification before and after cell cycling. Cycling performed at 0.1 C for 10 cycles at room temperature. A lithium metal counter/reference electrode was used in LP57 electrolyte (1M $LiPF_6$ in EC/EMC (vol:vol = 1:1)). (Top) Clear PAN sample, and (Bottom) Clear annealed PAN sample.

4.2.4 Cycling performance with varying film thickness

Clear PAN samples of different thicknesses were produced via chronoamperometry depositions within a Teflon cell using AN(0.05 mol dm^{-3} TBAP) electrolyte saturated with O_2 without water. The thicknesses were controlled by varying the time scales for deposition. These varying thicknesses were tested within Swagelok cells to assess the effect of the presence of the polymer. Primarily, the answer to whether capacity increases with decreasing thicknesses was explored with greater capacities experienced with thinner polymer films and a maximum at the capacity of pristine graphite-composite inks with no film. It was assumed that the introduction of the PAN film added internal losses to the cell causing a capacity loss and that these losses were greater for thicker polymer films. These studies were performed for 10 galvanostatic cycles at 0.1 C-rate.

Capacity of graphite-composite inks tended to fall with increasing PAN film thickness, as shown in Figure 78. This was largely true across each of the 10 cycles studied. Ideally the PAN coated electrode should have as close a capacity to a pristine sample, under this criteria thinner samples

appeared to be better. Thicker films also appeared to have larger variations in capacity across the range, another detriment to their cell performance. This was obvious from the first to second cycles where 9 and 12 µm experienced a negligible change whilst 16 to 32 µm increased in capacity by more than 10 %. Comparative performance of an annealed PAN sample can also be seen with capacities around 10 to 15 mA h g^{-1}. Such low capacities were the expected performance for samples that experience a shutdown effect to prevent thermal runaway. It was hoped that the non-annealed PAN films would induce a similar shutdown when exposed to elevated temperatures whilst cycling.

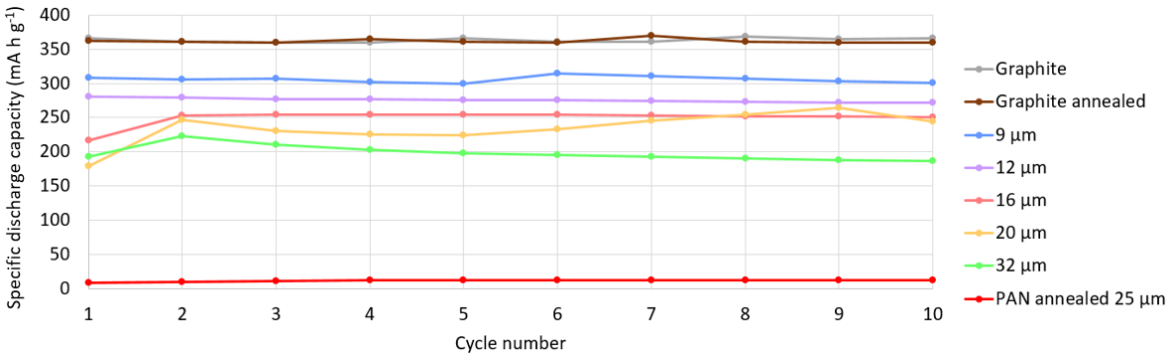

Figure 78: Discharge capacities per unit mass for the first 10 cycles of several graphite-composite ink electrodes. Electrodes had varying PAN film thicknesses from 9 µm to 32 µm. Data for pristine and annealed graphite are included, as well as data for annealed PAN coated graphite-composite inks. Cycling was performed in a Swagelok cell for 10 cycles at 0.1 C at room temperature.

Further evidence to the unpredictability of thicker PAN films can be seen in Figure 79a. The percentage difference between maximum and minimum capacities over the 10 cycles is shown against PAN film thickness. Up until 12 µm thickness negligible changes of 3 to 5 % were observed. However, this percentage difference would rapidly increase for thicker films recording 15 %, 32 %, and 17 % for 16 µm, 20 µm, and 32 µm respectively. These minimums and maximums were not between the first and final cycles as observed with pristine graphite in Figure 78; rather, large fluctuations are seen midway through the cycling of these PAN coated samples. This was evidence for instability in the PAN films that was exacerbated by increasing thickness.

An additional metric that is often used is the capacity retention of the cell, or the percentage remaining capacity between the first and final cycles. Cells will naturally degrade over time leading to lower capacities. Better performing cells will have a capacity retention closer to 100 % after cycling. Figure 79b highlights the problem with using thicker PAN films. Once again, from 0 µm to 12 µm behaviour was normal with near 100 % retention for pristine graphite over 10 cycles and slight drops with PAN films giving 98 % retention at 9 µm and 97 % at 12 µm. However,

capacity had increased by the tenth cycle for the 16 µm and 20 µm samples leading to a retention of 116 % and 136 % respectively. This increase largely happened between the first and second cycles and may be due to the increase in time taken for electrolyte to infiltrate thicker films. At 32 µm capacity retention behaviour returned to normal showing 96 %. This changeability was undesirable for cell operation where reliable and repetitive performance was key. As a result it was recommended to avoid PAN thicknesses of 16 µm and above.

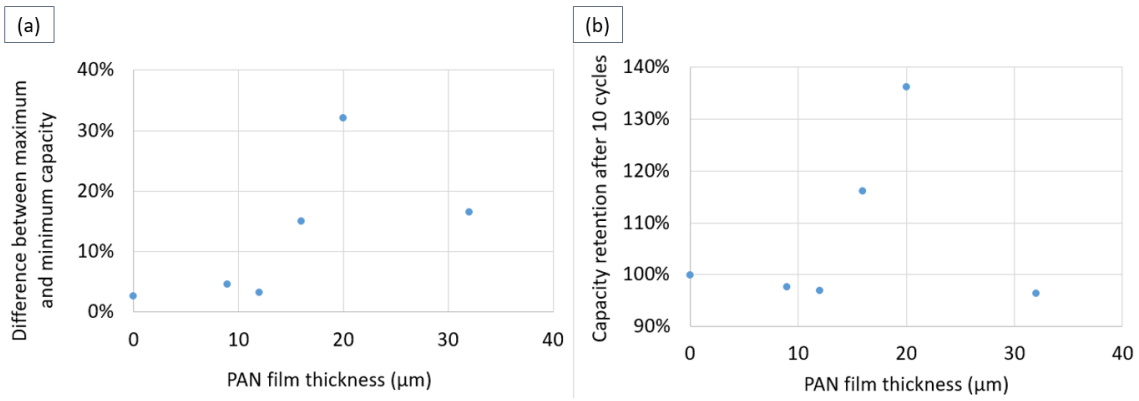

Figure 79: Additional metrics for cycling graphite-composite inks against PAN film coatings of varying thickness, cycling performed over 10 cycles in a Swagelok cell arrangement at a C-rate of 0.1 C at room temperature. (a) Percentage difference between maximum and minimum specific discharge capacities. (b) Capacity retention after 10 cycles as a percentage of first cycle discharge capacity.

Figure 80 shows the recorded discharge capacities of the samples after the tenth cycle. The annealed sample was not included due to the large difference in behaviour. Although the performance of thicker PAN coated samples was largely unpredictable from cycle to cycle, there remains a clear downward trend when looking at the final capacity for increasing PAN thicknesses. From a pristine sample of 0 µm PAN thickness to the maximum studied of 32 µm capacity fell from 366 mA h g^{-1} to 186 mA h g^{-1}. Drawing a line between these two data points would imply that capacity of a cell would decrease by 5.63 mA h g^{-1} per µm. However, because of the unpredictability of the data for thicker samples this value and whether the trend was linear was uncertain. What can be concluded was that thicker samples would lead to an overall decrease in cell capacity regardless of the fluctuation in capacity, which was also worsened with increasing PAN thickness.

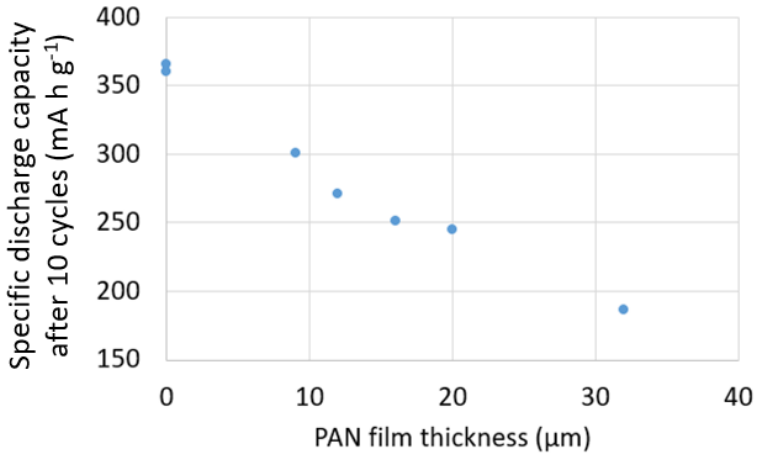

Figure 80: Specific discharge capacity after 10 cycles for graphite-composite ink electrodes coated with PAN films of varying thickness. Cycling was performed in a Swagelok cell for 10 cycles at 0.1 C at room temperature.

Another metric investigated over all the cycles was the coulombic efficiency, see Figure 81. For all samples coulombic efficiency was lowest during the first cycle, whether with pristine graphite, PAN films coatings, or with annealed PAN film coatings. Initial efficiency would start around 90 % and rise to around 99 % for most samples. Two exceptions were observed. Firstly, for the 20 µm sample efficiency appeared to fluctuate between 90 % and 100 %, similar to the effect seen on capacity for this sample in Figure 78. This was again linked to the unpredictability of the thicker PAN samples, but may also imply poorer electrolyte infiltration through the PAN film. The lower efficiency was unlikely to be due to the presence of side-reactions introduced by the presence of the PAN polymer films as it was not present in any other PAN samples. Secondly, an exception for the annealed PAN sample was observed. This was briefly discussed in Section 4.2.3, coulombic efficiency slowly increases and tends to a value above 90 %. The annealed PAN was likely to have reduced porosity making electrolyte infiltration more difficult and a longer process during cycling. By the end of the 10 cycles the efficiency had mostly recovered for the annealed sample but the result was a significantly lower capacity seen in Figure 78. Ionic resistance should therefore be substantially greater in the annealed samples compared with the non-annealed samples.

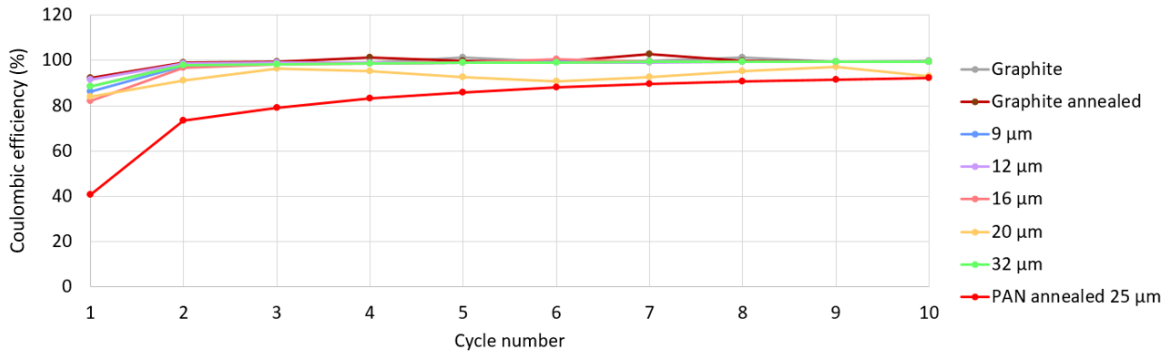

Figure 81: Coulombic efficiencies for the first 10 cycles of several graphite-composite ink electrodes. Electrodes had varying PAN film thicknesses from 9 µm to 32 µm. Data for pristine and annealed graphite are included, as well as data for annealed PAN coated graphite-composite inks. Cycling was performed in a Swagelok cell for 10 cycles at 0.1 C at room temperature.

4.2.5 Varying film thickness potential drops

To give insight on why capacity of PAN coated graphite electrodes falls with increasing thickness, analysis was performed on the uncompensated resistances of the samples. Specifically, attention was given to the IR drop of each sample. This is the potential drop of an electrical system across a resistive element commonly calculated by multiplying current by resistance. This is expressed in an electrochemical cell by higher than ideal potentials during a discharge half-cycle and lower than ideal potentials during a charge half-cycle [154] [155]. This results in lower capacities as potential limits set within the cell are reached earlier through the cycle. With graphite cycling, as there is a long plateau near to the lower potential limit a change in internal resistance and the subsequent shift in potential can substantially change the capacity of the cell.

The effect of IR on the potentials of different samples at different states of discharge is shown in Figure 82. Data was taken from the second discharge half-cycle to avoid the initial effects of SEI formation during the first cycles. A simple observation of the graphs shows that an increase in polymer thickness resulted in a higher potential at each state of discharge for the majority of the half-cycle. The greater the potential experienced the greater the IR drop. This increase was even greater for the annealed sample. From previous studies in Section 4.2.4, a drop in capacity was experienced as polymer thickness increases. Hence, there is a reliable connection between greater IR drops and greater losses in capacity. The result was greater resistance to ionic transport, likely as a result of lessened electrolyte infiltration at greater thicknesses.

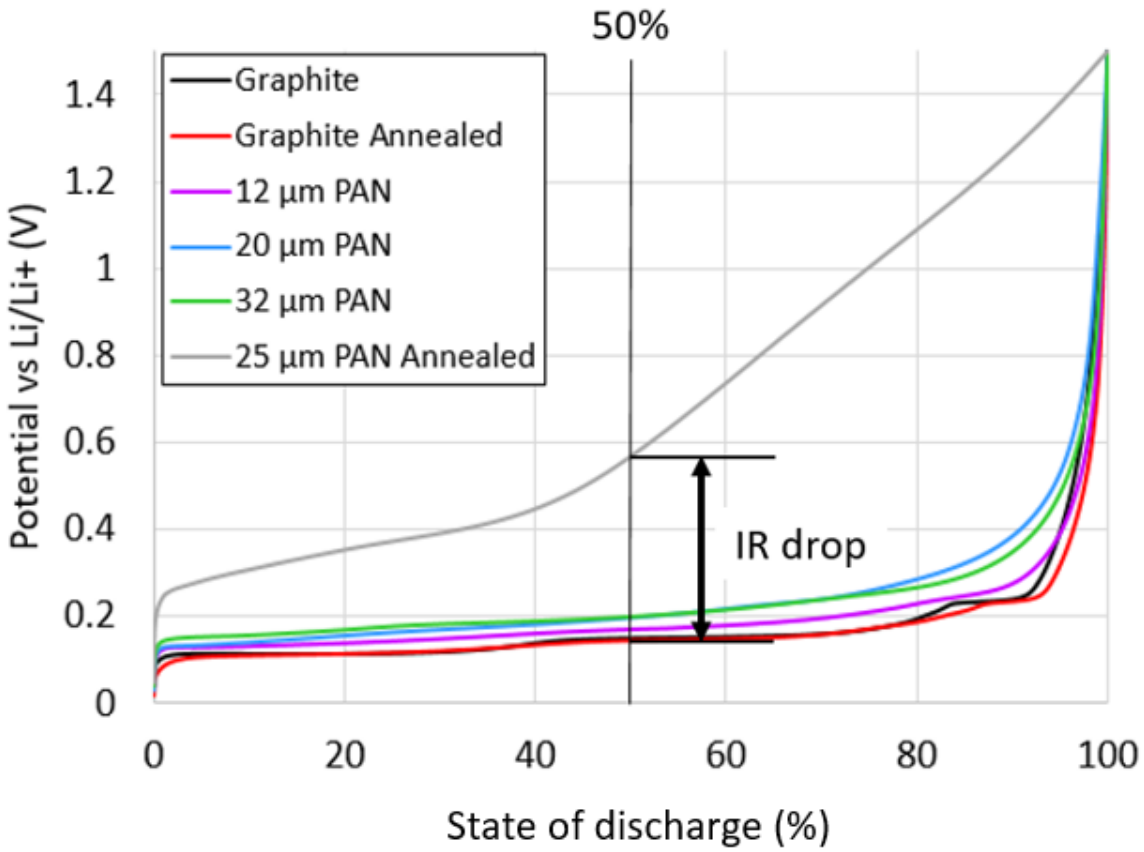

Figure 82: Second discharge half-cycle data for graphite-composite ink electrodes, cycling was performed in a Swagelok cell for 10 cycles at a C-rate of 0.1 C at room temperature. Potentials are plotted against state of discharge for pristine graphite and annealed graphite sample data as well as PAN coated samples of varying thicknesses along with an annealed PAN sample. A line representing 50 % state of discharge as well as the IR drop between the annealed PAN sample and pristine graphite are annotated.

To quantify these resistances, potential data was taken at 50 % state of discharge for each sample as this would characteristically be met with a plateau in the cycling behaviour of a pristine graphite electrode. This was also one of the easiest plateaus to identify in PAN coated samples, with the exception of the annealed PAN sample where no plateau could be observed. The IR drop was simply measured as the difference in potential from pristine graphite to the potential of the PAN coated sample at this 50 % state of charge. These values are represented in Figure 83. A clear upward trend was observed for increasing PAN film thicknesses to IR drops. Figure 83b further included the annealed PAN sample showing a dramatic increase in potential drop by an order of magnitude despite comparable film thickness to other PAN samples.

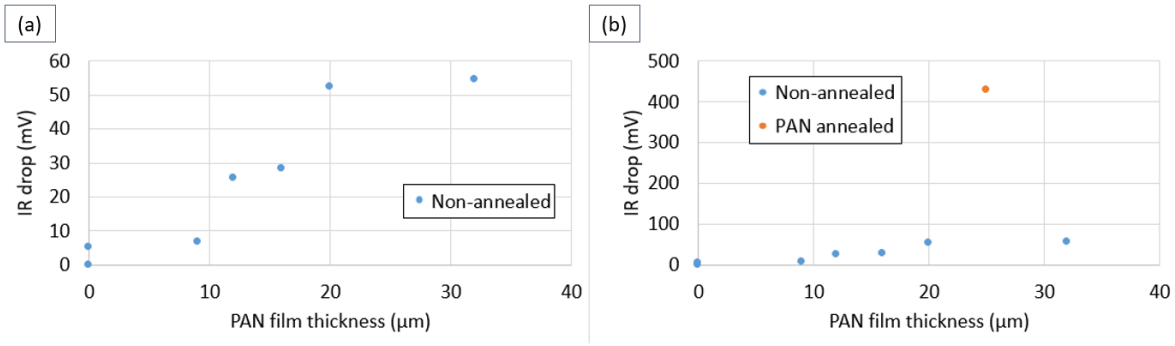

Figure 83: IR potential drop against PAN film thickness for several graphite-composite electrodes. (a) Non-annealed PAN data. (b) Annealed and non-annealed PAN data.

The values obtained for the potential IR drops were further used to make predictions of the discharge capacity of the samples. The shift introduced by the drop was added to the lower potential limit of 5 mV and the capacity of pristine graphite at this shifted potential was taken. This was taken from the total pristine graphite capacity and the remaining capacity was taken as the estimate of capacity. Figure 84 shows the relationship between the expected and actual capacities for the corresponding IR drops. For all PAN coated samples, annealed or non-annealed, actual discharge capacity found during cycling was around 20 % lower than the expected discharge capacity. For the two pristine graphite samples, there was no difference between expected and actual values despite an IR drop. Two inferences can be made from this data. Firstly, IR drops were responsible for a drop in capacity. Secondly, the IR drop was not wholly responsible for capacity loss and around 20 % of all capacity lost is due to other factors. The only difference is the presence or not of a PAN coating. Therefore, additional capacity loss must either be due to degradation caused by the electrodeposition of PAN or a decrease in accessible active material due to complete insulation by the PAN.

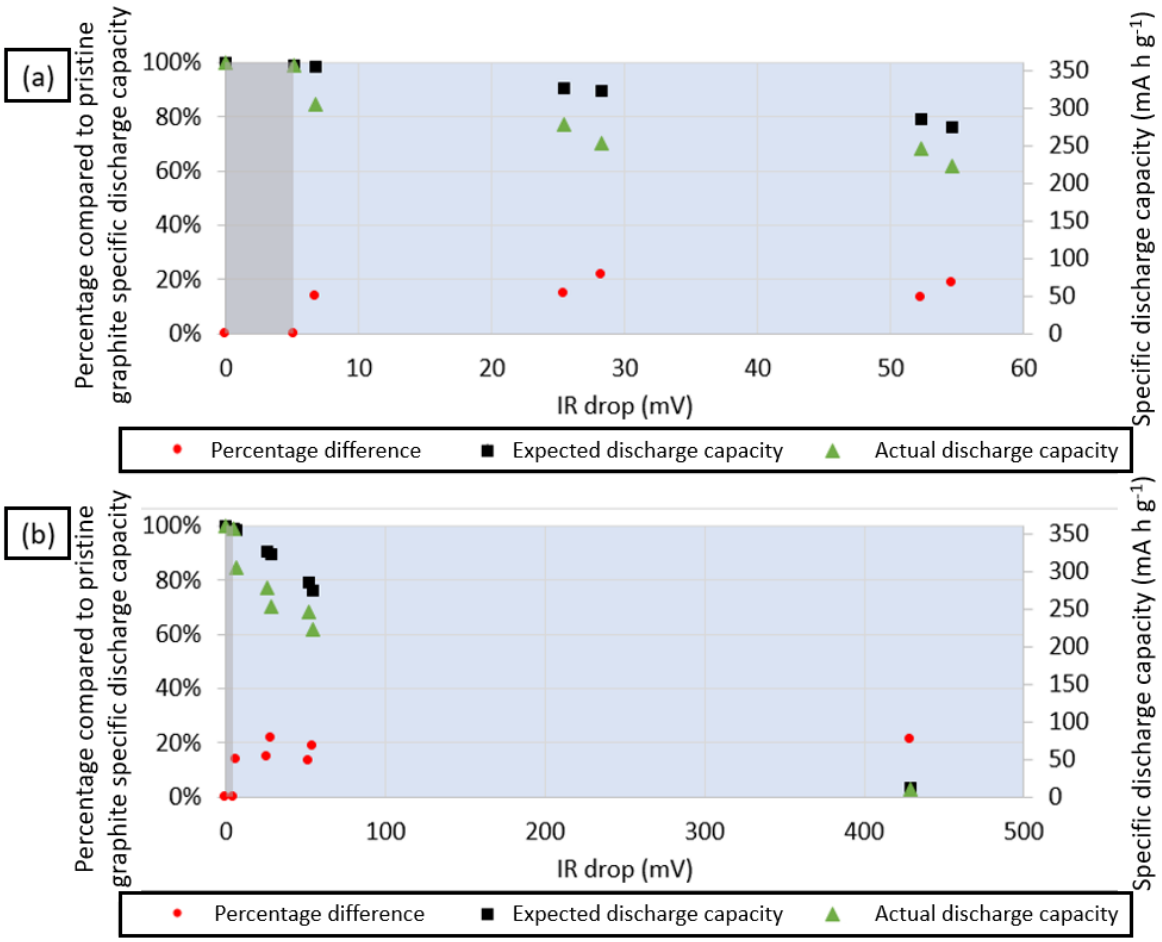

Figure 84: Expected and actual discharge capacities at the end of the second discharge half-cycles against IR drops for PAN coated graphite-composite ink electrodes. Expected data estimated from the capacity lost due to the IR potential shifts on the pristine graphite samples. Data are also given as a percentage of the pristine graphite discharge capacity. The percentage difference between the points of the two data sets is also given. The grey region represents data for graphite samples without PAN coatings and the blue region represents data with PAN coatings. (a) Data for non-annealed PAN samples. (b) Data for annealed and non-annealed PAN samples.

4.3 Elevated temperature studies

Thermal runaway is experienced by lithium-ion cells at elevated temperatures. Hence, to determine if the PAN coating can provide a shutdown response to aid in the prevention of thermal runaway, studies were planned at higher than room temperatures. It was expected that observed responses would occur near to or above the glass transition temperature of PAN at 95 °C [35]. TGA was further used to identify key temperatures where other responses may occur.

4.3.1 Thermogravimetric analysis

To help inform analysis of elevated temperature data TGA was performed on the materials present within the graphite-composite electrodes, see Figure 85. Should any notable changes in cell performance be noticed, this would be compared with any notable changes in the TGA data. Base electrode materials analysed with TGA were: Super C65 carbon conductive additive, PVDF binder, and graphite powder active material. These materials were essential for forming graphite-composite inks. Further analysis was then performed on the electrodeposited PAN samples, which was compared to an industrial PAN standard.

For the most part, there was little to no change for the base electrode materials. Variations in mass for graphite, carbon, and PVDF were all near to 0.1 % for the entire 250 °C range. Results for the PAN standard differed slightly falling by 0.30 % by 75 °C and remaining fairly stable until 200 °C only dropping an additional 0.09 % total. A more significant drop was then seen in the last 50 °C of a further 0.26 %. In total the PAN standard mass fell by 0.65 % by 250 °C.

Compared to the changes for the standards, the drop in mass for the electrodeposited PAN was significantly greater. Trends initially mirror the PAN standard with an initial drop by 0.36 % that plateaus around 75 °C. This continues through the glass transition temperature at 95 °C [35]. However, at 100 °C the trend diverges from the PAN standard and falls from 0.37 % down to 1.11 % at a second plateau at 150 °C. Mass then begins to rapidly drop ending on 9.17 % total mass loss at 250 °C. To avoid significant mass loss and prevent degradation of the battery electrolyte and other materials during half-cell cycling studies a maximum temperature of 120 °C was decided. At 120 °C PAN mass loss for the deposited samples was recorded at 0.49 %.

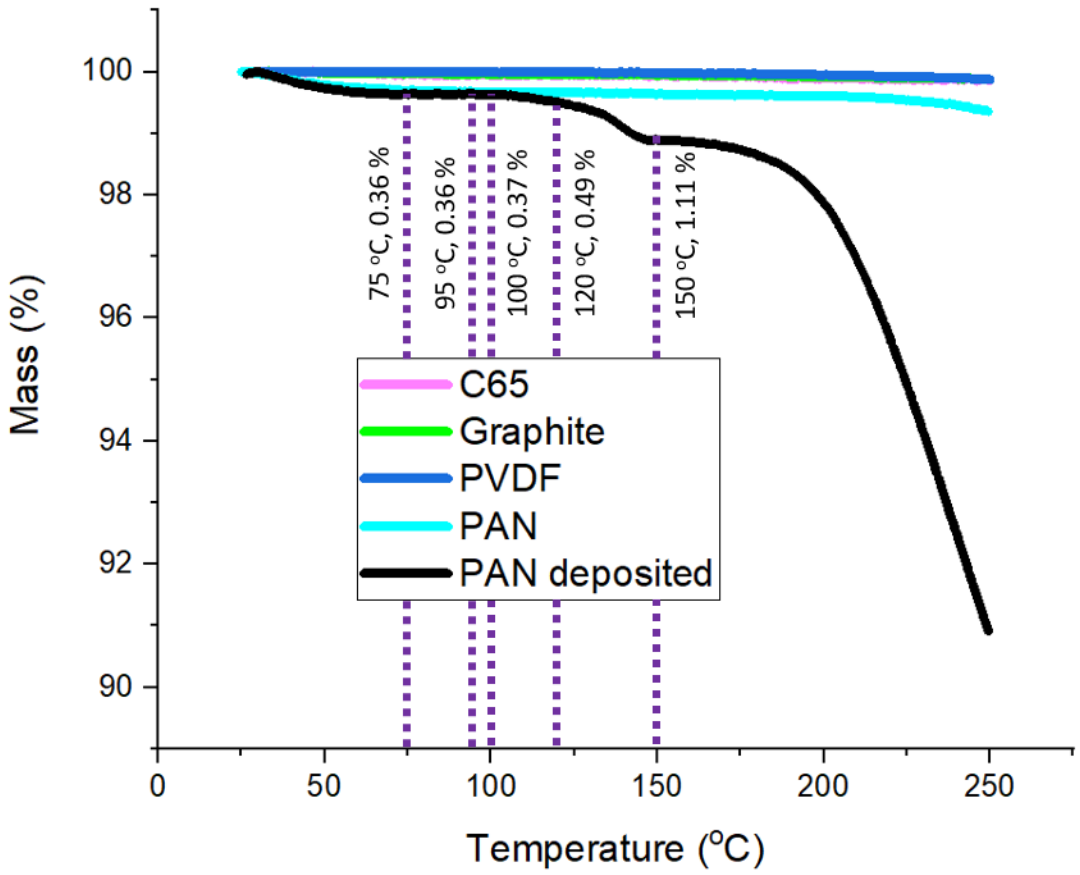

Figure 85: TGA performed on various electrode materials and PAN samples under an argon environment, percentage remaining mass plotted against temperature. In black, PAN electrodeposited onto a copper surface using CA (-3.0 V, 100 seconds). In cyan, commercial PAN powder from Sigma-Aldrich. All other samples used were standard materials direct from suppliers. Studies ramped at 2 °C/minute from 25 °C to 250 °C. The annotated purple dotted line gives key temperatures and mass loss of the PAN deposited sample at each temperature.

4.3.2 Elevated temperature graphite study

The responses and effects on half-cells built with a pristine graphite-composite ink electrode were studied at elevated temperatures. These studies were performed as comparison for PAN coated samples. The cells were cycled for two cycles at a C-rate of 0.1 C at each temperature. The temperatures studied were: 25, 60, 80, 100, and 120 °C.

Figure 86 shows the first cycle discharge capacities and coulombic efficiencies for three identical pristine graphite samples at increasing temperatures. No difference was made in their method of manufacture. Capacities remain consistently high for most temperatures maintaining over 90 % of the theoretical discharge capacity of 372 mA h g^{-1}. For samples 1 to 3, initial discharge capacities

at room temperature were 361, 363 and 371 mA h g^{-1} respectively. Similarly, room temperature studies of pristine graphite in Section 4.2.1 found discharge capacities near 364 mA h g^{-1}. However a significant drop was observed at 120 °C, the discharge capacities for the first and third samples drops to 76 % and 70 % of theoretical, whilst the second sample drops less drastically to 92 %. These drops in active material utilisation from 25 °C to 120 °C were 21 %, 6 %, and 30 % for samples 1 through 3. This drop occurred after all temperature intervals over a total of 10 cycles. Conversely, room temperature measurements in Section 4.2 found only a 1 % drop over 10 cycles for graphite samples. It was immediately obvious that degradation had begun to occur due to the elevated temperature exposure. The most severe degradation occurred after the increase from 100 °C to 120 °C. Indeed, looking at the drop in capacity from 100 °C to 120 °C gave a 16 %, 3 %, and 29 % drop for each of the three samples respectively. Over half of the capacity loss occurs between these two temperatures. The large variability in graphite performance due to thermal degradation at 120 °C was also something to consider when performing these elevated temperature studies.

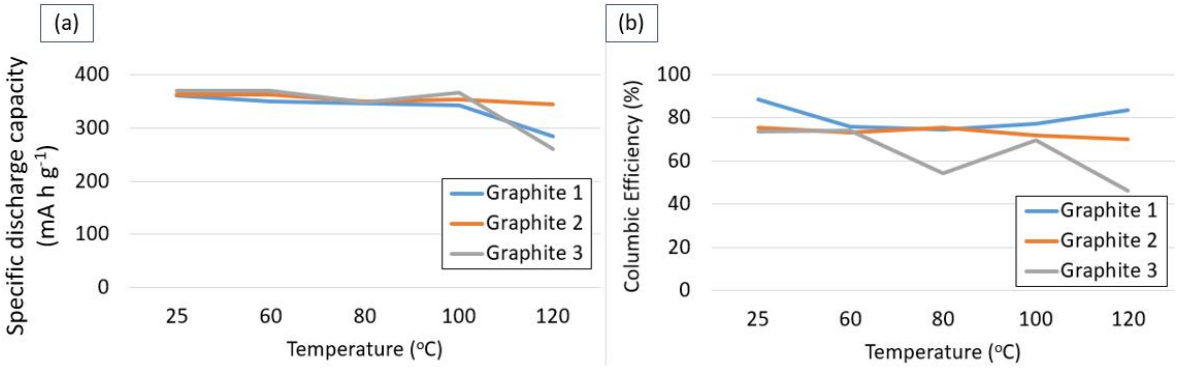

Figure 86: For pristine graphite-composite ink electrodes at increasing temperatures: (a) recorded discharge capacity during the first of two cycles, and (b) recorded coulombic efficiency during the first of two cycles. Cycling was performed in a Swagelok cell at a C-rate of 0.1 C, two cycles were performed at each temperature.

Insight as to why capacity was lost at elevated temperatures was provided by the coulombic efficiencies. Coulombic efficiency for a graphite electrode at room temperature would typically be lower during the first cycle, below 90 %, before climbing to between 98 % and 100 % for all successive cycles. This was due to the formation of an SEI that occurs only during the first cycle, excess lithium-ions were used during the first charge leading to an imbalance in coulombic efficiency. For these elevated temperature studies, however, efficiencies never climbed above 90 % implying a continual loss of capacity between charge and discharge. Previous studies have found that the SEI can breakdown around 69 °C [21], with some reports at temperatures as low as 57 °C [23]. This would mean for 60 °C and above lithium-ions were continuously leached in unwanted side-reactions leading to lower coulombic efficiencies.

Figure 87 shows a photo of a pristine graphite-composite electrode after cycling at elevated temperatures, as well as optical microscopy images from before and after cycling. The photo clearly shows part of the glass fibre separator fused to the electrode surface after cycling. This would have come from the separators within the Swagelok cell. In the optical micropscopy images, there is little obvious difference to the graphite surface itself after cycling with the exception of several glass fibres having fused to the electrode surface. Of note, these fibres did not fuse to the graphite surface after room temperature cycling studies in Section 4.2.1. Hence, the elevated temeperatures were introducing a more destructive enviroment that may be damaging to other materials within the half-cell arrangement.

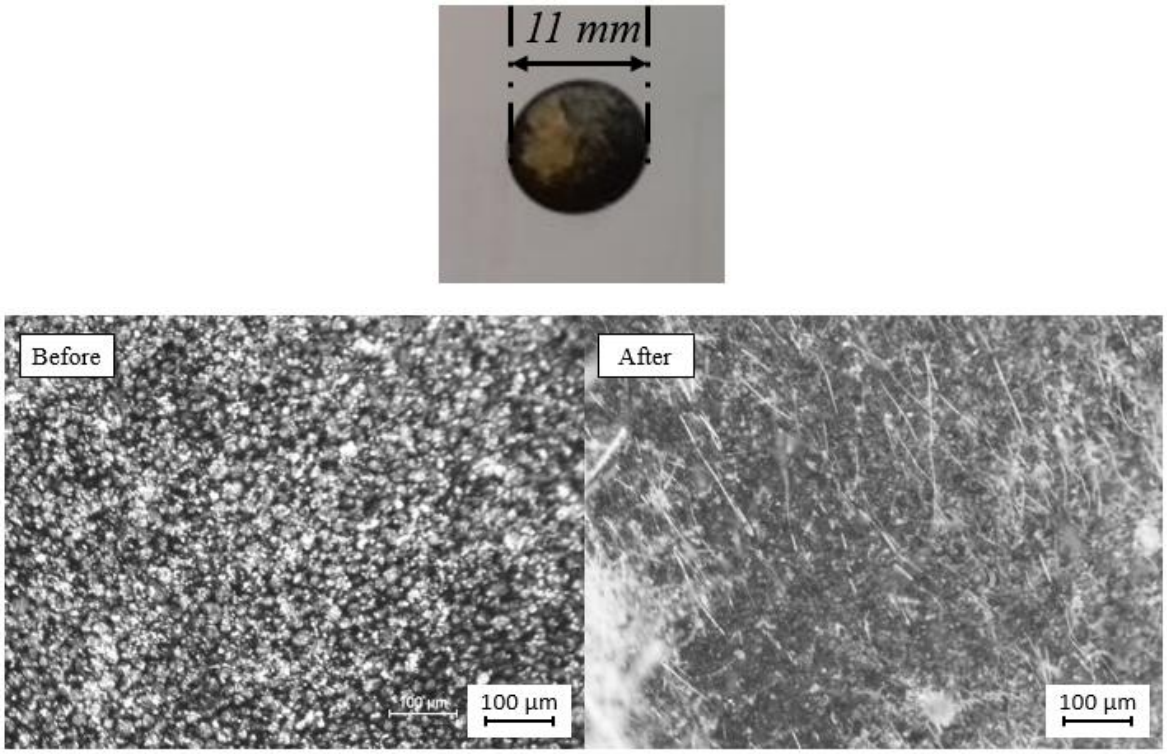

Figure 87: (Top) Photo of an 11 mm disc electrode of a pristine graphite-composite ink after cycling during elevated temperature studies. Part of the glass fibre separator is fused to the upper surface of the electrode. (Bottom) Optical microscopy images for a pristine graphite-composite ink electrode before and after cycling in a Swagelok cell at elevated temperatures at 0.1 C. Images taken at 10X magnification.

4.3.3 Elevated temperature PAN coating study

Studies on PAN coated graphite-composites were performed at elevated temperatures using data on pristine graphite-composites from Section 4.3.2 as a comparison. Studies were identical, performing two cycles at a C-rate of 0.1 C at each temperature. Temperatures were increased from 25 ^{o}C up to 120 ^{o}C in intervals.

Figure 88a, b, and c show performance at each temperature. For these PAN studies the greater the capacity loss at elevated temperatures the better the performance as the effect of any shutdown response was the intended avenue of investigation. An initial increase in capacity was seen for most PAN samples, with a maximum observed at 60 ^{o}C for most. A possible shutdown effect then appeared to begin around 80 ^{o}C with a decrease in capacity. It should be noted that in the pristine graphite samples, represented with 0 µm PAN film in the figures, no significant change in capacity was experienced until 120 ^{o}C. Capacity loss in the samples with PAN films then continues through 100 ^{o}C to 120 ^{o}C. However, it was unclear whether loss at 120 ^{o}C was due to the PAN film or just general loss experienced during the pristine graphite studies. Hence, 100 ^{o}C was considered the most reliable minimum in discharge capacity for these studies. With a glass transition of around 95 ^{o}C [35], there does appear to be a correlation between the polymer transition and the onset of the shutdown effect between 80 ^{o}C and 100 ^{o}C although it was unclear if this was the only cause.

In terms of coulombic efficiency, there was a general downward trend as temperature increased between 80 ^{o}C and 120 ^{o}C. This would imply a more significant portion of the charge during the charge half-cycle was used in unwanted side reactions (e.g. electrolyte decomposition) as temperature increases. The thickness of the film also appeared to play a role, with lower coulombic efficiencies for thicker films at these elevated temperatures. Thicker films would unavoidably have larger amounts of impurities but also greater coverage of graphite at room temperature to prevent SEI formation. Hence, it was unclear if these side reactions will be SEI formation or the effect of impurities in the PAN polymer itself.

Finally, looking at the ratio of capacity at each temperature to the maximum capacity there was no significant difference between pristine graphite samples and PAN coated samples at 120 ^{o}C until thicknesses greater than 18 µm. This is despite capacity loss at 80 ^{o}C and 100 ^{o}C for these thinner samples; thinner samples and pristine samples reached around 70 % of the maximum capacity at 120 ^{o}C. However, for 18 µm and 22 µm capacity had fallen to around 50 % by 100 ^{o}C and below 30 % by 120 ^{o}C. Shutdown was significantly more effective for the 24 µm sample reaching around 30 % at 80 ^{o}C and then near 0 % by 100 ^{o}C implying a complete shutdown of the cell was achieved.

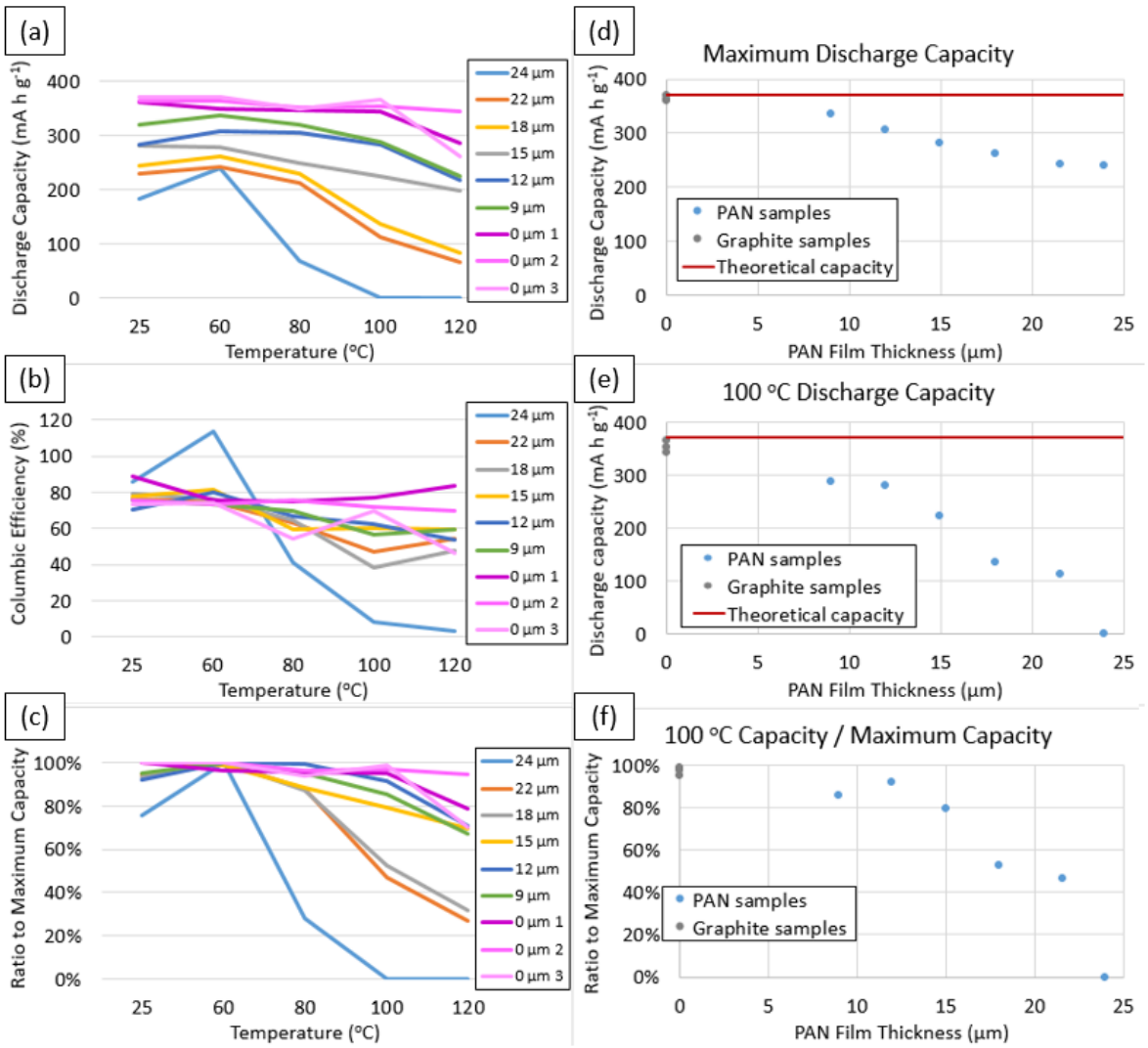

Figure 88: For pristine and PAN coated graphite-composite ink electrodes of varying thicknesses at increasing temperatures. (Left) data at each measured temperature showing: (a) recorded discharge capacity during the first of two cycles, (b) recorded coulombic efficiency during the first of two cycles, and (c) ratio of capacity at each temperature to the maximum capacity during the first of two cycles. (Right) data against PAN film thicknesses: (d) maximum discharge capacity, (e) 100 °C discharge capacity, and (f) ratio of 100 °C discharge capacity to maximum discharge capacity. Cycling was performed in a Swagelok cell at a C-rate of 0.1 C, two cycles were performed at each temperature.

Figure 88d, e, and f show the maximum discharge capacity, the capacity at 100 °C, and the ratio between these two values against film thicknesses. These figures highlight more easily the general downward trend in capacity with film thickness, a trend that was observed almost across all temperatures studied in the previous figures of Figure 88. Loss of capacity with increasing film thickness was significant. Even at the lowest studied film thickness of 9 µm a maximum discharge capacity of only 90 % theoretical capacity was achieved, far below the high 97 % to 100 %

obtained by pristine graphite samples. The more interesting details, however, came from the 100 °C data. Whilst pristine graphite maintained above 90 % capacity the PAN coated samples had fallen by 85 % at 9 µm down to 0 % at 24 µm. The trend appeared almost linear giving a 5 % drop in capacity for every micrometer thickness. In terms of overall performance, the initial capacity was lower for increasing PAN thickness but the effect of the shutdown became greater.

Temperature of shutdown around 80 °C to 100 °C was competitive to other shutdown coatings, with LCO-P3OT materials studied by Ji *et al.* [31] seeing shutdown around 90 °C down to 4 % theoretical. Baginska *et al.* [32] reported on shutdown for graphite coated with PE microspheres at 110 °C, shutdown was incredibly effective for these PE microspheres reporting a remaining 7 % theoretical capacity. Commercial Celgard shutdown separators see shutdown around 130 °C [36]. For the graphite-composites coated with PAN in Chapter 4, capacity fell to under 5 % for samples of 24 µm PAN. Achieving this great a shutdown for films with improved room temperature capacity would be desirable to provide acceptable performance under normal operating conditions.

Figure 89 shows a photo of a PAN coated sample after cycling, as well as optical microscopy images from before and after cycling. The glass fibre separator used as part of the Swagelok half-cell had completely fused to the surface of the electrode and was not possible to be removed without also removing the graphite ink from the copper disc, as shown in the photo. This was in contrast to pristine graphite samples where the separator was able to be removed from the electrode with minimal damage leaving behind only a few glass fibres, see Figure 87. As a result it was not possible to get a clear view of the PAN sample post-cycling using optical microscopy. The more complete fusing of PAN coated samples compared to pristine samples was not only due to the presence of the polymer but also the elevated temperatures as room temperature studies did not find this fusing of separator and electrode, see Figure 77. It has been observed that the polymer chains rearrange at higher temperatures during annealing. It was therefore likely that this rearrangement did occur above the glass transition temperature of 95 °C [35] leading to the separator fusing. The annealed polymers also provided substantially lower discharge capacities; this annealing effect was likely the cause of the lower capacities for non-annealed PAN coated samples at elevated temperatures.

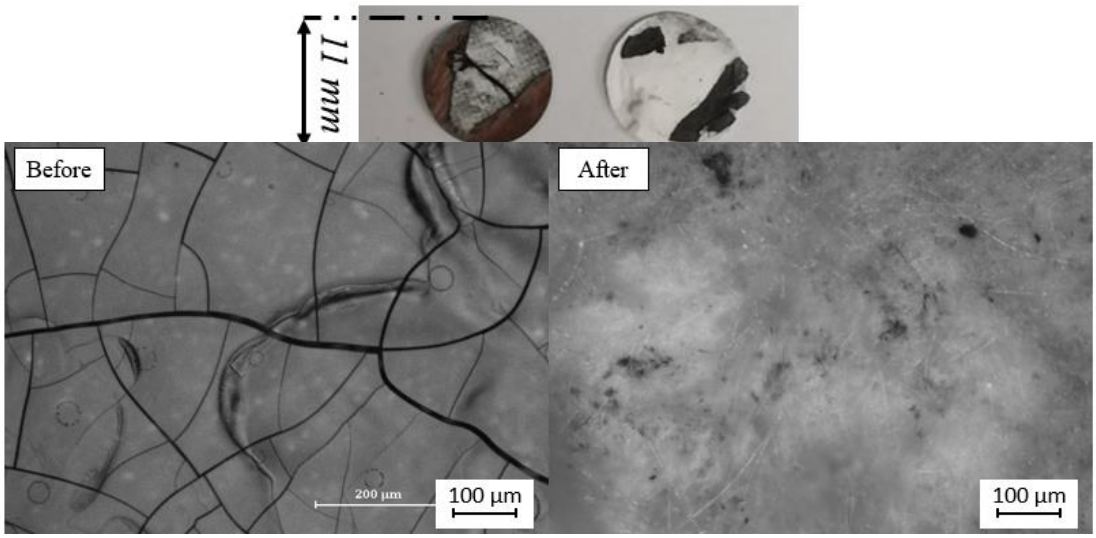

Figure 89: (Top) Photo of an 11 mm disc electrode of a PAN coated graphite-composite ink after cycling during elevated temperature studies. A glass fibre separator is wholly fused to the upper surface of the electrode, the separator on the right has come away from the electrode with pieces of the graphite-composite ink. (Bottom) Optical microscopy images for a PAN coated graphite-composite ink electrode before and after cycling in a Swagelok cell at a C-rate of 0.1 C at elevated temperatures. Images taken at 10X magnification.

4.3.4 Elevated temperature shutdown reversibility

Shutdown responses can be reversible [19] [31] or irreversible [36] [39] [40] depending on if a significant change occurs to the structure of the materials. It was believed that the effect of elevated temperatures would anneal the PAN polymer leading to an irreversible structural change that severely decreases discharge capacity. However, this was initially only tested for samples that were annealed before cycling and not for samples experiencing a shutdown effect due to annealing during cycling. Hence, it was critical to determine if the scenario within the Swagelok cell would lead to a similar irreversible effect. To this end, cells were cycled twice at each temperature interval from 25 °C to 120 °C before being rapidly cooled with a fan and removal from the oven back to 25 °C.

The galvanostatic cycling data for a pristine and PAN coated sample are shown in Figure 90. For the pristine sample, SEI formation was only evident during the first cycle at 25 °C. This was despite the lower coulombic efficiencies shown in Table 18 at every temperature. It was possible that because the SEI layer was broken down continuously at elevated temperatures it would be simultaneously regenerated at any potential lower than 0.7 V. Therefore, the typical SEI shoulder feature would not be present during later cycles leading to greater charge capacities at all

temperatures 60 °C and above. For the PAN coated samples, no apparent SEI formation was observed at any temperature.

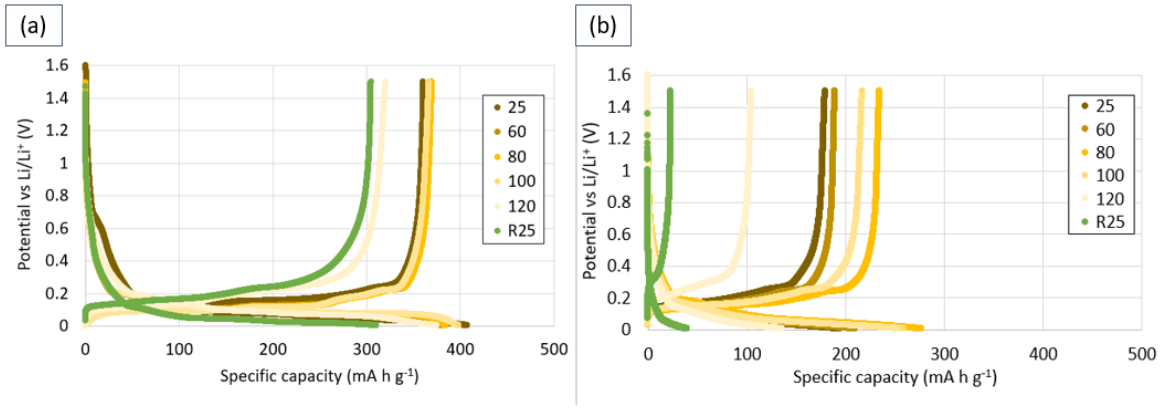

Figure 90: Galvanostatic cycling of a (a) pristine graphite-composite ink electrode and a (b) PAN coated graphite-composite ink electrode performed at a C-rate of 0.1 C in a Swagelok cell. A lithium metal counter/reference electrode was used in LP57 electrolyte (1M $LiPF_6$ in EC/EMC (vol:vol = 1:1)). Cycling was performed at varying temperatures in the order shown in the legend. R25 represents the 'return' to room temperature after elevated temperature cycling.

Table 18: Specific capacity data for elevated temperature studies of a graphite-composite ink electrode and a PAN coated graphite-composite ink electrode. Temperature was increased in increments before returning to room temperature and being cycled once more. 'R25' represent this return to room temperature data. Corresponding coulombic efficiency and active material utilisation percentages for the first cycle at each temperature is also given.

	Temperature (°C)	**25**	**60**	**80**	**100**	**120**	**R25**
Pristine graphite	**Discharge capacity (mA h g^{-1})**	361	367	370	367	320	305
	Charge capacity (mA h g^{-1})	407	380	385	398	375	310
	Coulombic efficiency (%)	88.6	96.7	96.1	92.0	85.5	98.2
	Active material utilisation (%)	97.0	98.7	99.4	98.5	86.1	81.9
PAN coated graphite, 21 µm thickness	**Discharge capacity (mA h g^{-1})**	179	189	234	217	105	23.4
	Charge capacity (mA h g^{-1})	194	210	277	259	135	39.1
	Coulombic efficiency (%)	92.4	90.3	84.8	83.9	77.2	59.9
	Active material utilisation (%)	48.2	50.9	63.0	58.3	28.1	6.30

Figure 91 shows metrics for both samples using data from Table 18. A similar trend was followed for discharge capacity and coulombic efficiency to other elevated temperature studies. Figure 91a shows the discharge capacity at each temperature. For the pristine sample, no significant change in discharge capacity occurred until 120 °C; active material utilisation fluctuated between 97 % and 99 % before falling to 86 %, a fall of 13 % between 100 °C and 120 °C. After returning to room temperature capacity was slightly lower than at 120 °C. This was due to continued degradation as the cell passes through elevated temperatures on cooling. The degradation of graphite was not reversible simply by reducing temperatures. Only 82 % utilisation remained upon returning to room temperature at the second 25 °C, this was 4 % lower than at 120 °C.

Discharge capacity of the PAN coated sample was much lower upon returning to 25 °C. There was an initial climb between 25 °C to 80 °C of 48 % to 63 %; a different behaviour than experienced for thicker PAN samples in Section 4.3.3 where capacities fell at 80 °C. Capacity began to fall at 100 °C down to 58 % before suffering a more catastrophic shutdown at 120 °C down to 28 %. This value was 20 % lower than the initial and 35 % lower than the maximum material usage, far greater losses than the pristine graphite. Upon returning to 25 °C capacity continued to fall leaving 6 % remaining after cycling. This was a further 22 % loss during cooling. Performance had not returned to the initial values and was even lower than at 120 °C, implying an irreversible shutdown effect.

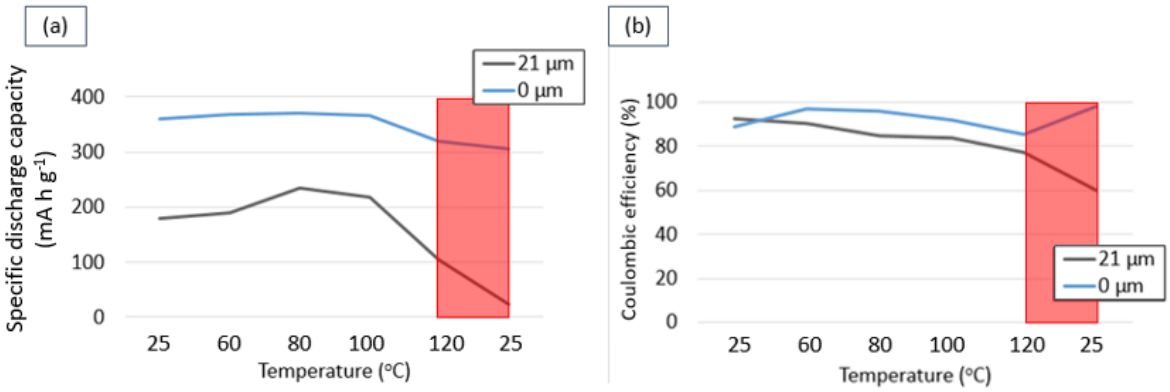

Figure 91: Data for a pristine graphite-composite and a 21 µm PAN coated graphite-composite at each temperature interval. (a) Discharge capacity at each interval and (b) coulombic efficiency at each interval. The red highlighted section is the trend from 120 °C to the return at the second 25 °C after elevated temperature cycling.

Figure 91b shows coulombic efficiency for both samples. For pristine graphite, a similar trend to other elevated temperature studies was observed, starting at 89 % at room temperature due to SEI formation. Efficiencies are higher for 60 °C and 80 °C from 97 % to 92 %, but this was below the 98 % seen for successive cycles at room temperature. After returning to room temperature the efficiency was above 98 %. This implies further SEI formation did not occur despite breakdown at 120 °C. It was possible the SEI self-regenerated; however, the direct cause was not known.

Of more interest was the behaviour of the PAN coated samples. Coulombic efficiency fell with each temperature increment, from 92 % at 25 °C down to 77 % at 120 °C. This lower efficiency at elevated temperatures was in line with values seen for annealed samples at room temperature. Annealed samples led to lower efficiencies, this implies an annealing process has occurred for the PAN coated samples. Initial coulombic efficiencies for room temperature studies were typically below 50 % and it can be seen that upon returning to room temperature an efficiency of 60 % was obtained. Contrast this with pristine graphite that returned to its initial efficiency after cooling.

4.4 Conclusion

In this chapter, comparisons were made between the cycling performance of graphite-composite ink electrodes with and without PAN film coatings. The aim of the research was to produce a PAN coated graphite material that had comparable performance to pristine samples under normal operating conditions and also showed potential shutdown applications at elevated temperatures.

Room temperature graphite studies showed standard graphitic features. SEI formation was observed at 0.7 V leading to lower coulombic efficiency during the first cycle. Several plateaus were observed in all cycles linked to the stages of lithium intercalation. Capacities were promising showing 98 % of the theoretical capacity of 372 mA h g^{-1}, which remained stable over a 10 cycle period. Similar performance was achieved for annealed graphite inks showing that any change at elevated temperatures was unlikely due to the breakdown or change of the graphite material.

Following pristine graphite studies, several PAN film morpholgies were tested: clear, white, clear annealed, and white annealed. The distinction from clear to white films was the manufacturing procedure, whilst annealed versions were produced by heating films prior to cycling to seal any cracks in the film surface. Interestingly, clear films appeared to seal their cracks during cycling implying wetting by the electrolyte under an applied potential facilitated chain movement. Conversely, little change was observed in the surface of annealed PAN films. Only clear PAN was promising for electrode applications as all other samples gave below 5 % theoretical capacity.

The low capacity of annealed clear PAN compared to non-annealed clear PAN was promising for potential shutdown effects. If exposure to high temperature can produce the annealing effect within the cell during cycling then low capacities could be achieved upon raising the temperature. Non-annealed clear PAN coated graphite was subsequently given more attention than other PAN films. However, several changes were noticed in performance compared to pristine graphite.

Firstly, it was difficult to observe many of the graphitic features, such as SEI formation and several of the stages of intercalation. Indeed, the only indication that SEI formation did occur was the lower coulombic efficiency during the first cycle. Secondly, discharge capacity decreased with increasing film thickness. Capacity seemed to decrease by 5.63 mA h g^{-1} per µm. A tentative link was made between uncompensated resistances and this loss in capacity [154] [155], which appeared to correlate. However, around 20 % of the capacity lost for all PAN samples was not accounted for when purely looking at the IR drops of the samples. Thicker films not only had lower discharge capacity, but the performance was also more variable and fluctuated seemingly randomly. Sometimes this fluctuation was over 30 % capacity over the 10 cycles. These greater resistances for thicker films and the variable performance were likely a result of lessened electrolyte infiltration within the PAN film, which was not present in the absence of PAN.

Room temperature studies suggested thinner films were better for performance at normal operating conditions. However, thicker films showed stronger shutdown effects at elevated temperatures with complete shutdown first observed for a 24 µm PAN thickness sample. This sample also showed around 50 % theoretical capacity under normal operating conditions, which was not ideal for a practical cell. Some effect was still observed for thinner films on the shutdown of the cell and may still provide a safety benefit to prevent thermal runaway.

Temperature of the shutdown behaviour was promising. TGA measurements showed deposited PAN films were stable up to 120 ^{o}C. The onset of the shutdown effect was around 80 ^{o}C and was most effective at 100 ^{o}C. This was likely a response to glass transition of PAN at 95 ^{o}C [35] and not to any effect on the graphite as pristine sample capacity was stable until 120 ^{o}C. This shutdown response was also irreversible, with PAN films showing a drastic capacity decrease upon returning to room temperature. Upon returning to room temperature the coulombic efficiency of the non-annealed clear PAN films was comparable to annealed clear PAN samples under normal operating conditions, implying an annealing process had occurred during cycling at elevated temperatures. Coulombic efficinecies for pristine graphite did not show any significant change upon returning to room temperature. This supports the idea that the PAN films had annealed during cycling and this was the reason for lower coulombic efficiency upon returning to normal operating temperatures.

In conclusion, thinner films gave better performance at normal operating conditions. However, thicker films proved better at shutdown receiving far lower capacity between 80 ^{o}C and 100 ^{o}C. Further research into improving capacity for thicker films could alleviate this issue, developing the pore structure of the PAN to enhance ambient temperature performance. It may also be of interest to examine PAN coated electrodes within a half-cell without a separator as the film may be able to perform this role, potentially lowering internal resistance and improving capacity.

Chapter 5 Percolation composite studies

Studies in the previous chapters investigated the production and use of a polymer PAN film for potential PTCR application. These films restrict the flow of ions to the electrode surface. This chapter focuses on an alternative application of polymers to restrict electron transport by taking advantage of percolation effects.

Composite percolation materials were manufactured using a high thermal expansion polymer matrix and a low electrical resistivity filler. Expansion of the matrix with temperature has been reported to break the conductive pathways formed by the filler, resulting in a PTCR [19] [33] [51]. By tailoring the proportion of filler to matrix, resistivity of the composite and intensity of the PTCR effect can be controlled. Any PTCR observed should occur near to transition temperatures of the polymer matrix, the point at which the greatest change in thermal expansion should be observed. This transition may take the form of a glass transition temperature or a melting point.

Several different variations of matrices and fillers were produced, all selected for their stability within a lithium-ion system. PAN composites were produced to compare the performance of a percolation-binder PAN to the PAN films in previous chapters. PAN would also be the only material experiencing a glass transition at 95 ^{o}C [35], within the measured temperature range, providing insight to the effectiveness of such polymer transitions for PTCR purposes. The other films were PVDF, HDPE, and LDPE. LDPE [19] and HDPE [52] [92] have previously been examined as percolation-composites, experiencing a melting point and PTCR across a large range from 82 to 140 ^{o}C depending upon polymer density. PVDF percolating-composites are less well documented but should experience a melting point at 155 to 185 ^{o}C [30].

Filler materials were carbon and TiC. Varying the filler materials can alter transition temperatures of polymer-composites [33] [55]. As such, composites of each of the polymers were made with both fillers to study potential impacts on performance. Transition temperatures were measured using DSC measurements whilst SEM was performed to identify any physical changes due to varying filler materials. Resistivity measurements were performed at room temperature on all composite variations, with the most promising compositions then being studied at elevated temperatures for any observable PTCR effect. Due to restrictions imposed by the COVID-19 pandemic, SEM and DSC training and usage was limited and so measurements within this chapter were performed by super users. SEM was performed by Dr Tauqir Nasir, DSC by post-graduate research student Wilma Anyfanti, data analysed by the author of this theses post-graduate research student Jonathan Allen.

5.1 Experimental

Percolation composites made from a polymer matrix and a conductive filler were produced either using solvent cast ink methods or through molten casting. These composites then underwent physical characterisation in the form of DSC (to detect any changes to transition temperatures) and SEM (to observe morphologies). This physical charcterisation was essential for understanding later observed PTCR effects. Resistivity studies were then performed in a standard Swagelok arrangement to provide a constant observable electrode area. These Swageloks contained the percolation composites that were studied at room temperature to identify the percolation threshold. Elevated temperature studies were then performed on the most promising composites to identify a PTCR effect. A brief study was then performed on a practical lithium-ion half-cell arrangement to study the capability of the percolation composites under normal operating conditions. These Swagelok arrangments were detailed in Chapter 2.

5.1.1 Solvent cast composites

PAN and PVDF polymers were both made into composites with either Super C65 carbon black powder (supplier: Timcal) or TiC nanopowder (supplier: Sigma-Aldrich) using a solvent cast method [19] [3] [96]. As such, four unique sets of materials were prepared: PAN-C, PVDF-C, PAN-TiC, and PVDF-TiC. Taking advantage of the solubility of both PAN (supplier: Sigma-Aldrich) and PVDF (supplier: Solef) in NMP, thin composite films of µm thicknesses were produced.

Preparation of the composites was as follows:

1. Polymer powder was dissolved in NMP such that the solution was 10 % by weight of polymer. Typically 10 g of material was made at a time.
2. The desired ratio of conductive filler and polymer matrix was weighed and mixed. Typically 1 g was mixed in total.
3. 500 µL NMP was added to the mixture; PAN and PVDF are both soluble in NMP so increasing amount of solvent was used to reduce viscosity of the mixture for easier mixing and casting.
4. The mixture was stirred for 24 hours at room temperature at 100 rpm; performed on an IKA™ Digital Color Squid Magnetic Stirrer with Fisherbrand™ Magnetic Stirring Bars (PTFE, 12x4, 5mm cylindrical, small pivot ring). This produced a composite ink.

5. The ink was spread onto a polished copper foil surface. Spreading was performed using a K Hand Coater bar with 1.27 mm wire diameter and a close wound structure (RK Print Coat Instruments). Ink areas varied depending on volume of the ink due to varying ratios of matrix to filler.
6. The ink was left to dry in a fumehood at room temperature for 72 hours.
7. Electrodes were then cut to 11 mm diameter with a precision punch (EL-CELL, EL-Cut).

The ratio of filler to polymer was varied from 0 % by weight and up in values of 10 % until a percolation threshold was observed where resistivity turned from polymer insulating to filler conductive. Smaller steps of 5 % were taken around the percolation thresholds when seen as valuable for data collection.

5.1.2 Molten cast composites

HDPE (supplier: Goonvean Fibres) and LDPE (supplier: Goonvean Fibres) polymers were not soluble in NMP solvent and so molten cast methods were investigated to produce composites with these polymers [33] [52] [55]. Both were made into composites with either Super C65 carbon black powder or TiC nanopowder producing four unique sets of materials: HDPE-C, LDPE-C, HDPE-TiC, and LDPE-TiC. HDPE and LDPE were sourced from Goonvean Fibres Ltd, which came with melting points of 124-136 ^{o}C and 98-113 ^{o}C respectively in the specifications [156]. As such, molten casting was performed at 130 ^{o}C. Thin composite films of μm thicknesses were then produced by compression rolling with a glass pin at 130 ^{o}C.

Preparation of the composites was as follows:

1. A mixture of conductive filler and polymer matrix powders was made to the desired ratio of weights. Typically 1 g was mixed in total.
2. Powders were stirred at room temperature at 500 rpm for 24 hours with a magnetic stirrer. This produced a composite powder.
3. Further mixing was then performed using a pestle and mortar for 20 minutes each sample.
4. Copper foil was heated to 130 ^{o}C on a hotplate with a temperature controller.
5. The composite powder mixture was applied to the copper foil and allowed to melt for 5 minutes. This was then rolled with a glass pin until a thin film was obtained.
6. Following this, the film was left to cool for 2 hours. The edges of the copper foil were secured to prevent warping on cooling.

7. Electrodes were then cut to 11 mm diameter with a precision punch (EL-CELL, EL-Cut).

Similar to solvent cast methods, ratios of filler to polymer were increased in increments of 10 % by weight until a percolation threshold was observed. Smaller steps of 5 % were taken around the percolation thresholds when seen as valuable for data collection.

5.1.3 Differential scanning calorimetry

Differential scanning calorimetry (DSC) is a method of thermal analysis similar to TGA. However, instead of recording mass change with increasing temperature, the amount of heat required to increase the temperature of a sample is measured as a function of temperature. This is done by comparing the rate of heat flow of a test sample and a known reference. The reference and sample are held at near to the same temperature and temperature is ramped up and then down either once or through many cycles. This technique is used to analyse material properties such as: glass transition temperature, melting, crystallisation, specific heat capacity, cure processes, purity, oxidation behaviour, and thermal stability.

DSC measurements were performed on a Discovery DSC instrument system. This was used for PAN, PVDF, HDPE and LDPE samples mixed with varying proportions of carbon or TiC. Material was scraped off the copper foil it was cast onto using a spatula into an alumina crucible. The DSC chamber was then purged with N_2 and temperature controlled using liquid N_2 and heating elements. Temperature was ramped at 20 ^oC/minute from 20 ^oC to 200 ^oC and then cooled at 20 ^oC/minute from 200 ^oC to 20 ^oC. Specific heat flow was then plotted against temperature. This was repeated for two cycles and transition temperatures identified and compared.

5.1.4 Scanning electron microscopy – percolation sample preparation

The basics of SEM were explained in Chapter 2. However, the preparation of samples in this chapter is detailed here. 11 mm diameter electrodes of the polymer-composites deposited onto copper foil were dipped into liquid N_2. The rapid cooling would ensure the samples were below their glass transition temperatures making them more brittle. Brittle materials fracture and break more cleanly with minimal deformation due to plastic ductile behaviours. After cooling in liquid N_2 the samples were cut in half using a pair of scissors and the two halves were collected.

SEM images were taken of the cross-sections of one half of the percolation composites along the break line of the samples. These images provided insight into how the filler material was arranged within the polymer matrix. Images were captured using a FEI/Philips XL30 FEG ESEM with Thermo Fisher Scientific Ultra Dry 10 mm^2 EDX. Samples were stuck to stubs with double-sided conductive carbon tape before being mounted onto the SEM sample holder and loaded into the microscope chamber. Images of the sample topography were captured using secondary electron imaging.

5.1.5 Resistivity measurements

Resistivity is a fundamental property of a material that measures how strongly it resists the flow of electric or ionic current. It is useful for comparing like materials with differing lengths and areas. The equation is:

$$\rho\ (\Omega\, m) = \frac{R\ (\Omega).A\ (m^2)}{L\ (m)}$$

Where ρ is resistivity, *R* is resistance of the electrode, *A* is surface area, and *L* is length. Electrodes were punched to 11 mm diameter and assembled within Swagelok cells. For the case of the electrode measurements within this chapter the geometric values represent the area of the electrode *A*, 11 mm diameter giving 95 mm^2, and the thickness of the films L of the composite electrodes not including the copper foil. Film thicknesses were measured using an External Digital Micrometer (0-25 mm/0-1 inches, RS Components) with an absolute uncertainty of ± 1 µm. Potentio electrochemical impedance spectroscopy (PEIS) measurements were taken to find resistance values of polymer-composites.

PEIS is a method for calculating resistance and capacitance values of components within an electrical system by measuring the impedance response over a range of frequencies to perturbations of an applied voltage. An electrical system will often have conductive and inductive elements, introducing conductive or inductive loading. The resulting effect is a phase difference between the voltage and current where one leads or lags the other. Mathematically, this is represented by complex numbers using Euler's formula, see Figure 92. Impedance is the complex form of the circuit element resistance, defined by both real (Z') and imaginary (Z'') parts.

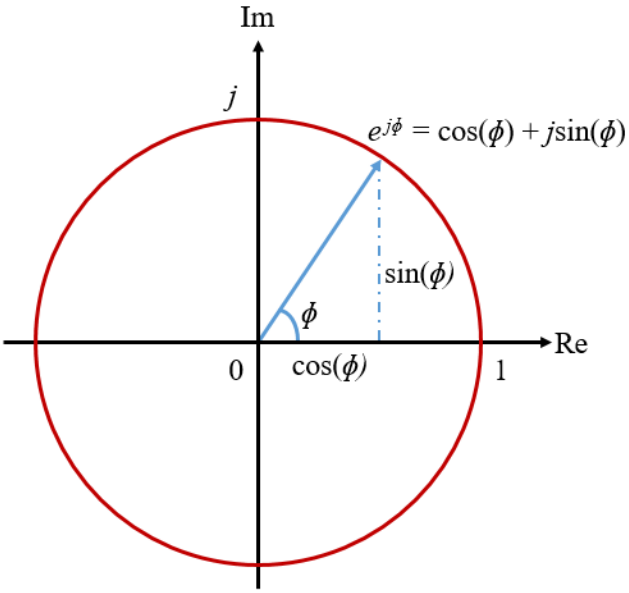

Figure 92: Phase diagram representation of Euler's formula.

An oscillating sinusoidal potential is applied across the system and the resulting current is recorded. Impedance is then calculated using the following equations:

$$E_t = E_0 exp(j\omega t)$$

$$I_t = I_0 exp(j(\omega t - \phi))$$

$$Z(\omega) = \frac{E}{I} = Z_0 exp(j\phi) = Z_0(\cos\phi + j\sin\phi)$$

Where *E* is the potential (sometimes represented by *V*), *I* is the current, *Z* is the impedance, ωt is the angular frequency multiplied by the time which gives a phase angle, ϕ is the phase difference between the current and voltage angles.

Impedance spectra can be represented by a Bode plot or the more common Nyquist plot. A Nyquist plot shows $-Z_{im}$ against Z_{Re} and is most commonly used to identify distinctive patterns and shapes corresponding to values of resistance and capacitance. Electrical components measured using PEIS can be modelled by resistors, capacitors and inductors in series or parallel. The elements present will have a characteristic effect on the plots. A resistor in series will shift the plot to the right by its resistance, *R*, and a capacitor in series will create a line vertically upwards allowing capacitance, *C*, to be found, see Figure 93. This is because capacitors are -90° out of phase, which is represented by a vertical imaginary impedance, whilst resistors have no frequency dependence. The equations for capacitive and resistive impedance are respectively:

$$Z_c = \frac{1}{j\omega C} \qquad Z_R = R$$

As a result, resistance values can be determined by looking at the intercepts with the real axis.

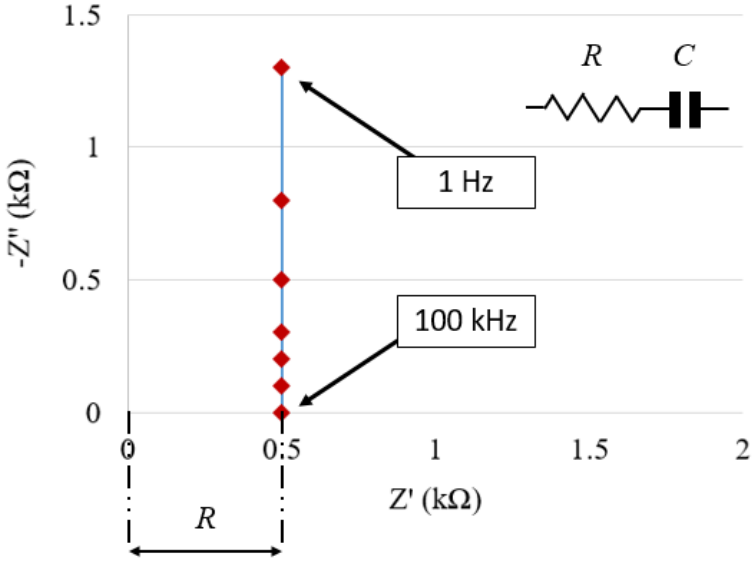

Figure 93: Typical Nyquist plot for a resistor and capacitor in series.

A resistor and capacitor in parallel will have a more interesting effect. A semi-circle is created where the maximum is equal to the time constant $\tau = RC$, see Figure 94. This difference is because the impedances of components in series are additive:

$$Z_{Total} = \sum_n Z_n$$

However, in parallel the admittances of the components is additive:

$$Z_{Total} = \sum_n Y_n \qquad \frac{1}{Z_{Total}} = \sum_n \frac{1}{Z_n}$$

A parallel RC circuit is therefore expressed by:

$$Y_{RC} = \frac{1}{R} + j\omega C = \frac{1+j\omega RC}{R} \qquad Z_{RC} = \frac{R}{1+j\omega RC}$$

It can be seen that at zero frequency, the impedance tends towards the resistive value *R*. The whole relationship is represented on a Nyquist plot with a high frequency intercept at the origin and a low frequency intercept at *R*. The maximum of the semicircle is associated with a frequency relating to the inverse of the RC time constant:

$$\frac{1}{\tau} = \frac{1}{RC} = 2\pi f$$

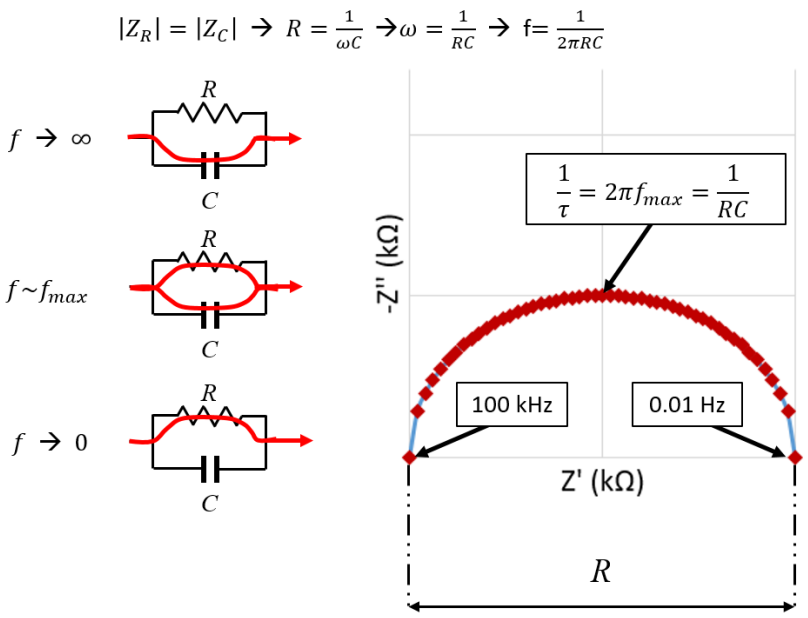

Figure 94: Typical Nyquist plot for a resistor and capacitor in parallel.

In an electrochemical system, several features can be observed corresponding to different materials and structures. This can be modelled as several components and parallel arrangements in series. An example of this can be seen in Figure 95. Each semi-circle corresponds to a different parallel RC combination appearing in order of decreasing relaxation frequency from left to right. Each intercept with the real axis corresponds to an R value; semi-circles may need to be extrapolated as they often overlap and do not meet the axis. The final 90° line corresponds to the capacitor in series.

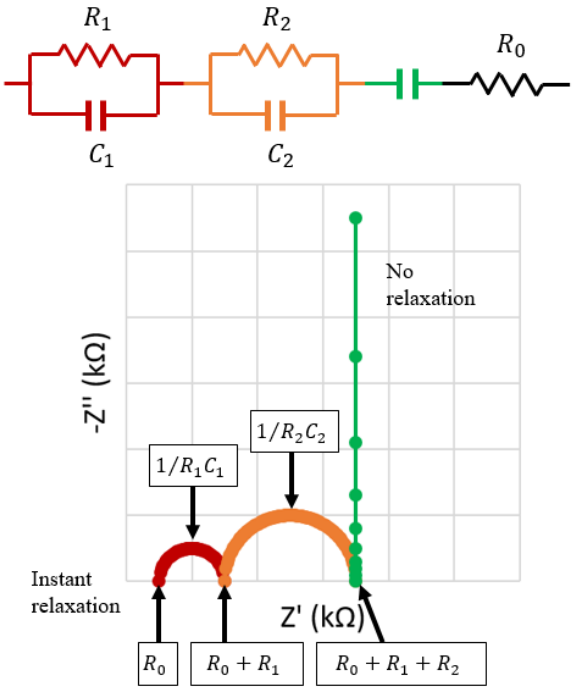

Figure 95: Typical Nyquist plot from several resistor and capacitor components in parallel and series arrangements.

PEIS measurements were performed using the SP-150 potentiostat with EC-Lab software to find the resistivity of polymer-composites. PEIS measurements were taken between 200 kHz and 100 mHz at 10 mV sinus amplitude. Initially measurements were made for the full range of conductive filler ratios for: PAN-C, PVDF-C, HDPE-C, LDPE-C, PAN-TiC, PVDF-TiC, HDPE-TiC, and LDPE-TiC. This was done to identify the percolation threshold where resistivity transitions from the insulating polymer values to the conductive filler values. Ratio values around identified percolation threshold regions were then taken and resistivities were measured at elevated temperatures to identify a PTCR. This was also performed for a copper disc without polymer-composite to determine the R_0 value, this was subsequently subtracted from the resistance of the percolation composites to find the resistance of the composite without the resistance of wires, the copper disc, and other components other than the material being studied.

The polymer-composite sample to be measured was placed between the two current collectors in a Swagelok arrangement, detailed in Chapter 2. Polymer-composites on copper foil were punched to 11 mm diameter to fit the Swagelok.

5.1.6 Elevated temperature resistivity studies

A Genlab classic oven from the laboratory range (Agar Scientific, MINO/6) was used to achieve elevated temperatures for PTCR studies, the setup of which was explained in Chapter 2. Measurements were performed similar to room temperature studies using PEIS on a SP-150 potentiostat with EC-Lab software to find the resistivity of polymer-composites. PEIS measurements were taken between 200 kHz and 100 mHz at 10 mV sinus amplitude.

The selected elevated temperature samples would be placed in an assembled Swagelok and heat treated at 200 ^{o}C for 12 hours prior to elevated temperature studies, above the transition temperatures of interest for PAN, PVDF, HDPE, and LDPE. This was done to encourage polymer deformation within the Swagelok at temperature prior to PEIS measurements. Polymer deformation will occur at elevated temperatures without prior treatment, which can lead to unwanted variations in resistance during measurements.

For PEIS measurements, temperatures were increased in increments and a resistance reading performed. The temperature would be held at each point for 15 minutes to ensure uniform temperature within the Swagelok. PTCR responses were identified and the strength of said responses compared. The temperature intervals measured are shown in Table 19. These temperature values were chosen to fall as closely to the transition temperatures of the polymers

as possible whilst maintaining a reasonable number of cycles for each sample. The transition temperatures aimed for were the melting points of PVDF [30], HDPE [156], and LDPE [156] occurring around 155-185 °C, 124-136 °C, and 98-113 °C respectively, and the glass transition of PAN occurring at 95 °C [35]. Maximum resistivity should occur near to these transition points. PTCR intensity was then simply calculated using the following:

$$PTCR\ intensity = \frac{Resistivity\ at\ elevated\ temperatures}{Resitivity\ at\ room\ temperature}$$

Table 19: Temperature increments used during elevated temperature studies of percolation composites.

Cycle number	1	2	3	4	5	6	7	8	9	10	11	12	13	14	15	16
Temperature (°C)	25	40	60	80	90	100	110	120	130	140	150	160	170	180	190	200

5.2 Room temperature resistivity measurements – percolation effect

The percolation effect is the transition from an electrically insulating to an electrically conducting behaviour. This is seen in polymer-composites as ratio of conductive filler to insulating matrix is increased until the conducting behaviour of the filler takes priority. This results in a transition region, see Figure 96. The three regions of resistivity are from region I to region III [55]: polymer insulating as distance between filler particles is too great, conduction via quantum tunnelling between particles, and conduction via an extensive conductive filler framework. It is the transition between region II and region III where the percolation threshold exists. At this threshold any small changes in filler content creates a drastic change in resistivity, which can be caused by a thermal expansion of the polymer matrix that subsequently breaks down the conductive framework [33]. Hence it is the percolation threshold that is of interest in creating a PTCR response.

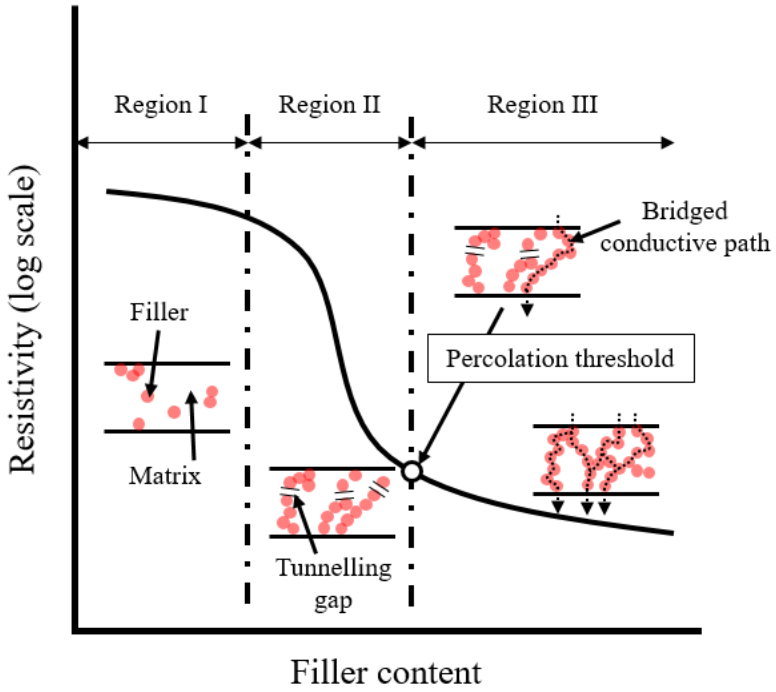

Figure 96: Schematic illustrations of the general percolation curve and the presumptive cluster structure of conductive fillers. Figure adapted from: [55].

Resistivity measurements were performed on the polymer-composites at increasing filler contents to identify where this percolation threshold would occur. The choice of filler and the shape of the particles is crucial on the resistivity performance also. Hence, large discrepancies may be seen in the percolation threshold region when changing filler from carbon particles to TiC particles.

5.2.1 Polymer-carbon composites

Easily identifiable percolation thresholds were observed for resistivity measurements on all polymer-carbon composites, see Figure 97. This can be easily seen from the averages of the resistivity data where PAN-C, HDPE-C, and LDPE-C experienced a threshold around 25 % whilst PVDF required a lower carbon proportion at 15 %.

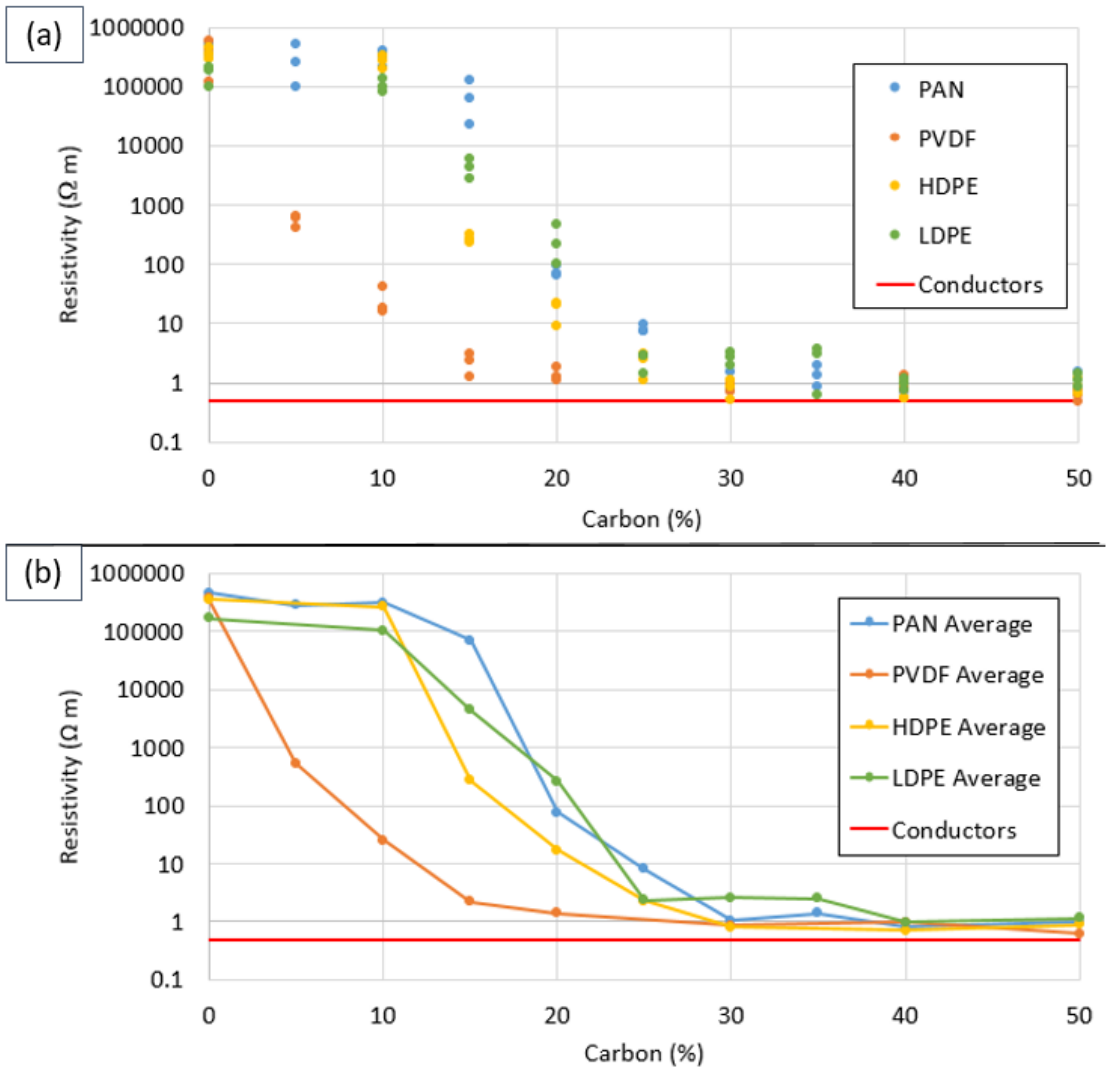

Figure 97: Room temperature resistivity measurements for various polymer-carbon composites at varying carbon filler content. Polymers are: PAN, PVDF, HDPE, and LDPE. A red line is included representing resistivity of cabling and conductors within the system. Resistivity measurements performed using PEIS between 200 kHz and 100 mHz at 10 mV sinus amplitude. (a) Data points for polymer-carbon composites, three repeats taken at each proportion of carbon for each polymer. (b) Average of data points in (a).

On the graphs in Figure 97 the resistivity measured for the conductors (including cabling and current collectors of the cells) is shown at 0.5 Ω m; this was the resistivity in the absence of a polymer-composite. At the higher proportions of carbon the polymer-composite resistivity became near negligible as the carbon particles formed a conductive framework. This resulted in a resistivity close to the conductors of the system. The transient region of the graphs relating to resistivity being dominated by tunnelling was between 15 to 20 % of carbon filler, ending in the percolation threshold. Below this transient region an insulating region was observed for PAN, HDPE and LDPE. Interestingly, the insulating polymer behaviour region for PVDF was not visible at

5 % unlike for the other polymers where it was seen up until 10 %; this implies that the PVDF material exhibited insulating behaviour at far lower carbon percentages. As a result, PVDF required less mass of conductive additive to show conductive behaviour.

There was a concern with the manufacturing of the electrodes, shown in Figure 97a. Three samples were tested for each set, which were used to calculate the averages in Figure 97b. Unfortunately, a wide variation was seen in some samples, sometimes up to an entire magnitude difference between the most and least resistive. This variation was not ideal, especially for measuring small changes in resistivity for PTCR at elevated temperatures and may be an issue with the packing density of the polymer-composites. The manufacturing methods used were difficult to alter and pressing higher filler proportion samples resulted in cracking and flaking. Care must therefore be taken to study samples that fall close to the average of resistivity. Certain studies have found compression moulding techniques to be useful for polymer-composites with high-packing density [52] and may provide improvements in manufacture; manufacture with such equipment should be explored with the polymer-carbon composites studied if available.

5.2.2 Polymer-TiC composites

For the polymer-TiC composites, the percolation threshold required a much higher proportion of filler to transition to a conductive state. Other studies have linked the requirement for higher filler proportions to smaller particle sizes [51]. It was therefore likely that the TiC powder had a smaller particle size than the carbon powder. Higher filler proportions unfortunately compromise the polymer-composite structure. The matrix acts to bind the composite together, so when the composite had a greater filler percentage the composite structure was more degraded. As a result, above 60 % the composite became increasingly more brittle and fractured leading to much wider variation in sample resistivities for each filler to matrix ratio, see Figure 98a.

Percolation thresholds were identified from Figure 98b. The molten cast HDPE and LDPE showed a clear threshold around 70 % TiC. For the solvent cast PAN and PVDF the threshold could only be identified within a range hinting that this manufacturing method may not be ideal for polymer-composites of high filler proportion. PVDF was identified at either 60 or 70 % TiC whilst PAN would likely experience a percolation threshold between 70 to 80 % TiC. For PAN with 70 % TiC filler, samples showed such a wide variation in Figure 98a that the sample must not be uniform. It was therefore possible that PAN-TiC would have a percolation threshold around 70 %. This large variation was a result of the higher filler proportions required, higher than the 50 % maximum explored in polymer-carbon studies. The higher filler proportions made mixing with the methods

used, such as the employment of a stir plate to achieve homogenisation, difficult leading to non-uniform samples. Loosely, it can be determined that TiC composites experienced percolation at a 45 % higher filler ratio than their carbon composite equivalents.

Other conclusions that can be seen were the tunnelling conduction region occurring over a 10 % filler ratio for HDPE and LDPE, a similar relationship for this region occurred in carbon composites in Section 5.2.1. PVDF also appeared to exit the insulating region around 10 % lower than other polymer-composites. This much lower filler requirement to becoming conductive explains why no insulation region was observed in the carbon studies; PAN, HDPE, and LDPE all exit the insulating region around 10 % carbon and so PVDF would exit the insulating region at below 5 % carbon should the relationship be similar as it was in TiC composites.

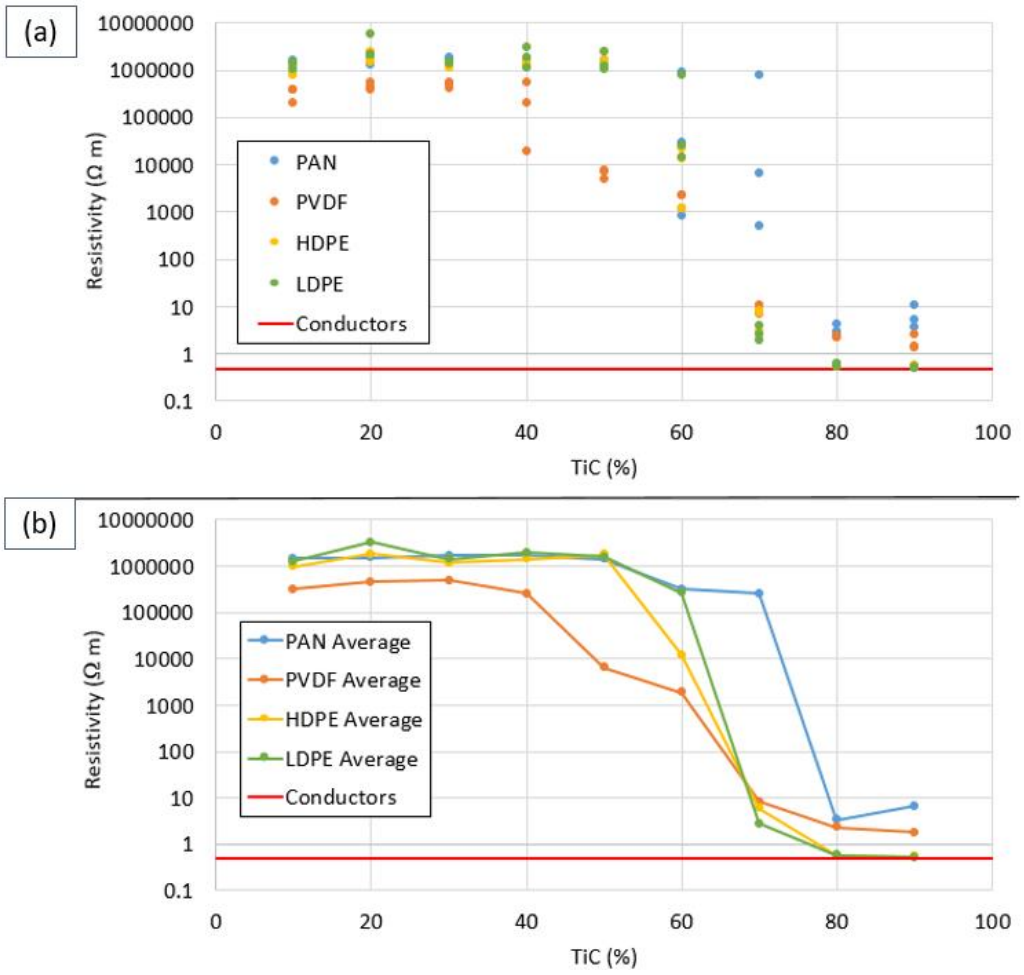

Figure 98: Room temperature resistivity measurements for various polymer-TiC composites at varying TiC filler content. Polymers are: PAN, PVDF, HDPE, and LDPE. A red line is included representing resistivity of cabling and conductors within the system. Resistivity measurements performed using PEIS between 200 kHz and 100 mHz at 10 mV sinus amplitude. (a) Data points for polymer-TiC composites, three repeats taken at each proportion of TiC for each polymer. (b) Average of data points in (a).

5.3 Scanning electron microscopy – sample cross-sections

SEM was performed on polymer-composites looking at the topography of composite cross-sections. Understanding the spread of filler particles within polymers can provide key insight as to how conductive pathways are likely to form. Specifically, size and shape of the filler particles can affect the fraction of filler required for a percolation threshold to be observed [51]. Filler spacing also has potential consequences for how a PTCR effect is exhibited and how great the PTCR intensity is, which may be influenced by manufacturing methods.

For previous resistivity measurements, it was assumed that all conductive filler particles were perfectly spherical in shape with equal geometry at any orientation. However, several irregular shapes and sizes were observed under SEM imaging. A range of particle sizes for the carbon and TiC particles was observed and given. Significant observable differences in their spacing within different polymer matrices was also noted. All samples studied by SEM were at or as close as possible to the percolation thresholds identified in Section 5.2.

5.3.1 Polymer-carbon composites

SEM images for PAN-carbon cross-section is shown in Figure 99. The filler content was 15 % by weight. The 50 µm thick copper foil is seen on the bottom of Figure 99a with a PAN film thickness of 10 µm cast on top. From Figure 99b it was difficult to distinguish between the PAN matrix and carbon particles except in obvious areas of protrusion. At these areas, a carbon particle size of near to 100 nm was recorded. What can be noted was the uniformity of the solvent cast, with little to no obvious visual discrepancies in areas of the PAN-carbon composite even at 30,000 X magnification.

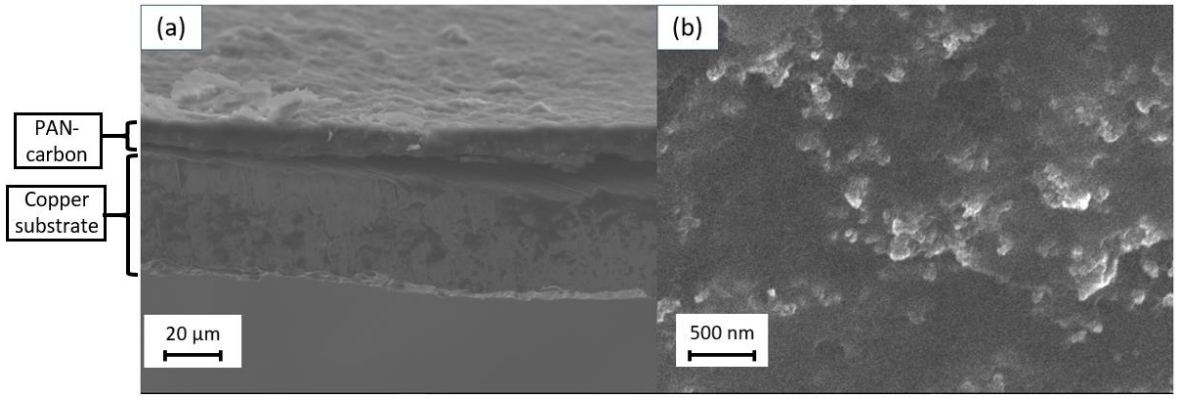

Figure 99: SEM images for PAN-carbon composite with 15 % carbon by weight. (a) Image of polymer film on copper foil at 650 X magnification. (b) Image of PAN-carbon at 30,000 X magnification.

Images of the PVDF-carbon film using the solvent cast method are shown in Figure 100. This PVDF-carbon samples was of 5 % carbon filler content by weight. Figure 100b was taken of a region where the matrix had split apart allowing easier determination of particle sizes. Carbon particle sizes of around 100 nm were once again recorded with an even distribution. Unlike with the PAN-carbon sample there were areas where carbon particles were easily distinguished due to the PVDF matrix breaking apart in sections, however much smoother areas where the matrix had not come apart (such as in the bottom-right of Figure 100b) showed difficult to distinguish areas even at 43,000 X magnification as seen in the PAN-carbon sample. Solvent cast method appeared to produce uniform films with even carbon distribution for both the PAN and PVDF samples. In Figure 100a, a film thickness of 15 µm was noted on top of the copper foil.

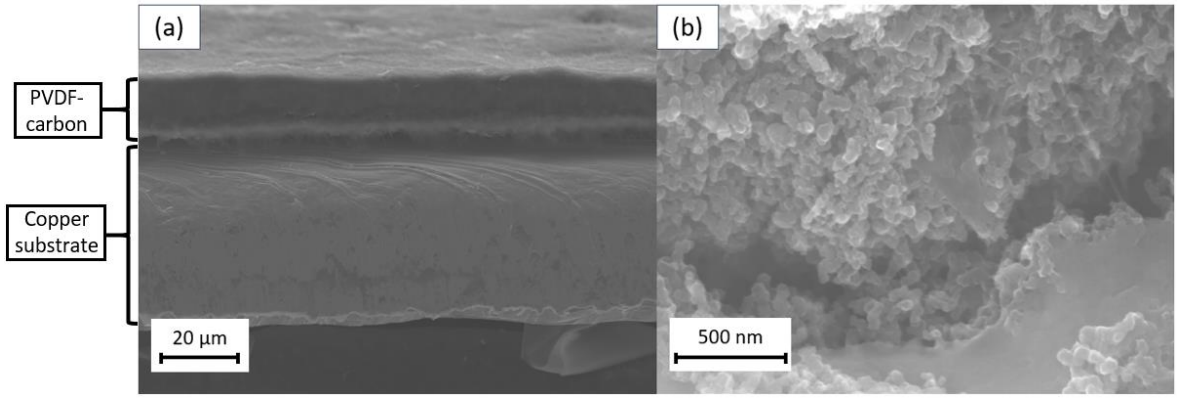

Figure 100: SEM images for PVDF-carbon composite with 5 % carbon by weight. (a) Image of polymer film on copper foil at 800 X magnification. (b) Image of PVDF-carbon at 43,000 X magnification.

The greatest difference between polymer-composites was between the solvent cast samples and the molten cast. Large scale differences can be seen in the macrostructure for HDPE-carbon composites in Figure 101a. Carbon filler ratio was 15 % by weight. The polymer-composite films were much thicker at 600 µm, 40 times the thickness for the PVDF-carbon composite. There also appeared to be several areas of darker and lighter patches, this may have been due to a poor break when making the cross-section due to ductile deformation or inhomogeneity of the particle distribution. There was however a clear difference at the top of the film compared to the middle and the bottom. The top had far fewer darker patches whilst the bottom appeared more squashed an elongated. The top layer was likely different due to a much cleaner fracture when making the cross-section. The difference in lower layers was likely a result of the glass-pin rolling when compressing the polymer-composite resulting in areas of varying density. Carbon particles of near 100 nm were recorded.

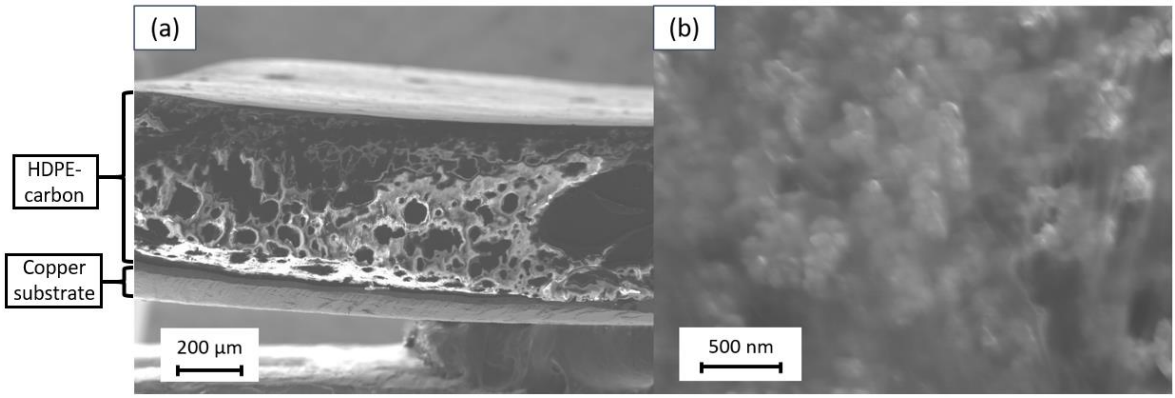

Figure 101: SEM images for HDPE-carbon composite with 15 % carbon by weight. (a) Image of polymer film on copper foil at 65 X magnification. (b) Image of HDPE-carbon at 30,000 X magnification.

Images for LDPE-carbon composites showed similar tendencies to HDPE-carbon. Figure 102 shows a LDPE sample with 15 % carbon filler by weight. A LDPE film of 550 µm was observed with clear brighter and darker areas throughout. A clear top layer was observed in the film, similar to the HDPE sample. LDPE microstructure in Figure 102b shows carbon particles of near 100 nm with a seemingly even distribution. Overall, molten and solvent composites were uniform with the exception of density variation across the molten sample cross-sections. This could potentially be improved with better manufacturing techniques such as compression moulding to allow improved packing density [52].

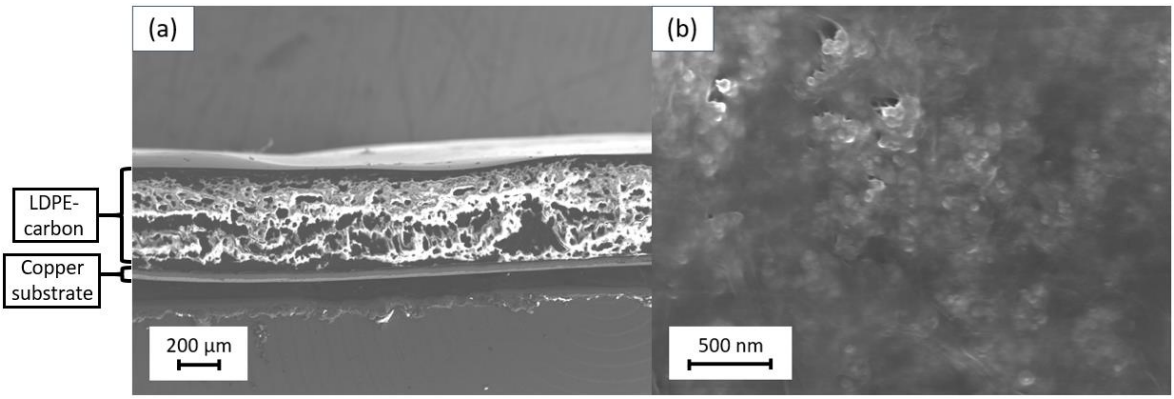

Figure 102: SEM images for LDPE-carbon composite with 15 % carbon by weight. (a) Image of polymer film on copper foil at 37 X magnification. (b) Image of LDPE-carbon at 30,000 X magnification.

5.3.2 Polymer-TiC composites

SEM images for polymer-TiC composites were similar to polymer-carbon composites when viewed at a large scale. However, at higher magnifications clear differences could be observed. For example, as seen for PAN-TiC composites with 70 % TiC in Figure 103a a uniform film was solvent cast onto a copper foil of around 30 µm thickness. This was three times thicker than the 15 % PAN-carbon imaged in Figure 99 with a thickness of 10 µm. This change may be due to the far higher filler content and the increased amount of solvent required during casting to produce an ink of similar viscosity. Far greater differences were seen on the micro-scale in Figure 103b. Filler particles were clearly non-spherical with varying length and width dimensions. One such particle was measured at 50 by 67 nm, such a variation was not immediately obvious for the carbon particles. Although this change in aspect ratio was slight, particles with aspect ratios larger than one (non-spherical particles) have been reported as reducing percolation threshold [51]. Counter to this, the percolation threshold for polymer-TiC composites was much larger than the carbon composites. This was likely due to another major influencing factor, decreasing particle size will increase the resistivity of the composite increasing the percolation threshold fraction [51]. For the PAN-TiC particle sizes between 50 nm and 100 nm were recorded, as much as half the particle size of 100 nm for carbon particles in some cases.

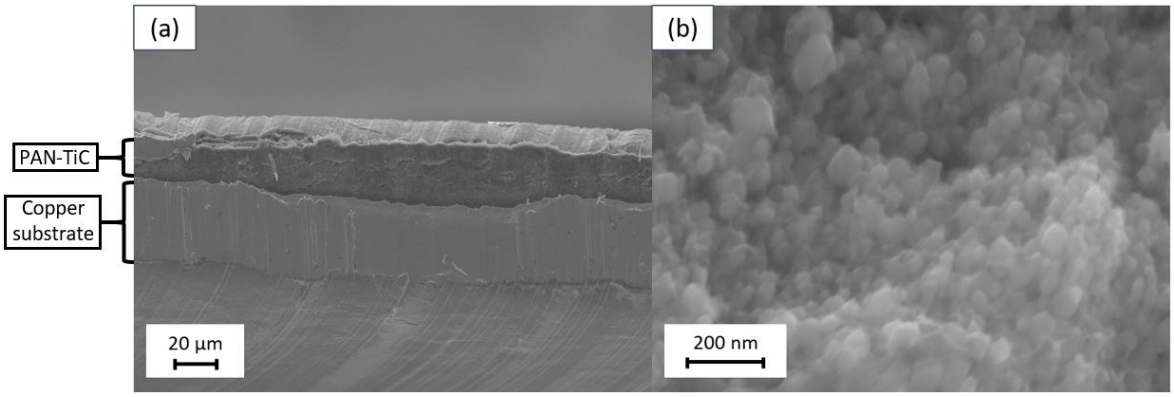

Figure 103: SEM images for PAN-TiC composite with 70 % TiC by weight. (a) Image of polymer film on copper foil at 400 X magnification. (b) Image of PAN-TiC at 80,000 X magnification.

Similar differences between carbon and TiC composites were seen for PVDF-TiC with 60 % filler by weight, shown in Figure 104. A film thickness three times the carbon sample was seen at 48 µm compared to the carbon sample 15 µm. Film surface was visibly rough, something not seen in the PVDF-carbon sample. This roughness was due to the higher filler fraction. Particle sizes were of a greater range of 20 nm to 100 nm. Clear agglomerates were observed among particles. However, the distribution of particles appeared mostly uniform. Solvent cast methods, therefore, appeared to encourage good uniformity regardless of the filler material used even at higher filler ratios.

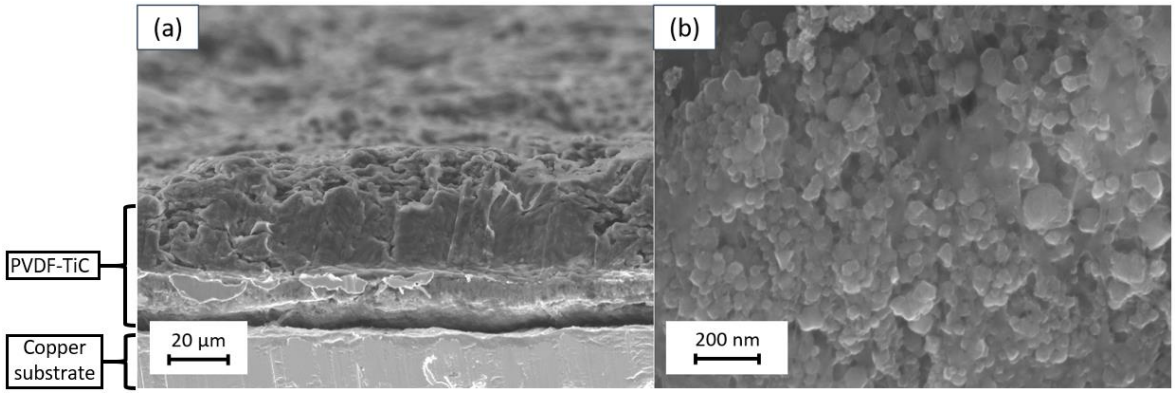

Figure 104: SEM images for PVDF-TiC composite with 60 % TiC by weight. (a) Image of polymer film on copper foil at 600 X magnification. (b) Image of PVDF-TiC at 65,000 X magnification.

For molten composites, a stark difference was obvious at macro-scales when comparing polymer-carbon to polymer-TiC. Figure 105 shows a HDPE-TiC sample with 70 % filler content. The HDPE-carbon samples had distinct differences between the top and lower layers of the polymer film. For the HDPE-TiC sample, the film break was uniform throughout. Film thicknesses were also of comparable size with 509 µm for the TiC sample and 600 µm for the carbon sample. Both HDPE-carbon and HDPE-TiC samples were manufactured using the same techniques. Therefore, rather

than better mixing of the TiC to remove the distinct layers it was more likely that the sample had become more brittle due to the increased filler ratio. This increased brittleness allowed a cleaner break to expose the cross-section removing many of the issues seen in the HDPE-carbon cross-section. On a micro-scale, non-spherical particles were observed with a wide range of 30 nm to 100 nm. Agglomerates were observed, but the spacing of particles appears mostly uniform.

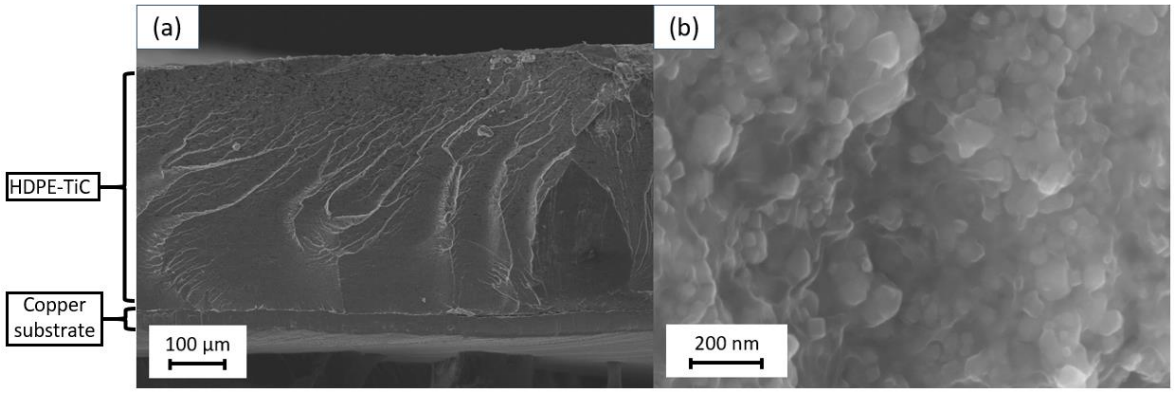

Figure 105: SEM images for HDPE-TiC composite with 70 % TiC by weight. (a) Image of polymer film on copper foil at 120 X magnification. (b) Image of HDPE-TiC at 75,000 X magnification.

The effect on LDPE-TiC composites was similar to HDPE-TiC, see Figure 106. The variation seen on the macro-scale in LDPE-carbon samples was gone with the LDPE-TiC sample uniform throughout. There was slight variation in film thickness from carbon to TiC LDPE samples, 550 µm to 315 µm respectively. However, film thicknesses were still of similar magnitude so would have minimal effect on performance. Particle sizes were the same as the HDPE-TiC sample with non-spherical particles between 30 nm to 100 nm. Overall, the only difference between carbon and TiC samples was the range of particle sizes, which would be influenced by supplier. Molten samples also had a cleaner cross-section due to higher filler percentages making them more brittle.

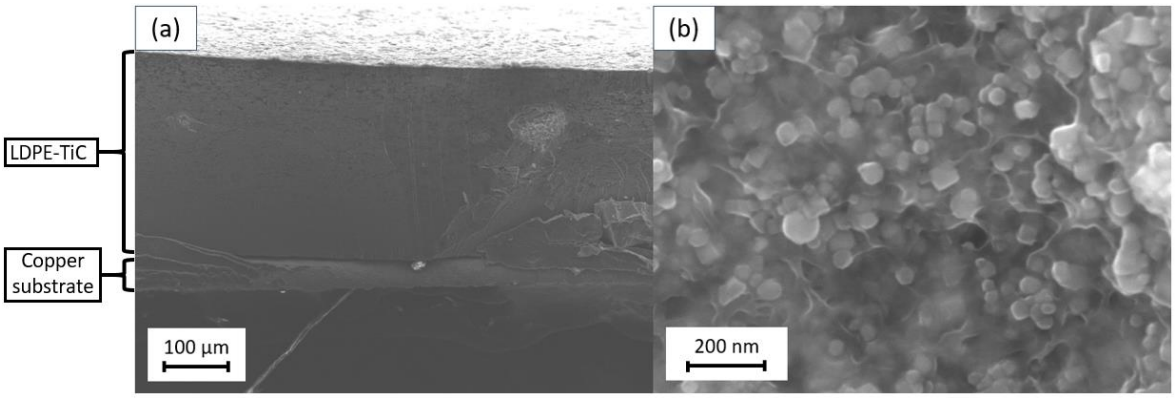

Figure 106: SEM images for LDPE-TiC composite with 70 % TiC by weight. (a) Image of polymer film on copper foil at 140 X magnification. (b) Image of LDPE-TiC at 80,000 X magnification.

5.4 Differential scanning calorimetry – transition temperatures

To properly understand the PTCR behaviour of polymer-composites studies into certain physical properties are required. DSC was used to measure transition temperatures of the composites. These temperatures were the point at which PTCR effects were expected to occur. A lower transition temperature would provide a lower point in which cell shutdown and thermal runaway prevention can occur preventing unnecessary elevated temperatures. Should certain compositions of filler materials or the filler material selection itself provide lower transition temperatures then this would be beneficial to thermal runaway prevention.

5.4.1 Differential scanning calorimetry – PAN

DSC data for PAN-carbon composites in intervals of 10 % from 0 % to 50 % carbon by weight can be seen in Figure 107. As carbon content was increased the heat flow to increase and decrease the temperature was reduced. This resulted in features becoming less pronounced with smaller step heights in the signal. Decreasing step height of DSC studies is a known outcome for increasing filler content within a polymeric system [157]. The step height is commonly proportional to the polymer content of the material composite.

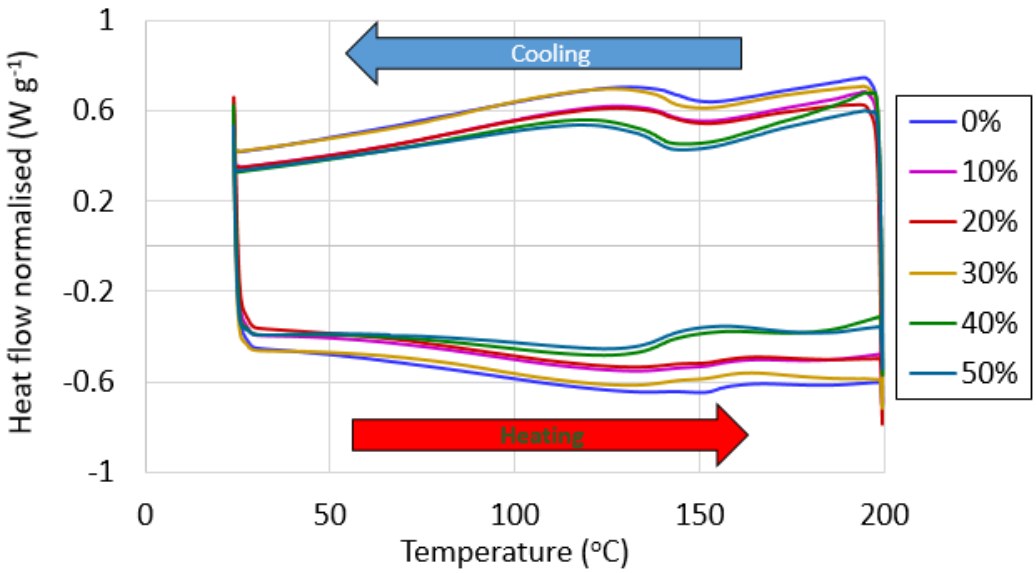

Figure 107: DSC data for PAN-carbon samples from 0 % to 50 %. Heat flow plotted against temperature. DSC performed from 20 °C to 200 °C and then reversed from 200 °C to 20 °C at 20 °C/minute. Studies performed under a nitrogen environment.

PAN-TiC studies were mostly identical to the PAN-carbon, see Figure 108. Heat flow was reduced with increasing TiC filler content with DSC features becoming less pronounced tending towards a near flat line by 90 %. The reduction in DSC features was due to the polymer requiring more heat flow to undergo a transition whilst the filler does not transition within the studied range. Hence PAN features in DSC were less obvious with a decrease in the proportion of PAN.

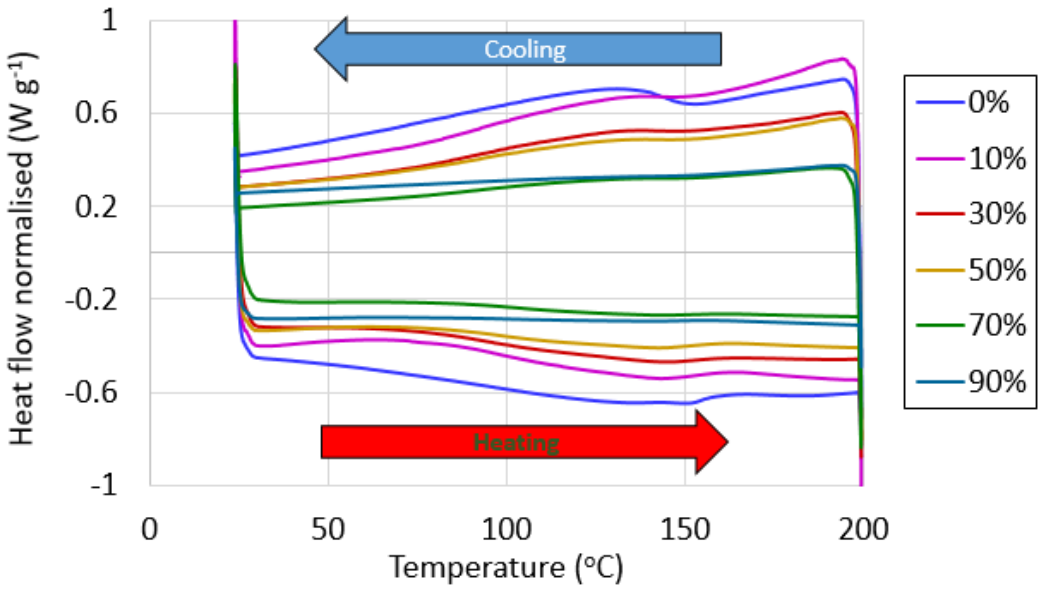

Figure 108: DSC data for PAN-TiC samples from 0 % to 90 %. Heat flow plotted against temperature. DSC performed from 20 °C to 200 °C and then reversed from 200 °C to 20 °C at 20 °C/minute. Studies performed under a nitrogen environment.

DSC data for PAN did not show a pair of pronounced peaks, which would indicate a melting point. The glass transition of PAN, however, was expected within the temperature range near to 95 °C [35] [58]. DSC data expresses glass transition as a point of inflection and hence must be determined by looking at the gradient around the expected range. Gradients of PAN data were calculated between 70 and 120 °C during heating to identify the glass transition temperature; the minimum of the gradient within this range was at the temperature of the point of inflection.

The glass transition temperatures identified by analysing the points of inflection are shown in Table 20. Overall, a general increase in transition temperature was observed for both PAN-carbon and PAN-TiC. Generally speaking, increasing filler content should have a small effect on glass transition temperature at low proportions. However, when increasing by a significant amount as in these studies the material composite would tend towards a more rigid crystalline structure and away from the amorphous behaviour of a polymer. The structure would also become denser as the fillers have a higher density than the polymer matrix (TiC density ≈ 4.9 g cm^{-3}, carbon black density ≈ 2.1 g cm^{-3}, PAN density ≈ 1.2 g cm^{-3}). The denser, more rigid structure provided the composite with more hindrance to chain mobility resulting in greater temperatures required for

glass transition [158]. PAN-carbon experienced a steady increase from 92.9 °C at 0 % to 99.9 °C at 50 %. PAN-TiC data showed a rapid increase at 10 % TiC with a glass transition at 98.5 °C. This glass transition remained consistent until 60 % where another rapid increase was observed to 100.4 °C and ending at a glass transition of 104.8 °C at 90 %. What can be concluded was that the addition of both carbon and TiC filler increased the glass transition by a similar magnitude by 50 % content and loosely that an increase in filler content increased the glass transition temperature.

Table 20: Glass transition temperatures for PAN composites at varying filler contents of carbon and TiC by percentage weight. Filler contents shown in red were not studied.

Carbon (%)	0	10	20	30	40	50	60	70	80	90
Transition (°C)	92.9	93.4	93.2	94.6	94.2	99.9				
TiC (%)	0	10	20	30	40	50	60	70	80	90
Transition (°C)	92.9	98.5	97.7	98.0	97.8	98.5	100.4	105.1	104.3	104.8

5.4.2 Differential scanning calorimetry – PVDF

DSC data for PVDF-carbon is seen in Figure 109. Similar to PAN-composites, DSC features reduced with increasing filler content. The crystallisation peak, which appeared during cooling, occurs at a lower temperature than the melting peak for all samples. This behaviour is typical of a semi-crystalline polymer structure [159]. Further, the tall peak with a sharp increase at higher temperatures transitioning to a slower decline at lower temperatures is also inidicative of a semi-crystalline polymer behaviour [157] [160]. Peaks appeared to increase in temperature with increasing filler content by noticeable amounts. A melting peak could be seen on heating around 125 °C for the different filler contents. However, these temperatures were far lower than the expected 155 to 185 °C for the PVDF melting point [30].

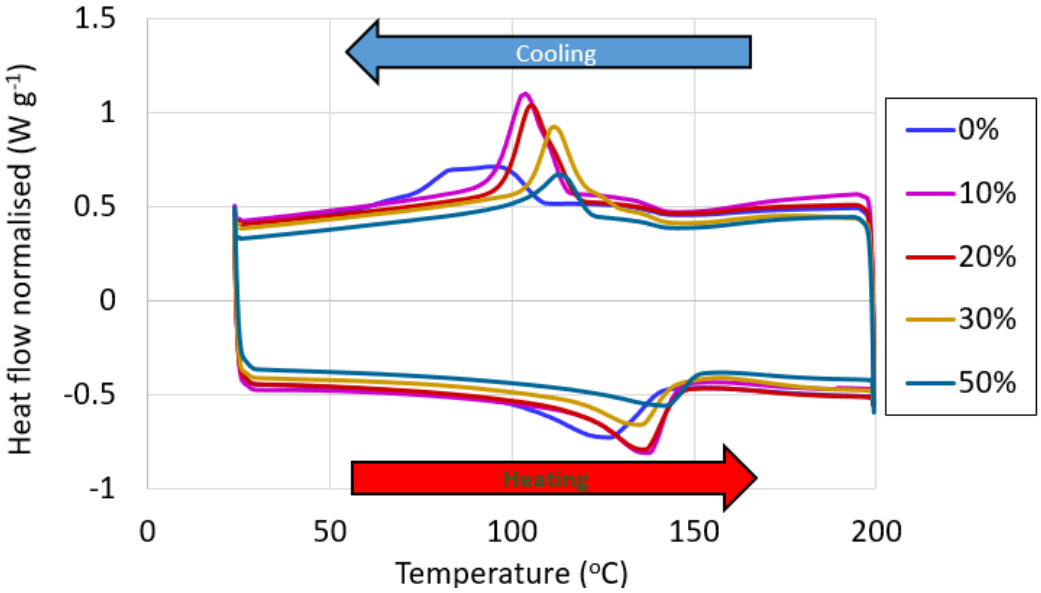

Figure 109: DSC data for PVDF-carbon samples from 0 % to 50 %. Heat flow plotted against temperature. DSC performed from 20 °C to 200 °C and then reversed from 200 °C to 20 °C at 20 °C/minute. Studies performed under a nitrogen environment.

Similarly, DSC data for PVDF-TiC composites is shown in Figure 110. Peaks were much sharper for samples containing TiC with greater heat flow magnitudes, implying better heating than the PVDF-carbon composite studies. The PVDF-TiC composites were much closer to the expected melting point of 155 to 185 °C [30] at around 160 °C initially. These peaks remained closer together when compared to the PVDF-carbon data until 70 % where temperature decreased substantially. It was around 70 % where the features of the DSC reduced substantially and are near flat.

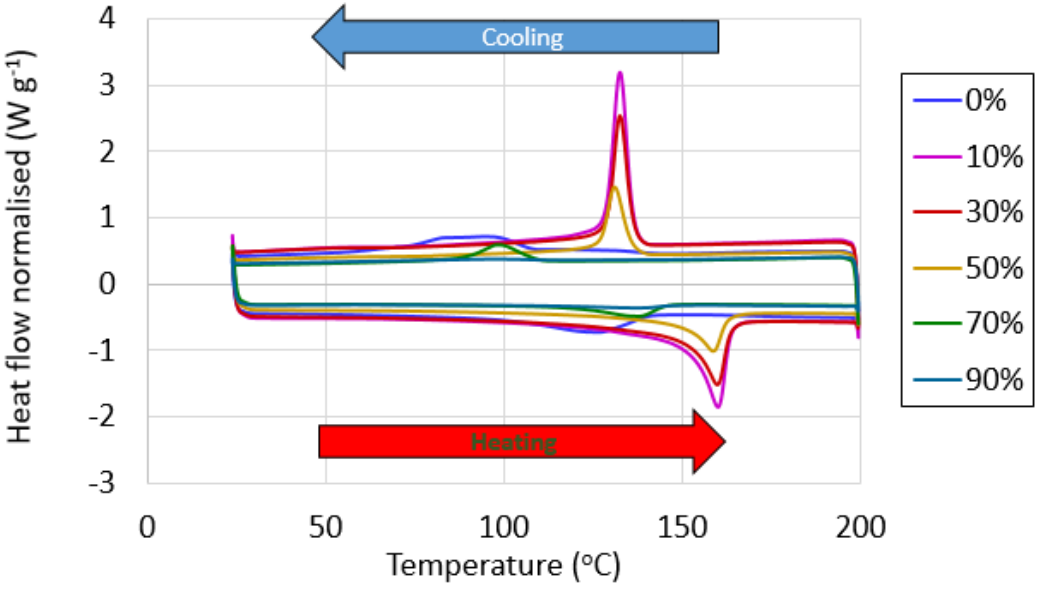

Figure 110: DSC data for PVDF-TiC samples from 0 % to 90 %. Heat flow plotted against temperature. DSC performed from 20 °C to 200 °C and then reversed from 200 °C to 20 °C at 20 °C/minute. Studies performed under a nitrogen environment.

Specific values for the PVDF-composite melting transition temperatures are shown in Table 21. Values were taken from the peak of heat flow against temperature during the heating cycle of the DSC. PVDF-carbon samples showed a tendency to increase in melting point with temperature, increasing from 127.1 °C at 0 % carbon up to 142.8 °C at 50 %. Values for PVDF-TiC were much closer to the expected melting point at 155 to 185 °C [30], starting from 160.1 °C at 10 % content. Melting temperatures then gradually decreased until 50 % with 158.5 °C, after which melting point rapidly decreased to 138.2 °C at 90 %. Increasing filler materials within a composite has been documented as reducing melting temperatures [161] [162]. This is because melting is related to the enthalpy of recrystallization, filler materials hinder crystallisation of the polymer lowering the energy required to melt the composite resulting in lower melting temperatures. Shifting melting-crystallisation peaks can occur due to several other factors (including: heating rate, molar mass of the polymer, density of the composite, pre-treatment of the material, etc.) [163]. These other factors can lead to an increase in melting point and could be the cause of the increasing melting point of PVDF-carbon composites. However, only the effect of filler content on the transition temperatures was investigated and further studies would be required to identify a specific source of the increasing melting temperatures.

Table 21: Melting transition temperatures for PVDF composites at varying filler contents of carbon and TiC by percentage weight. Filler contents shown in red were not studied.

Carbon (%)	0	10	20	30	40	50	60	70	80	90
Transition (°C)	127.1	136.2	137.2	135.9		142.8				
TiC (%)	0	10	20	30	40	50	60	70	80	90
Transition (°C)	127.1	160.1	158.0	159.9	158.7	158.5	150.7	138.4	132.6	138.2

5.4.3 Differential scanning calorimetry – HDPE

HDPE-carbon composite DSC data can be seen in Figure 111. Melting points, seen as the peaks during the heating cycle, remained fairly stable at just above 100 °C with features reducing in intensity with increasing filler content.

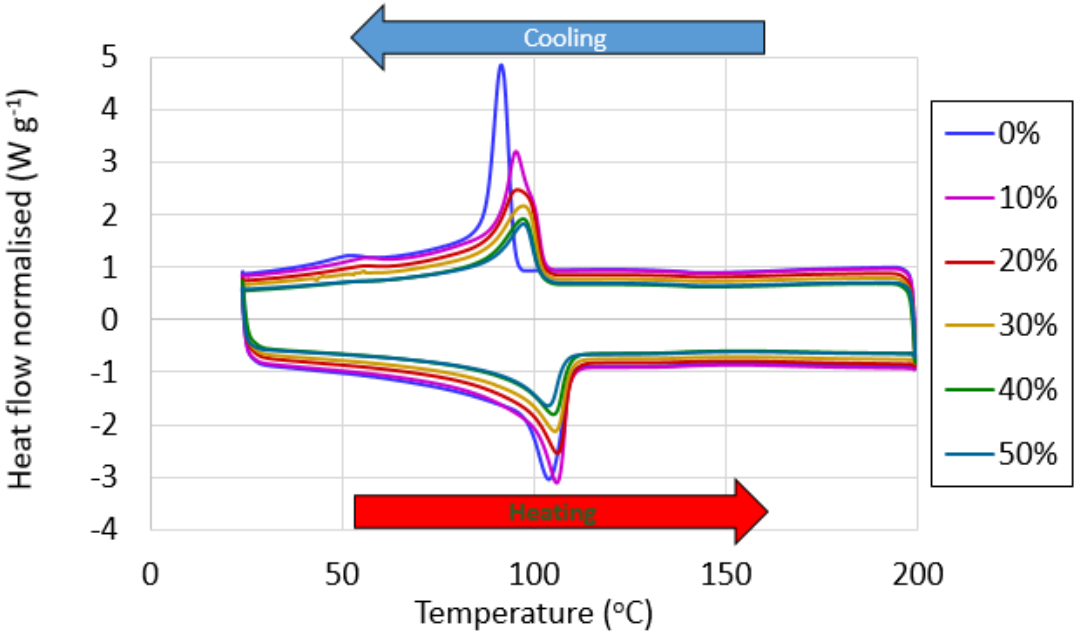

Figure 111: DSC data for HDPE-carbon samples from 0 % to 50 %. Heat flow plotted against temperature. DSC performed from 20 °C to 200 °C and then reversed from 200 °C to 20 °C at 20 °C/minute. Studies performed under a nitrogen environment.

Figure 112 shows the HDPE-TiC data. Unlike PVDF-TiC data, melting point features remained close together for the entire range of data with slightly increased changes around 70 %. By 90 %, the feature became difficult to distinguish, but a slight peak was observed. A general decrease in melting point with increasing filler content was observed.

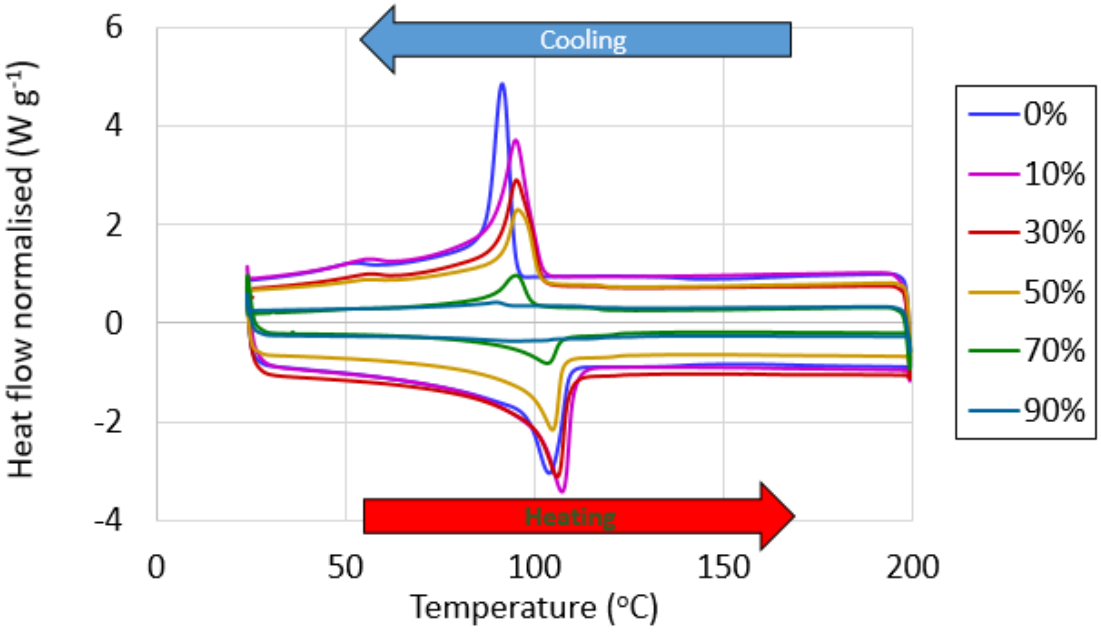

Figure 112: DSC data for HDPE-TiC samples from 0 % to 90 %. Heat flow plotted against temperature. DSC performed from 20 °C to 200 °C and then reversed from 200 °C to 20 °C at 20 °C/minute. Studies performed under a nitrogen environment.

Expected melting temperatures for the HDPE polymer, according to the supplier, were around 124 to 136 °C [156]. Table 22 shows the melting points taken from the peaks during heating cycles of DSC data for HDPE-carbon composites and HDPE-TiC composites. At 0 %, an initial melting point of 104.2 °C was observed. A slight increase to 105.9 °C was seen at 10 % carbon, which tended to decrease until 103.9 °C at 50 % filler. Similarly, an initial increase for 10 % TiC was observed at 107.6 °C. A gradual decrease was seen until 70 % where the fall became more rapid ending at 94.2 °C for 90 %. The trend of falling melting temperatures with increasing filler content was similar to the PVDF-TiC studies and was likely a result of the filler materials hindering recrystallization of the polymer lowering the energy required to melt [161] [162].

Table 22: Melting transition temperatures for HDPE composites at varying filler contents of carbon and TiC by percentage weight. Filler contents shown in red were not studied.

Carbon (%)	0	10	20	30	40	50	60	70	80	90
Transition (°C)	104.2	105.9	106.2	105.5	105.3	103.9				
TiC (%)	0	10	20	30	40	50	60	70	80	90
Transition (°C)	104.2	107.6	106.0	106.1	106.2	105.0	104.1	103.5	100.7	94.2

5.4.4 Differential scanning calorimetry – LDPE

Figure 113 shows LDPE-carbon composite DSC data. Trends appeared similar to HDPE-carbon data with melting peaks close together at all filler contents. Peaks once again reduced with increasing filler content. Unlike HDPE-carbon, these melting features appeared within the expected range given by the supplier of 98 to 113 °C [156].

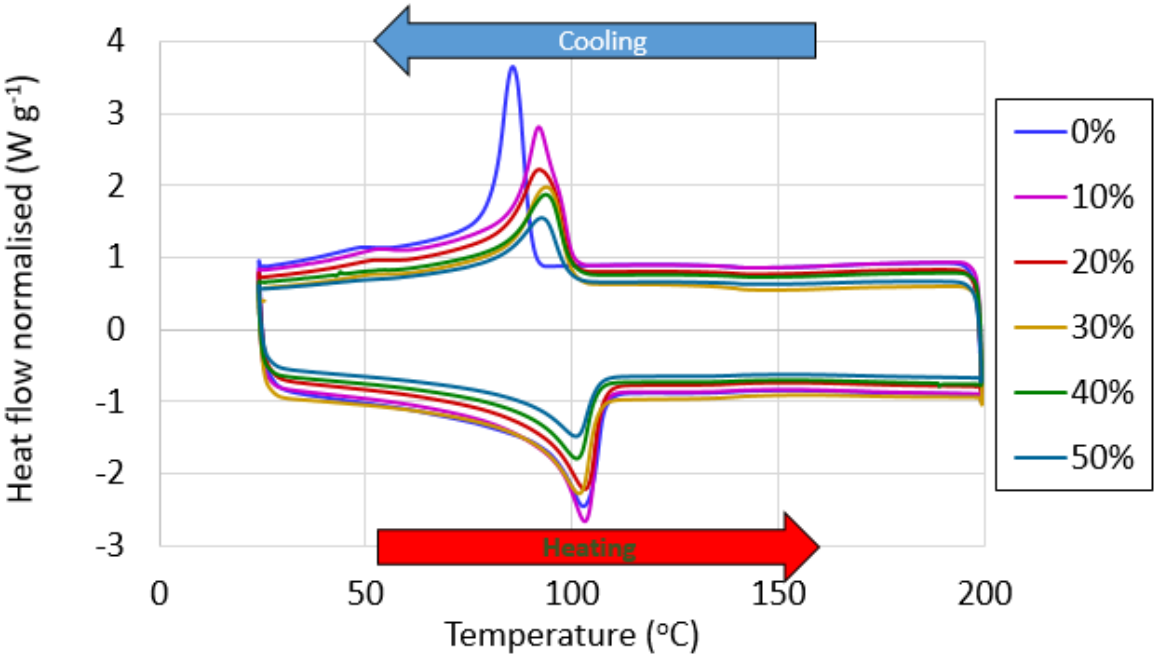

Figure 113: DSC data for LDPE-carbon samples from 0 % to 50 %. Heat flow plotted against temperature. DSC performed from 20 °C to 200 °C and then reversed from 200 °C to 20 °C at 20 °C/minute. Studies performed under a nitrogen environment.

The same trends were seen for LDPE-TiC composites. Peaks were close together with reducing intensity as filler content increased. By 90 %, the DSC features became difficult to distinguish. A general trend downward was observed, passing below 100 °C at higher filler contents.

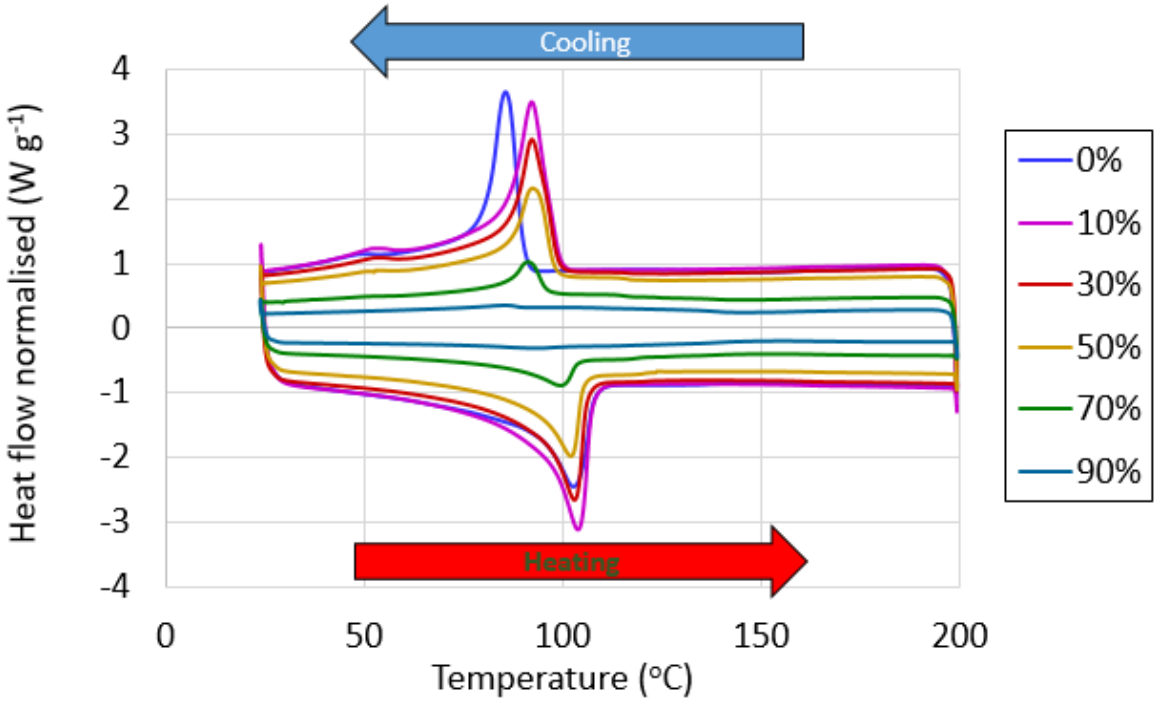

Figure 114: DSC data for LDPE-TiC samples from 0 % to 90 %. Heat flow plotted against temperature. DSC performed from 20 °C to 200 °C and then reversed from 200 °C to 20 °C at 20 °C/minute. Studies performed under a nitrogen environment.

Table 23 shows melting points for the LDPE composites taken from the peaks of DSC data during the heating cycle. A general decrease was observed for melting temperatures of LDPE-carbon and LDPE-TiC. This decrease was seemingly more rapid in LDPE-carbon composites with lower melting points recorded at each carbon content up until 50 %, ending with 50 % carbon with 101.0 °C and 50 % TiC with 102.1 °C. This fall continued for TiC up until 90 % where melting temperature fell out of the expected 98 to 113 °C range [156] at 94.7 °C. Once more, similar to the other HDPE and PVDF composites with melting transition temperatures the increasing filler content was likely reducing the enthalpy of melt resulting in decreasing melting temperatures [161] [162].

Table 23: Melting transition temperatures for LDPE composites at varying filler contents of carbon and TiC by percentage weight. Filler contents shown in red were not studied.

Carbon (%)	0	10	20	30	40	50	60	70	80	90
Transition (°C)	103.1	103.4	103.4	101.8	101.3	101.0				
TiC (%)	0	10	20	30	40	50	60	70	80	90
Transition (°C)	103.1	103.9	103.4	103.0	102.4	102.1	101.3	99.8	97.9	94.7

5.5 Elevated temperature resistivity measurements – PTCR effect

Prevention of thermal runaway can be achieved via the PTCR effect where increasing temperatures increases the resistivity of the sample. To this end, resistivity measurements were made at elevated temperatures using the polymer-composites studied in previous sections. These were performed in a Swagelok cell arrangement to provide a constant area of 95 mm^2 from a diameter of 11 mm for easy resistivity calculations. Swagelok cells were dried in a laboratory oven before being assembled within an argon environment to provide a dry and inert atmosphere at higher temperatures. These assembled Swagelok cells with polymer-composite samples were pre-heated at 200 °C for 24 hours to avoid any variation due to polymer chain rearrangement in resistivity measurements, only the effects of thermal expansion on resistivity were of interest. These samples could then be used directly in studies using a lithium-ion half-cell chemistry within a Swagelok.

Resistivity measurements were used at and around the identified percolation thresholds of filler contents in Section 5.2; it is at the percolation threshold where PTCR effects are reported at their greatest magnitude [33]. The most effective polymer-composites were identified considering their base resistivity at room temperature and the size of their PTCR intensity at various filler ratios. This PTCR effect should initiate when temperatures approach a transition temperature, glass transition or melting point, of the polymer-composite. The transition temperatures are where the greatest thermal expansion change of the polymer-composites is experienced and conductive pathways are most likely to break. For the polymers studied, these transition temperatures were identified in Section 5.4 and varied depending on the ratio of filler. Transition minimums and maximums identified were: PAN glass transition at 92.9 to 104.8 °C, PVDF melting point at 127.1 to 160.1 °C, HDPE melting point at 94.2 to 107.6 °C, and LDPE melting point at 94.7 to 103.9 °C. Resistivity temperatures were studied in intervals until 200 °C to cover the transitions occurring.

Thermal expansion due to a glass transition or due to a melting event are inherently dissimilar. In the absence of a phase transition, the rate of change of thermal expansion remains almost constant. However, at a phase transition an abrupt change occurs that can be of first order or second order [164] [165]. First order transitions consist of a large increase in volume without much change in temperature, which is seen at the melting point of materials. It is defined more specifically as a discontinuity in the first derivative of the Gibbs free energy. A second order transition is an increase in the rate of expansion at the transition temperature, which is seen at the glass transition temperature in all polymeric materials. Or in terms of the Gibbs free energy, a discontinuity in the second derivative but not always in the first. Hence, the volume of a material during a glass transition changes as a slope whilst the melting point volume changes as a jump providing pressure is constant, see Figure 115.

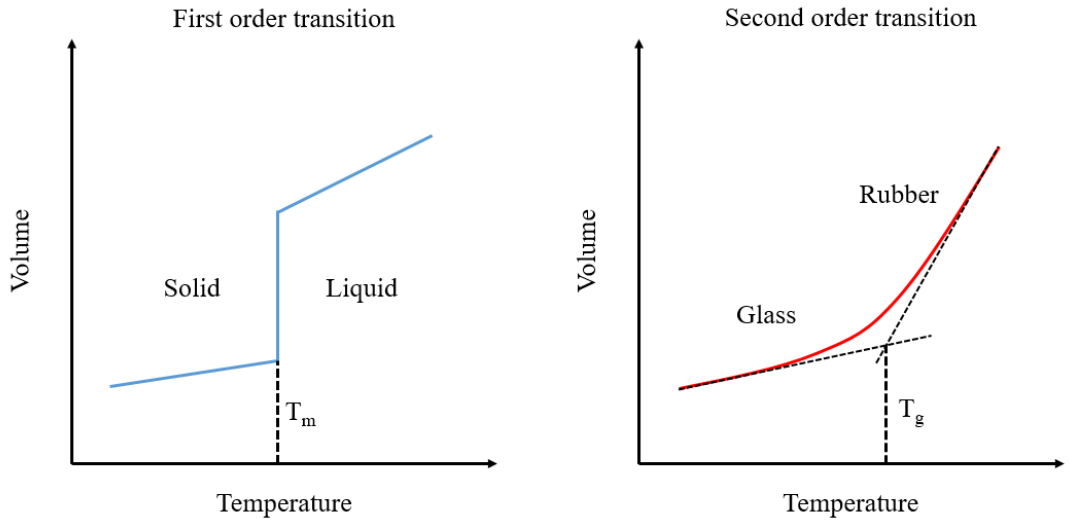

Figure 115: Representation of a first order and second order transition of volume against temperature. T_m is the melting point, T_g is the glass transition point.

5.5.1 Thermogravimetric analysis

TGA analysis was performed prior to any elevated temperature studies to identify any possible thermal degradation experienced by filler or polymer materials. TGA was performed under an inert argon environment, the same environment Swagelok cells were assembled under for studying the percolating-composite resistivities. The materials analysed were: Super C65 carbon, TiC, PAN, PVDF, HDPE, and LDPE. TGA data can be seen in Figure 116.

Very little thermal degradation, if any, was observed for all of the materials studied over the 25 to 250 °C temperature range. The key temperature looked at was the maximum of the elevated temperature studies of 200 °C. At this point, no material had lost more than 0.5 % of their mass. Taken to three significant figures, the remaining masses for the filler materials were 99.9 % for carbon and 99.8 % for TiC. For the polymer materials PVDF, HDPE, and LDPE negligible changes in mass occurred with all three recording 100 % at three significant figures. The material with the greatest mass loss was PAN at 99.6 %. It was therefore concluded that thermal degradation of polymer-composite materials was not significant within the temperature range of measurements studying the PTCR effect.

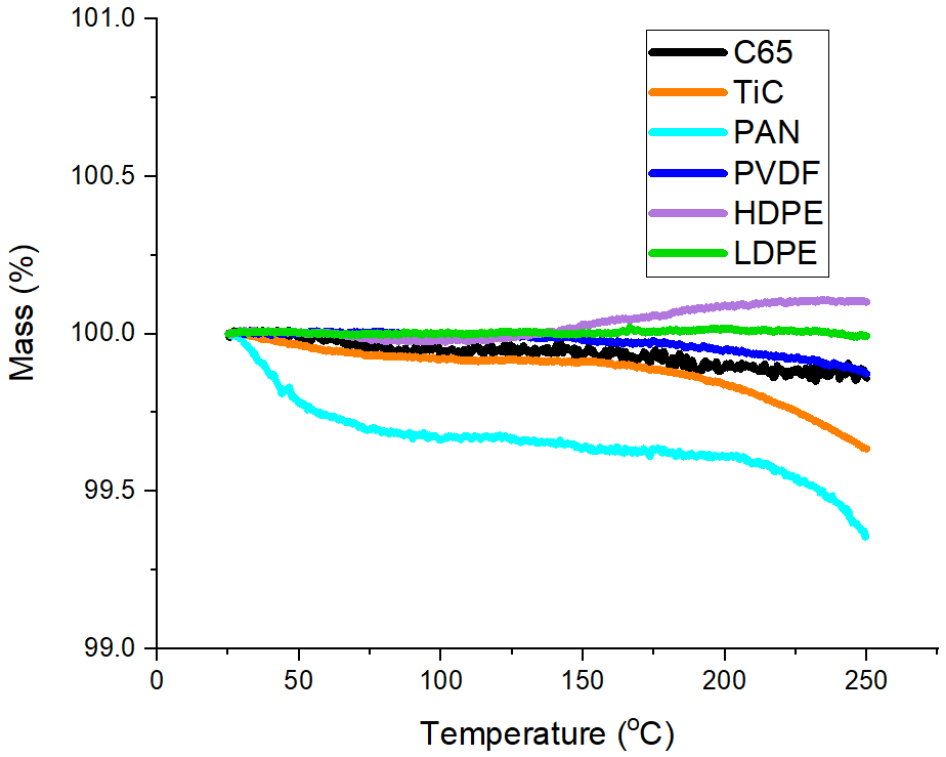

Figure 116: TGA performed on materials used in polymer-composites under an argon environment, percentage remaining mass plotted against temperature. Conductive filler materials: in black C65 (carbon), in orange TiC. Polymer matrix materials: in cyan PAN, in blue PVDF, in purple HDPE, in green LDPE. Studies ramped at 2 °C/minute from 25 °C to 250 °C.

5.5.2 Elevated temperature resistivity – PAN

From studies in Section 5.2.1, the PAN-carbon composite percolation threshold was identified around 25 % carbon by weight. PTCR studies were performed on several filler contents around this value as this was where maximum changes in resistivity would occur due to small changes in volume. Ratios studied were: 15 %, 20 %, 25 %, and 30 %. PAN-composite glass transition should occur between 92.9 °C and 104.8 °C according to DSC measurements in Section 5.4.1; between these temperatures a PTCR effect could be expected.

Figure 117 shows resistivity measured at several temperature intervals for PAN-carbon composites. Increasing filler content led to a decrease in resistivity. Ideally, since PAN-carbon composites should act as an electronic conductor at room temperature resistivity should be minimised if possible without hindering any PTCR observed. When considering room temperature resistivity, resistivity of conductors without the polymer-composites was 0.5 Ω m, significant increases to this should be avoided. From 15 % to 30 %, resistivity values recorded at room temperature were: 100.6 Ω m, 14.6 Ω m, 7.8 Ω m, and 3.1 Ω m. Typical internal resistances for 18650 lithium-ion cells are around 25 mΩ [166]; even with the lowest resistivity value of 3.1 Ω m the equivalent internal resistance was 1622 mΩ when calculated from the 95 mm^2 area with a thickness of 49 µm. It is not advisable to risk excessive resistivities without risking loss of power and capacity of any lithium-ion cell incorporating the polymer-composite.

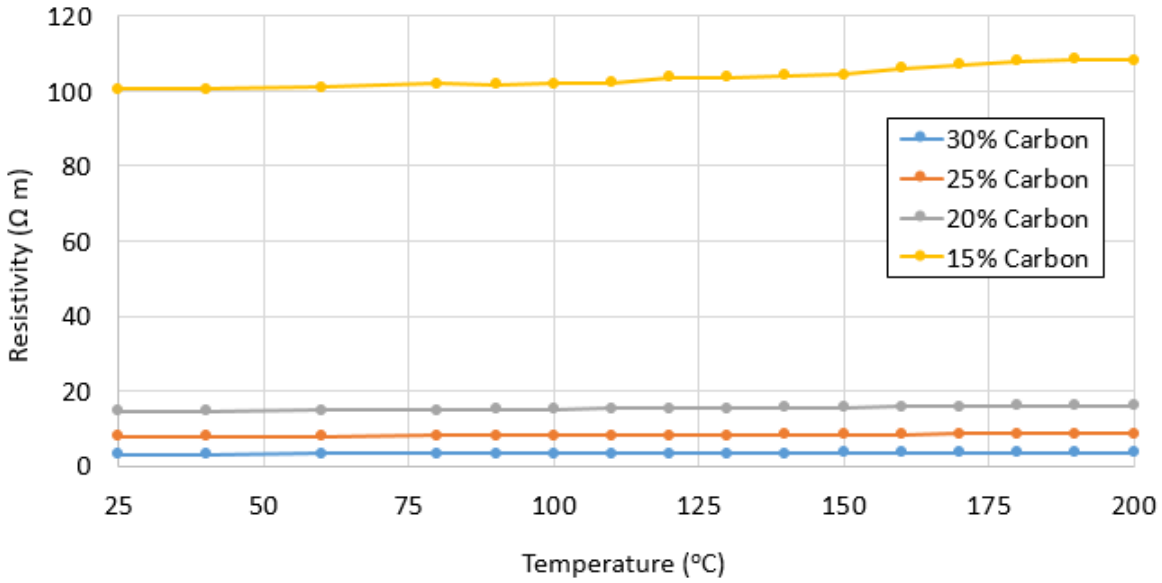

Figure 117: Resistivity against temperature for PAN-carbon composites at varying carbon filler percentages by weight. Temperatures increased in intervals and allowed to reach temperature over 15 minutes. Resistivity measurements performed using PEIS between 200 kHz and 100 mHz at 10 mV sinus amplitude.

Unfortunately, from the data shown in Figure 118 no significant change in resistivity with temperature was found for PAN-carbon composites. This was because of the volume expansion before and after a glass transition. A second-order change with temperature of volume is experienced for glass-transition points. This leads to an increased volume expansion rate after glass transition and not a large step as experienced in the first order changes of melting points. The second-order expansion was not significant enough to cause a substantial change in the PTCR intensity. In fact, the gradient of PTCR intensity with temperature for PAN-carbon composites appeared constant across the temperature range. This steady increase in resistivity observed was likely due to temperatures increasing internal resistance and not due to the critical breakdown of conduction pathways via volume expansion; this behaviour is expected from common conductors such as copper wiring upon increasing temperature. All changes were reversible upon returning the polymer-composites to room temperature.

A result that was interesting was that increasing filler content would lead to a decrease in room temperature resistivity, shown in Figure 117, but increase PTCR intensity, shown in Figure 118. The reason for this trend was likely because similar perturbations in resistance at elevated temperatures would lead to a greater percentage change if initial resistivity was much smaller. Because higher filler contents have lower initial resistance then they would experience a greater percentage change. As PTCR intensity is a ratio of elevated temperature resistivity to room temperature resistivity, larger percentage changes in resistivity for the higher filler proportions is expressed as larger PTCR intensities.

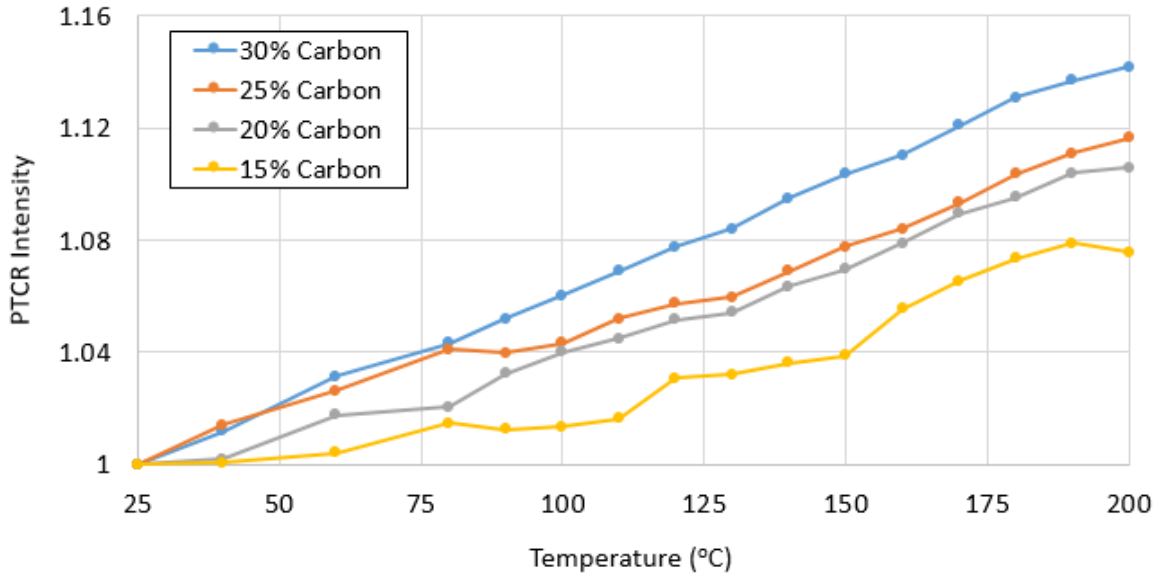

Figure 118: PTCR intensity against temperature for PAN-carbon composites at varying carbon filler percentages by weight. Temperatures increased in intervals and allowed to reach temperature over 15 minutes. PTCR intensity calculated by dividing resistivity at each temperature by the resistivity at room temperature.

5.5.3 Elevated temperature resistivity – PVDF

Section 5.2.1 data showed a PVDF percolation threshold around 15 % carbon by weight. Therefore similar to PAN-carbon studies, ratios close to this threshold were chosen: 5 %, 10 %, 15 %, and 20 %. Figure 119 shows resistivity at different temperature intervals for PVDF-carbon composites. Similar to PAN-carbon increasing filler content reduced resistivity. Unfortunately, a similar issue of excessive resistivity was observed for these filler contents. From 5 % to 20 %: 47.7 Ω m, 11.0 Ω m, 8.6 Ω m, and 4.5 Ω m. Taking 25 mΩ as a typical internal resistance for a battery [166], the minimum resistivity of 4.5 Ω m equates to a resistance of 1663 mΩ. This was again far above the norm and would likely to lead to reduced power and capacity of lithium-ion cells.

A clear PTCR was observed initiating around 130 °C. PVDF-carbon melting point should occur between 127.1 °C to 137.2 °C, according to DSC data in Section 5.4.2. The previous PAN-carbon studies (see Section 5.5.2) did not show a PTCR effect; this difference was likely because PVDF shows a melting point within the temperature range explored whilst PAN shows only a glass transition. Melting points are associated with a first-order change of volume with temperature where volume should increase significantly in a step upon reaching melting point. The glass transition second-order change only increases the rate of volume expansion and does not have a sudden increase. The melting point volume expansion is sudden and great enough to cause a PTCR, hence why PVDF showed a PTCR whilst PAN did not.

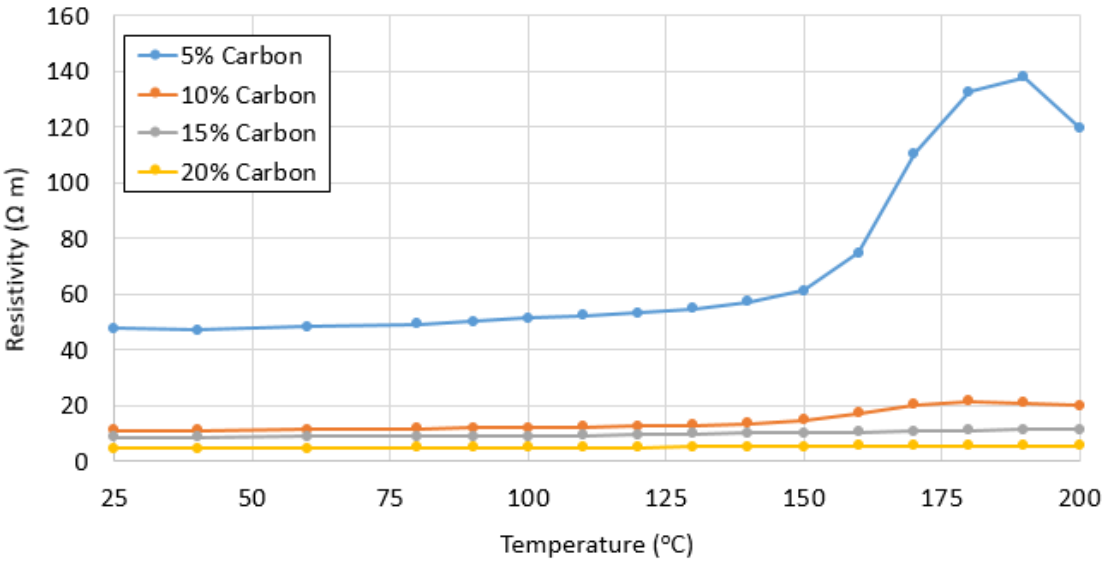

Figure 119: Resistivity against temperature for PVDF-carbon composites at varying carbon filler percentages by weight. Temperatures increased in intervals and allowed to reach temperature over 15 minutes. Resistivity measurements performed using PEIS between 200 kHz and 100 mHz at 10 mV sinus amplitude.

Figure 120 shows the PTCR intensity for PVDF-carbon samples. It was immediately obvious that the magnitude of the PTCR effect decreased with increasing filler content with a peak appearing around 180 °C to 190 °C. From 5 % to 20 %, PTCR intensity was: 2.8, 2.0, 1.3, and 1.2. This was expected behaviour as more conductive filler creates a more substantial conductive framework. As this framework takes up more of the volume the composite acts more like a standard conductor where resistivity slowly increases with temperature. Resistivity began to fall after the observed peaks in what is known as a negative temperature coefficient of resistivity (NTCR) [52]. This phenomena occurs because the conductive filler particles reorganise within the mobile phase of the polymer matrix. Changes to resistivity and PTCR intensity were reversible upon returning the polymer-composites to room temperature.

Unfortunately, the PTCR observed may occur at too high a temperature to be useful in thermal runaway prevention. Significant damage to the cell and potential fire hazards are likely to occur before 180 °C is reached due to the thermal decomposition of materials within the battery before this temperature, as discussed in Section 1.2.

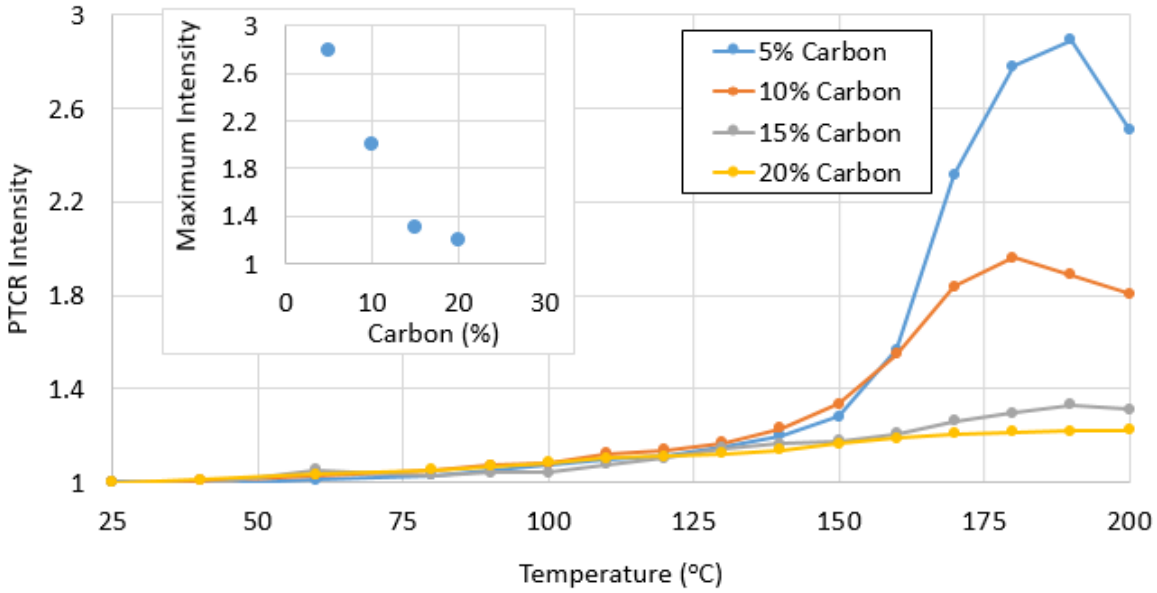

Figure 120: PTCR intensity against temperature for PVDF-carbon composites at varying carbon filler percentages by weight. Temperatures increased in intervals and allowed to reach temperature over 15 minutes. PTCR intensity calculated by dividing resistivity at each temperature by the resistivity at room temperature. The inset shows the PTCR intensity at peak against carbon filler percentage by weight.

5.5.4 Elevated temperature resistivity – HDPE

The HDPE-carbon percolation threshold was found near 25 % carbon by weight in Section 5.2.1. Filler ratios selected around this threshold were: 15 %, 20 %, 25 %, and 30 %. Figure 121 shows resistivity for the HDPE-carbon composites at each temperature interval. Immediately obvious was the lower room temperature resistivity compared to previous PVDF-carbon and PAN-carbon, 47.7 Ω m and 100.6 Ω m at 10 % below the percolation threshold respectively. The same value for HDPE-carbon was 4.9 Ω m, an entire magnitude lower. From 15 % to 30 %, room temperature resistivity was: 4.9 Ω m, 3.3 Ω m, 0.7, Ω m, and 0.3 Ω m. The resistance value for 0.3 Ω m was 1880 mΩ, far above a typical lithium-ion battery 25 mΩ [166]. However, much of this resistance was due to the excessive thickness of 707 µm, 70 times greater than some solvent cast samples. This was due to difficulties when manufacturing the molten cast composites and more refined techniques were required to reduce thickness further. At the same thickness as the solvent cast samples with the same resistivity this would provide 26.9 mΩ, an increase in internal resistance in the same magnitude as a typical lithium-ion battery.

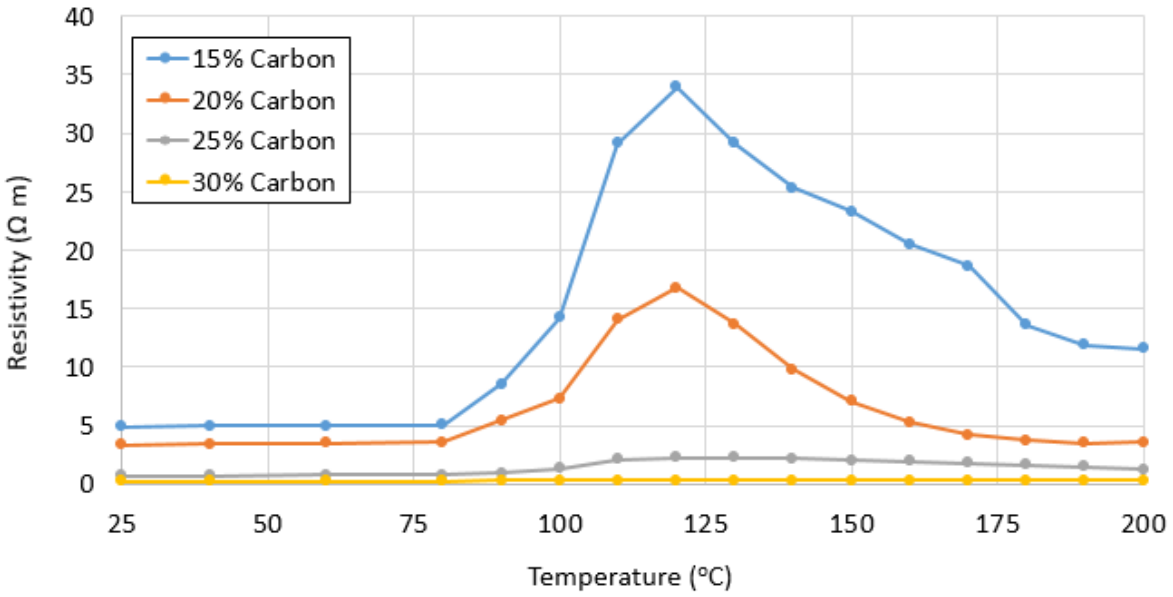

Figure 121: Resistivity against temperature for HDPE-carbon composites at varying carbon filler percentages by weight. Temperatures increased in intervals and allowed to reach temperature over 15 minutes. Resistivity measurements performed using PEIS between 200 kHz and 100 mHz at 10 mV sinus amplitude.

Not only were the room temperature resistivities an improvement on the previous PAN-carbon and PVDF-carbon samples, but the PTCR intensity was also greater than the PVDF-carbon data. From DSC data in Section 5.4.3, HDPE-carbon should experience a melting point between 103.9 °C and 106.2 °C. Initiation of the PTCR appeared before this at 80 °C to 90 °C, highlighting potential volume expansion prior to melting or hotspots leading to melting before the required

temperature of the oven was reached. The resulting PTCR intensity maximum occurred at 120 °C. From 15 % to 30 % filler content, the maximum values were: 6.9, 5.0, 3.3, and 1.4. After this maximum a NTCR was observed. The greater PTCR intensity experienced for HDPE-carbon samples than PVDF-carbon samples suggests a greater thermal expansion coefficient. However, additional studies were required to verify the expansion of the polymer-composite samples. Also in favour of HDPE against the PVDF composites was the far lower temperature for the maximum PTCR, 120 °C for HDPE as opposed to 180 °C for PVDF. Lower temperatures for the PTCR would result in a more prompt response to thermal runaway before excessive temperatures preventing unnecessary damage. All changes were reversible upon returning the polymer-composites to room temperature.

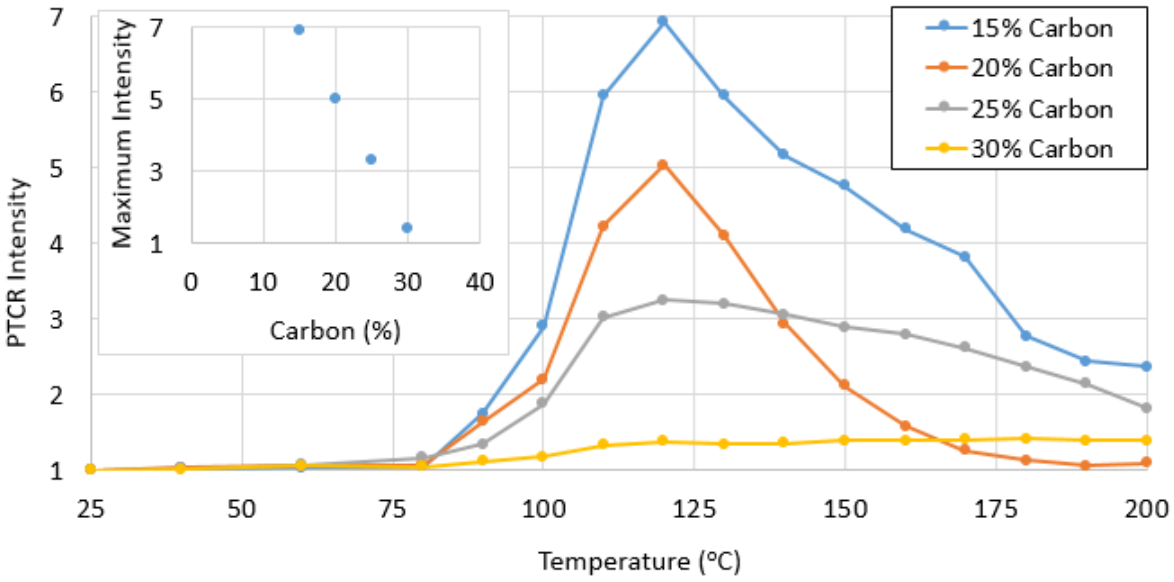

Figure 122: PTCR intensity against temperature for HDPE-carbon composites at varying carbon filler percentages by weight. Temperatures increased in intervals and allowed to reach temperature over 15 minutes. PTCR intensity calculated by dividing resistivity at each temperature by the resistivity at room temperature. The inset shows the PTCR intensity at peak against carbon filler percentage by weight.

5.5.5 Elevated temperature resistivity – LDPE

Resistivity against temperature data for LDPE-carbon composites is shown in Figure 123. Similarly to HDPE-carbon, the percolation threshold was identified near 25 % carbon by weight in Section 5.2.1. The selection of filler ratios was therefore: 15 %, 20 %, 25 %, and 30 %. Resistivity at room temperature was higher than HDPE-carbon, but still below PVDF-carbon and PAN-carbon. At 10 % carbon below the percolation threshold PVDF and PAN showed 47.7 Ω m and 100.6 Ω m

respectively. At the same difference from percolation HDPE-carbon showed 4.9 Ω m. LDPE-carbon showed 22.3 Ω m. For the full range of 15 % to 30 %, room temperature resistivity values were: 22.3 Ω m, 12.7 Ω m, 0.9 Ω m, and 0.4 Ω m. Thickness for the molten cast samples was typically far higher than the solvent cast. As a result, the HDPE and LDPE samples were far thicker than the PAN and PVDF samples. This led to excessively high resistance values at even lower resistivities. At 0.4 Ω m, the corresponding resistance was 2730 mΩ. This LDPE samples was around 58 times thicker than the solvent cast samples at 577 µm. At a similar thickness, the resistance would be 47 mΩ. This is of a similar magnitude to a typical lithium-ion battery at 25 mΩ [166].

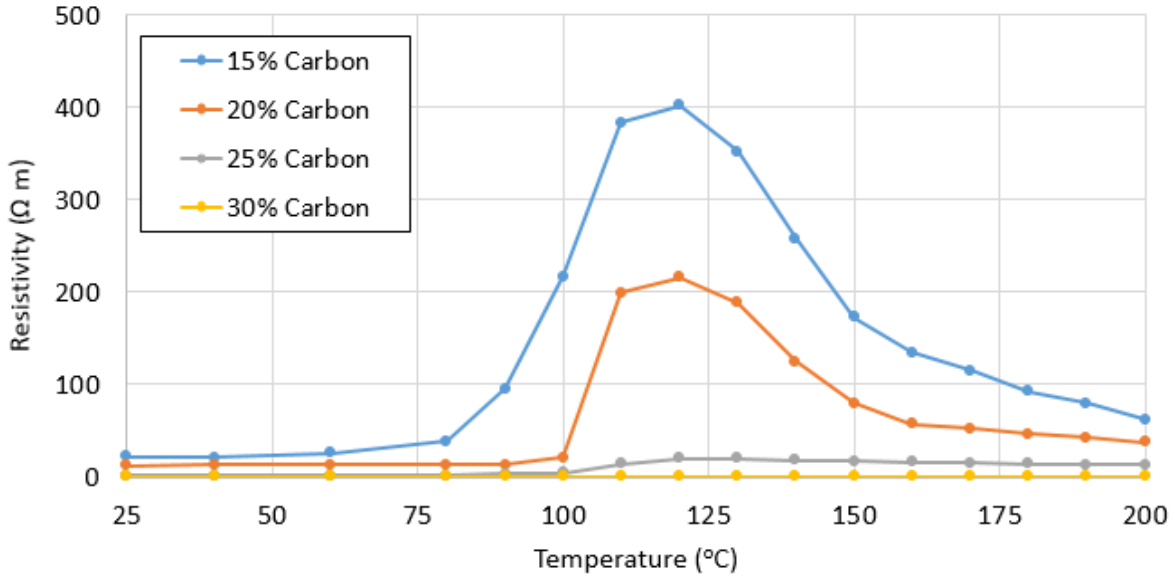

Figure 123: Resistivity against temperature for LDPE-carbon composites at varying carbon filler percentages by weight. Temperatures increased in intervals and allowed to reach temperature over 15 minutes. Resistivity measurements performed using PEIS between 200 kHz and 100 mHz at 10 mV sinus amplitude.

Both molten cast HDPE-carbon and LDPE-carbon composites provided far better room temperature resistivities than the solvent cast PAN-carbon and PVDF-carbon composites. Out of all of these LDPE-carbon also showed the greatest PTCR intensity, see Figure 124. The DSC data in Section 5.4.4 showed a melting point for LDPE-carbon between 101.0 °C and 103.4 °C. Initiation of PTCR appeared just below this temperature at 90 °C. Maximum PTCR intensity was observed at 120 °C before a NTCR was seen. This was at a suitable temperature to provide a response to thermal runaway, as opposed to PVDF that experienced a PTCR maximum at 180 °C. Maximum PTCR intensity values from 15 % to 30 % filler content were: 18.0, 17.0, 11.5, and 0.8. The highest value at 15 % for HDPE and LDPE respectively were 6.9 and 18.0. This implies a far greater thermal expansion for LDPE samples. All changes were reversible upon returning the polymer-composites to room temperature.

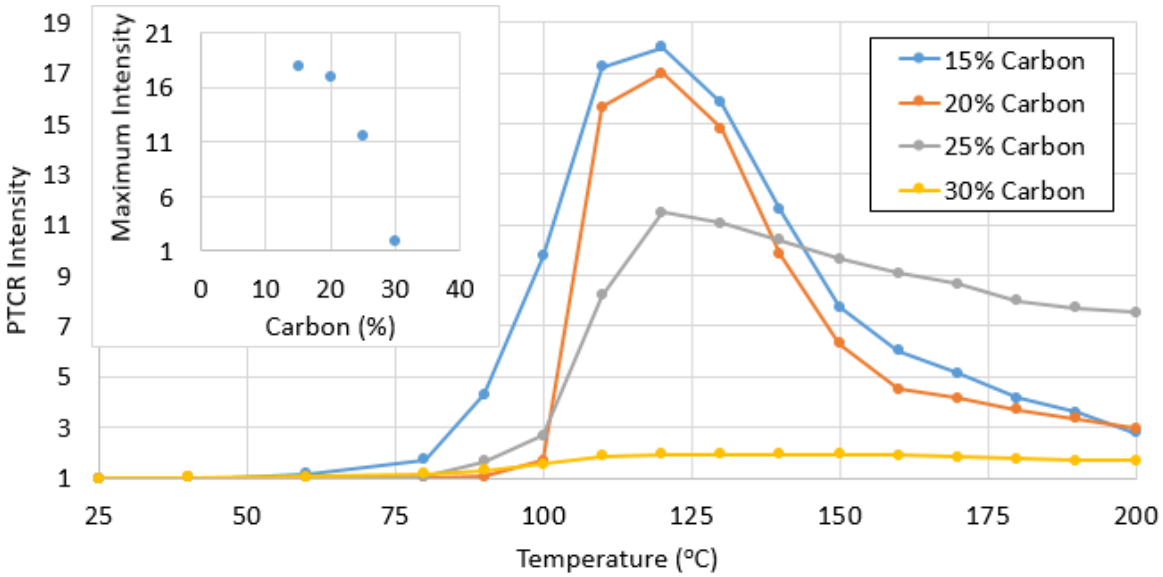

Figure 124: PTCR intensity against temperature for LDPE-carbon composites at varying carbon filler percentages by weight. Temperatures increased in intervals and allowed to reach temperature over 15 minutes. PTCR intensity calculated by dividing resistivity at each temperature by the resistivity at room temperature. The inset shows the PTCR intensity at peak against carbon filler percentage by weight.

5.5.6 Elevated temperature resistivity – polymer-TiC composites

From data on polymer-carbon composites, it appeared that the percolation threshold provided a low room temperature resistivity with a measurable PTCR effect. As such, polymer-TiC samples were tested at their threshold proportions. These were by percentage weight of filler: PAN-TiC 70 %, HDPE-TiC 70 %, and LDPE-TiC 70 %. The PVDF-TiC threshold was within 60 % to 70 % and therefore both percentages were studied.

Figure 125 shows room temperature resistivity against temperature for the polymer-TiC composites. The molten cast HDPE-TiC 70 % and LDPE-TiC 70 % both experienced a resistivity below 1 Ω m, at 0.3 Ω m and 0.4 Ω m respectively. Meanwhile the solvent cast composites of PAN-TiC 70 %, PVDF-TiC 60 %, and PVDF-TiC 70 % experienced 2.1 Ω m, 2.8 Ω m, and 2.1 Ω m. An identical relationship was seen for the polymer-carbon samples where the molten cast composites experienced far lower room temperature resistivities than the solvent cast by an order of magnitude for some samples.

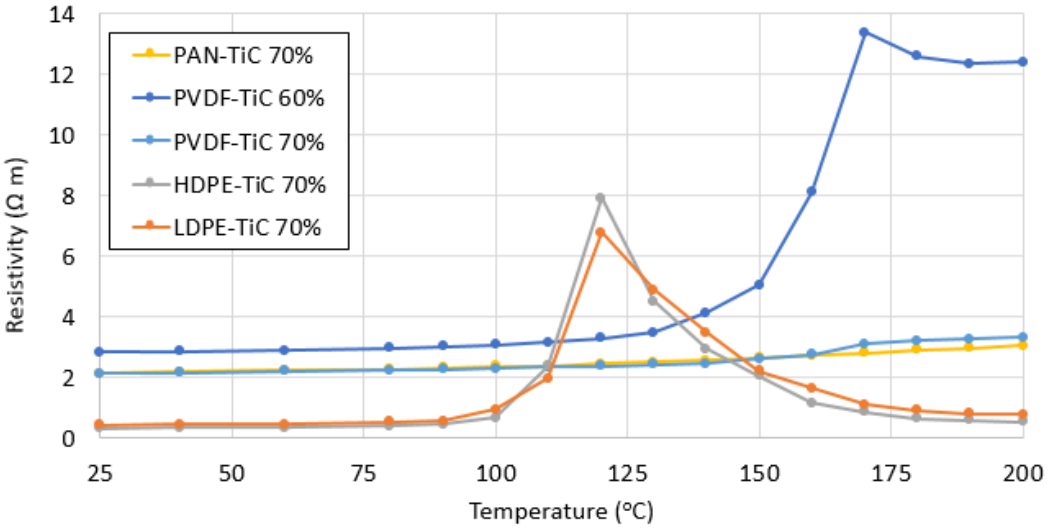

Figure 125: Resistivity against temperature for polymer-TiC composites. Samples were varied by the polymer matrix material and the percentage weight of TiC filler. These were: PAN-TiC with 70 % filler, PVDF-TiC with 60 % filler, PVDF-TiC with 70 % filler, HDPE-TiC with 70 % filler, and LDPE with 70 % filler. Temperatures increased in intervals and allowed to reach temperature over 15 minutes. Resistivity measurements performed using PEIS between 200 kHz and 100 mHz at 10 mV sinus amplitude.

PTCR intensity data is shown in Figure 126. PAN-TiC did not show a PTCR effect, same as PAN-carbon studies. PVDF-TiC with 70 % filler by weight also failed to show a PTCR, likely because the sample had a too extensive conductive framework from an excess of filler. For those samples that did show a PTCR, samples of similar room temperature resistivity for polymer-carbon data had substantially lower PTCR intensities as shown in Table 24. The result was a PTCR 3.9 times greater for the PVDF-TiC sample of comparable resistivity. For the molten cast samples, this change was even greater with HDPE-TiC and LDPE-TiC recording 17.5 and 19.6 times greater respectively. All changes were reversible upon returning the polymer-composites to room temperature.

Table 24: Polymer-carbon and polymer-TiC composite materials of comparable room temperature resistivity that showed a PTCR effect. The percentage of filler content, room temperature resistivity, and maximum PTCR intensity are all shown.

Carbon samples			TiC samples		
Composite material	**Room temperature resistivity**	**Maximum PTCR intensity**	**Composite material**	**Room temperature resistivity**	**Maximum PTCR intensity**
PVDF-carbon (20 %)	4.5 Ω m	1.2	PVDF-TiC (60 %)	2.8 Ω m	4.7
HDPE-carbon (30 %)	0.3 Ω m	1.4	HDPE-TiC (70 %)	0.3 Ω m	24.5
LDPE-carbon (30 %)	0.4 Ω m	0.8	LDPE-TiC (70 %)	0.4 Ω m	15.7

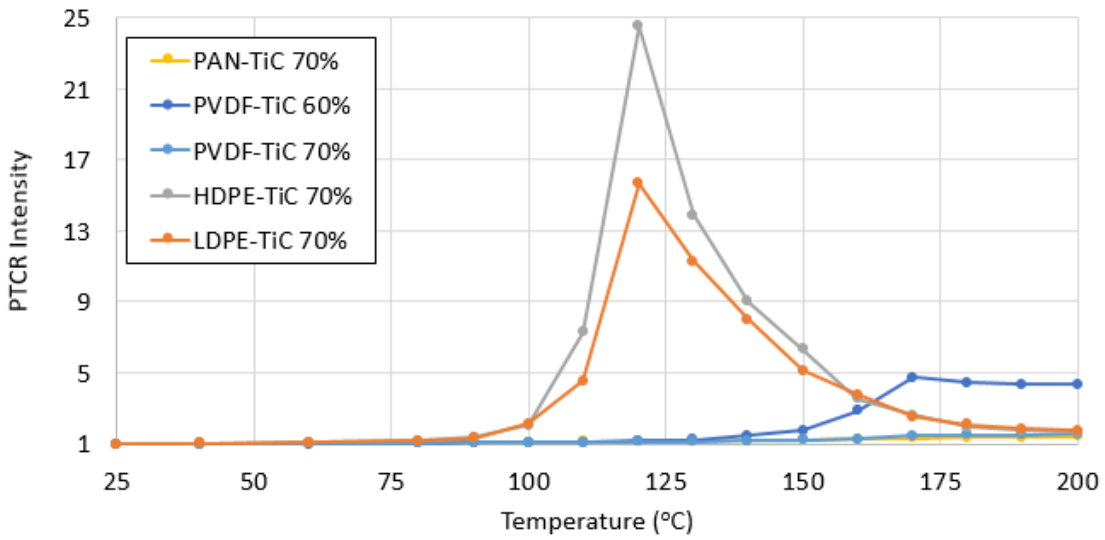

Figure 126: PTCR intensity against temperature for polymer-TiC composites. Samples were varied by the polymer matrix material and the percentage weight of TiC filler. These were: PAN-TiC with 70 % filler, PVDF-TiC with 60 % filler, PVDF-TiC with 70 % filler, HDPE-TiC with 70 % filler, and LDPE with 70 % filler. Temperatures increased in intervals and allowed to reach temperature over 15 minutes. PTCR intensity was calculated by dividing resistivity at each temperature by the resistivity at room temperature.

5.6 Initial lithium-ion half-cell study

For initial testing in lithium-ion studies, two LDPE-carbon ratios were selected to study the effect different room temperature resistivities may have on Swagelok performance. Figure 127 shows the elevated temperature resistivity study for the two LDPE-carbon samples used for these lithium-ion tests. Sample filler content was 20 % carbon and 25 % carbon by percentage weight. The resistivity study was performed in the absence of the lithium-ion half-cell, mimicking studies performed in Section 5.5.5.

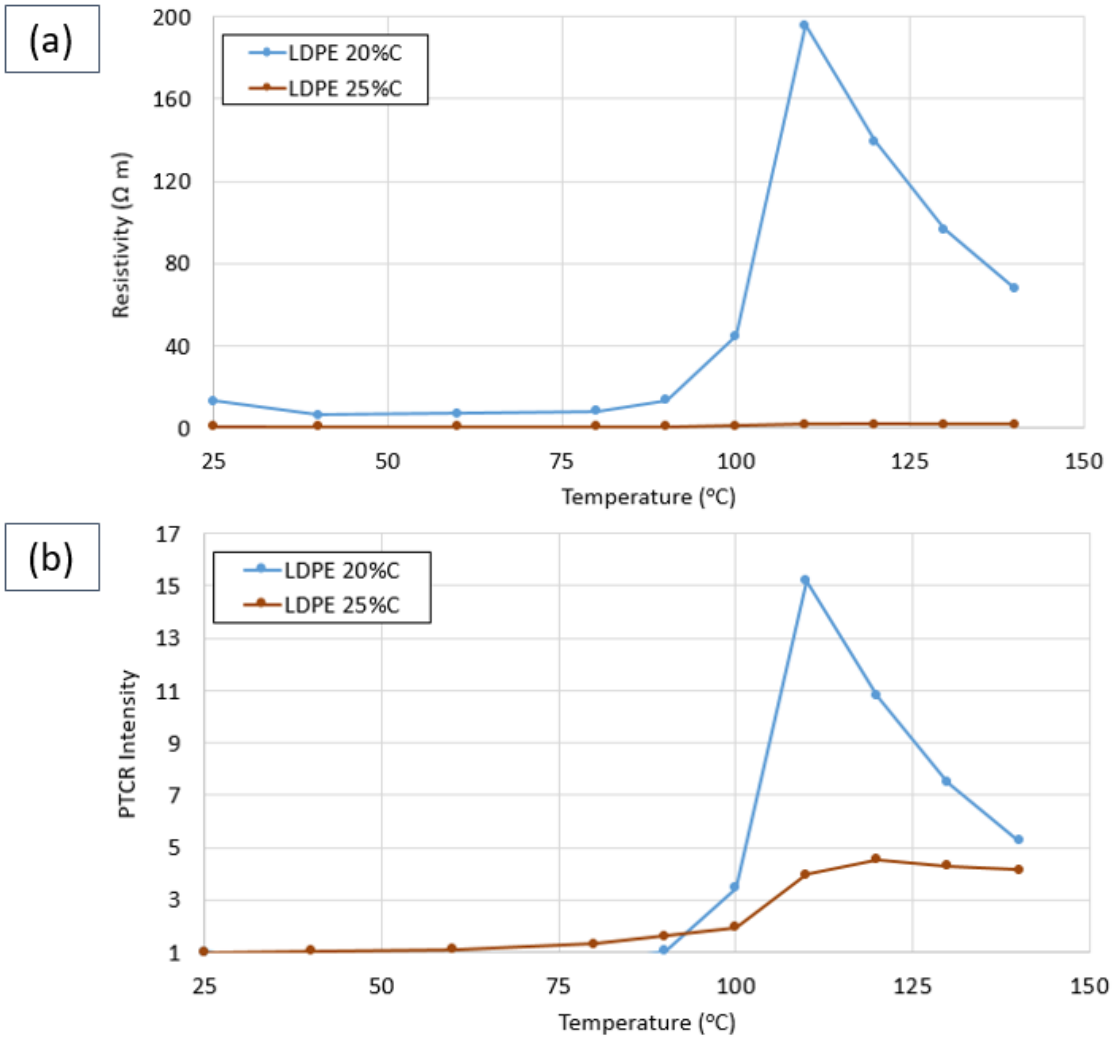

Figure 127: (a) Resistivity and (b) PTCR intensity data against temperature for LDPE-carbon composites used in initial lithium-ion half-cell testing. Temperatures increased in intervals and allowed to reach temperature over 15 minutes. Resistivity measurements performed using PEIS between 200 kHz and 100 mHz at 10 mV sinus amplitude. PTCR intensity calculated by dividing resistivity at each temperature by the resistivity at room temperature.

At room temperature, the 20 % carbon and 25 % carbon had resistivity values of 12.9 Ω m and 0.4 Ω m respectively. This corresponds to internal resistances of 12,892 mΩ and 2,860 mΩ. Peak PTCR appears between 110 °C and 120 °C. Maximum PTCR intensity for 20 % and 25 % samples were 15.1 and 4.5 respectively.

Cycling was performed in a standard Swagelok cell arrangement with a graphite-composite anode. A LDPE-carbon composite was placed between the anode and the current collector. The counter reference was a lithium metal electrode, electrolyte used was LP57. A C-rate of 0.1 C was used over 4 cycles for each sample. Figure 128 shows the first four cycle charge-discharge data for the two LDPE composites at room temperature. The first cycle of both showed a greatly extended charge capacity, reaching 675 mA h g^{-1} for 20 % and 662 ma h g^{-1} for 25 %. The resulting coulombic efficiencies were 48.7 % and 55.2 % respectively. This was far below normal behaviour for SEI formation during the first cycle. One possible cause was the intercalation of lithium ions into the carbon of the LDPE-carbon composite [167] [168] [169] [170]. However, there was no effect of this on the rest of the data, no increase in discharge capacity was observed and this phenomenon only occurred during the first cycle. Should the intercalation of lithium into carbon be the cause then this can be greatly reduced by decreasing the thickness of the polymer-carbon composites to reduce the mass of carbon present. Other than this, the samples appeared to perform similar to standard graphite cycling reaching 372 mA h g^{-1} for 20 % and 366 mA h g^{-1} for 25 %. Graphite theoretical capacity is 372 mA h g^{-1}.

A study was attempted to see the effects of elevated temperatures on lithium cycling. A shutdown effect was observed, however no capacity was returned after returning to room temperature. This was unexpected as all elevated temperature studies in Section 5.5.5 maintained performance after heating and did not have any significant structural changes despite having been melted at elevated temperatures. However, within the lithium-ion half-cell arrangement the LDPE-carbon was forced out and coated the entire current collector, see Figure 129. It was unclear if the catastrophic failure of the cell was due to the PTCR effect of the binder or from the graphite-composite anode being covered by LDPE.

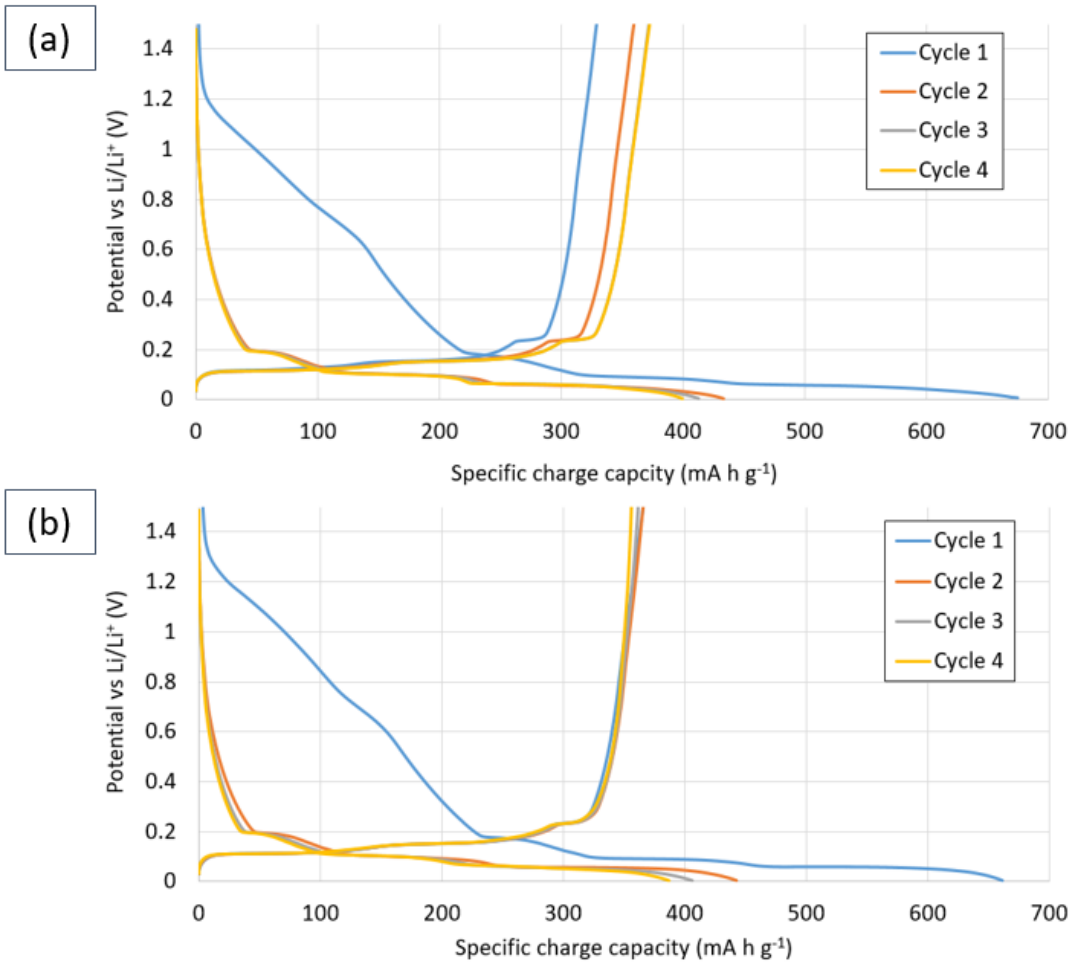

Figure 128: Galvanostatic cycling of graphite-composite ink electrodes backed by a conductor of (a) LDPE-carbon with 20 % filler by weight, and (b) LDPE-carbon with 25 % filler by weight. Cycling was performed for four cycles at a C-rate of 0.1 C at room temperature. A lithium metal counter/reference electrode was used in LP57 electrolyte (1M $LiPF_6$ in EC/EMC (vol:vol = 1:1)).

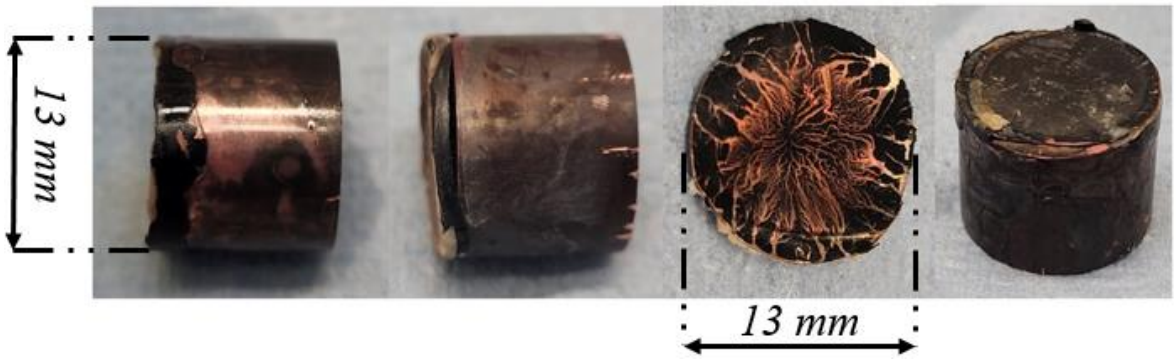

Figure 129: Current collector after being exposed to 120 °C. The current collector was used in lithium-ion half-cells with a LDPE-carbon of 20 % filler by weight between the electrochemistry and the current collector. From left to right, the current collector at: side-on, reverse of the side-on, birds-eye view, and isometric view.

5.7 Conclusion

The percolation thresholds for several polymers (PAN, PVDF, HDPE, and LDPE) were identified with one of two filler materials (carbon, and TiC). Polymers with the carbon filler tended to have lower percolation thresholds around 15 % to 25 %, whilst TiC gave much higher thresholds from 60 % to 70 %. This difference has been tentatively linked to particle sizes, with the carbon particles typically having around 100 nm whilst the TiC varied from 20 nm to 100 nm. These particle sizes were decided by supplier and can be controlled through laboratory means if needed. Smaller particle sizes have been linked to higher percolation thresholds in past studies [51]. Naturally, these higher filler ratios for TiC formed a more brittle polymer-composite and led to greater variation in surface roughness for solvent cast methods. A post-treatment method of compression under temperature could be employed to improve the uniformity in the surfaces.

Both the solvent and molten cast samples appeared to have uniform particle distribution in SEM images for both carbon and TiC fillers. The most prominent difference was the thickness of composites produced by the two methods with the molten cast being above 500 µm while the solvent cast was close to 10 µm. The molten cast samples were produced by hand and so reducing thickness was difficult, employing a mechanical compression moulding setup that can control temperature and pressure would likely allow thinner molten cast samples.

DSC measurements provided useful insight into how transition temperatures were affected by the presence of fillers. Whilst there was not a great variation when switching between carbon and TiC fillers, there was a significant difference depending on the transition temperature being studied. The glass transition of PAN increased with increasing filler content for both carbon and TiC composites. Meanwhile, the melting point of almost all other polymer-composites decreased with increasing filler content. The only exception was that for PVDF-carbon composites, potentially requiring a broader range of filler contents from 0 % to 90 % carbon to verify if melting point continues to increase with increasing filler content.

The transition temperatures identified in DSC played a significant role in later elevated temperature studies on the PTCR effect of the composites. The glass transition of PAN did not appear significant enough to initiate a PTCR, but all materials that experienced a melting point within the elevated temperature range did exhibit a PTCR around the percolation threshold of the material. This was likely because of the thermal expansion of glass transition being of second-order whilst the melting point expansion is of first-order. First order expansions typically have a large step in volume at the melting point whilst second order only increases in thermal expansion

rate. An additional study to quantify how much thermal expansion occurs around these transitions would aid in this understanding. It has been shown in other studies that glass transition materials can experience a PTCR effect [33]. Between the different polymers, HDPE and LDPE showed the most significant PTCR intensity with the lowest room temperature resistivities when compared with PVDF. PVDF also unfortunately had a very high melting point and so PTCR maximum was measured at 180 ^{o}C compared to the HDPE and LDPE at 120 ^{o}C. TiC filler composites showed improved performance compared to carbon filler composites with increased PTCR intensity for the same room temperature resistivity, implying a greater potential for the TiC filler in shutdown materials.

LDPE-carbon composites were briefly tested in a half-cell arrangement. The electrochemistry of graphite against lithium appeared largely unaffected with the exception of the first charge cycle where far greater capacities than typical were drawn. This may be due to the capacity introduced by carbon within the LDPE-composite material. This could be alleviated by reducing the thickness of the composite through better manufacturing techniques. The added benefit would also be a lower internal resistance introduced by the LDPE-carbon at room temperature allowing the cell to function closer to ideal. Unfortunately, Swagelok studies were not further continued due to a melt problem encountered at higher temperatures where the LDPE-carbon composite coated the entirety of the anode and current collector. Further studies should look at controlling this effect by applying thinner composite films through varying manufacture and post-treatment. Should this problem be solved, lithium-ion cell testing can be further explored at elevated temperatures. Should the PTCR effect of the LDPE-carbon fail to produce a complete shutdown of the cell, the increase in resistance should be measureable to the point that an external electronic system can detect and manually shutdown the cell. Additional studies into the trade-off between room temperature resistivity and maximum PTCR intensity with their effects on cell capacity would be beneficial to the practicality of the percolating composites.

Chapter 6 Conclusion

The overall aim of this research was to *improve lifetime performance and safety of lithium-ion batteries through the application of functional polymer materials to prevent thermal runaway*. PTCR effects to induce a shutdown were investigated to facilitate this aim. To this end two different material systems were studied, electrodeposited film coatings of PAN and percolating polymer-composites. Ideally these materials would fulfil the role of inducing a PTCR with minimal impact on the capacity and other performance metrics of the electrode materials.

Electrodeposited PAN coating production onto graphite-composite anodes was studied in Chapter 3 along with an in depth study on the effects of said PAN coatings on lithium-ion half-cell performance in Chapter 4. Several literature has been published investigating electrodeposition methods for PAN onto glassy carbon [41] [42] and other conductive surfaces [67]; however, no attempts had been performed onto standard electrode materials for use within lithium-ion cells. Standard electrodes are not typical planar surfaces as often studied for electrodeposition, but are a composite of powders. The materials that form an electrode are typically: active materials, conductive additives, and binders. The stability of these materials under electrodeposition techniques was unknown. Therefore, the novelty for electrodeposited PAN-based gel-electrolytes onto graphite-composite anodes within lithium-ion cells was explored.

Work in Chapter 3 showed electrodeposition of PAN onto a graphite-composite anode was possible whilst maintaining the structure of the anode itself. An understanding of the underlying electrochemistry of the PAN coatings on graphite-composite anodes was established. An initiator was required for PAN nucleation to occur, in the case for these studies this was superoxide anions produced via electro-reduction of oxygen. An applied potential was also required to facilitate film growth even after the production of superoxide. Film growth was found to be non-faradaic, therefore film thicknesses could not be directly controlled by passing a known amount of charge through the electrodes. Another method of controlling film thickness via electrodeposition is by controlling the concentration of the depositing solvent [70]. However, a commonly used solvent for the AN monomers, acetonitrile, was found to delaminate the composite electrode ink from the substrate surface due to swelling of the polymeric binder. This means control of monomer concentration was difficult. Water contamination was found to greatly promote PAN deposit mass but caused blistering of the electrode ink surface and facilitated side reactions such as polymerisation in solution that was not adhered to the electrode surface. It is advised that any future upscaling of the electrodeposition procedure would therefore have to be performed within a dry environment, something easily achievable within a dry room.

Chapter 3 further expanded upon work by Lacey *et al.* [41] and reliably quantified the film growth of PAN electrodeposits to allow controlled film thicknesses as well as studying the impurities created by the manufacturing route. Film thickness growth was apparent as a linear pattern between 1 and 100 seconds of having a potential applied during chronoamperometry studies, with good coverage and minimal cracking of the PAN films appearing around 20 seconds. Performing depositions at more negative potentials produced PAN films with less dehydrogenation impurities but more cyclization impurities. The increase in cyclization to dehydrogenation resulted in more thermally stable PAN films with less mass loss in TGA studies. Thermal degradation is detrimental for preventing pressure build-ups and thermal runaway within a lithium-ion cell so more negative potentials were concluded to be more desirable. However, thermal degradation resulted in around 10 % higher mass loss than commercial PAN standards. Further refinement of the level of impurities is therefore possible and advised by exploring deposition potential and other parameters such as monomer concentration.

The chemistry and structure of these PAN films was far simpler compared to other competitive polymers used to prevent thermal runaway. For instance, commonly used Celgard separators make use of a trilayer of PP/PE/PP that are formed through several manufacturing stages such as coating and calendaring laminated layers [36] as opposed to a single-step electrodeposited PAN layer. For electrodeposited PAN, no cross-linking or co-polymerisation was required unlike PAN separator materials for thermal runaway prevention reported on by Huai *et al.* [34]. The Teflon cell design employed in many of the electrodepositions produced electrodes of uniform film thickness across a circular area. Altering the size and shape of the deposition area is simply tailorable by editing the Teflon cell design and could be used in future manufacture to facilitate electrodepositions to any two-dimensional geometry required, such as that of a pouch cell.

Dry cracking was a persistent problem for the PAN films. Several methods were identified that improved this, including producing thinner films by reducing deposition time and two post-treatment methods. Annealing removed all cracking by encouraging polymer chain movement. Redeposition at lower deposition times also removed cracks. However, both the post-treatment methods adversely affected the uniformity of the PAN films. It was found that the presence of air above the electrodeposition chemistry facilitated the production of clear and continuous PAN films, with white discontinuous films produced in the absence of air. Annealing of both morphologies produced clear films and facilitated polymer chain movement causing changes in the film structure. It was these clear and white films, either annealed or non-annealed, that were tested within a lithium-ion half-cell arrangement. Standard electrodes of 11 mm diameter were punched out from the graphite-composite deposition areas and studied within a Swagelok cell arrangement.

Graphite and annealed graphite samples were found to have capacity near to theoretical in Chapter 4. On the other hand for graphite samples with an electrodeposited PAN film, white PAN films and any annealed PAN films showed incredibly poor capacity below 5 % of the theoretical. Only non-annealed clear PAN films showed a suitable capacity for lithium-ion performance that decreased with increasing film thickness. Capacity of pristine graphite was 366 mA h g^{-1} (98 % theoretical) and fell to 186 mA h g^{-1} (50 % theoretical) for graphite coated with 32 µm PAN, or a fall of 5.63 mA h g^{-1} per µm. This result was promising as annealing the PAN films at temperature clearly reduced capacity of the cell, whilst annealing the pristine graphite had negligible effect on performance. Should exposure to annealing temperature during cell cycling produce a similar effect on a non-annealed clear PAN sample then a shutdown effect would be easily obtained in response to thermal runaway conditions. The reasons for lower capacity of PAN coated samples were linked to greater uncompensated resistances to ionic transport. Annealed samples in particular were thought to reduce porosity due to polymer chain rearrangement resulting in poorer infiltration of the LP57 electrolyte. However, capacities as close to theoretical were still the ideal for the non-annealed clear PAN coated graphite-composites. Further investigations into the tailoring the pore structure and film thickness are necessary to produce an electrode that is competitive to standard materials.

Studies into the shutdown possibilities of the graphite-composites coated with PAN in Chapter 4 found an inverse relationship between capacity at room temperature and the intensity of the shutdown with changing film thickness. Thinner film samples provided greater capacity under normal operating conditions whilst thicker films proved better at shutdown receiving far lower capacity between 80 °C and 100 °C. This loss of capacity was not due to thermal degradation, as electrodeposited PAN films were found to be stable up until 120 °C despite the presence of impurities. Pristine graphite cycling was also found to be stable up until 120 °C. Therefore, the shutdown was likely a response due to the glass transition of PAN around 95 °C [35]. This shutdown was irreversible upon returning to room temperature. Whilst this was not necessarily a problem, as other thermal runaway prevention methods such as Celgard separators result in the permanent shutdown of the cell, it would be ideal to recover the cell after a thermal runaway event as damage is often caused by external factors such as overcharging and overpotentials.

Coulombic efficiencies of samples that returned to room temperature were comparable to annealed samples under normal operating conditions implying an annealing process had occurred for the non-annealed clear PAN films at elevated temperatures. The shutdown was therefore due to the structural changes that occurred during the annealing process. Temperature of shutdown around 80 °C to 100 °C was competitive to other shutdown coatings, with LCO-P3OT by Ji *et al.* [31] seeing shutdown around 90 °C down to 4 % theoretical. Baginska *et al.* [32] reported on

shutdown for graphite coated with PE microspheres at 110 ^{o}C, this shutdown was incredibly effective reporting a remaining 7 % theoretical capacity. Celgard shutdown separators experience shutdown around 130 ^{o}C [36]. For the graphite-composites coated with PAN in Chapter 4, capacity only fell to under 5 % for samples of 24 µm thickness PAN, samples around 18 µm to 22 µm had around 50 % capacity. 9 µm saw a fall only down to 85 % of the maximum capacity.

Despite thinner films showing poorer shutdown it may be possible to still pursue them in practical applications to prevent thermal runaway. Further studies are required, but a complete shutdown is not necessary to prevent thermal runaway. External systems can be used to detect measurable changes in resistance and manually turn off the cell. A study of the impedance of the PAN films introduced at these elevated temperatures was not performed but a measurable increase in resistance could be monitored by a battery management system to isolate cells, a potential area for future study for practical application. Alternatively, research into improving capacity for thicker films could alleviate this issue. By better understanding the exact working mechanism for the shutdown the PAN film porosity could be tailored or the pore structure enhanced in some way to enhance performance at ambient temperatures.

The other set of materials studied to prevent thermal runaway, the percolating composite route, also showed promise. The manufacture of these percolating composites was studied in Chapter 5. PAN, PVDF, HDPE, or LDPE polymer matrix materials were mixed with carbon or TiC conductive fillers. The resultant composites were studied for any PTCR response resulting from an increase in resistance to electron transport, as opposed to the resistance to ionic transport experienced for electrodeposited PAN films. These percolating composites were therefore suited as a coating of current collectors rather than the electrodes of the lithium-ion cell.

Percolation thresholds were identified for each of the composites studied in Chapter 5, with carbon filler composites experiencing this threshold around 45 % to 55 % less mass by weight than TiC filler composites. A link was made between this result and the particle sizes of the fillers, carbon filler was uniformly at 100 nm particle size whilst TiC varied between 20 nm and 100 nm. For these studies particle size was determined by the supplier. However, further studies using carbon and TiC fillers of the exact same size would be ideal to confirm if the change in percolation threshold was indeed due to particle size or some inherent property of the material itself. TiC composites around the percolation threshold were naturally more brittle due to the lower mass percentage of the polymer matrix leading to greater variation in surface roughness. Additionally, the molten cast HDPE and LDPE composites were much thicker than the solvent cast PAN and PVDF composites. Both these issues may be addressed through compression moulding at high temperature after forming the composite, such post-treatment is recommended for further study.

PTCR responses were found to occur near to the transition temperatures of the composites. Whilst no PTCR was identified for the glass transition of PAN composites, a PTCR was identified for the melting point of the other materials. PTCR of percolating composites is caused by the thermal expansion of the polymer matrix and it was likely that the thermal expansion of the PAN material was much less as it is a second-order expansion leading to an increase change in the rate of volume with temperature. Meanwhile, melting points are a first order expansion involving a large increase in volume at the transition point. Additional studies are required to quantify the thermal expansion of different composites to verify this understanding. It should be noted that PTCR responses have been previously reported for glass transition materials, poly(styrene-co-acrylonitrile composites were studied by Kar *et al.* [33] and found to have a PTCR near to the glass transition at 107 ^{o}C. Therefore, glass transition materials such as PAN should not be ruled out for percolation applications. Filler materials can be hugely influential, Kar *et al.* [33] reported 130 ^{o}C for a PTCR with carbon particles and 97 ^{o}C for PTCR with stainless steel particles. Therefore, PTCR may be induced in a PAN-composite with selection of alternative filler materials and may be a subject of future study.

The effect of filler materials on transition temperatures in Chapter 5 was quantified with DSC measurements. TiC and carbon fillers largely had the same effect, increasing the temperature of glass transition whilst decreasing the temperature of melting. TiC composites were found to have a far greater PTCR intensity than carbon composites for the same room temperature resistivity, indicating a far greater possibility for application of polymer-TiC in the prevention of thermal runaway. This was a very significant result as there is currently limited research papers on the effects of TiC in such an application with many focusing solely on the room temperature percolation thresholds of TiC composites. The data on polymer-composites with PAN, PVDF, HDPE, and LDPE is therefore significant to help the understanding of polymer-TiC and with further research TiC may prove a valuable competitor to other conductive filler alternatives.

Whilst both PVDF and PE experienced a PTCR, the temperature for maximum intensity of the PVDF was too extreme. PVDF experienced a maximum at 180 ^{o}C while HDPE and LDPE experienced a maximum at 120 ^{o}C. Therefore, LDPE was selected for initial lithium-ion studies. Carbon was chosen as the filler due to known electrochemical stability. The results of these studies showed a far greater capacity of the first charge cycle of LDPE-carbon. This was likely a result of the significant carbon mass within the composite. Possible solutions involve reducing the thickness of the composite through manufacturing or post-processing methods such as compression moulding. Thinner composites would naturally reduce the volume of carbon present. This may also remove the issues encountered of the polymer matrix melt covering the anode.

However, this would also impact the resistance of the composite perhaps effecting the magnitude of resistance at PTCR.

Future work should be considered to reduce thickness of the LDPE composites before application within a Swagelok arrangement. Lithium-ion testing should then be performed to gather data similar to that in Chapter 4. Comparisons may then be made with the PAN electrodeposited films on normal operating performance and the effectiveness of shutdown. Additionally, data may be gathered on the change in resistance at elevated temperatures. Should this change be measureable then external system may be employed to shut down the cell, such as a battery management system to monitor the impedance of individual cells. This would allow any trade-off between room temperature capacity of the cell and maximum PTCR intensity to be minimised for the best possible performance of both metrics.

Chapter 7 References

[1] D. Ihm, J. Noh and J. Kim, “Effect of polymer blending and drawing conditions on properties of polyethylene separator prepared for Li-ion secondary battery,” *Journal of Power Sources,* vol. 109, pp. 388-393, 2002.

[2] X. Feng, M. Ouyang, X. Liu, L. Lu, Y. Xia and X. He, “Thermal runaway mechanism of lithium ion battery for electric vehicles: A review,” *Energy Storage Materials,* vol. 10, pp. 246-267, 2018.

[3] L. Gong, M. Nguyen and E. Oh, “High polar polyacrylonitrile as a potential binder for negative electrodes in lithium ion batteries,” *Electrochemistry Communications,* vol. 29, pp. 45-47, 2013.

[4] A. Stephan and K. Nahm, “Review on composite polymer electrolytes for lithium batteries,” *Polymer,* vol. 47, pp. 5952-5964, 2006.

[5] A. Stephan, “Review on gel polymer electrolytes for lithium batteries,” *European Polymer Journal,* vol. 42, pp. 21-42, 2006.

[6] J. Song, Y. Wang and C. Wan, “Review of gel-type polymer electrolytes for lithium-ion batteries,” *Journal of Power Sources,* vol. 77, pp. 183-197, 1999.

[7] A. Cholewinski, P. Si, M. Uceda, M. Pope and B. Zhao, “Polymer Binders: Characterization and Development toward Aqueous Electrode Fabrication for Sustainability,” *Polymers,* vol. 13, p. 631, 2021.

[8] H. Yang, W. Leow and X. Chen, “Thermal-Responsive Polymers for Enhancing Safety of Electrochemical Storage Devices,” *Advanced Materials,* vol. 30, pp. 1-8, 2018.

[9] L. Xia, L. Zhu, H. Zhang and X. Ai, “A positive-temperature-coefficient electrode with thermal protection mechanism for rechargeable lithium batteries,” *Chinese Science Bulletin,* vol. 57, no. 32, pp. 4205-4209, 2012.

[10] L. Xia, S.-L. Li, X.-P. Ai, H.-X. Yang and Y.-L. Cao, "Temperature-sensitive cathode materials for safer lithium-ion batteries," *Energy & Environmental Science,* vol. 4, pp. 2845-2848, 2011.

[11] A. Le, M. Wang, D. Noelle, Y. Shi and Y. Qiao, "Mitigating thermal runaway of lithium-ion battery by using thermally sensitive polymer blend as cathode binder," *Journal of Applied Polymer Science,* vol. 135, pp. 45737-45747, 2018.

[12] J. Hewson and S. Domino, "Thermal runaway of lithium-ion batteries and hazards of abnormal thermal environments," 9th U.S. National Combustion Meeting, Cincinnati, 2015.

[13] C. Orendorff, "The Role of Separators in Lithium-Ion Cell Safety," The Electrochemical Society Interface, 2012.

[14] C. Criddle, "Why is the Samsung Galaxy Note 7 catching fire? The lithium-ion battery explained," The Telegraph, 11 October 2016. [Online]. Available: https://www.telegraph.co.uk/technology/2016/10/11/why-is-the-samsung-galaxy-note-7-catching-fire-the-lithium-ion-b/. [Accessed 13 January 2019].

[15] R. Whitwam, "Tesla Battery Reignited Days After Fatal Model X Crash," Extreme Tech, 14 May 2018. [Online]. Available: https://www.extremetech.com/extreme/269169-tesla-battery-reignited-days-after-fatal-model-x-crash. [Accessed 13 January 2019].

[16] "Exploding hoverboard battery fire leaves Smethwick mum in coma," BBC, 16 November 2021. [Online]. Available: https://www.bbc.co.uk/news/uk-england-birmingham-59304020. [Accessed 11 March 2022].

[17] "Accident analysis of the Beijing lithium battery explosion which killed two firefighters," The International Association of Fire Services (CTIF), 25 May 2021. [Online]. Available: https://www.ctif.org/news/accident-analysis-beijing-lithium-battery-explosion-which-killed-two-firefighters. [Accessed 11 March 2022].

[18] L. Kong, C. Li, J. Jiang and M. Pecht, "Li-Ion Battery Fire Hazards and Safety Strategies," *Energies,* pp. 1-11, 2018.

[19] Z. Chen, P.-C. Hsu, J. Lopez, Y. Li, J. To, N. Liu, C. Wang, S. Andrews, J. Liu, Y. Cui and Z. Bao, "Fast and reversible thermoresponsive polymer switching materials for safer batteries," *Nature Energy,* vol. 1, pp. 1-8, 2016.

[20] E. Asare, A. Basir, W. Tu, H. Porwal, H. Zhang, Y. Liu, J. Evans, M. Newton, T. Peijs and E. Bilotti, "Effect of mixed fillers on positive temperature coefficient of conductive polymer composites," *Nanocomposites,* vol. 2, pp. 58-64, 2016.

[21] Q. Wang, J. Sun, X. Yao and C. Chen, "Thermal Behaviour of Lithiated Graphite with Electrolyte in Lithium-Ion Batteries," *Journal of Electrochemical Soceity,* vol. 153, pp. A329-A333, 2006.

[22] N. Ryall and N. Garcia-Araez, "Highly Sensitive Operando Pressure Measurements of Li-ion Battery Materials with a Simply Modified Swagelok Cell," *Journal of The Electrochemical Society,* vol. 167, 2020.

[23] Q. Wang, J. Sun, X. Yao and C. Chen, "Thermal stability of LiPF6/EC+DEC electrolyte with charged electrodes for lithium ion batteries," *Thermochimica Acta,* vol. 437, pp. 12-16, 2005.

[24] M. Richard and J. Dahn, "Accelerating rate calorimetry study on the thermal stability of lithium intercalacted graphite in electrolyte. I. Experimental," *Journal of the Electrochemical Society,* vol. 146, pp. 2068-2077, 1999.

[25] R. Spotnitz and J. Franklin, "Abuse behavior of high-power, lithium-ion cells," *Journal of Power Sources,* vol. 113, pp. 81-100, 2003.

[26] B. Lei, W. Zhao, C. Ziebert, N. Uhlmann, M. Rohde and H. Seifert, "Experimental Analysis of Thermal Runaway in 18650 Cylindrical Li-Ion Cells Using an Accelerating Rate Calorimeter," *Batteries,* vol. 3, 2017.

[27] A.-W. Golubkov, F. Fuchs, J. Wagner, H. Wiltsche, C. Stangl, G. Fauler, G. Voitic, A. Thaler and V. Hacker, "Thermal-runaway experiments on consumer Li-ion batteries with metal-oxide and olivin-type cathodes," *RSC Advances,* vol. 4, pp. 3633-3642, 2014.

[28] C.-Y. Jhu, Y.-W. Wang, C.-Y. Wen and C.-M. Shu, "Thermal runaway potential of LiCoO2 and Li(Ni1/3Co1/3Mn1/3)O2 batteries determined with adiabatic calorimetry methodology," *Applied Energy,* vol. 100, pp. 127-131, 2012.

[29] P. Balakrishnan, R. Ramesh and T. Kumar, “Safety mechanisms in lithium-ion batteries,” *Journal of Power Sources,* vol. 155, pp. 401-414, 2006.

[30] “MP, Tg, and Structure of Common Polymers,” Perkin Elmer, [Online]. Available: https://resources.perkinelmer.com/corporate/cmsresources/images/44-74863tch_mptgandstructureofcommonpolymers.pdf. [Accessed 23 November 2020].

[31] W. Ji, F. Wang, D. Liu, J. Qian, Y. Cao, Z. Chen, H. Yang and X. Ai, “Building thermally stable Li-ion batteries using a temperature-responsive cathode,” *Journal of Materials Chemistry A,* vol. 4, pp. 11239-11246, 2016.

[32] M. Baginska, B. Blaiszik, R. Merriman, N. Sottos, J. Moore and S. White, “Autonomic shutdown of lithium-ion batteries using thermoresponsive microspheres,” *Advanced Energy Materials,* vol. 2, pp. 583-590, 2012.

[33] P. Kar, N. Shrivastava, S. Mallick and B. Khatua, “PTCR charcteristic of poly(styrene-co-acrylonitrile) copolymer/stainless steel powder composites,” *Journal of Applied Polymer Science,* vol. 124, pp. 607-615, 2012.

[34] Y. Huai, J. Gao, Z. Deng and J. Suo, “Preparation and characterization of a special structural poly(acrylonitrile)-based microporous membrane for lithium-ion batteries,” *Ionics,* vol. 16, pp. 603-611, 2010.

[35] “PROPERTIES OF POLYACRYLONITRILE,” Granado Institute of Polyacrylonitrile Research, [Online]. Available: https://www.igtpan.com/propriedade-poli.asp. [Accessed 23 November 2020].

[36] X. Huang, “Separator technologies for lithium-ion batteries,” *Journal of Solid State Electrochemistry,* vol. 15, pp. 649-662, 2011.

[37] D. Doughty and A. Pesaran, “Vehicle battery safety roadmap guidance,” National Renewable Energy Laboratory, 2012.

[38] X. Feng, M. Fang, X. He, M. Ouyang, L. Lu and H. Wang, “Thermal runaway features of large format prismatic lithium ion battery using extended volume accelerating rate calorimetry,” *Journal of Power Sources,* vol. 255, pp. 294-301, 2014.

[39] D. Wu, C. Shi, S. Huang, X. Qiu, H. Wang, Z. Zhan, P. Zhang, J. Zhao, D. Sun and L. Lin, “Electrospun nanofibers for sandwiched polyimide/poly(vinylidene fluoride)/polyimide

separators with the thermal shutdown function," *Electrochimica Acta,* vol. 176, pp. 727-734, 2015.

[40] Y.-M. Lee, J.-W. Kim, N.-S. Choi, J.-A. Lee, W.-H. Seol and J.-K. Park, "Novel porous separator based on PVDF and PE non-woven matrix for rechargeable lithium batteries," *Journal of Power Sources,* vol. 139, pp. 235-241, 2005.

[41] M. Lacey, M. Sosna and J. Owen, "An electrochemical quartz crystal microbalance study of poly(acrylonitrile) deposition initiated by electrogenerated superoxide," *Electrochimica Acta,* vol. 29, pp. 23-26, 2013.

[42] G. El-Enany, M. Lacey, P. Johns and J. Owen, "In situ growth of polymer electrolytes on lithium ion electrode surfaces," *Electrochemistry Communications,* vol. 11, pp. 2320-2323, 2009.

[43] T. Winie, A. Arof and S. Thomas, Polymer Electrolytes Characterization Techniques and Energy Applications, Wiley-VCH, 2019.

[44] J. Kalhoff, G. Eshetu, D. Bresser and S. Passerini, "Safer electrolytes for lithium-ion batteries: state of the art and perspectives," *ChemSusChem,* vol. 8, pp. 2154-2175, 2015.

[45] M. Wakihara, Y. Kadoma, N. Kumagai, H. Mita, R. Araki and K. Ozawa, "Development of nonflammable lithium ion battery using a new all-solid polymer electrolyte," *Journal of Solid State Electrochemistry,* vol. 16, pp. 847-855, 2012.

[46] D. Wright, N. Garcia-Araez and J. Owen, "Review on high temperature secondary Li-ion batteries," *Energy Procedia,* vol. 151, pp. 174-181, 2018.

[47] P. Novák and P. Podhájecký, "A high-temperature lithiumcopper oxide cell with a solid polymer electrolyte," *Journal of Power Sources,* vol. 35, pp. 235-247, 1991.

[48] E. Quartarone, P. Mustarelli and A. Magistris, "PEO-based composite polymer electrolytes," *Solid State Ionics,* vol. 110, pp. 1-14, 1998.

[49] Y.-H. Li, X.-L. Wu, J.-H. Kim, S. Xin, J. Su, Y. Yan, J.-S. Lee and Y.-G. Guo, "A novel polymer electrolyte with improved high-temperature-tolerance up to 170 °C for high-temperature lithium-ion batteries," *Journal of Power Sources,* vol. 244, pp. 234-239, 2013.

[50] X. Wang, Z. Liu, C. Zhang, Q. Kong, J. Yao, P. Han, W. Jiang, H. Xu and G. Cui, "Exploring polymeric lithium tartaric acid borate for thermally resistant polymer electrolyte of lithium batteries," *Electrochimica Acta,* vol. 92, pp. 132-138, 2013.

[51] R. Strumpler and J. Glatz-Reichenbach, "Conducting Polymer Composites," *Journal of Electroceramics,* vol. 3, pp. 329-346, 1999.

[52] S. Luo and C. Wong, "Conductive Polymer Composites with Positive Temperature Coefficient," International Symposium on Advanced Packaging Materials, 1999.

[53] M. El-Hasnaoui, M. Graça, M. Achour, L. Costa, A. Outzourhit, A. Oueriagli and A. El-Harfi, "Effect of temperature on the electrical properties of copolymer/carbon black mixtures," *Journal of Non-Crystalline Solids,* vol. 356, pp. 1536-1541, 2010.

[54] H. Pang, Y. Zhang, T. Chen, B. Zeng and Z. Li, "Tunable positive temperature coefficient of resistivity in an electrically conducting polymer/graphene composite," *Applied Physics Letters,* vol. 96, 2010.

[55] A. Kono, K. Shimizu, H. Nakano, Y. Goto, Y. Kobayashi, T. Ougizawa and H. Horibe, "Positive-temperature-coefficient effect of electrical resistivity below melting point of poly(vinylidene fluoride) (PVDF) in Ni particle-dispersed PVDF composites," *Polymer,* vol. 53, pp. 1760-1764, 2012.

[56] K. Sada, K. Kokado and Y. Furukawa, "Polyacrylonitrile (PAN)," *Encyclopedia of Polymeric Nanomaterials,* pp. 1-19, 2015.

[57] M. Rahaman, A. Ismail and A. Mustafa, "A review of heat treatment on polyacrylonitrile fiber," *Polymer Degradation and Stability,* vol. 92, pp. 1421-1432, 2007.

[58] R. Beevers, "Dependence of the glass transition temperature of polyacrylonitrile on molecular weight," *Journal of Polymer Science Part A,* vol. 2, no. 12, 1964.

[59] J. Brandrup and E. Immergut, Polymer Handbook, volume 57, 3rd edition, New York: Wiley Interscience, 1989.

[60] Z. Reyes and C. R. C. Rist, "Grafting vinyl monomers to starch by ceric ion. I. Acrylonitrile and acrylamide," *Journal of Polymer Science Part A-1: Polymer Chemistry,* vol. 4, no. 5, 1966.

[61] K. Matyjaszewski, S.-M. Jo, H.-j. Paik and S. Gaynor, "Synthesis of well-defined polyacrylonitrile by atom transfer radical polymerization," *Macromolecules,* vol. 30, no. 20, pp. 6398-6400, 1997.

[62] C. Tang, T. Kowalewski and K. Matyjaszewski, "RAFT Polymerization of Acrylonitrile and Preparation of Block Copolymers Using 2-Cyanoethyl Dithiobenzoate as the Transfer Agent," *Macromolecules,* vol. 36, no. 23, 2003.

[63] D. Benoit, V. Chaplinski, R. Braslau and C. Hawker, "Development of a Universal Alkoxyamine for "Living" Free Radical Polymerizations," *Journal of the American Chemical Society,* vol. 121, no. 16, pp. 3904-3920, 1999.

[64] D. Li and W. Brittain, "Synthesis of poly(N,N-dimethylacrylamide) via nitroxide-mediated radical polymerisation," *Macromolecules,* vol. 31, no. 12, pp. 3852-3855, 1998.

[65] H. Ono, K. Hisatani and K. Kamide, "NMR Spectroscopic Study of Side Reactions in Anionic Polymerization of Acrylonitrile," *Polymer Journal,* vol. 25, pp. 245-265, 1993.

[66] F. Schaper, S. Foley and R. Jordan, "Acrylonitrile Polymerization by Cy3PCuMe and (Bipy)2FeEt2," *Journal of the American Chemical Society,* vol. 126, no. 7, pp. 2114-2124, 2004.

[67] G. Lécayon, Y. Bouizem, C. Le Gressus, C. Reynaud, C. Boiziau and C. Juret, "Grafting and growing mechanisms of polymerised organic films onto metallic surfaces," *Chemical Physics Letters,* vol. 91, pp. 506-510, 1982.

[68] C. Boiziau and G. Lécayon, "Adhesion of polymers to metals: A review of the results obtained studying a model system," *Surface and Interface Analysis,* vol. 12, no. 9, pp. 475-485, 1988.

[69] C. Boiziau, S. Leroy, C. Reynaud, G. Lécayon, C. Le Gressus and P. Viel, "Elementary Mechanisms in the Interaction of Organic Molecules with Mineral Surfaces," *The Journal of Adhesion,* vol. 23, no. 1, pp. 21-44, 1987.

[70] S. Gabriel, R. Jérôme and C. Jérôme, "Cathodic electrografting of acrylics: From fundamentals to functional coatings," *Progress in Polymer Science,* vol. 35, pp. 113-140, 2010.

[71] N. Baute, L. Martinot and R. Jérôme, “Investigation of the cathodic electropolymerization of acrylonitrile, ethylacrylate and methylmethacrylate by coupled quartz crystal microbalance analysis and cyclic voltammetry,” *Journal of Electroanalytical Chemistry,* vol. 472, no. 1, pp. 83-90, 1999.

[72] M. Mertens, C. Calberg, L. Martinot and R. Jérôme, “The Electroreduction of Acrylonitrile: A New Insight into the Mechanism,” *Macromolecules,* vol. 29, pp. 4910-4918, 1996.

[73] O. Hammerich and H. Lund, Organic Electrochemistry, 4th Edition, Revised and Expanded, New York: Marcel Dekker, 2001.

[74] D. Vasudevan and H. Wendt, “Electroreduction of oxygen in aprotic media,” *Journal of Electroanalytical Chemistry,* vol. 392, pp. 69-74, 1995.

[75] C. Laoire, S. Mukerjee, K. Abraham, E. Plichta and M. Hendrickson, “Influence of Nonaqueous Solvents on the Electrochemistry of Oxygen in the Rechargeable Lithium−Air Battery,” *Journal of Physical Chemistry C,* vol. 114, pp. 9178-9186, 2010.

[76] R. Dietz, A. Forno, B. Larcombe and M. Peover, “Nucleophilic reactions of electrogenerated superoxide ion,” *Journal of the Chemical Society (B),* pp. 816-820, 1970.

[77] Y.-K. Han, J.-H. Kim and S.-K. Choi, “Polymerisation of vinyl monomers initiated by KO2-charge transfer agent systems,” *Journal of Polymer Science Part A: Polymer,* vol. 29, pp. 281-286, 1991.

[78] D. Bélanger and J. Pinson, “Electrografting: a powerful method for surface modification,” *Chemical Society Reviews,* no. 7, 2011.

[79] T. Ribelli, K. Augustine, M. Fantin, P. Krys, R. Poli and K. Matyjaszewski, “Disproportionation or Combination? The Termination of Acrylate,” *Macromolecules,* vol. 50, pp. 7920-7929, 2017.

[80] M. Watanabe, M. Kanba, K. Nagaoka and I. Shinohara, “Ionic conductivity of hybrid films composed of polyacrylonitrile, ethylene carbonate, and LiClO4,” *Journal of Polymer Science: Polymer Physics Edition,* vol. 21, no. 6, 1983.

[81] K. Abraham and M. Alamgir, “Li+-conductive solid polymer electrolyte with liquid-like conductivity,” *Journal of the Electrochemical Society,* vol. 137, no. 5, pp. 1657-1658, 1990.

[82] G. Appetecchi, F. Croce, P. Romagnoli, B. Scrosati, U. Heider and R. Oesten, "High-performance gel-type lithium electrolyte membranes," *Electrochemistry Communications,* vol. 1, no. 2, pp. 83-86, 1999.

[83] A. Pasquier, F. Disma, T. Bowner, A. Gozdz, G. Amatucci and J. Tarascon, "Differential scanning calorimetry study of the reactivity of carbon anodes in plastic Li-ion batteries," *Journal of The Electrochemical Society,* vol. 145, pp. 472-477, 1998.

[84] H. Maledi, G. Deng, A. Anari and J. Howard, "Thermal stability studies of Li-ion cells and components," *Journal of The Electrochemical Society,* vol. 146, pp. 3224-3229, 1999.

[85] S. Zhang and T. Jow, "Study of poly(acrylonitrile-methyl methacrylate) as binder for graphite anode and LiMn2O4 cathode of Li-ion batteries," *Journal of Power Sources,* vol. 109, pp. 422-426, 2002.

[86] A. Grabanov and Y. Sazanov, "Polyacrylonitrile: carbonization problems," *Russian Journal of Applied Chemistry,* vol. 81, pp. 919-932, 2008.

[87] C. Nan, Y. Shen and J. Ma, "Physical Properties of Composites Near Percolation," *Annual Reviews,* vol. 40, pp. 131-151, 2010.

[88] C. Wei, D. Srivastava and K. Cho, "Thermal Expansion and Diffusion Coefficients of Carbon Nanotube-Polymer Composites," NASA Ames Research Center.

[89] D.-W.-V. Krevelen, "Properties of Polymers," p. 167, 1990.

[90] P.-J. Hendra, H.-P. Jobic and K.-J. Holland-Moritz, *Journal of Polymer Science Part C-Polymer Letters,* vol. 13, p. 365, 1975.

[91] R. Lam and P.-H. Geil, *Journal of Macromolecular Science Part B Physics,* vol. 20, p. 37, 1981.

[92] M. Hasnaoui, M. Graca, M. Achour, L. Costa, A. Outzourhit, A. Oueriagli and A. Harfi, "Effect of temperature on the electrical properties of copolymer/carbon black mixtures," *Journal of Non-Crystalline Solids,* vol. 356, pp. 1536-1541, 2010.

[93] K. Lozano, L. Espinoza, K. Hernandez, A.-R. Adhikari, G. Radhakrishnan and P.-M. Adams, "Investigation of the electromagnetic interference shielding of titanium carbide coated nanoreinforced liquid crystalline polymer," *Journal of Applied Physics,* vol. 105, 2009.

[94] C. Nan, R. Yuan and Z. Yang, “Percolation Phenomena in Niobium-doped TiC1-x,” *Materials Science and Engineering,* pp. 283-286, 1991.

[95] Y. Liu, S. Hino, K. Oshima, T. Yamauchi, M. Shimomura and S. Miyauchi, “Polymerisation of 3-Hexylthiophene in the Presence of Titanium Carbide and Conductivity-Temperature Characteristics of the Conductive Composite Product,” *Kobunshi Ronbunshu,* vol. 56, no. 7, pp. 440-444, 1999.

[96] L. Shen, L. Shen, Z. Wang and L. Chen, “In Situ Thermally Cross-linked Polyacrylonitrile as Binder for High-Performance Silicon as Lithium Ion Battery Anode,” *ChemSusChem,* vol. 7, pp. 1951-1956, 2014.

[97] M. Roberts, P. Johns, J. Owen, D. Brandell, K. Edstrom, G. El-Enany, C. Guery, D. Golodnitshy, M. Lacey, C. Lecoeur, H. Mazor, E. Peled, E. Perre, M. Shaijumon, P. Simon and P. Taberna, “3D lithium ion batteries - from fundamentals to fabrication,” *Journal of Materials Chemistry,* vol. 21, no. 27, pp. 9876-9890, 2011.

[98] H. Zhang, Y. Yang, D. Ren, L. Wang and X. He, “Graphite as anode materials: Fundamental mechanism, recent progress and advances,” *Energy Storage Materials,* vol. 36, pp. 147-170, 2021.

[99] A. Bard and L. Faulkner, Electrochemical Methods Fundamentals and Applications Second Edition, John Wiley & Sons, 2001.

[100] T. Reddy and D. Linden, Linden's Handbook of Batteries Fourth Edition, Mc Graw Hill, 2011.

[101] S. Saxena, Y. Xing, D. Kwon and M. Pecht, “Accelerated degradation model for C-rate loading of lithium-ion batteries,” *International Journal of Electrical Power & Energy Systems,* vol. 107, pp. 438-445, 2019.

[102] P. Keil, “Aging of Lithium-Ion Batteries in Electric Vehicles,” Technical University of Munich, 2017.

[103] J. Metz, Introduction to Optical Microscopy, Roberts and Company Publishers, 2009.

[104] J. Goldstein, D. E. Newbury, D. C. Joy, C. E. Lyman, P. Echlin, E. Lifshin, L. Sawyer and J. R. Michael, Scanning Electron Microscopy and X-Ray Microanalysis: Third Edition, Boston: Springer, 2003.

[105] L. Reimer, Scanning electron microscopy : physics of image formation and microanalysis, Springer, 1998.

[106] R. Egerton, Physical principles of electron microscopy : an introduction to TEM, SEM, and AEM, Springer, 2005.

[107] A. Clarke, Microscopy techniques for materials science, CRC Press, 2002.

[108] "Overview of Reference Electrodes and Alternative Reference Electrodes Alternative Reference Electrodes Brief Discussion about Standard and Pseudo Reference Electrodes," Pine Research Instrumentation, 2016.

[109] "Reference Electrode Product Guide," Pine Research Instrumentation .

[110] A. M. Helmenstine, "Table of Electrical Resistivity and Conductivity," ThoughtCo, 27 June 2019. [Online]. Available: https://www.thoughtco.com/table-of-electrical-resistivity-conductivity-608499. [Accessed 8 May 2020].

[111] "Diffusion Coefficient," Comsol, 22 February 2017. [Online]. Available: https://uk.comsol.com/multiphysics/diffusion-coefficient. [Accessed 10 May 2020].

[112] T. Richard, "Calculating the Oxygen Diffusion Coefficient in Water," Cornell Waste Management Institute, [Online]. Available: http://compost.css.cornell.edu/oxygen/oxygen.diff.water.html. [Accessed 10 May 2020].

[113] D. Pletcher, A First Course in Electrode Processes, RSCPublishing, 2009.

[114] D. Pletcher, R. Greff, R. Peat, L. Peter and J. Robinson, Instrumental Methods in Electrochemistry, Elsevier Science & Technology, 2001.

[115] J. Ferraro, K. Nakamoto and C. Brown, Introductory Raman Spectroscopy, Academic Press, 2003.

[116] B. Schrader, Infrared and Raman Spectroscopy: Methods and Applications, VCH, 1995.

[117] R. McCreery, Raman Spectroscopy for Chemical Analysis, John Wiley & Sons, 2000.

[118] D. Chowdhury, L. Spiccia, S. Amritphale, A. Paul and A. Singh, "Electronic supplementary information for A robust iron oxyhydroxide water oxidation catalyst operating under near

neutral and alkaline conditions," *Journal of Materials Chemistry A,* vol. 4, pp. 3655-3660 , 2016.

[119] X. Li, D. Heryadi and A. Gewirth, "Electroreduction Activity of Hydrogen Peroxide on Pt and Au Electrodes," *Langmuir,* vol. 21, pp. 9251-9259, 2005.

[120] S. Patra and N. Munichandraiah, "Electrochemical reduction of hydrogen peroxide on stainless steel," *Journal of Chemical Sciences,* vol. 121, pp. 675-683, 2009.

[121] Z. Deng, L. Li, Y. Ren, C. Ma, J. Liang, K. Dong, L. Qian, L. Yonglan, T. Li, B. Tang, Y. Liu, S. Gao, A. Asin, S. Yan and X. Sun, "Highly efficient two-electron electroreduction of oxygen into hydrogen peroxide over Cu-doped TiO2," *Nano Research,* 2021.

[122] K. Stewart and A. Gewirth, "Mechanism of Electrochemical Reduction of Hydrogen Peroxide on Copper in Acidic Sulfate Solutions," *Langmuir,* vol. 23, pp. 9911-9918, 2007.

[123] T. Ozawa and A. Hanaki, "Reactions of Superoxide with Water and with Hydrogen Peroxide," *Chemical and Pharmaceutical Bulletin,* vol. 29, no. 4, pp. 926-928, 1981.

[124] X. Cai, E. Tanner, C. Lin, K. Ngamchuea, J. Foord and R. Compton, "The mechanism of electrochemical reduction of hydrogen peroxide on silver nanoparticles," *Physical Chemistry Chemical Physics,* no. 3, 2018.

[125] C. Bureau, "Polymerization reaction coupled to charge transfer: propagation versus termination as asource of permanent travelling waves and multi-peak voltammograms," *Journal of Electroanalytical Chemistry,* vol. 43, p. 479, 1999.

[126] M. Mertens, C. Calberg, N. Baute, R. Jérôme and L. Martinot, "Solvent effect on the electrografting of acrylonitrile on nickel," *Journal of Electroanalytical Chemistry,* vol. 441, pp. 237-244, 1998.

[127] B. Singh-Tomar, A. Shahin and M. Tirumekudulu, "Cracking in drying films of polymer solutions," *Soft Matter,* no. 14, 2020.

[128] J. Mark, Polymer Data Handbook, Oxford: Oxford Universiy Press, 1999.

[129] J. Pellon, N. Smyth, R. Kugel and W. Thomas, "Cast polyacrylonitrile. I. Casting methods," *Journal of applied polymer science,* vol. 10, no. 3, pp. 421-428, 1966.

[130] A. Oplatka, M. Konigsbuch and N. Shavit, “Casting of transparent polyacrylonitrile,” *Journal of polymer science. Part C. Polymer symposia,* vol. 16, no. 5, pp. 2795-2804, 1967.

[131] N. Shavit, M. Konigsbuch and A. Oplatka, “New transparent plastics of polyacrylonitrile,” *Journal of polymer science. Part C. Polymer symposia,* vol. 16, no. 3, pp. 1247-1255, 1967.

[132] L. Zhang, H. Li and J. Zhang, “Kinetics of oxygen reduction reaction on three different Pt surfaces of Pt/C catalyst analyzed by rotating ring-disk electrode in acidic solution,” *Journal of Power Sources,* vol. 255, pp. 242-250, 2014.

[133] P. Easter and D. Taylor, “Azine bridge formation during the electrografting of acrylonitrile,” *Journal of Polymer Science Part A: Polymer Chemistry,* vol. 47, no. 6, pp. 1685-1695, 2009.

[134] H. Singh, S. Zhuang, B. Ingis, B. Nunna and E. Lee, “Carbon-based catalysts for oxygen reduction reaction: A review on degradation mechanisms,” *Carbon,* vol. 151, pp. 160-174, 2019.

[135] B. Jung, J. Yoon, B. Kim and H. Rhee, “Effect of crystallization and annealing on polyacrylonitrile membranes for ultrafiltration,” *Journal of Membrane Science,* vol. 246, pp. 67-76, 2005.

[136] P. Correia, P. Carvalho and F. Farelo, “Discoloration in PAN during production of acrylic fibre,” Fisipe – Fibras Sintéticas de Portugal, Lisbon.

[137] G. Konstantopoulos, S. Soulis, D. Dragatogiannis and C. Charitidis, “Introduction of a Methodology to Enhance the Stabilization Process of PAN Fibers by Modeling and Advanced Characterization,” *Materials,* vol. 13, no. 12, 2020.

[138] A. Kaniyoor and S. Ramaprabhu, “A Raman spectroscopic investigation of graphite oxide derived graphene,” *AIP Advances,* vol. 2, no. 3, 2012.

[139] C. Shendhe, W. Smith, C. Brouillette and S. Farquharson, “Drug Stability Analysis by Raman Spectroscopy,” *Pharmaceutics,* vol. 6, pp. 651-662, 2014.

[140] F. Beck, “Electrodeposition of polymer coatings,” *Electrochimica Acta,* vol. 33, no. 7, pp. 839-850, 1988.

[141] X. Wang, J. Yang, Y. Liu, J. Liu, Z. Shen and J. Liang, “Rapid and Continuous Preparation of Polyacrylonitrile-Based Carbon Fibers with Electron-Beam Irradiation Pretreatment,” *Materials,* vol. 11, 2018.

[142] F. Sebasta, J. John, A. Motl and K. Stamberg, “Evaluation of Polyacrylonitrile (PAN) as a Binding Polymer for Absorbers Used to Treat Liquid Radioactive Wastes,” Czech Technical University, Prague, 1995.

[143] “Raman bands explained,” Renishaw, [Online]. Available: https://www.renishaw.com/en/raman-bands-explained--25808#:~:text=The%20frequencies%20of%20vibration%20depend,bonds%20have%20high%20Raman%20shifts.. [Accessed 24 June 2020].

[144] S. Choudhury, Rational Design of Nanostructured Polymer Electrolytes and Solid–Liquid Interphases for Lithium Batteries, New York: Springer Theses, 2019.

[145] U.-S. Agarwal and D.-V. Khakhar, “Simulation of diffusion-limited step-growth polymerization in 2D: Effect of shear flow and chain rigidity,” *The Journal of Chemical Physics,* vol. 99, pp. 3067-3074, 1993.

[146] F. Yang, “Diffusion-Limited Growth of a Spherical Nanocrystal in a Finite Space,” *Langmuir,* vol. 37, pp. 3912-3921, 2021.

[147] E. Dartois and F. Langlet, “Carbon dioxide clathrate hydrate formation at low temperature: Diffusion-limited kinetics growth as monitored by FTIR,” *Astronomy & Astrophysics,* vol. 652, 2021.

[148] “Polyacrylonitrile,” Sigma-Aldrich, [Online]. Available: https://www.sigmaaldrich.com/catalog/product/aldrich/181315?lang=en&region=GB&gclid=EAIaIQobChMIme-DrYHU6gIV0u3tCh2BMwYUEAAYASAAEgL9fvD_BwE. [Accessed 20 July 2020].

[149] A. Gupta and N. Chand, “Effect of copolymerization on the crystalline structure of polyacrylonitrile,” *European Polymer Journal,* vol. 15, no. 10, pp. 899-902, 1979.

[150] L. Wang, A. Menakath, F. Han, Y. Wang, P. Zavalij, K. Gaskell, O. Borodin, D. Luga, S. Brown, C. Wang, K. Xu and B. Eichhorn, “Identifying the components of the solid–electrolyte interphase in Li-ion batteries,” *Nature Chemistry,* vol. 11, pp. 789-796, 2019.

[151] S.-J. An, J. Li, C. Daniel, D. Mohanty, S. Nagpure and D.-L. Wood, "The state of understanding of the lithium-ion-battery graphite solid electrolyte interphase (SEI) and its relationship to formation cycling," *Carbon,* vol. 105, pp. 52-76, 2016.

[152] J. Asenbauer, T. Eisenmann, M. Kuenzel, A. Kazzai, Z. Chen and D. Bresser, "The success story of graphite as a lithium-ion anode material – fundamentals, remaining challenges, and recent developments including silicon (oxide) composites," *Sustainable Energy Fuels,* 2020.

[153] S. Gantenbein, M. Schonleber, M. Weiss and E. Ivers-Tiffee, "Capacity Fade in Lithium-Ion Batteries and Cyclic Aging over Various State-of-Charge Ranges," *Sustainability,* vol. 11, pp. 1-15, 2019.

[154] K. Wang, K. Jiang, Y. Luo and Q. Li, "Sandwich-structured Cathodes with Cross-stacked Carbon Nanotube Film as Conductive Layer for High Performance Lithium-ion Batteries," *Journal of Materials Chemistry A,* vol. 351, pp. 160-168, 2017.

[155] L. Zhang, J. Jiang and W. Zhang, "Capacity Decay Mechanism of the LCO + NMC532/Graphite Cells Combined with Post-Mortem Technique," *Energies,* vol. 10, p. 1147, 2017.

[156] "Polyethylene Fibres," Goonvean Fibres Limited, [Online]. Available: https://goonveanfibres.com/products-services/polyethylene/. [Accessed 2020 August 19].

[157] J. Schawe, R. R, J. Widmann, M. Schubnell and U. Jorimann, "Artifacts in DSC UserCom," Mettler Toledo, 2000.

[158] T. Landsman, S. Jessen, E. Ungchusri and S. Hasan, "Design and Verification of a Shape Memory Polymer Peripheral Occlusion Device," *Journal of the Mechanical Behavior of Biomedical Materials,* vol. 63, pp. 195-206, 2016.

[159] L. Thomas, "Interpreting Unexpected Events and Transitions," TA Instruments.

[160] B. Sickler, "Interpreting DSC Data," Tempo Labs.

[161] A. Araújo, M. Bezerra, S. Storpirtis and J. Matos, "Determination of the melting temperature, heat of fusion, and purity analysis of different samples of zidovudine (AZT) using DSC," *Brazilian Journal of Pharmaceutical Sciences,* vol. 46, no. 1, pp. 37-43, 2010.

[162] M. Rodríguez-Laguna, P. Gómez-Romero, C. Torres, M. Lu and E. Chávez-Ángel, "Development of low-melting point molten salts and detection of solid-to-liquid transitions by alternative techniques to DSC," *Solar Energy Materials and Solar Cells,* vol. 292, pp. 1-9, 2019.

[163] C. Schick, "Calorimetry," Elsevier, Rostock, 2012.

[164] M. Dannis, "Thermal Expansion Measurements and Transition Temperatures, First and Second Order," *Rubber Chemistry and Technology,* vol. 32, no. 4, pp. 1005-1015, 1959.

[165] N. Fasanella and V. Sundararaghavan, "Atomistic modeling of thermomechanical properties of SWNT/Epoxy nanocomposites," *Modelling and Simulation in Materials Science and Engineering,* vol. 23, no. 6, 2015.

[166] T. Waldmann, R.-G. Scurtu, K. Richter and M. Wohlfahrt-Mehrens, "18650 vs. 21700 Li-ion cells – A direct comparison of electrochemical, thermal, and geometrical properties," *Journal of Power Sources,* vol. 472, 2020.

[167] J. Dahn, T. Zheng, Y. Liu and J. Xue, "Mechanisms for Lithium Insertion in Carbonaceous Materials," *Science,* vol. 270, pp. 590-593, 1995.

[168] R. Fong, U. Socken and J. Dahn, "Studies of Lithium Intercalation into Carbons Using Nonaqueous Electrochemical Cells," *Journal of The Electrochemical Society,* vol. 137, no. 7, pp. 2009-2013, 1990.

[169] D. Stevens and J. Dahn, "The Mechanisms of Lithium and Sodium Insertion in Carbon Materials," *Journal of The Electrochemical Society,* vol. 148, no. 8, pp. 803-811, 2001.

[170] F. Guo, Y. Wang, T. Kang, C. Liu, Y. Shen, W. Lu, X. Wu and L. Chen, "A Li-dual carbon composite as stable anode material for Li batteries," *Energy Storage Materials,* vol. 15, pp. 116-123, 2018.